Tailoring spintronic terahertz emitters for special applications

Dissertation

zur Erlangung des
Doktorgrades der Naturwissenschaften (Dr. rer. nat.)

der

Naturwissenschaftlichen Fakultät II - Chemie, Physik und Mathematik

der Martin Luther Universität
Halle-Wittenberg

vorgelegt von

Herrn Bikash Das Mohapatra

Doctoral Defense

Date : 28.04.2025

Supervisor: Prof. Dr. Georg Schmidt

1st referee : Prof. Dr. Georg Schmidt
2nd referee : Prof. Dr. Jörg Schilling
3rd referee : Prof. Dr. Benjamin Jungfleisch

Chair of the examination committee : Prof. Dr. Thorid Rabe

Dedication

To Romy and my parents

Abstract

Ultrafast spintronics is fast gaining interest for its potential to facilitate the next generation of spintronic devices with high operating speeds. The generation of THz electromagnetic radiation, upon femtosecond laser excitation, from magnetic materials has demonstrated the underlying spin physics to achieve magnetisation control at terahertz frequencies. Broadband and efficient THz emission could be realised with the state-of-the-art Spintronic terahertz emitters. This study explores spintronic effects induced by femtosecond laser excitation in diverse magnetic multilayers, with a focus on magnetic heterostructures for terahertz spintronic applications. It delves into the geometric influence on emitted response due to electrical, magnetic, and thermal dynamics, and investigates techniques to devise new spintronic devices. The impact of charge equilibration on ultrafast currents in spintronic THz emitters is investigated. The conversion of spin current to charge current, the subsequent charging phenomena at the edge of the illuminated area, and the resulting current backflow are explored. The importance of delayed charge equilibration in enabling the detection of the primary current pulse via THz emission is highlighted. Additionally, the modifications in the emission spectrum caused by charge dynamics in miniaturised periodically patterned spintronic THz emitters are addressed, emphasising the systematic spectral changes with emitter size including reductions at lower frequencies. The optical excitation and detection of emitted THz radiations are facilitated by a free space pump-probe setup. The development of an analytical model, that quantitatively reproduces these results and aligns well with control experiments, is mentioned, paving the way for a detailed investigation of the charge dynamics in spintronic THz emitters and the provision of insights for controlled shaping of emission spectra through nanopatterning. Several ultrafast applications are demonstrated using on-chip electrical detection of ultrafast currents. Notable contributions in terms of applications are the engineering of narrowband terahertz emitter and the successful realisation of Digital-to-Analog converters for ultrafast signals. Furthermore, the electrical control of magnetisation switching for THz response is highlighted. The impact of fs-laser excitation on pseudo-spin valve structures is also explored, unveiling a transient decrease in magnetoresistance due to demagnetisation. Moreover, this study uncovers compelling insights into thermoelectric effects in magnetic heterostructures under fs-laser excitation, emphasising the potential for further unravelling of spincaloritronics physics. This culminates in the design of a switchable terahertz emitter using a heterostructure with a non-magnetic layer sandwiched between two ferromagnetic layers. Overall, the research presented in this thesis holds the potential to achieve transformative advancements in ultrafast signal processing and terahertz applications in spintronic devices.

Contents

List of Figures **xiii**

1 Introduction **1**

2 Theoretical Background **5**
- 2.1 Spintronic Terahertz Emitter . . . 5
- 2.2 Excitation of metals by fs-laser pulse . . . 8
  - 2.2.1 Generation of hot electrons . . . 8
  - 2.2.2 Spin-Orbit interactions . . . 8
- 2.3 Magnetic ordering in solids . . . 10
  - 2.3.1 Exchange interaction . . . 10
  - 2.3.2 Stoner Model . . . 11
- 2.4 Magnetisation behaviour in external magnetic field . . . 12
  - 2.4.1 Spin dynamics . . . 12
  - 2.4.2 Hysteresis . . . 13
  - 2.4.3 Magnetic anisotropy . . . 14
- 2.5 Spin transport . . . 17
  - 2.5.1 Spin injection across FM|NM interface . . . 18
  - 2.5.2 Super-diffusive spin current . . . 19
  - 2.5.3 Magnons . . . 20
- 2.6 Effects due to electric and magnetic fields . . . 21
  - 2.6.1 Spin dependent Hall effects . . . 21
  - 2.6.2 Magneto-resistive effects . . . 25
  - 2.6.3 Oersted field . . . 27
- 2.7 Thermal effects . . . 27
  - 2.7.1 Joule heating . . . 27
  - 2.7.2 Thermoelectric effects . . . 28
- 2.8 Ultrafast Demagnetisation induced by hot-electron transport . . . 31

3 Experimental Methods **33**
- 3.1 Ultra High Vacuum (UHV) deposition systems . . . 33
  - 3.1.1 RF/DC Magnetron Sputtering . . . 33
  - 3.1.2 Electron beam Evaporation . . . 34
- 3.2 Etching systems . . . 34
  - 3.2.1 Ar-ion milling . . . 34
  - 3.2.2 Oxygen Plasma Etching . . . 35

3.3 Lithography 35
3.3.1 Optical Lithography 35
3.3.2 Electron-beam Lithography 36
3.3.3 Laser Interference Lithography 36
3.4 Fabrication 37
3.4.1 Additive approach to patterning 37
3.4.2 Subtractive approach to patterning 37
3.5 Characterisation 39
3.5.1 Magneto-optic Kerr effect (MOKE) 39
3.5.2 DC Probe Station 40
3.6 Terahertz measurement setups 41
3.6.1 Pump and probe electro-optic sampling in free space 41
3.6.2 Ultrafast electrical detection 42

4 Charge Dynamics in Spintronic THz Emitters 45
4.1 Simulation details 47
4.2 Charge dynamics in a thin film STE 49
4.2.1 Charge dynamics Circuit model 53
4.3 Factors affecting RC time constant 55
4.3.1 Effect of laser beam size and shape 55
4.3.2 Effect of laser temporal width and shape 57
4.3.3 Effect of STE electrical conductivity 59

5 Nanopatterned Spintronic THz emitters 65
5.1 Experimental details 68
5.2 Nanopatterned STEs 69
5.2.1 THz emission from square nanoSTEs 69
5.2.2 Charge dynamics in nanoSTE 73
5.2.3 THz emission from rectangular nanoSTEs 75
5.2.4 Effect of spacing between nanoSTEs 77
5.2.5 Charge accumulation in nanoSTEs 78
5.2.6 Modelling the THz spectrum for nanoSTE 79
5.3 STE stripes 86
5.4 STE metastructures 92

6 Terahertz Spintronic Devices 99
6.1 Frequency-specific Narrowband THz emission 101
6.1.1 Experimental details 102
6.1.2 Sequentially emitting STEs 104
6.1.3 Pulse burst from coplanar waveguide 109
6.1.4 Frequency selectivity for narrowband emission 111
6.1.5 Optimisation for high Q-factor of narrowband spectrum 112
6.2 Digital to Analog Converter for ultrafast signals 114
6.2.1 Experimental details 114

6.2.2 Coercive fields of STE stripes . . . 115
6.2.3 4-bit DAC with STE stripes . . . 117
6.2.4 3-bit DAC with STEs of different FMs . . . 119
6.3 Ultrafast current control by Oersted fields . . . 122
6.3.1 Experimental details . . . 123
6.3.2 Fluence and magnetisation dependence of Cu/STE stripes . . . 124
6.3.3 Extraction of electrical response contributions . . . 125

7 THz excitation of magnetic multilayers 133
7.1 Pseudo spin-valve multilayer optimisation for GMR . . . 135
7.2 Ultrafast excitation of CIP-GMR device . . . 139
7.2.1 Experimental details . . . 139
7.2.2 Ultrafast electrical response from pseudo spin-valve stripe . . . 140
7.2.3 Joule heating due to dc-bias current . . . 141
7.2.4 Heating of metal interface thermocouple by fs-laser pulse . . . 143
7.2.5 Ultrafast excitation of pseudo spin-valve on waveguide . . . 144
7.3 THz excitation of FM|NM|FM trilayer . . . 147
7.3.1 SSE mediated ultrafast electrical response . . . 149
7.3.2 Understanding the contribution of FM layers . . . 149
7.3.3 Influence of FM|substrate interface . . . 151
7.3.4 Influence of spacer layer . . . 152
7.4 Switchable THz emitters . . . 154

8 Summary 161

A Appendix 165
A.1 Wave Propagation . . . 165
A.1.1 TE/TM modes . . . 165
A.1.2 CST electromagnetic simulation . . . 165
A.2 COMSOL AC/DC Simulation . . . 166
A.3 Fourier Transform of differential equation . . . 166
A.4 Signal Processing . . . 167
A.4.1 Von Hann Window . . . 167
A.5 Fitting of Spectral Amplitude using analytical model . . . 168
A.5.1 Square nanoSTEs on sapphire substrate . . . 169
A.5.2 Square nanoSTEs on glass substrate . . . 171
A.5.3 Rectangular nanoSTEs . . . 172
A.5.4 Square nanoSTEs with varying spacing . . . 174
A.5.5 Rectangular nanoSTEs with varying spacing . . . 175
A.6 Electronics . . . 176
A.6.1 Differential Non Linearity . . . 176
A.6.2 Integral Non Linearity . . . 176

B References 179

List of Publications(s) **xxi**

Curriculum vitae **xxiii**

Eidesstattliche Erklärung (Statutory declaration) **xxv**

Acknowledgement **xxvii**

List of Figures

2.1 Illustration showing a Spintronic Terahertz Emitter and its underlying mechanisms upon fs-laser excitation. 6

2.2 Spin-Orbit Coupling. 9

2.3 Stoner Model representation for a ferromagnetic and a nonmagnetic metal. . 11

2.4 Magnetisation precession and Damping. 12

2.5 Illustration showing Magnetic hysteresis through *M-H* curve. 14

2.6 Illustration showing the effect of shape anisotropy reflected by the difference in Coercive fields. 16

2.7 Spin and charge transport. 17

2.8 Illustration showing spinwaves also known as magnons. 20

2.9 Spin-dependent scattering mechanisms 21

2.10 Illustration showing hall effects: OHE, AHE, SHE and ISHE. 22

2.11 GMR in two ferromagnets separated by a spacer magnetic layer in CIP configuration. 25

2.12 Thermoelectric effects: Seebeck effect, ANE, SDSE and SSE 28

3.1 Fabrication Process with liftoff 37

3.2 Fabrication Process with etching 38

3.3 MOKE Schematics 40

3.4 THz pump and probe setup 41

3.5 THz electrical setup 42

4.1 Current vs. Time for reference emitter 50

4.2 Charge and Current distribution at different times 51

4.3 Spectral Intensities for the current densities and their derivatives 52

4.4 Schematics for charge dynamics in STE and equivalent circuit 54
4.5 Effect of laser beam size on current density 55
4.6 Current density with Gaussian beam profile and its charge distribution 56
4.7 Effect of laser temporal width on current density 57
4.8 Current density for antisymmetric bipolar pulse 58
4.9 Effect of current density due to material conductivity 59
4.10 Effect of current density due to material thickness 60
4.11 Filter characteristics 61
4.12 Effect of substrate dielectrics on filter characteristics 62

5.1 Schematics showing THz emission from nanoSTE 68
5.2 SEM images of nanoSTEs 70
5.3 Time domain EOS signals and spectral amplitudes from nanoSTEs on sapphire and glass substrates 71
5.4 CST simulation for TE/TM modes in transmission for electromagnetic wave propagation 72
5.5 Charge and current densities from COMSOL simulation of square nanoSTEs 73
5.6 Comparison of filter factors for square nanoSTEs 74
5.7 Time domain EOS signals and spectral amplitudes for rectangular nanoSTEs and comparison of their filter factors via COMSOL simulation 76
5.8 Time domain EOS signals and spectral amplitudes for nanoSTEs with varying spacing 77
5.9 Schematics showing charge dynamics in nanoSTE and equivalent circuit . . . 78
5.10 Relative amplitude and phase for square nanoSTES on sapphire and glass substrates from both experiment and model 80
5.11 Relative amplitude and phase for rectangular nanoSTES on sapphire substrate from both experiment and model 83
5.12 Relative amplitude and phase for nanoSTES with varying spacing on sapphire substrate from both experiment and model 84
5.13 Schematics showing geometrical influence of charge dynamics 85
5.14 SEM image of STE stripes and their EOS signal and spectral amplitude in parallel and perpendicular configurations 86

5.15 EOS signals for different polarisation of incident laser pulse for both parallel and perpendicular configurations of STE stripes 88
5.16 Normalised amplitude and phase for the transfer function obtained for striped STEs in both parallel and perpendicular configurations for both polarisation states of incident laser pulse 89
5.17 COMSOL simulation showing current density, spectral amplitude and filter factor for both parallel and perpendicular configurations. 91
5.18 SEM image of STE-SRR and corresponding EOS signal, spectral amplitudes and transfer functions for **U** and **C** configurations 93
5.19 Incident light polarisation study on STE-SRR 95

6.1 Ultrafast electrical response from a single STE on transmission line 102
6.2 Illustration showing spectral shapes as a result of various temporal shapes and requirements for narrowband spectrum 103
6.3 Schematics for meander design for alternating electrical pulses 105
6.4 Ultrafast electrical response from a meander shaped transmission line with multiple STEs 106
6.5 Responses for different STE configurations on meander shaped transmission line 107
6.6 PSD for different STE configurations on meander-shaped transmission line . 108
6.7 Pulse burst from CPW 109
6.8 Pulse burst from CPW of different STE configurations 110
6.9 Frequency modification based on inter-STE path length in CPW pulse burst emitter 112
6.10 High Gain CPW pulse burst emitter 113
6.11 STE stripes on transmission line 115
6.12 Coercive fields of STE stripes of varying width 116
6.13 4-bit THz DAC device based on STE stripes of different widths having different coercive fields 117
6.14 4-bit DAC for different digital codes and the corresponding DNL and INL for the device 118
6.15 3-bit DAC device with different ferromagnetic bits of different coercivities . . 120
6.16 Illustration showing Oersted Field induced ultrafast current pulse 122

6.17 COMSOL simulation showing magnetic flux densities for different dc-bias currents . . . 123
6.18 Optical microscope images of Cu/STE stripes . . . 123
6.19 Fluence dependence of the Cu/STE stripes . . . 124
6.20 Magnetisation dependence of the Cu/STE stripes . . . 125
6.21 Extraction of Joule heating and ISHE signals for low magnetic field responses 126
6.22 Extraction of Joule heating and ISHE signals for for saturation magnetic field 127
6.23 Extraction of Oersted field and external magnetic field induced ISHE signals from mixed signals due to Joule heating and ISHE . . . 128
6.24 Extraction of Oersted Field induced ISHE signal for different dc-bias currents 129

7.1 MOKE and MR for different FM/spacer/FM layer stacks . . . 136
7.2 Optimised pseudo spin-valve device with maximum GMR of 4.7% . . . 138
7.3 Ultrafast excitation setup for CIP-GMR device with dc-bias current . . . 139
7.4 Ultrafast electrical responses from pseudo spin-valve stripes with dc-bias current for parallel and antiparallel states for parallel and perpendicular $\vec{H}$ directions. . . . 140
7.5 Ultrafast electrical response from pseudo spin-valve device on waveguide and the effect of Joule heating due to dc-bias current . . . 142
7.6 Thermovoltage generation from fs-laser heating . . . 143
7.7 Ultrafast electrical response from pseudo spin-valve device on waveguide with $I_{\text{dc-bias}}$ for both parallel and antiparallel alignments of the $\vec{M}$ . . . 145
7.8 Extraction of ISHE and dc-bias current components from the ultrafast electrical response from pseudo spin-valve device on waveguide and effect of fs-laser excitation on magnetoresistance . . . 146
7.9 Ultrafast $\vec{M}$ dependent electrical signal from the FM|NM|FM trilayer due to $\vec{\nabla}T$ in the layer stack . . . 147
7.10 Interaction between FM and substrate due to the heat gradient from fs-laser heating . . . 148
7.11 Ultrafast electrical signal from FM1|NM|FM2 trilayer as compared to SSE mediated signal in YIG/Pt bilayer . . . 149
7.12 Role of FMs in ultrafast $\vec{M}$ dependent electrical signals . . . 150
7.13 Role of FM material and substrate interface on Ultrafast electrical signal . . 151

7.14 Role of spacer layer on Ultrafast $\vec{M}$ dependent electrical signals 152
7.15 Switchability of the spin-valve based STEs w.r.t. the amplitudes corresponding to parallel and antiparallel $\vec{M}$ states 154
7.16 Switchable STE based on sandwiched configuration of FM/spacer/FM with a heavy metal spacer 156
7.17 Ultrafast electrical response from FM/Cu/HM/Cu/FM layer stacks with switchability based on amplitudes of parallel and antiparallel $\vec{M}$ states 157

A.1 Illustration showing Hann function. 167
A.2 Conductivity and electrical permittivity of STE layers and analytical model fitting on thin film STE, ... 168
A.3 Analytical model fitting for square nanoSTEs on sapphire substrate. 170
A.4 Analytical model fitting for square nanoSTEs on glass substrate. 171
A.5 Analytical model fitting for rectangular nanoSTEs (for $\vec{M} \parallel h$) on sapphire substrate. 172
A.6 Analytical model fitting for rectangular nanoSTEs (for $\vec{M} \perp h$) on sapphire substrate. 173
A.7 Analytical model fitting for square nanoSTEs with varying spacing on sapphire substrate. 174
A.8 Analytical model fitting for rectangular nanoSTEs with varying spacing on sapphire substrate. 175

List of Abbreviations

AHE	Anomalous Hall Effect
AMR	Anisotropic Magnetoresistance
ANE	Anomalous Nernst Effect
CIP	Current-in-plane
CPP	Current-perpendicular-to-plane
CPW	Coplanar Waveguide
DAC	Digital to Analog Converter
DNL	Differential Non-Linearity
DOS	Density of States
EOS	Electro-optic Sampling
FFT	Fast-Fourier Transform
FM	Ferromagnet
FWHM	Full Width at Half Maximum
GMR	Giant Magnetoresistance
HM	Heavy Metal
INL	Integral Non-Linearity
ISHE	Inverse Spin Hall Effect
LL	Landau-Lifshitz
LLG	Landau-Lifshitz-Gilbert
LSb	Least Significant bit
LSSE	Longitudinal Spin Seebeck Effect
MOKE	Magneto-optic Kerr Effect
MR	Magnetoresistance
NM	Non-magnet

OHE	Ordinary Hall Effect
PSD	Power Spectral Density
RKKY	Ruderman-Kittel-Kasuya-Yosida
RMS	Root Mean Square
RT	Room Temperature
SDSE	Spin-dependent Seebeck Effect
SEM	Scanning Electron Microscope
SHE	Spin Hall Effect
SOT	Spin Orbit Torque
SRR	Split Ring Resonator
SSE	Spin Seebeck Effect
STE	Spintronic Terahertz Emitter
STT	Spin Transfer Torque
TE	Transverse Electric
TM	Transverse Magnetic
TMR	Tunneling Magnetoresistance
TSSE	Transverse Spin Seebeck Effect
UHV	Ultra High Vacuum

1 Introduction

Evolving over decades, extensive research has been dedicated to the manipulation and control of the magnetic state of materials. The quest to comprehend the physics of underlying magnetisation dynamics has been propelled by the vast potential for technological applications, including magnetic hard disk drives, memory devices, and sensors. As traditional silicon technology based on charge currents approached its physical limitations [1], the pursuit of next-generation devices that transcend Moore's Law was at the forefront. Enter the realm of spintronics, aimed at catalysing the speed and density of data storage while concomitantly reducing energy consumption through the creation, manipulation, and detection of spin currents [2]. This led to a significant breakthrough in the realisation of spintronic magnetic memories, sensors, and data storage devices after the discovery of giant magneto-resistance [3, 4] and tunnel magneto-resistance [5]. Nevertheless, spintronic concepts are required to continuously progress in tandem with other technologies [1].

In response to the ever-increasing demands for higher speeds in modern information technology, notable mechanisms for magnetisation switching using ultrashort magnetic pulses [6], electric field pulses [7, 8] and spin-polarised currents [9] have been demonstrated. Besides the electrical and magnetic mediation for magnetisation switching, various thermal [10, 11] and mechanical [12] means have also been demonstrated. In addition, the imminent attainment of terahertz bandwidths in fibre-based telecommunication and wireless local area networks [13] highlights the pressing need to transition spintronic functionalities from gigahertz to terahertz frequencies. This shift is undoubtedly necessary to lay the groundwork for future spin-based applications to operate at unprecedented speeds.

Recent demonstrations on control of magnetic order in ultrafast timescales using light represent a highly promising avenue of research, with the potential to reverse magnetisation using polarised femtosecond laser pulses, opening up the field of Femtomagnetism [14–29]. The study of ultrafast spin dynamics in magnetic materials lies at the core of femtomagnetism research. In magnetic materials, the dynamics and lifetimes of hot electrons are influenced by their spin polarisations, leading to the development of ultrafast spin current pulses. These advancements offer crucial insights into the mechanisms driving ultrafast magnetisation dynamics and present exciting new possibilities for manipulating magnetisation on a femtosecond timescale in magnetic materials. Nevertheless, it requires efficient generation and detection of terahertz radiation to understand and realise various spintronic devices for ultrafast applications.

Over the past few years, several thin film material systems have been investigated [22–24, 30–33] for the generation of terahertz radiation. Besides, the state-of-the-art spectroscopy techniques for detection of THz radiation [34] and optoelectronic setups for electrical detection of fast currents [35] have provided a direct medium to examine the ultrafast spin physics. Recently, terahertz emission from Spintronic Terahertz Emitters (STEs) with metallic heterostructures of Ferromagnet (FM)|Non-magnet (NM) [15, 16, 18] has received significant attention due to its efficiency and large bandwidth of 0-30 THz [15].

Depending on the application of the terahertz emitters, tuning the spectrum of the emitted THz pulse is highly desirable. To achieve the tunability, the characteristics of the emitted THz signal have been studied based on several factors, such as layer thicknesses [15, 18, 19, 36], geometric stacking order [15, 37–41], interface quality [21, 40, 42], material selection [25, 43–46], and excitation wavelength [20, 47]. In addition, efforts have been made to manipulate the time and frequency profile of the THz pulse employing various antenna-coupled configurations [48–50] for metal heterostructures.

This thesis aims at gaining a deeper understanding of various electrical, magnetic and thermal aspects of magnetic materials affecting terahertz emission, using theoretical, analytical and experimental perspectives. The spatial and temporal dependencies of these emitters on these non-linear dynamics will be explored to conceptualise, design and optimise spintronic devices for ultrafast applications.

The necessary theoretical and experimental backgrounds required to explore ultrafast spintronics are provided in chapters 2 and 3.

This is followed by chapter 4 where a theoretical insight will be provided on a fundamental level to understand the role of charge dynamics in the STEs and their significance in relating the induced spin current and the emitted THz radiation.

Accordingly, the knowledge about charge dynamics will be further explored experimentally in chapter 5 where the study on miniaturised STEs, and the geometrical influences of charge dynamics on emitted spectra will be analytically established.

In chapter 6, various applications of terahertz emitters to realise various spintronic devices operating in ultrafast timescales will be discussed. The first device will be aimed at achieving a narrowband emission spectrum at high frequencies. The second device will be designed to achieve a Digital to Analog Converter (DAC), which could operate for ultrafast signals. The third device will be designed to explore the possibility of electrical control of the functionality of a terahertz emitter.

In chapter 7, the influence of THz excitation on various metallic heterostructures will be explored. This includes Giant Magnetoresistance (GMR) metal stacks, in which the effect of THz excitation on magnetoresistance will be studied. This will be followed by the study of spin-caloritronic effects on ferromagnetic multilayers. Then, the applications of parallel and antiparallel magnetisation states of decoupled ferromagnets in a multilayer will be explored.

Finally, the conclusions and outlook of the entire study will be summarised and discussed in chapter 8.

2 Theoretical Background

This chapter contains a delve into the intricate mechanisms that are involved in the generation of a Terahertz emission. This begins with the excitation of metal layers using femtosecond laser pulses and its subsequent effect on the dynamics of the spin system with the interactions affecting the magnetic order. These interactions eventually lead to spin transport on ultrafast timescales. Additionally, the influence of magnetic and electric fields and the various spin-to-charge conversion mechanisms are important, which results in Terahertz emission.

2.1 Spintronic Terahertz Emitter

Significant progress has been made in the development of highly efficient, scalable, and broadband THz emitters, typically consisting of a FM|NM bilayer metal stack [15]. When ultrafast demagnetisation occurs due to fs-laser excitation, a transient spin-polarised current is produced in the FM layer. The NM heavy metal layer acts as a spin sink channel leading to a spin current $\vec{j}_s$ from the FM to the NM, which is followed by a spin-to-charge conversion in the NM layer by various mechanisms also described later in the chapter. In previous studies, the charge current $\vec{j}_c$ is typically described by assuming the plane wave propagation along the $z-$direction perpendicular to the thin film surface since the laser beam diameter is much larger than the thickness of the STE. However, this does not take into account the boundary effects of laser spots which leads to further modifications in $\vec{j}_c$ due to charge dynamics, which are derived later in the thesis. The modified charge current $\vec{j}_c^*$ gives rise to the electric field in the emitter which is typically obtained via wave equation [51] as

$$\vec{E}(\omega) \propto e\tilde{\eta}(\omega) \int_0^d dz\, \vec{j}_c^*(z,\omega) \tag{2.1}$$

where $e\tilde{\eta}(\omega)$ is the electron charge times the frequency-dependent complex wave-impedance [15] of the STE of thickness d and e is the elementary charge.

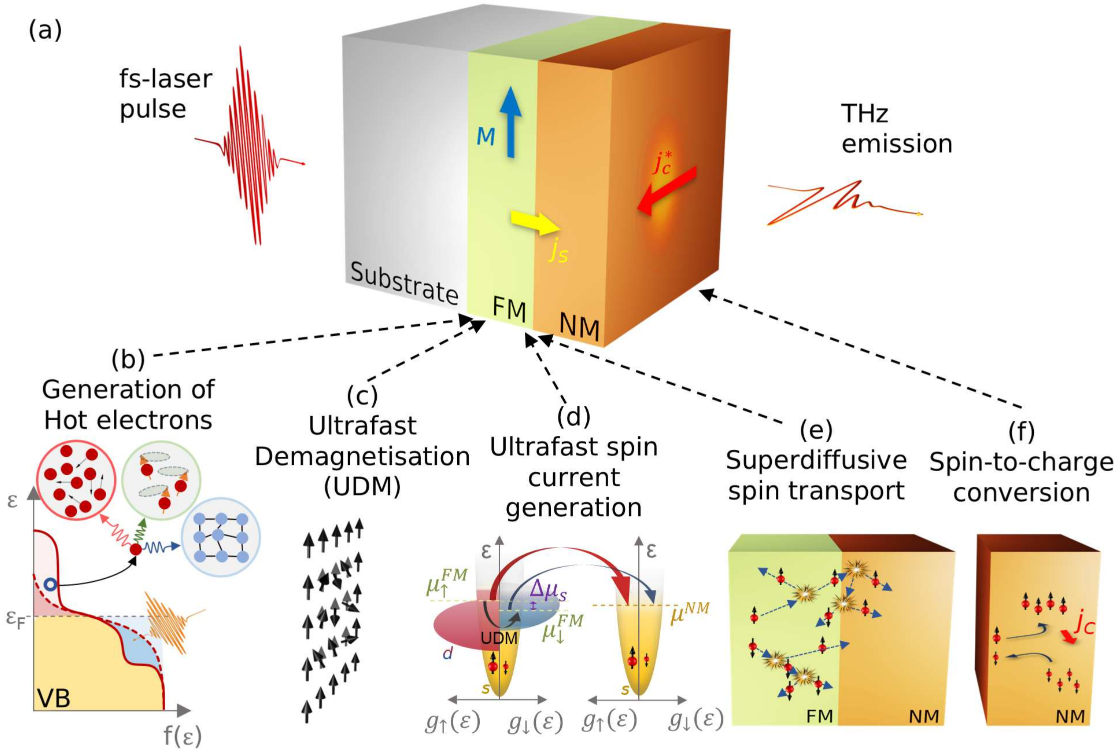
(a)
fs-laser pulse
M
j_c^*
j_s
Substrate
FM
NM
THz emission
(b) Generation of Hot electrons
ε
ε_F
VB
f(ε)
(c) Ultrafast Demagnetisation (UDM)
(d) Ultrafast spin current generation
ε
$\mu_\uparrow^{FM}$
$\Delta\mu_s$
$\mu_\downarrow^{FM}$
μ^{NM}
UDM
d
s
$g_\uparrow(\varepsilon)$
$g_\downarrow(\varepsilon)$
(e) Superdiffusive spin transport
FM
NM
(f) Spin-to-charge conversion
j_c
NM

Figure 2.1: (a) Illustration showing a THz emission from a STE upon fs-laser excitation leading to a spin current $\vec{j}_s$ from FM to NM layer and subsequently a charge current $\vec{j}_c$ generated perpendicular to the magnetisation $\vec{M}$ and $\vec{j}_s$ upon spin-to-charge conversion via the Inverse Spin Hall Effect (ISHE). The modified charge current $\vec{j}_c^*$ taking into account the charge dynamics, is the source of the THz emission. Various steps are involved after fs-laser excitation which are illustrated below. (b) Generation of hot electrons interpreted using Fermi-Dirac statistics and interaction of electron system with phonons and magnons. (c) Ultrafast Demagnetisation in FM and (d) Generation of ultrafast spin current in FM|NM interface due to the difference of chemical potentials of spin up and spin down electrons, $\Delta\mu_s$ with an associated transfer of spin angular momentum as interpreted by the density of states for spin-up and spin-down electrons [52]. (e) Superdiffusive spin transport with different mean-free-paths for the majority and minority spin carriers and scattering events, and (f) spin-to-charge conversion via ISHE [15, 29].

Here, $\tilde{\eta}(\omega)$ can be calculated with the help of Green's function approximation as,

$$\frac{1}{\tilde{\eta}(\omega)} = \frac{\tilde{n}_1(\omega) + \tilde{n}_2(\omega)}{\eta_0} + \int_0^d \tilde{\sigma}(z,\omega)dz \tag{2.2}$$

where $\tilde{n}_1(\omega)$ and $\tilde{n}_2(\omega)$ are the complex refractive indices of air and the substrate, respectively, $\eta_0 \approx 377\,\Omega$ [53] is the free space impedance, $\tilde{\sigma}$ is the complex conductivity of the metal layers, and d is the thickness of the metal layers.

The induced electric field (see equation 2.1) can be further quantified and described [19] as,

$$\vec{E}(\omega) \propto \left[\frac{P_{abs}(\omega)}{d_{\mathsf{FM}} + d_{\mathsf{NM}}}\right] \cdot \left[\tanh \frac{d_{\mathsf{FM}} - d_0}{2\lambda_{\mathsf{FM}}^{pol}}\right] \cdot \left[\tanh \frac{d_{\mathsf{NM}}}{2\lambda_{\mathsf{NM}}}\right] \cdot \left[\frac{\tilde{\eta}(\omega)}{\eta_0(\omega)}\right] \cdot \left[e^{-\frac{d_{\mathsf{FM}}+d_{\mathsf{NM}}}{S}}\right] \tag{2.3}$$

where the process steps from the laser absorption to the spin current generation and spin-to-charge conversion are taken into consideration. Here, the first term shows the energy absorption by the STE layers from the laser where d_{FM} and d_{NM} are the thicknesses of the FM and the NM layers, respectively, and P_{abs} is the absorbed laser power. The second term shows the spin current generated in the FM layer where d_0 is an effective thickness below which its ferromagnetism is lost and $\lambda_{\mathsf{FM}}^{pol}$ is a characteristic length for which the spins saturate in the FM. The diffusion of the spins in the NM layer is expressed in the third term, where λ_{NM} is the spin diffusion length in the NM. The fourth term $\tilde{\eta}(\omega)$ is the frequency-dependent complex wave-impedance for the STE as shown in the previous equation (see equation 2.2). The final term takes into account the attenuation of the THz wave in the metal layer, where S is the attenuation factor.

Although this approximates the electric fields for large-area thin films, the influence of electrical charge impedance Z cannot be ignored. The effect of charge dynamics originating due to the frequency dependent complex electrical charge impedance $\tilde{Z}(\omega)$ is addressed in chapter 4 where a conversion factor is introduced as a function of $\tilde{Z}(\omega)$ based on charge dynamics [54]. However, the effect of $\tilde{Z}(\omega)$ becomes significant for confined geometry which is also investigated later in the chapter 5. Finally, this electric field becomes the source of the THz radiation which can be detected using THz time-domain spectroscopy or ultrafast electrical detection, which are described in the chapter 3. Different layer stacks comprising of multiple FM and NM materials were used as STEs as described in chapters 5, 6 and 7.

2.2 Excitation of metals by fs-laser pulse

2.2.1 Generation of hot electrons

Upon fs-laser excitation, photon energy is transferred to the metal layers, which excites the electronic system to higher energy levels above the Fermi level. This causes the electronic system to shift out of balance and to deviate from an equilibrium Fermi-Dirac distribution [55] which characterises the electron distribution and is given by,

$$f(\epsilon,\mu,T) = \frac{1}{1+\exp\left[(\epsilon-\mu)/k_B T\right]} \tag{2.4}$$

where $f(\epsilon,\mu,T)$ is the occupation probability for a quantum state of energy ϵ at temperature T, k_B is the Boltzmann's constant, and μ is the chemical potential, which accounts for the conservation of the total electron number. The outcome of this phenomenon is the creation of hot electrons that occupy the higher energy states (see figure 2.1 (b)).

During the initial femtoseconds of exposure, there are electron-electron scattering processes that take place, leading to the establishment of a thermal equilibrium within the electronic system. Consequently, an electronic temperature can be assigned. Over the following picoseconds time frame, the lattice temperature and electronic temperature may differ, initiating the restoration of equilibrium between the electron and lattice systems through electron-phonon scattering. Additionally, the electron-magnon interaction also aids in this process of thermal equilibration (see figure 2.1 (b)).

2.2.2 Spin-Orbit interactions

Electrons possess orbital angular momentum resulting from their movement around the nucleus, which is expressed by $\vec{L}$. Although the analogy of $\vec{L}$ is comparable to a classical object, the presence of an internal motion in a quantum mechanical particle such as electrons can also be interpreted as an intrinsic angular momentum [56] which is expressed as spin angular momentum $\vec{S}$. Since it is an intrinsic property and does not exist in real space, a new abstract vector space (spin-subspace) is realised with the spin quantum number 's' having a value of 1/2 [56, 57]. This gives the spin magnetic quantum number m_s corresponding to the z-component of the spin, s_z, as $m_s = +\frac{1}{2} = \uparrow$ for "spin up" state and $m_s = -\frac{1}{2} = \downarrow$ for "spin down" state.

The electron's magnetic moment $\mu_S = -\frac{2\mu_B}{\hbar}\vec{S}$ is created by the spin of the electron where $\mu_B = e\hbar/2m_e$ is a Bohr magneton. Additionally, a magnetic moment is also created by the orbital moment as $\mu_L = -\mu_B l$. This can be interpreted as an induced magnetic field due to the current created by the electron orbital [58]. Since $\vec{S}$ and $\vec{L}$ both possess the same dimensions, the total angular momentum $\vec{J}$ of the particle can be expressed as $\vec{J} = \vec{L} + \vec{S}$. This results in a total magnetic moment $\vec{\mu} = \vec{\mu_L} + \vec{\mu_S} = \gamma(\vec{L} + 2\vec{S}) = \gamma(\vec{J} + \vec{S}) = g\gamma\vec{J}$, where $\gamma = -|e|/2m_e$ is the electron gyromagnetic ration and g represents the Lande-g factor. For $l = 0$ and $s = 1/2$, the g-factor is 2, which is the electronic g-factor.

Thus, the interaction energy, $\vec{\epsilon}_{SO}$ between the magnetic dipoles corresponding to both spin and orbital motion can be approximated as $-\vec{\mu_S}\cdot\vec{B}_{\text{orb}}$ (see figure 2.2) where $\vec{B}_{\text{orb}} = \mu_0\hat{H}_{\text{orb}}$.

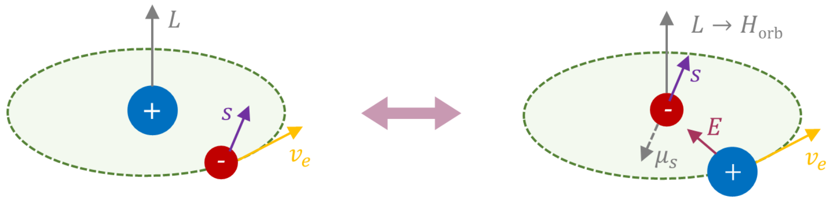

Frame of nucleus

Frame of electron

Figure 2.2: Spin-Orbit Coupling between the spin $\vec{S}$ of an electron and orbital angular momentum $\vec{L}$. The electron revolves around a nucleus as seen from the frame of references of the nucleus (left) and the electron (right). The electron experiences a net magnetic field strength $\vec{H}_{\text{orb}}$ directed upwards from the orbital plane as seen from the electron frame of reference.

Since, $\vec{H}_{\text{orb}} \propto \vec{L}$ and $\vec{\mu_S} \propto \vec{S}$, the coupling of the electron spin $\vec{S}$ with the electron orbital moments, also referred to as the Spin-Orbit interaction is expressed by the term $\hat{\mathcal{H}}_{SO}$ in the relativistic Hamiltonian of a single electron system $\hat{\mathcal{H}}_{rel}$ [56] and is given by,

$$\hat{\mathcal{H}}_{SO} = \xi(r)\vec{L}\cdot\vec{S} \tag{2.5}$$

where $\xi(r) = \frac{1}{2m^2c^2}E(|\vec{r}|)$ with the electric field $E(|\vec{r}|) \simeq \frac{\mathcal{Z}e}{r^3}$ at a position $\vec{r}$ from the nucleus of the material with the atomic number $\mathcal{Z}$. Thus, spin-orbit coupling is responsible for spin relaxation which leads to different scattering events in the bulk material. It also plays a vital role in the spin-to-charge conversion mechanism in heavy metals with large $\mathcal{Z}$ facilitating strong ISHE which is discussed later in this chapter.

The single electron relativistic Hamiltonian [56] can be extended to accommodate interactions in a many-electron system and can be expressed as,

$$\hat{\mathcal{H}}_{ME} = \sum_i \left(\hat{\mathcal{H}}_{Ki} + \hat{\mathcal{H}}_{Vi} + \sum_{j>i} \hat{\mathcal{H}}_{Cij}^{ee} \right) + \hat{\mathcal{H}}_{rel} \tag{2.6}$$

where $\hat{\mathcal{H}}_{Ki}$ and $\hat{\mathcal{H}}_{Vi}$ correspond to the kinetic energy and potential energy for ith electron, respectively, which also includes induced external and internal fields from the nuclei [58]. The inter-electron Coulomb interactions are expressed by $\sum_{j>i} \hat{\mathcal{H}}_{Cij}^{ee}$ and the relativistic corrections are accommodated in $\hat{\mathcal{H}}_{rel}$, which includes spin-orbit and spin-spin magnetic dipole interactions [59, 60].

2.3 Magnetic ordering in solids

2.3.1 Exchange interaction

The exchange interaction for a two-electron model [61] is useful for describing the magnetic ordering. The wavefunction for a two-electron system $\Psi(1,2) = \psi(\vec{r_1}, \vec{r_2})\chi(1,2)$, where $\psi(\vec{r_1}, \vec{r_2})$ and $\chi(1,2)$ are spatial and spin parts, respectively. Since electrons are fermions, $\Psi(1,2) = -\Psi(2,1)$, then either $\psi(\vec{r_1}, \vec{r_2})$ or $\chi(1,2)$ is required to be anti-symmetric with respect to the electron exchange. This gives the Hamiltonian corresponding to the exchange interaction based on the Heisenberg model as

$$\hat{\mathcal{H}}_{ex} = -2J_{ex}\vec{S}_1 \cdot \vec{S}_2 \tag{2.7}$$

where J_{ex} is defined as $J_{ex} = \mathcal{E}_{singlet} - \mathcal{E}_{triplet}$ with $\mathcal{E}_{singlet} = \mathcal{E}_1 + \mathcal{E}_2 + K_{12} + J_{12}$ and $\mathcal{E}_{triplet} = \mathcal{E}_1 + \mathcal{E}_2 + K_{12} - J_{12}$ [61]. Here J_{12} and K_{12} denote the exchange integral and the overlap integral of the two spin states with energies $\mathcal{E}_i$, respectively. It should be noted that this interaction is sufficient for the orientation of neighbouring magnetic dipoles at room temperature, although it exponentially decays with distance. In general, the dipoles behave paramagnetically.

The strength of J_{ex} plays a role in segregating materials of different magnetic orders. For $J_{ex} > 0$, the exchange energy is minimised when $\hat{S}_i \uparrow\uparrow \hat{S}_j$ and this type of magnetic ordering is referred to as ferromagnetic. Similarly, for $J_{ex} < 0$, $\hat{S}_i \uparrow\downarrow \hat{S}_j$ and this is referred to as ferri- or anti-ferromagnetic order.

In addition, the effect of neighbouring magnetic dipoles together on individual magnetic dipoles can be interpreted in terms of a magnetic exchange field $\vec{B}_m$ as $-\sum_j J_{ij} S_j = \frac{\mu_B}{\hbar}\vec{B}_m$ and the magnetic portion of the Hamiltonian can be expressed as,

$$\hat{\mathcal{H}}_{magnetic} = \frac{\mu_B}{\hbar}\sum_i [\vec{B}_m + \vec{B}_{\text{ext}}] \cdot \vec{S}_i \tag{2.8}$$

where $\vec{B}_{\text{ext}}$ is applied external magnetic field. This implies that the mean exchange field is responsible for ordering magnetic dipoles in the absence of the external magnetic field in a ferromagnet, thus creating a net magnetisation $\vec{M}$ at zero external field in the case of a ferromagnet.

2.3.2 Stoner Model

In contrast to the Heisenberg model, the Stoner Model is the simplest model used to describe magnetic order in metals, e.g., solids with itinerant electrons, which are treated as nearly free moving particles [62].

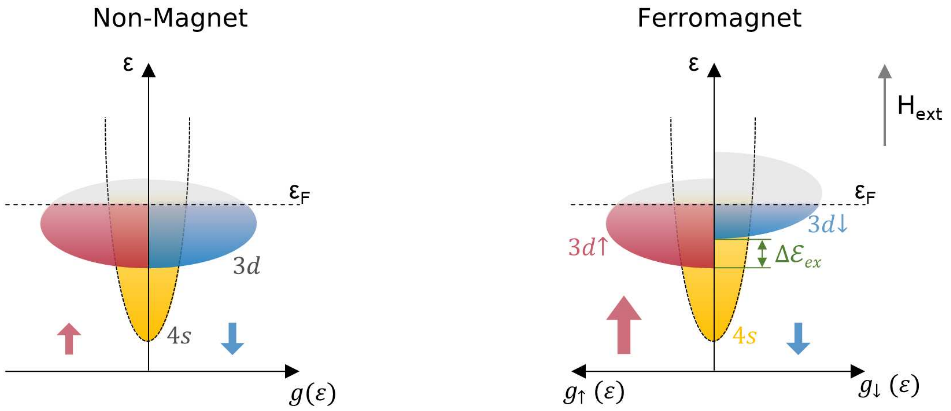

Figure 2.3: Schematic illustration of the Stoner-band model for a non-magnet and a ferromagnet. The exchange splitting is shown in $3d$ Density of States (DOS) with an exchange splitting energy $\Delta\mathcal{E}_{ex}$. An imbalance of occupied states for majority and minority spin channels arises up to the Fermi level energy (ϵ_F). Here $\vec{H}_{\text{ext}}$ is an external field to represent the quantisation direction.

According to the Stoner model, ferromagnetism is possible under certain assumptions. As per the first assumption, the magnetic moments are predominantly influenced by the electrons present in the d-shell. These electrons establish energy bands as a result of periodic bonding between spins. For the second assumption, it is proposed that the average exchange field shifts the spin up and spin down energy bands relative to each other by $\Delta\mathcal{E}_{ex}$. Lastly, the third assumption states that the electrons obey Fermi statistics and occupy energy bands up to the Fermi energy ϵ_F level. But unlike the ferromagnets, in non-magnetic materials both the up and down spins are equally populated (see figure 2.3).

2.4 Magnetisation behaviour in external magnetic field

2.4.1 Spin dynamics

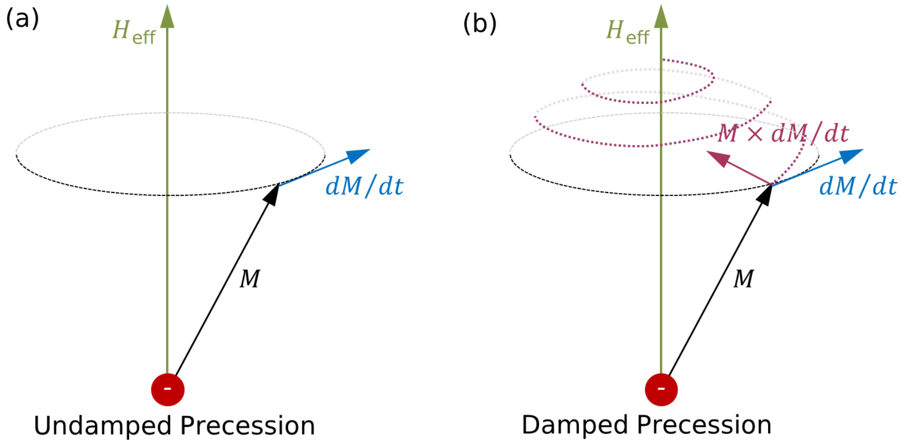

Figure 2.4: Illustration showing precession movement of the magnetisation $\vec{M}$ around an effective magnetic field strength $\vec{H}_{\text{eff}}$. The motion takes place on a spherical surface since the absolute value of $\vec{M}$ is conserved. The torque $d\vec{M}/dt$ is always oriented perpendicular to $\vec{M}$. (a) In the case of undamped precession, the deflection of the moment relative to the field direction remains constant over time. (b) In contrast, damping leads to the relaxation of the $\vec{M}$ along the $\vec{H}_{\text{eff}}$.

The dynamics of the spin system and their effects beyond the equilibrium states due to external sources, such as magnetic field, are given by the Landau-Lifshitz (LL) equation [63] as,

$$\frac{d\vec{M}}{dt} = -\gamma\mu_0\vec{M} \times \vec{H}_{\text{eff}} \tag{2.9}$$

which represents a constant precession of $\vec{M}$ with the angular frequency ω_0 around the effective magnetic field strength $\vec{H}_{\text{eff}}$ and γ is the electron gyromagnetic ratio. Here, ω_0 exhibits a linear dependency on the $\vec{H}_{\text{eff}}$ [64] which is described as $\omega_0 = \gamma_0 \left|\vec{H}_{\text{eff}}\right|$, where $\gamma_0 = -\gamma\mu_0$. Generally, the application of a sufficiently large $\vec{H}_{\text{eff}}$ leads to a uniform $\vec{M}$ aligned along the $\vec{H}_{\text{eff}}$ direction (see figure 2.4 (a)).

However, the $\vec{M}$ relaxes towards the direction of $\vec{H}_{\text{eff}}$ in actual systems, in the form of a damped precession movement due to dissipation effects. Hence, this resulted in the extension of the LL equation to the phenomenological Landau-Lifshitz-Gilbert (LLG) equation [65, 66] given as,

$$\frac{d\vec{M}}{dt} = -\gamma\mu_0\vec{M} \times \vec{H}_{\text{eff}} + \frac{\alpha}{M_s}\left(\vec{M} \times \frac{d\vec{M}}{dt}\right) \tag{2.10}$$

where γ is the electron gyromagnetic ratio and equal to the inverse relaxation time τ [67], α corresponds to the dimensionless Gilbert damping parameter and the effective saturation magnetisation is given by M_s. Here, LL equation satisfies the basic assumption that the magnitude of $\vec{M}$ is conserved during precession and the effective torque $d\vec{M}/dt$ is always perpendicular to $\vec{M}$ (see figure 2.4 (b)). Moreover, it also accounts for the systems with high damping constants [66]. Physically, the damping can be interpreted as the loss of spin angular momentum to the lattice which eventually results in relaxation of $\vec{M}$ in the direction of $\vec{H}_{\text{eff}}$ [67].

2.4.2 Hysteresis

Ferromagnetic materials also possess the property of hysteresis, which refers to the irreversibility of the magnetisation and demagnetisation process, and this can be analysed through a $B - H$ curve which illustrates the relationship between the resulting magnetic flux density $\vec{B}$ and the applied magnetic field strength $\vec{H}$. The hysteresis can be also plotted as an $M - H$ curve since $\vec{B} = \mu_0\vec{H} + \vec{M}$ where μ_0 is the magnetic permeability in vacuum.

When the associated magnetisation $\vec{M}$ reaches its maximum, it is referred to as the saturation magnetisation $\vec{M}_{\text{s}}$. The residual $\vec{M}$ upon removal of $\vec{H}$ is termed the remanence magnetisation $\vec{M}_{\text{r}}$. The magnetic field when $\vec{H}$ can fully demagnetise the magnetic material is termed the Coercive Field $\vec{H}_C$, and the net $|\vec{H}|$ corresponding to the Coercive Fields in either direction is referred to as the Coercivity. Magnetic materials can be categorised as hard or soft magnet based on whether they have a higher or lower $\vec{H}_C$, respectively, in the hysteresis loops (see figure 2.5 (a)). The hysteresis loops [68] can also be categorised as major loops or minor loops for $\vec{H}_{\text{max}} = \vec{H}_{\text{s}}$ or $\vec{H}_{\text{max}} < \vec{H}_{\text{s}}$, respectively (see figure 2.5 (b)).

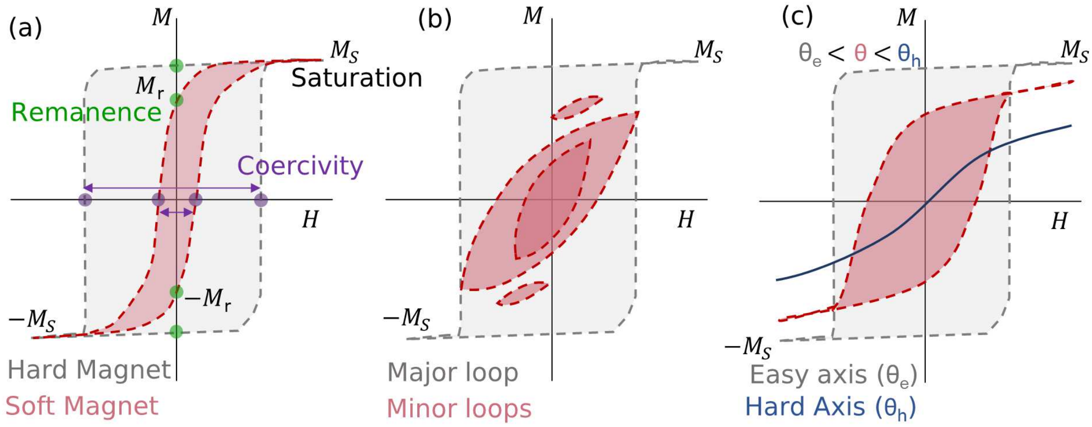

Figure 2.5: Illustration showing Magnetic Hysteresis for (a) different coercivities for Hard and Soft magnets and remanence magnetisation $\vec{M}_\mathrm{r}$, (b) major loops and minor loops for ferromagnetic materials, and (c) magnetic behaviour dependent on magnetisation orientation along the easy (θ_e) and hard axis (θ_h) determined by magnetocrystalline energy. Here θ corresponds to the angle with respect to the reference axis.

The study of hysteresis helps in the selection of ferromagnets for applications involving magnetic switching based on different coercive fields, which is primarily shown in chapters 6 and 7 for the case of switchable THz Emitters and Digital-to-analog converter for THz signals. It is also useful to determine the antiparallel states in GMR structures as shown in chapter 7.

2.4.3 Magnetic anisotropy

When a ferromagnetic material is placed in a large enough externally applied magnetic field strength $\vec{H}_{ext}$, the domain that has a direction closest to that of $\vec{H}_{ext}$ grows at the expense of the other domains via domain wall motion [68]. In other words, the spins align in the direction of $\vec{H}_{ext}$ due to the torque applied by the latter. However, these domain boundaries encounter crystal imperfections with an associated magnetostatic energy which is overcome with the energy of higher $\vec{H}$ in the direction of $\vec{H}_{ext}$, eventually leading to the elimination of domain walls. This leaves behind a single domain or spins oriented along the $\vec{H}_{ext}$ direction.

This switching process usually depends on the magnetic anisotropy energy barrier [68], which is determined primarily by the material and its shape. For a magnetic material, the energy required to change the orientation of the magnetic moment in a bulk single crystal from the easy axis to the hard axis is given by Magnetocrystalline anisotropy [59]. These directions or axes are determined by the interaction between the spin magnetic moment and the crystal lattice through spin-orbit coupling, and usually, the preferred axis is called the easy axis, which provides the stable states for the $\vec{M}$ direction [68]. The $M-H$ curve exhibits the highest H_C along the easy axis while the lowest H_C along the hard axis (see figure 2.5 (c)). The magnetocrystalline energy density of a crystal along the direction of $\vec{M}$ is given by,

$$\mathcal{E}_{crystal}(\vec{M}) = \mathcal{K}_0 + \mathcal{K}_1(\alpha_1^2\alpha_2^2 + \alpha_2^2\alpha_3^2 + \alpha_3^2\alpha_1^2) + \mathcal{K}_2(\alpha_1^2\alpha_2^2\alpha_3^2 + ... \tag{2.11}$$

where, α_1, α_2 and α_3 are spherical polar coordinates, and $\mathcal{K}_i$s are the anisotropy constants with $\mathcal{K}_0$ being the isotropic term. The magnetocrystalline anisotropy can be broadly categorised into Uniaxial anisotropy and Cubic anisotropy [59]. Uniaxial anisotropy has only one easy axis and the corresponding magnetocrystalline energy density can be derived from the equation above (see equation 2.11) and is given by,

$$\mathcal{E}_{crystal}(\vec{M}) = \mathcal{K}_0 + \mathcal{K}_u \sin\theta^2 - \frac{1}{4}\mathcal{K}_c \sin 2\theta^2 \tag{2.12}$$

where $\mathcal{K}_u$ is the uniaxial anisotropy constant and $\mathcal{K}_c$ is the magnetocrystalline anisotropy constant contributing to the fourfold symmetry due to biaxial characteristics. Both $\mathcal{K}_u$ and $\mathcal{K}_c$ correspond to $\mathcal{K}_1$ and $\mathcal{K}_2$ respectively in the previous equation (see equation 2.11). The biaxial characteristic is usually observed in thin films due to various factors such as growth conditions, multi-grain thin films or directional shape [69]. Additionally, cubic anisotropy with a cubic symmetry in the case of a cubic crystal due to spin-lattice coupling has three equivalent easy axes.

The anisotropy constants also depend on the strain associated with the magnetic crystal when it is magnetised after previous demagnetisation upon mechanical strain or change in magnetisation direction with respect to the lattice. This is referred to as magnetostriction and gives rise to Magneto elastic anisotropy [59]. The strain is quantified based on the applied magnetic field, where the magnetic crystal alters its dimensions upon magnetisation and thus, the magnetocrystalline anisotropy.

Shape anisotropy, also known as magnetic dipolar anisotropy, is attributed to the effect of shape on magnetic dipolar interaction in an ellipsoidal magnetic material [70] and is given by

$$\vec{H_{eff}} = \vec{H}_0 - N\vec{M} \tag{2.13}$$

where $\vec{H}_0$ is the external magnetic field, N is the shape-dependent demagnetising tensor and $\vec{M}$ is the magnetisation vector (see figure 2.6 (a)).

Its impact is significant in thin films and can result in the alignment of moments within the material's plane.

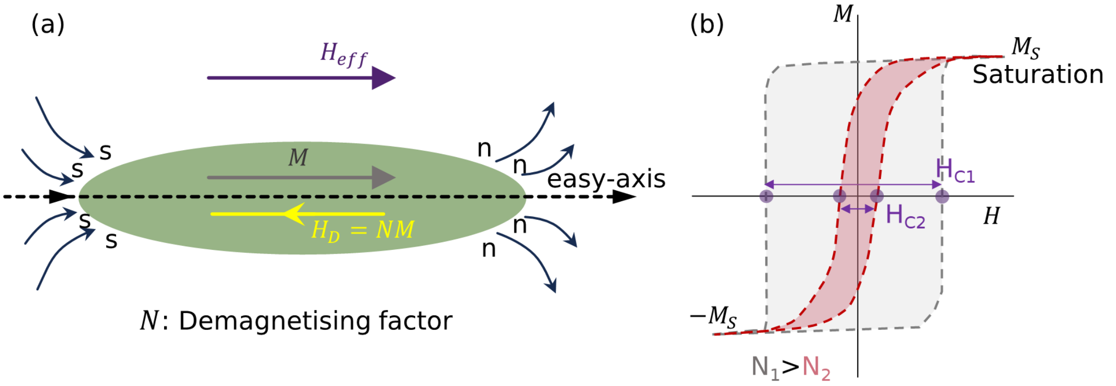

Figure 2.6: Illustration showing (a) apparent surface pole distribution due to shape anisotropy with easy axis along the longer side and corresponding demagnetising field with factor N and (b) hystereses with different coercivities which are dependent on N.

Favouring alignment along the grain's long axis, shape anisotropy [68, 70] helps minimise the internal demagnetising field $\vec{H}_D = N\vec{M}$. A higher demagnetising factor exhibits a higher coercive field (see figure 2.6 (b)).

The magnetic behaviour can also be affected due to the temperature. Although the entropy is minimised due to the spontaneous ordering of magnetic moments (see section 2.3.1), the thermal energy k_BT becomes greater than the exchange energy $\mathcal{E}_{ex}$ at a certain temperature known as Curie temperature T_C and the material becomes disordered. During this, the magnetocrystalline and magnetostriction constants decrease with temperature vanishing at T_C and the crystal starts behaving paramagnetically [68].

In magnetic materials, the domain structures are separated by domain walls which try to attain the lower magnetic energy state, usually via domain wall motion. The difference in magnetic switching fields also referred to as the coercive fields of various structures, is due to the difference in domain wall nucleation energy and propagation [71]. This is the primary factor considered in designing the magnetic bits of Digital-to-analog converters for ultrafast signals in chapter 6.

2.5 Spin transport

The electron spin flow and its manipulation form the basis of spintronics devices, as is the case for electron flow (charge current) in electronic devices. The charge current can be understood in terms of both spin and charge flow, where an equal number of both the spin-up and spin-down electrons flow in the same direction and there is a net zero spin current (see figure 2.7 (a)). When the number of spin-up and spin-down electrons are unequal, it leads to a net polarisation along with a charge current, and it is termed a spin-polarised current (see figure 2.7 (b)), and it is usually observed in the ferromagnets.

(a) Charge Current

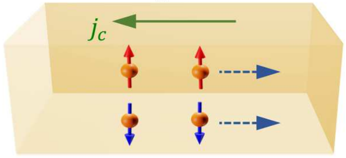

(b) Spin-polarised Current in FM

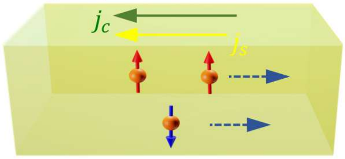

(c) Pure Spin Current

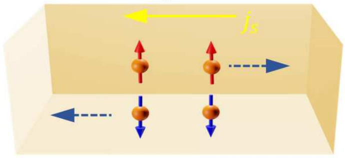

(d) Spin injection at FM/NM

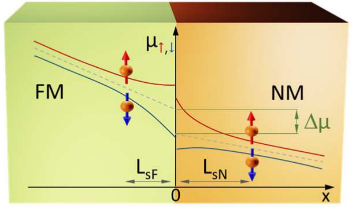

(e) Diffusive Spin Transport

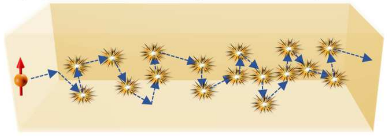

(f) Ballistic Spin Transport

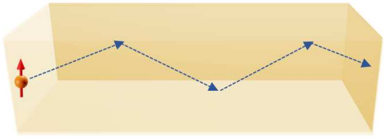

Figure 2.7: Schematics showing mechanisms involved in (a) charge current, (b) spin-polarised current in a FM, and (c) pure spin current. Illustration showing (d) spin injection at FM|NM interface due to splitting of the chemical potential ($\Delta\mu_s$) for spin up and spin down electrons, (e) diffusive and (f) ballistic mechanisms of spin transport.

When the spin-up and spin-down electrons move in opposite directions, it leads to a net zero charge current flow. However, it leads to a pure spin current (see figure 2.7 (c)) where only the flow of spin angular momentum is involved.

2.5.1 Spin injection across FM|NM interface

The next step involves the spin current propagation after its generation via processes described earlier in the chapter, and it is achieved by the injection of non-equilibrium spin polarisation in the NM heavy metal through the interface [72]. This results from the splitting of bands for spin-up and spin-down electrons, which is described using the Stoner Model (see section 2.2.2), leading to a difference in the numbers of occupied carriers and consequently the magnetisation $M \propto (n_\uparrow - n_\downarrow)$. This determines the spin transport by the net spin polarisation,

$$P = \frac{\sigma_\uparrow - \sigma_\downarrow}{\sigma_\uparrow + \sigma_\downarrow}. \tag{2.14}$$

The average chemical potential difference between the spin-up and spin-down channels, with chemical potentials $\mu_\uparrow$ and $\mu_\downarrow$, respectively, is represented as $\Delta\mu$ (see figure 2.7 (d)). Since both the channels have different conductivities, a current flow through the material results in the splitting of the chemical potential $\Delta\mu_s$ at the interface, according to Ohm's Law. Consequently, a non-equilibrium spin polarisation or spin accumulation μ_s occurs between the two spin channels at the interface, and the spin current is expressed by,

$$j_s = j_\uparrow - j_\downarrow = \sigma \nabla \mu_s \tag{2.15}$$

where, $\mu = (\mu_\uparrow - \mu_\downarrow)/2$ and $\sigma = \sigma_\uparrow + \sigma_\downarrow$.

This spin accumulation leads to the spin diffusion in the NM layer in the steady state, which is described by the spin diffusion equation [73] as,

$$\frac{d\mu_s}{dt} = D\nabla^2 \mu_s - \frac{\mu_s}{\tau_s} = 0 \tag{2.16}$$

where D is the diffusion constant and τ_s is the spin relaxation time. Here, τ_s defines the characteristic length constant $l_d = \sqrt{D\tau_s}$ also called the spin diffusion length in the NM layer. This determines the length from the interface over which the spin accumulation of both states returns to the equilibrium value. However, in non-ideal scenarios, the efficiency is primarily affected by the reflectivity [74, 75] and impedance mismatch [76–78] at the interface.

2.5.2 Super-diffusive spin current

The understanding of optically excited hot-electron transport in metals is complex in nature, which can be explained based on band theory as proposed earlier [79]. With regard to hot-electron transport for different timescales, it is possible to distinguish between two limits [80–82]. Over a short time frame, hot electrons move ballistically (see figure 2.7 (e)) in a straight line with constant velocity, without experiencing any scattering, thus conserving the angular momentum and energy [80]. Over a longer timescale, electrons can scatter elastically with phonons and impurities or inelastically with electrons at or below the Fermi energy. Although the hot electron's energy remains the same, its momentum becomes randomised. The electron movement in this scenario resembles Brownian motion, and the transport mechanism is termed standard diffusion (see figure 2.7 (f)). In addition, unidirectional transport only occurs when a gradient is present, which can be thermal, spin-related, or charge-related. After scattering, electrons continue to move ballistically.

As hot-electron transport is not reproduced using either the standard diffusion or ballistic cases it was necessary to take account of an intermediate regime. The transient evolution of the hot-electron's movement from the standard diffusion to ballistic regime characterises the superdiffusive regime [79] in which hot-electrons collide a few times before their energy and angular momentum are transferred, with an associated evolution of the energy distribution (see figure 2.1 (e)).

The inelastic mean free path is determined by the energy-dependent lifetime, and the velocity of the hot electrons, and these parameters depend on the spin if the material is ferromagnetic due to the presence of exchange splitting. Typically, laser excitation leads to the depletion of majority carriers on the surface owing to their higher mobility since they have a longer inelastic mean free path than minority carriers. Hence, pairing a FM layer with a NM metal leads to the transport of majority carriers from the FM to NM, while minority carriers stay confined in the former [80, 82].

2.5.3 Magnons

The considerations highlighted in the previous paragraphs are based on the assumption that all magnetic moments in the system are arranged in parallel. If disturbances of magnetic order occur in the form of a deviation of the spin of individual particles from the ground state, these will propagate as waves through the crystal lattice of the magnetic medium [83]. These disturbances are spatially periodic and are referred to as spin waves or magnons.

A magnon is a quantised spin wave that carries a fixed amount of energy $E_{\text{magnon}} = h \cdot f$ and lattice momentum in the context of quantum mechanics, where h is Planck's constant and f is precession frequency. As a "spin-1" particle, it obeys boson behaviour in the equivalent wave picture. The basic prerequisite for the existence of magnons is the spatial coupling between the magnetic moments of the medium. The direction of propagation of the spin waves is described by the wave vector k (see figure 2.8). The energy dissipation for spin angular momentum transfer via magnons is minimized due to reduced losses from ohmic heating [84].

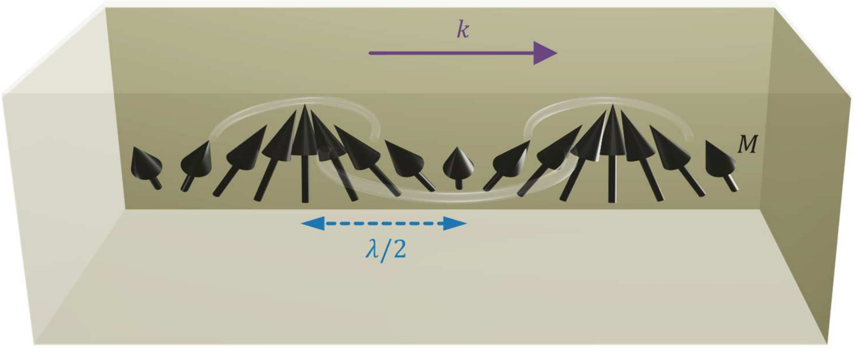

Figure 2.8: Illustration showing a magnon with wavelength λ propagating in the direction of wavevector k. The black arrows show the precessing spins due to the exchange interaction between neighbouring spins. The semi-transparent white curve effectively illustrates the collective wave-like motion.

2.6 Effects due to electric and magnetic fields

2.6.1 Spin dependent Hall effects

The optimisation of spin current generation, transport, and detection, particularly via spin-to-charge conversion, is a fundamental requirement for the development of spintronic devices. This section contains a discussion on various spintronic effects that facilitate these functionalities.

Spin-dependent scattering

The electron motion is influenced by various intrinsic and extrinsic mechanisms. They are represented [85] by,

$$\sigma^{SH} = \sigma^{int} + \sigma^{SS} + \sigma^{SJ}. \tag{2.17}$$

The intrinsic component (σ^{int}) is a quantum-mechanical property of perfect crystals [86] that generates transverse spin-dependent velocities through an inter-band coherence induced by an external field (see figure 2.9 (a)). Meanwhile, asymmetric scattering on defects and impurities causes the extrinsic component. This mechanism involves two types of scattering, namely skew scattering (σ^{SS}) [87] and side-jump scattering (σ^{SJ}) [88].

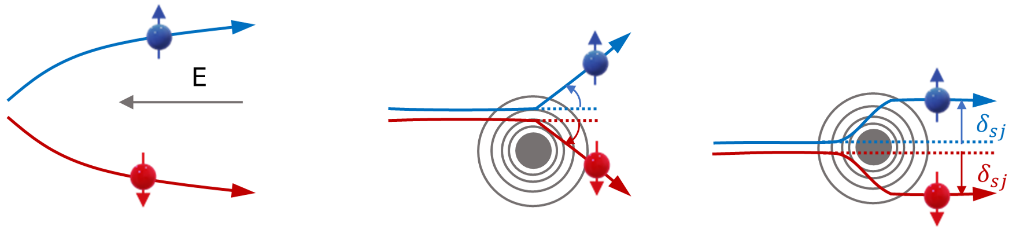

(a) Intrinsic deflection (b) Skew scattering (c) Side jump

Figure 2.9: Illustration showing spin-dependent scattering mechanisms responsible for the spin Hall effect. (a) Intrinsic interaction, (b) Skew scattering and (c) Side-jump scattering with spin-dependent displacement δ_{sj} at an impurity. The figure is redrawn from [89].

Skew scattering results from the spin-orbit interaction, which creates an effective magnetic field gradient within the scattering plane. This gradient acts as a driver of a net force towards or away from the scattering centre, depending on the spin polarisation of the scattered electron [86] (see figure 2.9 (b)). Contrastingly, side-jump scattering occurs due to the different acceleration and retardation of opposite spin polarisations during the scattering process. This leads to a net displacement of spins in the transverse direction (δ_{sj}) after multiple scattering processes (see figure 2.9 (c)).

Ordinary Hall effect

An Ordinary Hall Effect (OHE) or simply Hall effect is a classical electromagnetic effect which occurs in a current carrying conductor which when subjected to an external magnetic field perpendicular to the charge current induces a transverse voltage. This effect can be interpreted in terms of the Lorentz force acting on the moving electrons [90] (see figure 2.10 (a)) and The transverse induced voltage is proportional to the applied magnetic field and is termed the Hall voltage.

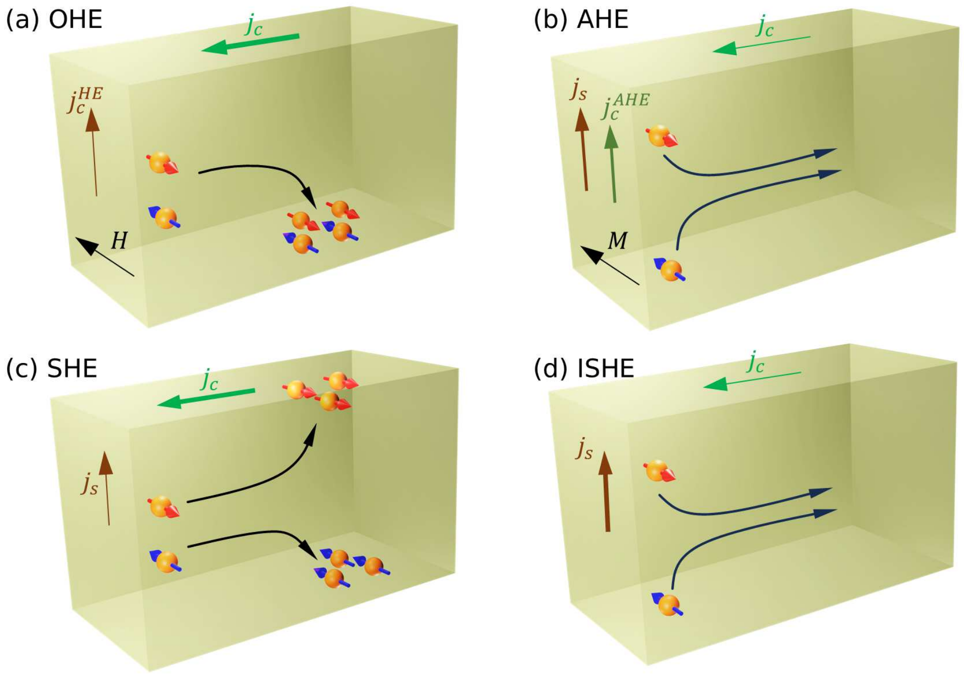

Figure 2.10: Illustration showing Hall effects.

Anomalous Hall effect

Similar to the OHE, the flow of charge current through a ferromagnet induces a transverse voltage; however, this effect is significantly stronger than in the ordinary Hall effect [91]. This phenomenon is known as the Anomalous Hall Effect (AHE), first described in the microscopic theory by Karplus and Luttinger [92], who attributed it to an additional contribution to the electronic group velocity also called the anomalous velocity.

In principle, this effect can be understood as follows. In ferromagnets, the intrinsic magnetisation, due to the alignment of magnetic moments from exchange interactions (see section 2.3.1), results in a net spin polarisation of the conduction electrons, with most spins preferentially aligned along the magnetisation direction. The electrons with different spin orientations experience distinct transverse deflections due to various spin-dependent scattering mechanisms [93] leading to Spin Hall Effect (SHE) which will be discussed in the next section. For the spin-polarized currents, this also leads to charge accumulation giving rise to an additional Hall voltage, characteristic of the AHE [93]. (see figure 2.10 (b)). Recently, a clearer physical picture of AHE was obtained based on topological phenomenon arising from the Berry curvature [92, 94, 95].

For THz experiments, a net backflow current $\vec{j}_{\text{AHE}}$ is created at the interfaces of the FM layer and the dielectrics (substrate and the capping layer, if present) [96] by the spin-polarised current in the longitudinal direction perpendicular to a net magnetisation $\vec{M}$ which is in the direction of a large external magnetic field. This results in a transient transverse charge current $\vec{j}_c$ defined as [97],

$$\vec{j}_c = \theta_{\text{AH}} \left(\vec{j_{\text{AHE}}} \times \hat{M} \right) \tag{2.18}$$

where θ_{AH} is the Anomalous Hall angle. The THz emission as a result of AHE for spin-to-charge conversion in the FM is shown and discussed in chapter 7.

Spin Hall effect

The phenomenon of the transverse velocities experienced by moving electrons, explored in the previous section (see section 2.5), depends on their spin orientation. Similarly, normal metals also exhibit a spin-dependent transverse velocity [86, 98, 99], but due to the absence of a distinct spin polarisation, it does not generate a noticeable voltage. However, it does cause spins with opposite polarisations (spin-up and spin-down) to separate, which in turn causes them to accumulate on opposite transverse edges of the sample. This effect is known as the Spin Hall Effect (SHE) (see figure 2.10 (c)) and the spin current (j_s) to charge current (j_c) conversion is expressed as,

$$\vec{j}_s = \theta_{\mathrm{SH}}\,\frac{2e}{\hbar}(\vec{\sigma} \times \vec{j}_c) \tag{2.19}$$

where e is the electron charge and $\hbar$ is the Planck's constant. σ is the spin polarisation tensor and θ_{SH} is the spin Hall angle, which determines the conversion efficiency between spin and charge.

The Onsager reciprocal relation [100, 101] allows for the inverse process, where a transverse charge current is produced by the injection of a pure spin current perpendicular to the layer, and it is termed the Inverse Spin Hall Effect (ISHE) [102] (see figure 2.10 (d)). This can be described [85] as,

$$\vec{j}_c = \theta_{\mathrm{SH}}\,\frac{2e}{\hbar}(\vec{j}_s \times \vec{\sigma}) \tag{2.20}$$

derived from the previous equation (see equation 2.19). It should be noted that the thickness of the metal layer should be lower than the spin diffusion length to avoid spin backflow and to maintain the validity of the equation.

Both SHE and ISHE have been observed in semiconductors and metals. In semiconductors, the intrinsic scattering mechanism (see figure 2.9 (a)) dominates, while in metals, the extrinsic scattering mechanisms (see figure 2.9 (b, c)) prevails as the intrinsic mechanism can be disregarded. These mechanisms determine the conversion efficiency between spin and charge.

The spin-to-charge conversion via ISHE in the NM is referred to in various THz emission processes throughout the thesis.

2.6.2 Magneto-resistive effects

In general, at room temperatures, electrons in metals interact with atoms, causing a change in their path due to scattering. The average distance between two scattering events is called the mean free path, which determines a metal's resistivity. A lower probability of electron scattering leads to lower resistivity, as electrons can travel a greater distance before encountering a scattering event [103, 104] given all other parameters are the same. In a metallic system, upon application of an electrical charge current in the presence of an external magnetic field, the electron trajectories are affected due to the Lorentz force with maximum Lorentz deflection for magnetic fields perpendicular to the current direction. As a consequence, the movement of electrons are now in curved paths, there is a reduction in the effective mean free path, thus higher resistivity. This magneto-transport phenomenon leads to a net change in resistance is termed as ordinary Magnetoresistance (MR).

Considering the case where the metal is a FM, applying an external magnetic field results in a net magnetisation within the FM which defines the spin orientation of electrons and their orbital motion relative to the crystal lattice. The application of electric current leads to anisotropic electron scattering, where the scattering probability varies depending on how the magnetisation-orbital alignment affects orbital overlap with scattering states, thereby changing the electrical resistance. This change in resistance is referred to as the Anisotropic Magnetoresistance (AMR) [105].

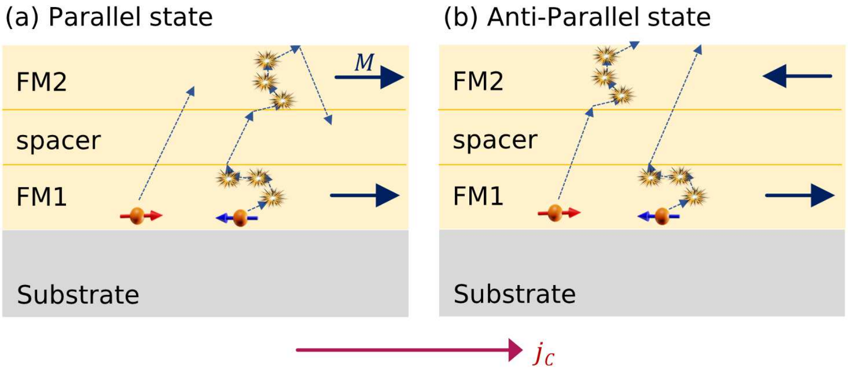

Figure 2.11: Illustration showing a simplified picture of spin-dependent scattering across the interfaces between the FM layers in (a) parallel and (b) antiparallel states for a GMR multilayer in Current-in-plane configuration.

For a FM|NM, upon application of an electrical current, spin-dependent scattering in the

FM leads to a spin-polarised current. When this current enters the NM, the mismatch in spin-dependent conductivities causes a nonequilibrium spin accumulation near the FM|NM interface manifesting as a difference in the spin-dependent electrochemical potentials $\mu_\uparrow$ and $\mu_\downarrow$ for spin-up and spin-down electrons [76] (see section 2.5). The spin-dependent interfacial scattering is dependent on matching of the electronic band and also the lattice [105] between the FM and NM, with the former typically being the dominant factor. For a FM|NM|FM multilayer system, in a parallel magnetisation state of the FMs, it usually undergoes less scattering at the FM|NM interfaces, thus leading to a lower resistivity as compared to that in the antiparallel state (see figure 2.11). This phenomenon is termed the Giant Magnetoresistance (GMR) [3, 4].

The magnitude of the GMR effect is determined by

$$\frac{\delta R}{R} = \frac{R_{\uparrow\downarrow} - R_{\uparrow\uparrow}}{R_{\uparrow\uparrow}} \tag{2.21}$$

where $R_{\uparrow\uparrow}$ and $R_{\uparrow\downarrow}$ are the resistances for parallel and antiparallel alignment, respectively.

The antiparallel alignment [105] of magnetisation for the FM layers can be obtained by using an antiferromagnetic interlayer coupling mediated via the Ruderman-Kittel-Kasuya-Yosida (RKKY) interaction or by using a spin valve medium an exchange coupled pinned FM layer and adjacent antiferromagnetic layer or alternatively a magnetisation alignment of embedded FM granules in a NM. Moreover, a pseudo spin valve structure with different coercive fields for successive FMs can also lead to antiparallel alignment. These layer structures provide a simplified approach to obtaining antiparallel states, as the magnetic moments can be controlled by external magnetic fields. As a result these mechanisms lead to a field dependent resistance change.

The measurement of a GMR multilayer can be done in either the Current-in-plane (CIP) or Current-perpendicular-to-plane (CPP) geometry depending on whether the current direction is parallel or perpendicular to the layers, respectively. The CPP-GMR configuration provides much larger MR as compared to the CIP-GMR [105, 106]. Although the relative effect is stronger in CPP-GMR, the smaller overall resistance is difficult to measure since it can easily be dominated by the lead and contact resistances in the measurement systems. Hence, CIP-GMR is much more favourable for measurements. To get a large enough resistance the CPP-GMR structures are required to be much smallerwith areas less than $10^{-2}\,\mu\text{m}^2$ [107], which can be achieved by nanolithography.

The effect of fs-laser excitation on magnetoresistance is discussed in chapter 7.

2.6.3 Oersted field

An electric current through a conductor creates a magnetic field called the Oersted field [108]. While a direct current generates a constant Oersted field, a current pulse generates a field pulse and an alternating current generates an oscillating Oersted field. In simple cases, the absolute value of the Oersted field follows from Ampère's law which can be described as,

$$\oint_C \vec{B} \cdot d\vec{l} = \mu_0 I_C \tag{2.22}$$

where the current I_C flows through the area bounded by curve C. $\vec{B}$ is the resulting Magnetic Flux density and $d\vec{l}$ is an infinitesimal fraction of C. Upon simplification, the relation can be described as,

$$\oint_C \vec{B} \cdot d\vec{l} = \vec{B} \oint_C \cdot d\vec{l}. \tag{2.23}$$

Furthermore, since the integral along a closed circle is its perimeter and I_c is the total dc-current through the conductor then $\vec{B}_\mathsf{e} = \mu_0 \vec{H}_\mathsf{e}$ outside the wire at a distance r can be described as,

$$\mu_0 H_\mathsf{e} = \frac{\mu_0}{2\pi} \frac{I_c}{r} \tag{2.24}$$

where μ_0 is the magnetic permeability in vacuum.

The application of Oersted fields in controlling the magnitude of the emitted ultrafast current is explored in chapter 6.

2.7 Thermal effects

2.7.1 Joule heating

Joule heating refers to the process whereby a conductor experiences a temperature increase resulting from the flow of electrical current [109] due to the conversion of electron kinetic energy into thermal energy, in line with the principle of energy conservation. According to Joule's first law [109],

$$\frac{H}{t} = P = I^2 R \tag{2.25}$$

where H is the heat induced in the conductor over time t, I is the dc-current flowing through the conductor, R is the electrical resistance of the conductor. Root Mean Square (RMS) values are used in the above relation For ac-currents.

An understanding of Joule Heating is necessary to account for the heat dissipation due to dc-current. This is observed as a large response in time domain signals in chapter 7 for GMR devices and chapter 6.

2.7.2 Thermoelectric effects

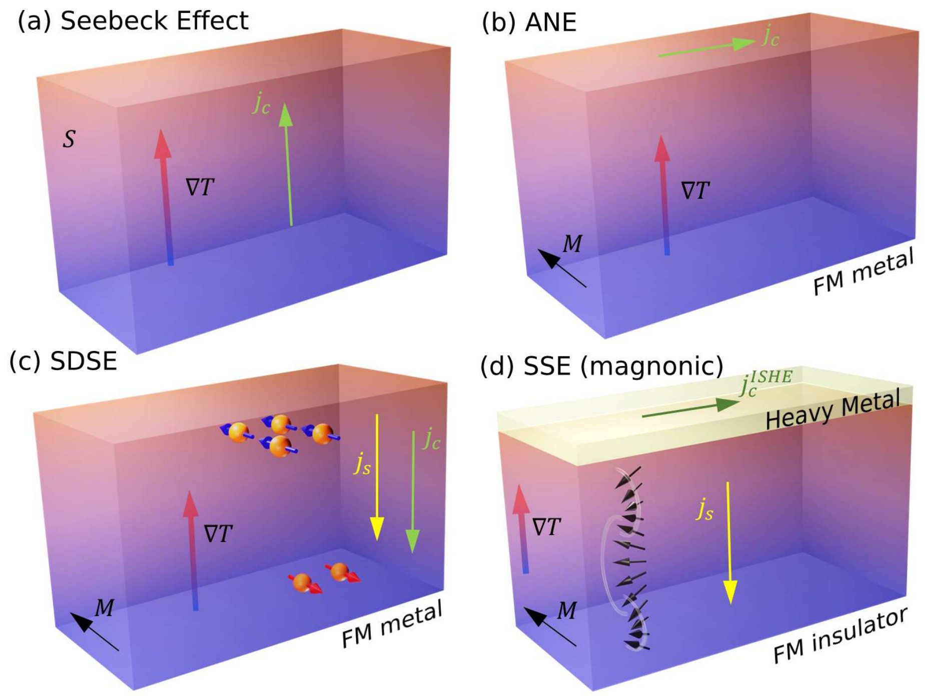
(a) Seebeck Effect
S
∇T
j_c
(b) ANE
j_c
∇T
M
FM metal
(c) SDSE
j_s
j_c
∇T
M
FM metal
(d) SSE (magnonic)
j_c^{ISHE}
Heavy Metal
∇T
j_s
M
FM insulator

Figure 2.12: Illustrations showing Thermoelectric effects: (a) Seebeck Effect, (b) Anomalous Nernst Effect (ANE), (c) Spin-dependent Seebeck Effect (SDSE) and Spin Seebeck Effect (SSE). The illustrations highlight the induced j_c^{ANE} and/or j_s in metals and insulators due to thermal gradient $\vec{\nabla} T$ and the presence of a net $\vec{M}$.

Spintronic effects, attributed solely to the electric and magnetic fields, which were discussed in the previous section (see section 2.6) are the primary mechanisms for spin-to-charge conversion. Nevertheless, temperature gradients can also produce significant heat-driven spin transport in magnetic metals and insulators. These thermal phenomena, namely, Anomalous Nernst Effect (ANE), Seebeck Effect, Spin-dependent Seebeck Effect (SDSE), and Spin Seebeck Effect (SSE), have been extensively explored in the field of spincaloritronics. These can be detected via THz emission spectroscopy or ultrafast electrical measurements on a femtosecond timescale.

Seebeck effect

The Seebeck effect [110] is a phenomenon that generates a charge current within the material due to a temperature gradient ∇T. The effect is governed by the energy dependence of the conductivity of the electrons. The distribution of electrons in different energy states can be described using Fermi-Dirac statistics as shown earlier in the chapter. In this process, electrons are transferred to the higher energy states at the hotter region, leading to an increase in the average energy per electron. A difference in the conductivity of a higher energy electron compared to a lower energy electron creates a diffusion of charge. This leads to a net flow of current from the colder to the hotter region due to an electromotive field,

$$\vec{\mathcal{E}}_{\text{emf}} = -S\vec{\nabla}T \tag{2.26}$$

where S is the Seebeck coefficient of the material (see figure 2.12 (a)).

This unique effect is detected via two electrically connected metals with different transport properties where the temperature gradient is transformed into a local charge current density. A pair of such metal junctions form the thermocouple which are used to measure the thermovoltage across the two junction.

The thermovoltage in ultrafast timescales is observed from an on-chip thermocouple in chapter 7.

Anomalous Nernst effect

The application of a thermal gradient ∇T leads to the creation of a transverse electric field E due to the transverse movement of electrons within a conductor or semiconductor upon application of a perpendicular magnetic field H. This phenomenon is known as the Nernst effect. Similar to the AHE, the thermoelectric analogue is termed the Anomalous Nernst

Effect (ANE) where the application of temperature gradient across a magnetic material produces a transverse anomalous voltage due to Lorentz force created by the internal magnetic field of the magnetisation M. The expression for the ANE [111] is,

$$\vec{j}_c^{ANE} = -\sigma_F \cdot Q_s \cdot 4\pi \cdot \vec{M}(t) \times \vec{\nabla} T \tag{2.27}$$

where σ_F is the electrical conductivity and Q_s is the anomalous nernst coefficient of the FM subject to a thermal gradient $\vec{\nabla} T$ perpendicular to the magnetisation $\vec{M}$ (see figure 2.12 (b)). It is an intrinsic property of the material similar to the AHE with its origin primarily dominated by the net Berry curvature [94, 112] of all bands near the Fermi level [95]. However, the intrinsic effects and scattering via spin-orbit coupling have been observed to increase the ANE contribution in ferromagnetic thin films [111].

The signature of an ANE mediated ultrafast response is obtained in FM, as shown in chapter 7.

Spin and spin-dependent Seebeck effect

The application of a thermal gradient along a ferromagnetic layer has been shown to be a viable approach for achieving a spin-polarised current or a pure spin current when the net transfer of opposite charges within the ferromagnetic metallic layer is equivalent. This effect is termed the Spin Seebeck Effect (SSE) and the mechanism is based on nonequilibrium physics and the transfer of energy between magnon, phonon, and electron systems [10]. However, the SSE is difficult to measure directly since the electron spins have a finite lifetime and they are not a conserved quantity, unlike the charge conservation. Hence, it is typically measured with the help of a Heavy Metal (HM) layer, which converts the spin current into a charge current through the ISHE (see figure 2.12 (d)). This effect was first reported in a $Ni_{81}Fe_{19}$ film, which was detected by the ISHE signal in a Pt layer [11] in a transverse geometry, where the temperature gradient is applied in the plane of the sample and was denoted as the Transverse Spin Seebeck Effect (TSSE).

In addition, the thermally excited spin current can propagate directly into the detection layer by parallel orientation with the heat flow in and out of plane direction. This configuration is termed the Longitudinal Spin Seebeck Effect (LSSE) [113].

In contrast to the SSE, a pure spin current can be generated [114, 115] in magnetic materials driven by a temperature gradient with the mechanism primarily governed by the spin-dependent single particles with a confined spin diffusion length [10]. This is termed as the Spin-dependent Seebeck Effect (SDSE). Moreover, this would suggest that the SDSE is not affected by the choice of substrates unlike the SSE, indicating that the response showing substrate dependence is not of SDSE origin, as observed in chapter 7. The spin-polarised current is induced due to the movement of majority and minority spin electrons in opposite directions which gives rise to a difference in the transport properties reflected in terms of the Seebeck coefficient, thus effectively creating two conductors (see figure 2.12 (c)).

Subsequently, studies were carried out based on thermally excited spin current in magnetic insulators via spin waves which are also referred to as magnons [10, 116–118], to obtain SSE. This is beneficial since the contributions to the SSE by conduction electrons are expected to be negligible in insulators and a pure spin current driven SSE results in less heat dissipation.

The SSE is likely to arise from an efficient exchange coupling that occurs at the interface between the FM insulator and HM [119]. In this context, a temperature difference between the metal electrons ($\mathsf{T_H}$) and the magnetic insulator magnons ($\mathsf{T_M}$) causes a pure spin current j_s given by [30],

$$j_s = -\mathcal{K}(\mathsf{T_H} - \mathsf{T_M}) \tag{2.28}$$

to flow through the bulk of the FM material to the HM via magnons and the spin Seebeck coefficient $\mathcal{K}$ relates the spin current to the temperature difference.

An SSE mediated ultrafast response is obtained in ferromagnet (both metal and insulator) and heavy metal heterostructures as shown in chapter 7.

2.8 Ultrafast Demagnetisation induced by hot-electron transport

Several investigations have been carried out to understand the microscopic origin of laser-induced demagnetisation, which occurs after the electronic states are excited with a fs-laser pulse. Strong evidence for the occurrence of magnetisation quenching in 3d-metals within a picosecond [14, 120–124], suggests the possibility of ultrafast demagnetisation in ferromagnets (see figure 2.12 (c)). The electric field induced due to ultrafast demagnetisation upon laser excitation along z-direction is given by [125],

$$\vec{E}_{\text{dem}} \propto \frac{\partial^2 \vec{M}(t)}{\partial t^2} \left(\hat{M} \times \hat{z}\right) \tag{2.29}$$

where $\vec{M}(t)$ is the time-dependent magnetisation and $\hat{z}$ is the unit vector in the direction perpendicular to the material surface.

However, the laser-induced demagnetisation is still a highly debated topic. To shed more light on this phenomenon, a phenomenological three-temperature model has been proposed [126, 127] to describe the system's dynamics. In this, three thermalised energy reservoirs, or baths, are proposed, namely electrons, lattice, and spin, each with corresponding temperatures denoted by T_e, T_l, and T_s, respectively. The absence of a microscopic basis for angular momentum transfer between the baths was a notable limitation. However, through further research, it has become evident that laser-heating of the electron system is a viable method for increasing scattering events that involve spin-flips, such as Elliot-Yaffet electron-phonon scattering [128, 129]. Such types of scattering involve coupling of spin-up and spin-down states as well as spin-orbit coupling, forming an overall spin state leading to spin relaxation. This, in turn, provides a channel for local spin dissipation (see figure 2.1 (d)).

Apart from the proposal of a microscopic three-temperature model, other mechanisms, such as electron-electron Coulomb scattering [130] and electron-magnon scattering [131, 132], also occur due to strong coupling between localised and mobile electrons in ferromagnetic materials. These models have proven effective in predicting typical experimental timescales. However, there is still an ongoing debate in the scientific community regarding the relative importance of local versus non-local processes. The latest development is the optically induced intersite spin transfer (OISTR) mechanism [133–135] according to which a direct spin transfer is possible across sublattices driven by a strong optical field. Furthermore, it has been shown recently that ultrafast demagnetisation and terahertz spin current generation have the same origin, which is the direct result of magnetisation differences in nonthermal electron distributions within the ferromagnet and heavy metal layer stack [52].

3 Experimental Methods

3.1 Ultra High Vacuum (UHV) deposition systems

3.1.1 RF/DC Magnetron Sputtering

The sputtering process involves the bombardment of a target surface with a beam of highly energetic ions, usually Ar, thereby ejecting atoms or molecules and subsequently forming a plume. If a substrate is placed in the plume's path, it will accumulate the particles and form films of the target material. It is possible to deposit thin films of various types by controlling various parameters such as exposure time, discharge voltage, the distance between target and substrate, and substrate temperature etc. The use of DC sputtering is limited to conductive samples such as metals and alloys. In contrast, RF sputtering is mostly used for dielectrics. The sputtering rate can be enhanced by creating a magnetic field at the target, which is achieved by positioning magnets behind the cathode to which the target is attached and is referred to as magnetron sputtering [136]. This results in an increased number of collisions and confinement of electrons near the target surface, thus, creating high plasma density. This increases the rate of deposition and higher sputtering yield.

The sputtering system used for the preparation of single and multilayer thin films has nine target slots and can be used to deposit films simultaneously on multiple substrates placed on a substrate holder. Additionally, various gases can be introduced, such as Ar or N_2, to create special films. The sample can be changed in a vacuum using the load lock chamber system, and contamination in the system is kept to a minimum by the use of a turbo pump backed by a scroll pump, thereby maintaining a base pressure of 5×10^{-8} mbar and a scroll pump is used as the backing pump. The amount of gas flowing into the chamber is adjusted by mass flow controllers, and the resulting process pressure is measured capacitively. In addition, the process pressure can also be increased by throttling the pump output using a butterfly valve.

The single-layer thin films and heterostructures comprising of the metals Ta, Ru, Pt, Cu, $Co_{50}Fe_{50}$, $Co_{20}Fe_{60}B_{20}$ and $Ni_{80}Fe_{20}$ were deposited using DC sputtering for the work done in this thesis in an Ar atmosphere with a constant flow rate of 10 sccm and gas pressure of $\sim 7 \times 10^{-4}$ mbar. Additionally, layers of MgO were sputtered using RF Sputtering in different layer stacks also in an Ar atmosphere with a constant flow rate of 100 sccm and gas pressure of $\sim 6.5 \times 10^{-3}$ mbar.

3.1.2 Electron beam Evaporation

Electron-beam evaporation is a physical vapour deposition method that involves the use of an electron beam originating from the joule heating of a charged tungsten filament. This beam is directed and accelerated towards a crucible containing the desired deposition material using a magnetic field and high voltage, respectively. This results in the transfer of energy into the atoms of the crucible material and subsequent heating into a gaseous state in the vacuum chamber. Thereafter the gaseous atoms condense into the solid phase at the substrate surface, thereby forming a film layer.

The Electron-beam evaporation system used in the scope of this thesis consists of an Ultra High Vacuum (UHV) chamber pumped down by a turbo pump and backed up scroll pump, creating a base pressure of 5×10^{-7} mbar. It is used for the deposition of layer stacks of Ti/Au or Ti/Ag/Au for the contact pads or the waveguides and AlO_x for its use as a capping layer or as an etching mask for the Ar-ion etching process due to its relatively slow etching rate. Additionally, the distance for the emitted material to the substrate is important for situations involving nanopatterns with thin resist layers. Thus a large distance prevents the melting of the nanopatterned polymer, which could affect the liftoff process. A larger distance was used as shown in chapter 5 for the fabrication of metaSTEs.

3.2 Etching systems

3.2.1 Ar-ion milling

Ion milling is a technique used to etch out material from a sample. It involves an ion beam exposure of a surface where the collision of the beam ions with atoms of the sample material leads to energy and momentum transfer and possible ejection of the atoms. Apart from factors such as ion energy and the binding energy of the atoms, the etching is favourable in the case of heavier ions such as Argon ions, due to higher momentum transfer.

The argon etching system used for this work consists of a UHV chamber with a base pressure of about 5×10^{-8} mbar, achieved using a turbomolecular pump and a scroll pump serves as a backing pump. It consists of an argon ion gun with an endpoint detector, which is a differentially pumped secondary ion mass spectrometer. This can, among other things, be used to analyse the positively charged secondary ions originating from the etched sample according to their mass and number in a time-resolved manner. The etching system is primarily used to etch the metallic thin films using an etching mask in order to produce metallic nanostructures.

3.2.2 O_2 plasma etching

O_2 plasma etching refers to the process of material removal from the surface via a low-pressure plasma. The plasma is formed by ionisation of oxygen molecules due to the application of high power radio waves along with the low pressure condition of the chamber. The plasma breaks the resist molecules and turns them into volatile components, which are removed via vacuum pumps. Within the scope of this work, it was primarily used to remove the residual resists after patterning in order to obtain a clean surface for material deposition.

3.3 Lithography

The lithography step involves various chemical processes to imprint patterns into substrates or layer stacks to create nano and microstructures. There are three types of lithography techniques primarily used under the scope of this thesis.

3.3.1 Optical Lithography

The process of optical lithography [137] involves projecting patterns onto a substrate that is coated with a photosensitive polymer material, called resist, either by using a mask or in a maskless process via irradiation. This leads to a change in the chemical structure of the underlying resist. Usually, a positive process involves the breakdown of the long polymer chain into smaller components, which are dissolved using suitable developer solutions. A negative process is achieved using a negative resist where the exposed area leads to crosslinking and the unexposed area is removed using a suitable developer solution. Alternatively, a negative process can be obtained by using an image reversal resist where the polymer chains crosslink to form longer polymer chains upon additional tempering followed by irradiation usually with UV light. However, this technique is limited by the diffraction limits from the masks and the internal reflections within the resist, which inhibits the patterning size below a micron size. Within the scope of this thesis, a DMO Microwriter ML3 maskless lithography system was used for patterning micrometer sized structures, for instance, contact pads.

3.3.2 Electron-beam Lithography

In order to overcome the limitation of patterning size, electron-beam lithography technique is helpful. It involves patterning structures using an accelerated electron beam, produced by an electron gun on a substrate surface. This process typically involves resists such as a two-layer polymer system consisting of Poly(methyl methacrylate) also known as PMMA [137–139], with different molecular weights. Typically, the lower resist layer has a low molecular weight and thus greater sensitivity in electron beam lithography, and as a result, a resist profile with an undercut is produced. In this way, structures can be produced with a resolution of a few nanometers. In the case of positive resists, the solubility of the exposed areas is locally increased so that they can be removed using the developer solution. However, in the case of a negative process, novolac-based resists with crosslinking agents are used which leads to crosslinking of the exposed area, thereby dissolving the unexposed resist layer in a suitable developer solution. Within the scope of this thesis, a Raith Pioneer e-beam lithography system was used for the nanopatterning of structures owing to its high resolution. Additionally, a secondary electron detector is used for imaging similar to a Scanning Electron Microscope (SEM).

3.3.3 Laser Interference Lithography

Laser interference lithography operates on the fundamental principle of superposition of two or more coherent light waves that meet certain light interference conditions to create periodic patterns pertaining to the maxima and minima of the interference pattern. Considering the angle θ between the superimposed waves of wavelength λ, a fringe pattern with a periodicity of $\frac{\lambda/2}{sin(\theta/2)}$ can be achieved on the resists which are sensitive to the incident wave intensities. This technique is useful for patterning periodic structures of stripes or dots over a large area with significantly less patterning time compared to e-beam or optical lithography, hence, it was used to pattern the STE stripes discussed in chapter 5.

3.4 Fabrication

The devices fabricated for the study within the scope of this thesis utilised deposition and etching techniques, along with patterning via lithography, which was mentioned above. The sequence of steps followed to realise the nanopatterned devices can be categorised into two sequences as shown below.

3.4.1 Additive approach to patterning

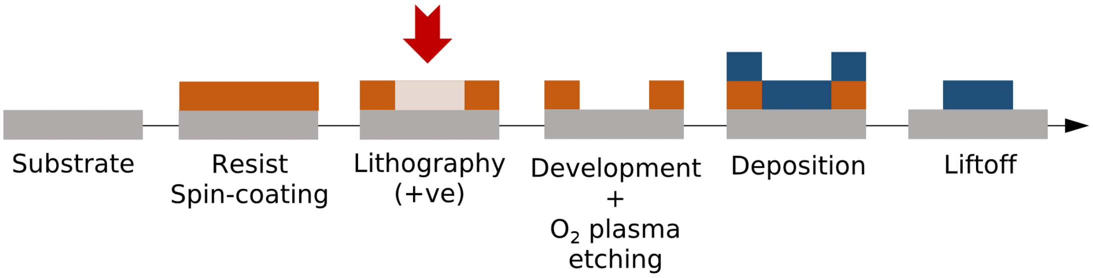

Figure 3.1: Fabrication Process involving nanopatterning by liftoff.

The additive approach involves fabrication process via liftoff which commences with the spincoating of a resist for positive lithography process on a substrate or on a thin film. The patterning is done either by e-beam or optical lithography. The patterned area is dissolved in the relevant solvent in the development step. This is followed by O_2 plasma etch to get rid of resist residues on the substrate. The material of interest is deposited using deposition techniques such as sputtering or e-beam evaporation. The final step is the liftoff, where the remaining resist is removed along with deposited material on top of it, leaving behind well-defined patterned material (see figure 3.1). This process is mostly used to pattern big structures such as waveguides or contact pads.

3.4.2 Subtractive approach to patterning

The subtractive approach in lithography process involves patterning and selectively removing unwanted areas from a uniform material layer (thinfilm) deposited by either sputtering or e-beam evaporation. It can be achieved through different pathways which are described as follows:

Process 1: This involves spincoating negative resist on a thinfilm followed by photolithography with exposure of the desired areas with a structure for patterning. This leads to crosslinking of these areas and in the subsequent development step, the resist is dissolved in areas other than the pattern area. The subsequent O_2 plasma etch is performed to remove the residues and is followed by an etch via Ar-ion milling where the resist acts as the etching mask. As a result the material in the areas other than the pattern area in the film are etched away and finally removal of the resist on top of the structure reveals the patterned structure.

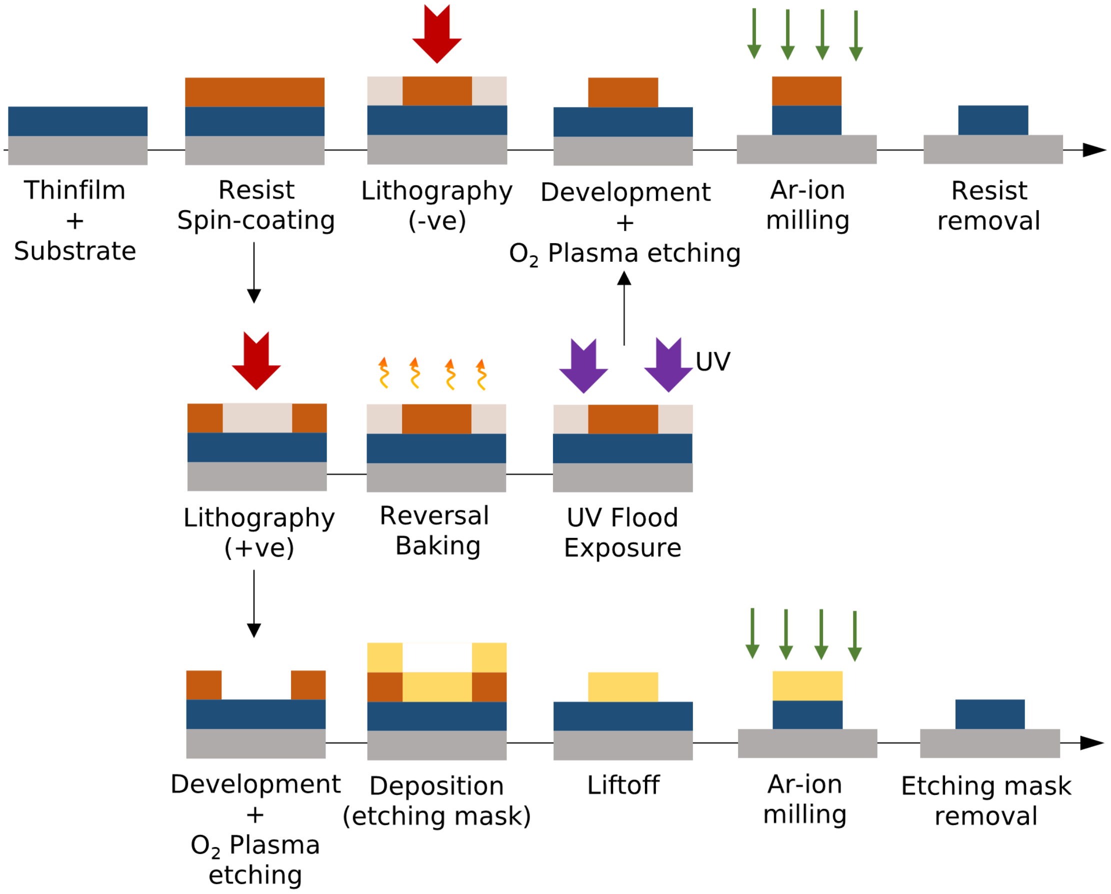
Thinfilm
+
Substrate
Resist
Spin-coating
Lithography
(-ve)
Development
+
O2 Plasma etching
Ar-ion
milling
Resist
removal
UV
Lithography
(+ve)
Reversal
Baking
UV Flood
Exposure
Development
+
O2 Plasma
etching
Deposition
(etching mask)
Liftoff
Ar-ion
milling
Etching mask
removal

Figure 3.2: Fabrication Process involving nanopatterning masks on thin films to achieve structures via Ar-ion etching where the mask prevents the etching of the desired areas of the layer stacks.

Process 2: This involves an intermediate image reversal step. After the spincoating of an image reversal resist on the thinfilm, it is exposed in the areas where the pattern is desired. A subsequent baking step is performed, which is followed by flood exposure with an ultraviolet source which leads to the cross-linking of the exposed area while the unexposed areas are still photoactive. The resist in the unexposed areas is removed by a suitable developer solution (see figure 3.2). Subsequently, O_2 plasma etch is performed to get rid of the residues. This is followed by Ar-ion milling and removal of leftover resist to reveal the patterned material (see figure 3.2).

Process 3: This approach involves a positive process where the thinfilm is spincoated with a positive resist followed by e-beam, optical or laser lithography. These make the exposed area soluble in suitable solvent which is removed in the development step. After O_2 plasma etching for removal of the residues, an AlO_x etching mask is deposited using ebeam evaporation. A subsequent liftoff of the thin film in the desired pattern area is performed. This is followed by Ar-ion milling which etches away the exposed thin film, while the area beneath the etching mask is preserved. The subsequent removal of the etching mask exposes the desired pattern in the thin film (see figure 3.2). This process was used for most of the nanostructured devices discussed in this thesis.

3.5 Characterisation

Following the device fabrication by nanopatterning, the electrical and magnetic properties were characterised primarily using the following techniques.

3.5.1 Magneto-optic Kerr effect (MOKE)

Magneto-optic Kerr Effect (MOKE) involves the reflection of linearly polarised light from the surface of a material. The linearly polarised light undergoes a change in the polarisation direction accompanied with or without a reflectivity change, determined by the magnetisation of the material, which is either internal as in the case of a ferromagnetic or ferrimagnetic material or induced due to an external magnetic field. Unlike the Faraday effect, which is associated with transmission geometry, the MOKE is associated with the reflection of the incident light, although both effects involve interaction with light.

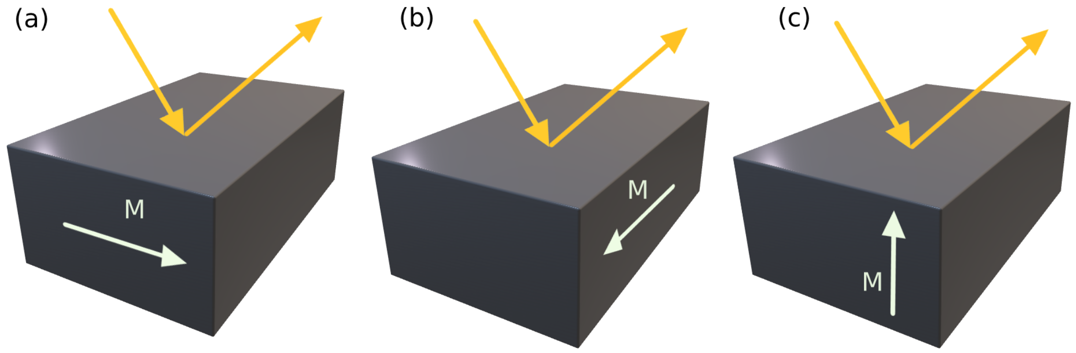

Figure 3.3: The three configurations of the magneto-optic Kerr effect (MOKE): (a) Longitudinal Kerr effect, (b) Transverse Kerr effect, and (c) Polar Kerr effect.

Based on the direction of magnetisation with respect to the plane of incident light and the surface plane, MOKE can be categorised into three different modes: the longitudinal MOKE when the magnetisation is parallel to the plane of incidence of the light and the surface plane (see figure 3.3 (a)), the transverse MOKE when the magnetisation is perpendicular to the plane of incidence and parallel to the surface plane (see figure 3.3 (b)), and finally the polar MOKE when the magnetisation is perpendicular to both the plane of incidence and surface plane (see figure 3.3 (c)).

In the scope of this thesis, only the longitudinal MOKE configuration was used to determine the inplane magnetisation for FM multilayers used in chapter 6 for THz DAC devices. This was used to determine the Coercive Fields or to determine the antiparallel states in GMR layer stacks as shown in chapter 7.

3.5.2 DC Probe Station

The room temperature DC Probe Station consists of four needle probes, which are used to apply a current across the device, and the output voltage is measured using a Keysight nanovoltmeter via a software-controlled DAC. Additionally, a magnetic field can be applied in-plane using an electromagnet with the possibility of rotation using a stepper motor. The magnetic field is measured using a calibrated Hall sensor with a maximum achievable magnetic flux density of the magnet of about 0.4 T.

The probe station was primarily used to measure the $I-V$ characteristics of the multilayer thin films, nanostructures and waveguide structures to obtain their resistance, particularly for devices in chapter 6 and 7. The probe Station was also used to measure the magnetoresistance under the application of the magnetic field at room temperature for GMR devices as seen in chapter 7.

3.6 Terahertz measurement setups

3.6.1 Pump and probe electro-optic sampling in free space

The free space detection of THz radiation from a sample is carried out with pump and probe electro-optic sampling [140] as a function of delay between the terahertz and the sampling pulse. This method involves a balanced detection setup consisting of a quarter wave-plate, a polarising beam splitter, and two balanced photodiodes (see figure 3.4). The linearly polarised laser pulses are pumped from a Ti:sapphire laser oscillator with an 80 MHz repetition rate. These are incident on the sample at an angle of approximately 5° to 10° to avoid reflection back to the laser. However, this angle does not affect the transmitted THz response due to the similar path length covered by the incident pulse for each fraction of the illuminated area. These pulses have a wavelength of 800 nm, a 10 fs pulse duration, and a pulse energy of 2 nJ. The approximate diameter of the pump beam is 30 µm at Full Width at Half Maximum (FWHM) of the intensity on the sample.

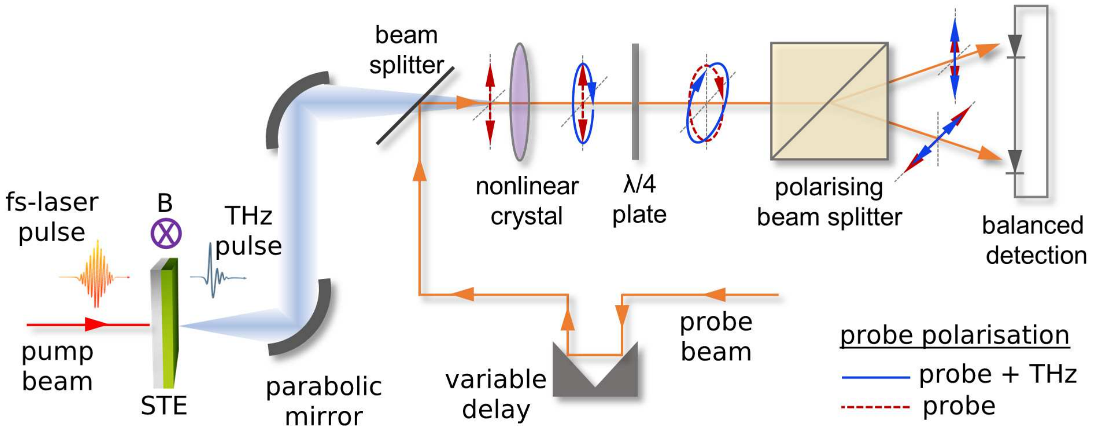
beam
splitter
nonlinear
crystal
λ/4
plate
polarising
beam splitter
balanced
detection
fs-laser
pulse
B
THz
pulse
pump
beam
STE
parabolic
mirror
variable
delay
probe
beam
probe polarisation
probe + THz
probe

Figure 3.4: Schematic showing THz free space detection setup using pump-probe electro-optic sampling.

After illumination, the resulting transient charge current induces a THz electric field $E(t)$ (see chapter 2) in the direction perpendicular to the direction of in plane magnetisation determined by an external magnetic field strength H. The electro-optic sampling is carried out using a probe pulse, with 0.6 nJ pulse energy and 10 fs pulse width, which copropagates alongside the terahertz pulse within an electrooptic crystal, specifically 10 μm thick ZnTe(110) [141]. The THz electric field leads to a proportional change of the refractive medium thus creating birefringes due to an electro-optic effect called the Pockel's effect. After the electrooptic crystal, the ellipticity of the copropagating probe pulse changes to elliptical polarisation from linear polarisation and is subsequently decomposed into two components in orthogonal directions by a polarising beam splitter, which is finally detected by two photodiodes. The difference in the obtained signals from the two photodiodes is proportional to the ellipticity, which in turn relates to the THz electric field. All experimental procedures are performed in ambient room conditions.

This technique is primarily used to detect THz radiation from nanopatterned STEs, STE stripes, and metaSTEs which is discussed in chapter 5.

3.6.2 Ultrafast electrical detection

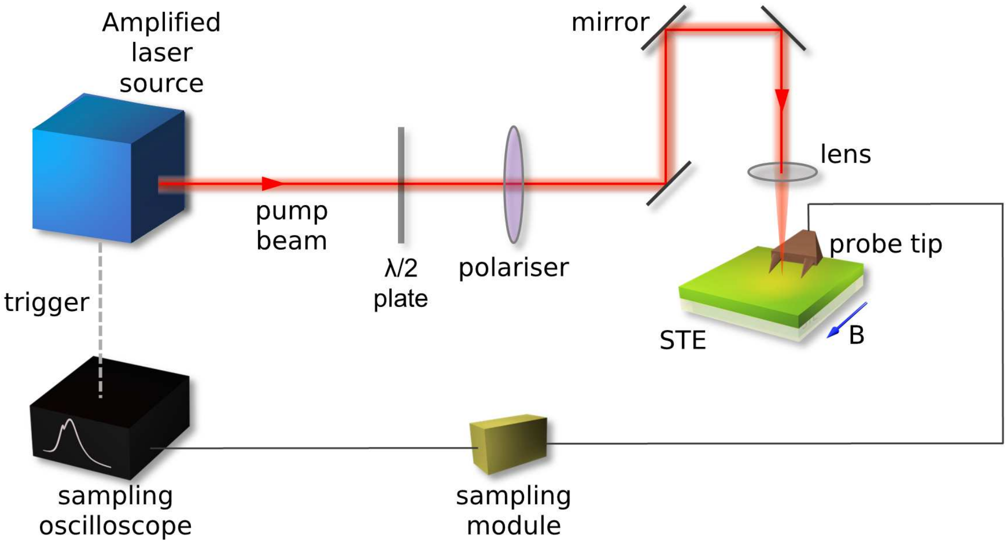

Figure 3.5: Schematic showing THz electrical detection setup.

An alternative method to detect THz excitation is through the direct measurement of ultrafast transient charge current via the use of a Sampling Oscilloscope (see figure 3.5).

The laser pulses are generated from an amplified Yb:KGW femtosecond laser source with 99.6 kHz repetition rate, a wavelength of 1030 nm, and a pulse duration of 300 fs. The laser power is controlled via a half-waveplate and linear polarisation through a polariser. The linearly polarised laser pulse is focussed using a lens to excite the STE in a normal incidence. The spot size can be varied in the range of 50 µm to 700 µm, determined by varying the focal distance of the lens from the STE, thus providing the possibility to control the excitation areas which are relevant for the nanostructured STEs. Together with control of laser power and the spot size, the desired fluence can be achieved.

The excitation of STEs leads to a spin current from the FM layer to the NM layer, thereby inducing a charge current pulse I_C proportional to THz electric field in the lateral direction established by the direction of magnetisation, which is determined by the external magnetic field strength H. The ultrafast electrical response is detected via the RF coplanar probe tips of 150 µm pitch and G-S (Ground-Signal) configuration by a Tektronix DSA 8200 sampling oscilloscope with an 80E10 sampling Time Domain Reflectometry (TDR) module of 50 GHz resolution [35]. The 80 MHz oscillator rate prior to the amplification stage is synchronised with the sampling oscilloscope's external trigger. The laser repetition rate after the amplification is 99.6 kHz. Furthermore, the optical path time delay is matched with the electrical detection time for data acquisition by adding a manual time delay to the electrical time delay of the signal path from the probe tips to the sampling oscilloscope. All the electrical connectors used operate with the 50 GHz bandwidth. Moreover, the nanopatterned waveguide structures have an additional transmission line path which leads to an added time delay. The data acquisition by multiple triggers, with each subsequent trigger corresponding to a small part of the pulse, eventually shapes the entire response pulse.

This technique is used to measure the time domain ultrafast electrical response from thin films as slab dielectric waveguides by direct contact of probe tips with the thin film surface and the laser focussed between the two tips. In the coplanar waveguides or transmission lines the measurement is done through probe tips connected via contact pads and the laser focussed on the nanostructures. This measurement technique was primarily used in the measurements discussed in chapters 6 and 7.

4 Charge Dynamics in Spintronic THz Emitters

In this chapter, ultrafast charge dynamics were shown to occur at the edge of the STE area illuminated by a fs laser. It is already known extensively that a fs laser can induce a perpendicular spin current, which is subsequently converted to a charge current by ISHE. This lateral charge current pulse leads to an ultrafast charging phenomenon at the edges of the illuminated area, and subsequent charge relaxation leads to a backflow current pulse. Depending on the conductivity and the dielectric behavior of the emitter, the backflow current pulse has a delay with a time constant related to the occurrence of the initial charge current pulse. The delayed charge equilibration is necessary to detect the primary current pulse electro-optically via THz radiation since instantaneous backflow would cancel the initial current pulse. As the analysis of spin dynamics is based on the charge current, it is necessary to consider the contribution of this phenomenon. Moreover, different illumination conditions which could modify the backflow and, hence, the spectrum, was also addressed in this study.

Publication information The major portion of this chapter was published as: *"Charge Dynamics in Spintronic Terahertz Emitters"* by G. Schmidt, B. Das-Mohapatra, and E. Th. Papaioannou in Phys. Rev. Applied 19, 4 (2023) p. L041001,

DOI: https://10.1103/PhysRevApplied.19.L041001

Author contributions BDM and GS conceived the experiments/simulations. BDM performed the simulations and analysed the data with the support of GS and ETP. The manuscript was written by GS with the help of, and after discussions with, BDM and ETP.

Introduction

The complex chain of events involved in terahertz emission from a Spintronic Terahertz Emitter (STE) has been thoroughly studied (see section 2.1). However, the analyses within these studies usually involve a simplifying assumption that the charge current derived from the measured terahertz radiation is directly proportional to the spin current [15, 18, 21, 34], i.e. $\vec{j}_{\mathrm{charge}}(t) = \theta_{\mathrm{SH}} \cdot \vec{j}_{\mathrm{spin}}(t)$ (see section 2.6) with $\vec{j}_{\mathrm{charge}}$ the charge current, θ_{SH} the spin Hall angle, and $\vec{j}_{\mathrm{spin}}$ the spin current, hence an identical time profile is maintained. In these studies, a current pulse is often observed which is made of a positive peak succeeded by a negative one. This has been attributed to the dominant contribution of majority spins entering the heavy metal first, followed by a lagged negative component induced by minority spins. However, recent studies have started to challenge the existence of a straightforward correlation between the terahertz signal, the laser pulse, and spin physics. For instance, it was found that the optical absorption of the laser pulse played a crucial role in determining the observed intensity [142], which could be mistaken for a spin diffusion length if not carefully examined.

4.1 Simulation details

In order to address the questions raised in the previous section, a thought experiment was devised using COMSOL [143] simulations to theoretically investigate the physics after the laser pulse induces a positive current pulse. This involved a simple Gaussian time dependence for different laser spot sizes, pulse shapes, temporal pulse widths, STE thicknesses, conductivities, and permittivities.

For the simulations, the COMSOL [143] electric current submodule under the 'AC/DC' module was used to study the electric current. A square metal sheet of dimensions $l \times w = 150 \times 150\,\mu\mathrm{m}^2$ was taken to approximate an infinite-sized STE compared to the laser spot with a spot diameter D. Both were centred at $x = y = 0$. Instead of a typical beam profile, a circular beam profile was assumed with constant laser intensity, which is sufficient to demonstrate the fundamental physics involved. A Gaussian peak with full width at half maximum of τ was taken for the temporal intensity of the beam. The input parameters required for the simulation were electrical conductivity (σ) and relative permittivity (ϵ_r) of the material. For the sapphire substrate, $\sigma = 10^{-12}$ S/m and $\epsilon_r = 3.064$ [144] were used. For the reference STE thin film (STE$_{\mathrm{ref}}$), an average $\sigma = 5 \times 10^6$ S/m, which was in good agreement with the conductivity values for a multilayer thin film of W(2 nm)/$Co_{20}Fe_{60}B_{20}$(1.8 nm)/Pt(2 nm) [15, 145, 146], and an ϵ_r of 903 for Pt [147] were taken. The setup also included a set of parameters originating from a laser pulse and subsequent induced current, namely pulse width, τ = 20 fs, laser spot diameter, D = 20 µm, and metal thickness, T = 10 nm (see appendix A.2). The modelling simulates the effects after the occurence of spin-to-charge conversion, inducing a lateral current density $\vec{j}_0$. The direction of $\vec{j}_0$ was defined as $+x$. For simplicity, $\vec{j}_0$ was set proportional to the local light intensity. In COMSOL [143], the transport equations in the 'AC/DC' module are described by

$$\vec{j} = \sigma\vec{E} \tag{4.1}$$

$$\frac{\partial\rho}{\partial t} + \vec{\nabla}\cdot\vec{j} = 0 \tag{4.2}$$

$$\epsilon_0\vec{\nabla}\cdot\vec{E} = \rho \tag{4.3}$$

corresponding to Ohm's law, the continuity equation, and Gauss's law [148], respectively. From these the charge current and charge relaxation can be derived based on the differential equation,

$$\frac{\partial\rho}{\partial t} + \left(\frac{\sigma}{\epsilon}\right)\rho = 0 \tag{4.4}$$

with solution,

$$\rho(t) = \rho_0 \exp\left(\frac{-t}{\tau}\right) \qquad \text{where} \qquad \tau = \frac{\epsilon}{\sigma}. \tag{4.5}$$

This was implemented to the generated charge current by extending Ohm's law to

$$\vec{j}_{\text{tot}} = \sigma\vec{E} + \vec{j}_0 \tag{4.6}$$

by a charge current density $\vec{j}_0(t)$ uniform in space within the circular spot. A boundary condition of $j = 0$ was assigned perpendicular to the surface and at the edges of the square, which were far away from the laser spot, in order to leave the system free to react to the imprinted current as far as possible. The far-field emission for a small STE reflects the integrated current, but not the local current density. Hence, it is important to take this into account in order to compare these results with any THz emission experiments. Consequently, the local current density was integrated over the whole emitter for each moment in time that was investigated:

$$\vec{I}(t) = \int_{\text{volume}} \vec{j}(\vec{x}, t) d\vec{x}. \tag{4.7}$$

Only the x-component of the charge current was considered in the analysis since the y- and z-components of the charge current cancel when integrated over the whole space for symmetry reasons.

4.2 Charge dynamics in a thin film STE

The time dependence of current for STE_{ref} was simulated (see figure 4.1). The current density induced by ISHE of the laser-excited spin current was taken as $\vec{j}_0(\vec{x}, t)$ and the corresponding integrated current density was $\vec{I}_0(t)$. The total integrated current density was given by $\vec{I}_{\text{tot}}(t)$. The total current can be written as $\vec{I}_{\text{tot}}(t) = \vec{I}_0(t) + \vec{I}_{\text{res}}(t)$ with $\vec{I}_{\text{res}}(t)$ being the system response. The integral over the response current density $\vec{j}_{\text{res}}(\vec{x}, t)$ gave $\vec{I}_{\text{res}}(t)$.

At the beginning of the pulse, $\vec{I}_{\text{tot}}(t)$ was seen to rise with the slope of $\vec{I}_0(t)$. After a very short time, the system response started, and the negative contribution by $\vec{I}_{\text{res}}(t)$ appeared. This contribution was asymmetric around its peak, and the peak was time delayed with respect to the peak of $\vec{I}_0(t)$. As a consequence, it was observed that the maximum of $\vec{I}_{\text{tot}}(t)$ was smaller than that of $\vec{I}_0(t)$. Secondly, the decay of $\vec{I}_{\text{tot}}(t)$ after its maximum was faster than would be expected from only the shape of $\vec{I}_0(t)$. Finally, the positive part of $\vec{I}_{\text{tot}}(t)$ was followed by a negative part when $\vec{I}_0(t)$ was almost at zero, and the backflow restored charge neutrality.

In order to understand these dependencies, the local charging $\rho(x, t)$ and current densities $\vec{j}_{\text{tot}}(\vec{x}, t)$ were simulated at different times of the experiment (see figure 4.2 (a, b)). The current density was expressed by arrows, where the direction of an arrow shows the direction of $\vec{j}$ while its length was proportional to $|\vec{j}|$. The current and charge distribution can be seen at a maximum of $\vec{I}_{\text{tot}}$ (t = 48,fs), which occurs at an earlier time than the maximum of $\vec{I}_0$ (see figure 4.2 (c)). Significant charging can be observed on the left and right sides in the x-direction, and considerable backflow ($\vec{I}_{\text{res}}$) on the outside of the laser spot area. Although the current inside the spot was determined mainly by $\vec{I}_0$, there was a contribution by $\vec{I}_{\text{res}}$ that is, however, over a large time of the process, obscured by the large value of $\vec{I}_0$ until the minimum of $\vec{I}_{\text{tot}}$ (t = 79 fs) (see figure 4.2 (d)) where $\vec{I}_0$ was reduced to zero. However, charging still exists, and a backflow $\vec{I}_{\text{res}}$ was observed both inside and outside the spot, resulting in $\vec{I}_{\text{tot}}$ in the negative direction.

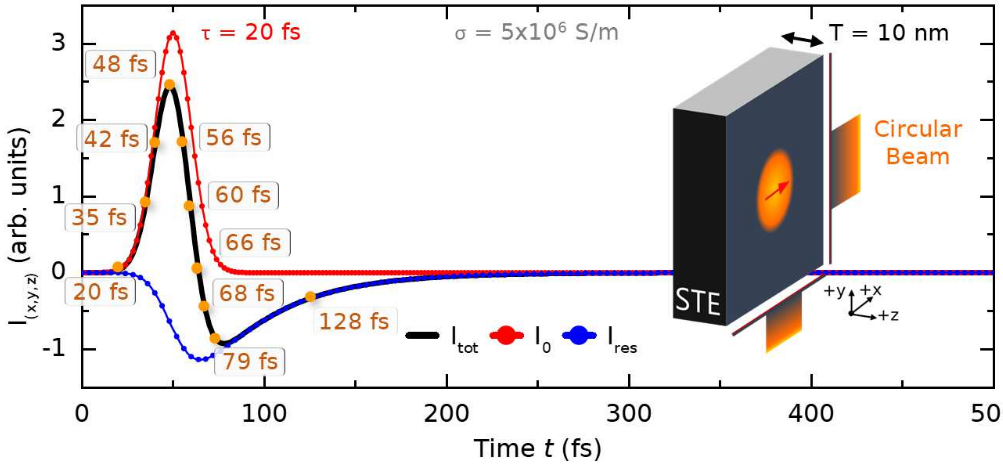

Figure 4.1: Current over time for the original excitation pulse $\vec{I}_0$ (red), the total current $\vec{I}_{\text{tot}}$ (black), and the response of the system $\vec{I}_{\text{res}}$ (blue) for a 10 nm thick emitter with a conductivity of 5×10^6 S/m. Since the initial current flows in the x-direction, symmetry forbids a contribution from any current in the y-direction to the integrated total in-plane current, even for the response of the system. The excitation pulse has a FWHM of 20 fs and is centered around t =50 fs. The charge distribution for the respective timestamps in the curve is shown in figure 4.2

In terms of charge conservation, it is apparent that even an emitter of significant size remains a closed system. Hence, the assumption of charge neutrality in the steady state requires that locally the condition

$$\int_{-\infty}^{\infty} \vec{\nabla} \cdot \vec{j}(x,t)dt = 0 \tag{4.8}$$

is fulfilled. Therefore, the total current integrated over time should be zero. However, this was not the case for $\vec{I}_0(t)$ and $\vec{I}_{\text{res}}(t)$.

The pattern of the current distribution can be explained by making a step-by-step analysis of the timeline after the fs-laser illumination, followed by spin current generation and spin to charge conversion. The charge current flowed solely in the $+x$ direction within the spot and $j = 0$ outside the spot. Despite the displacement of charge inside this spot, this did not lead

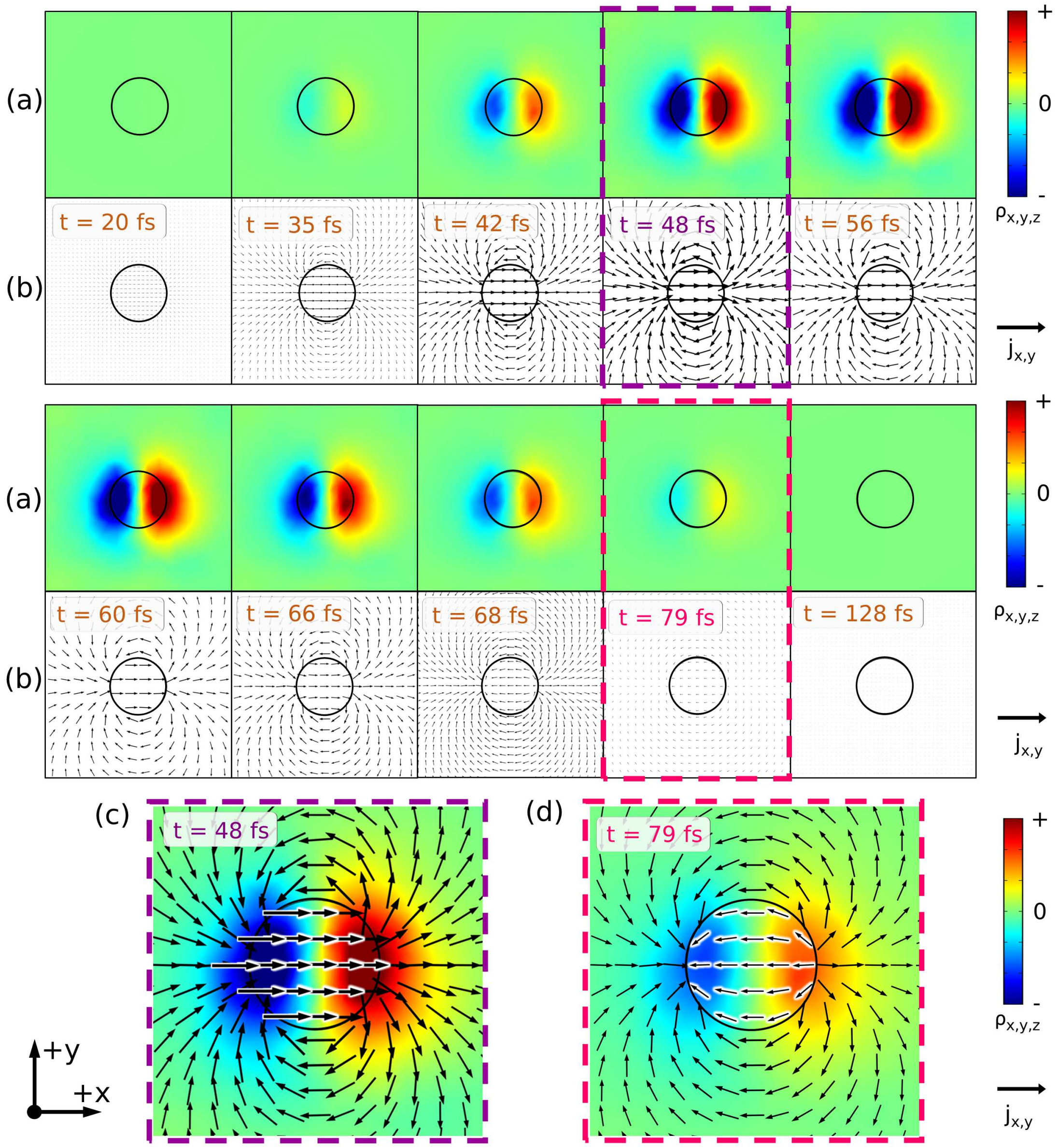

Figure 4.2: (a) The charge and (b) the current distributions for different times marked in figure 4.1. The current and charge distribution is shown at (c) t = 48 fs for $I_{\text{tot}}^{\text{max}}$ and (d) t = 79 fs for $I_{\text{tot}}^{\text{min}}$. The black circles in the charge distributions indicate the boundaries of the laser spot.

to any charge accumulation. However, $\vec{\nabla} \cdot \vec{j} \neq 0$ and thus, $\partial \rho / \partial t \neq 0$ occured solely at the circumference resulting in local charging. Eventually, the charging was maximised at y =0 and x = ±r and minimised for x =0 and y = ±r. Therefore, the positive charge started to accumulate on the $+x$ side while the negative charge was on the $-x$ side. As a result, $\vec{\nabla} \cdot \vec{j}$ became finite on very short timescales due to transient charging.

This charging phenomenon can be understood more easily by considering a fundamental principle of electrodynamics, which states that every segment of a metal sheet possesses some level of capacitance. Although minuscule, this capacitance can be charged and subsequently discharged through any linked material that exhibits finite conductivity. The slight capacitance of metal microstructures, for instance, is well-recognised and widely utilised in Coulomb blockade experiments. However, the corresponding time constants are seldom noticeable in sub-terahertz electronics.

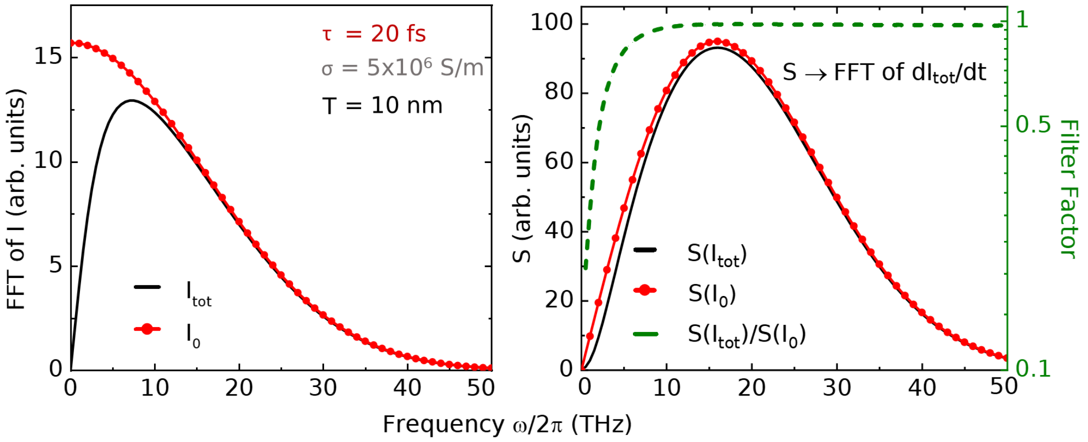

Figure 4.3: Spectral intensities for (a) the currents $\vec{I}_0$ and $\vec{I}_{\text{tot}}$ and (b) their time derivatives. At high frequencies, the spectral intensities were identical for both signals, while at lower frequencies they were suppressed. (b) Ratio of the spectral intensities for $\vec{I}_{\text{tot}}$ and $\vec{I}_0$ plotted over frequency is shown.

As soon as charge accumulation began, an immediate backflow also started due to the system response, leading to the capacitance being discharged. This discharge occured more or less symmetrically around the areas where the charge had built up. However, initially, this response current was not strong enough to completely reverse the current within the spot. Both the currents within the spot and the backflow outside the spot reached their peak when $\vec{I}_{\text{tot}}(t)$ was at its maximum. However, the charge density reached its maximum slightly later, precisely when $\vec{I}_{\text{tot}}(t)$ was already decreasing (see figure 4.2) at t = 56 fs. While the backflow around the spot persisted almost from the beginning of the excitation pulse, a complete reversal of the current inside the spot occured only when $\vec{I}_{\text{tot}}(t)$ turned negative. For t = 66 fs, it can be observed that the total current $\vec{I}_{\text{tot}}$ was zero because the outside backflow compensated for the positive current present inside the spot. It should be noted, however, that after this point $\vec{I}_0(t)$ was still positive, so the backflow overcompensated the initial excitation. Even 100 fs after the initial pulse, the total current did not decay to zero.

By analysing the time domain signal further by using Fast-Fourier Transform (FFT) it was possible to obtain the spectral amplitude for $\vec{I}_0(t)$ and $\vec{I}_{\text{tot}}(t)$, From this it was observed that the trailing negative current peak also modified the emitted THz spectrum (see figure 4.3 (a)). There was a strong suppression of lower frequencies, and the spectral amplitude for $\vec{I}_{\text{tot}}(t)$ approached that of $\vec{I}_0(t)$ until they were equal for frequencies higher than approximately 15 THz.

The Spectral Amplitude, $S(t)$, of $d\vec{I}/dt$ (see figure 4.3 (b)) was also obtained because the THz emission in the far field is proportional to the time derivative of the current and not the current itself. The FFT of the time derivative $d\vec{I}/dt$ was proportional to $\omega\hat{I}$ and thus already has a reduced intensity at low frequencies, making the effect appear less pronounced. To visualise the effect, the filter function was obtained by dividing the spectral intensity of the total current's derivative $d\vec{I}_{\text{tot}}/dt$ by that of the original current pulse $d\vec{I}_0/dt$. It was observed that certain parts of the low-frequency side of the spectrum (below 3 THz) were reduced, which clearly is a high-pass filter characteristic, with suppression by a factor of 2 or more (see figure 4.3 (b)). The maximum state was obtained for f > 10 THz.

4.2.1 Charge dynamics Circuit model

The system can be described by a fairly straightforward equivalent circuit (see figure 4.4) consisting of a resistor and a capacitor. The circuit is fed with an ISHE current, $\vec{I}_0(t)$, which charged the capacitor. This capacitor was then discharged through the resistance, R, of the surrounding material, resulting in the current $\vec{I}_{\text{res}}(t)$ flowing through R. Therefore, $\vec{I}_{\text{tot}}(t)$ is only relevant for far-field detection of THz emission, since $\vec{I}_0(t)$ and $\vec{I}_{\text{res}}(t)$ cannot be distinguished. However, the response current can be monitored using a near-field detector.

In the equivalent circuit, the current can be described by the simple differential equation:

$$C\frac{dU_C(t)}{dt} = I_0(t) - \frac{U_C(t)}{R} \tag{4.9}$$

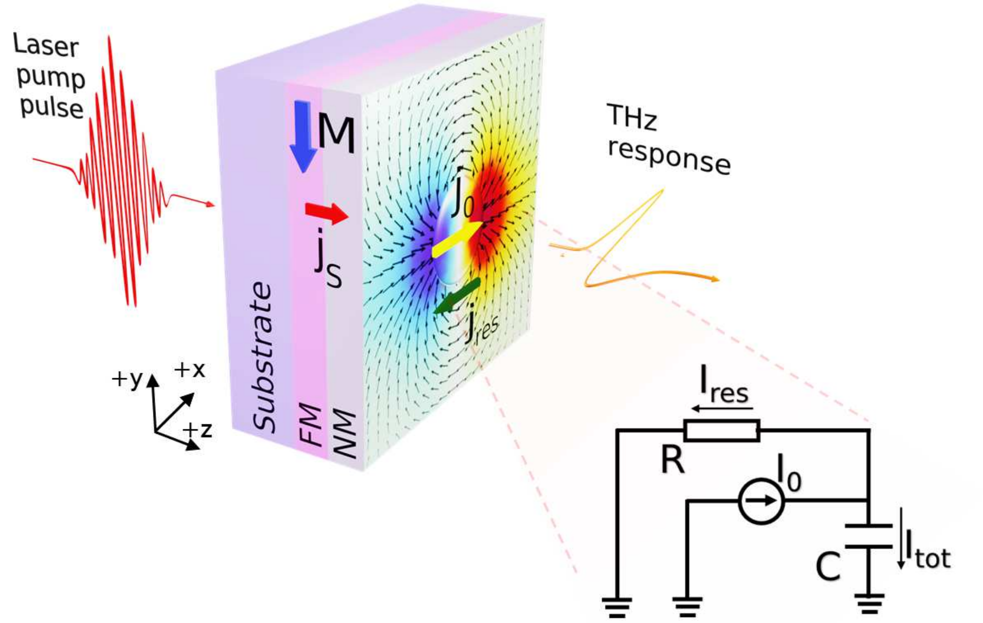

Figure 4.4: Typical arrangement for an STE where a fs-laser pulse induced spin current $\vec{j}_S$ generates a charge current $\vec{j}_0$ via ISHE leading to subsequent charge dynamics, represented in the form of an equivalent circuit. The current pulse charges the capacitor that can then discharge as $\vec{j}_{\text{res}}$ with a certain time constant through the resistor. This shapes the total current, which is the source of the THz response detected in the far-field.

where $U_C(t)$ is the voltage in the capacitor and $-U_{\text{C}}(t)/R$ corresponds to $\vec{I}_{\text{res}}(t)$, and in addition there is an ISHE current $\vec{I}_0(t)$. A Fourier transform of this differential equation (see appendix A.3) yields

$$i\omega C\tilde{U}_C(\omega) = \tilde{I}_0(\omega) - \frac{\tilde{U}_C(\omega)}{R}. \tag{4.10}$$

This can be transformed to find the total current

$$\tilde{I}_{\text{tot}}(\omega) = \tilde{I}_0(\omega) + \tilde{I}_{\text{res}}(\omega), \tag{4.11}$$

which results in

$$\tilde{I}_{\text{tot}}(\omega) = \left[\frac{1}{1 + \frac{1}{i\omega RC}}\right]\tilde{I}_0(\omega). \tag{4.12}$$

This describes the high-pass filter in the frequency domain with the cutoff frequency $\omega_{\text{cutoff}} = \frac{1}{RC}$, which allows the high-frequency components to pass through the capacitance C while the lower frequency components pass through the resistance R. As a result, the cutoff frequency or the time constant of this system was determined.

4.3 Factors affecting RC time constant

The circuit model in the previous section provides insight into the possible parameters that can influence $\vec{I}_{\text{tot}}(t)$ or eventually $\tilde{S}(\omega)$. The charging effect and especially the backflow, which might affect $\vec{I}_{\text{tot}}(t)$ and $\tilde{S}(\omega)$ can be understood in detail by analysing the effect of spatial and temporal variations of the laser beam. Furthermore, the material also plays an important role since $\vec{I}_{\text{tot}}(t)$ is dependent on the R and C of the material.

4.3.1 Effect of laser beam size and shape

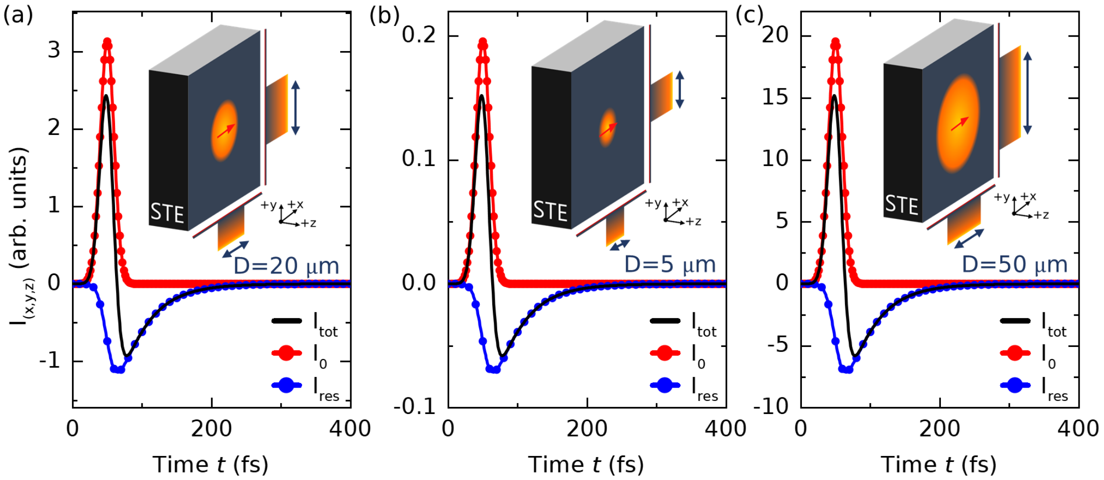

Figure 4.5: Current vs time for different beam sizes (a) 20 µm, (b) 5 µm, and (c) 50 µm with a similar temporal profile and amplitude proportional to the beam size.

First, the influence of spatial variation of the laser spot on the charge dynamics of the STE was addressed. Hence, subsequent simulations were performed with an alteration of the spot size, a variable that could potentially have an impact if the two accumulations of charge interact and function as a dipole. In a similar manner to a Hertzian dipole [149, 150], an increased spot size could potentially result in a lower frequency or, at the very least, a slower

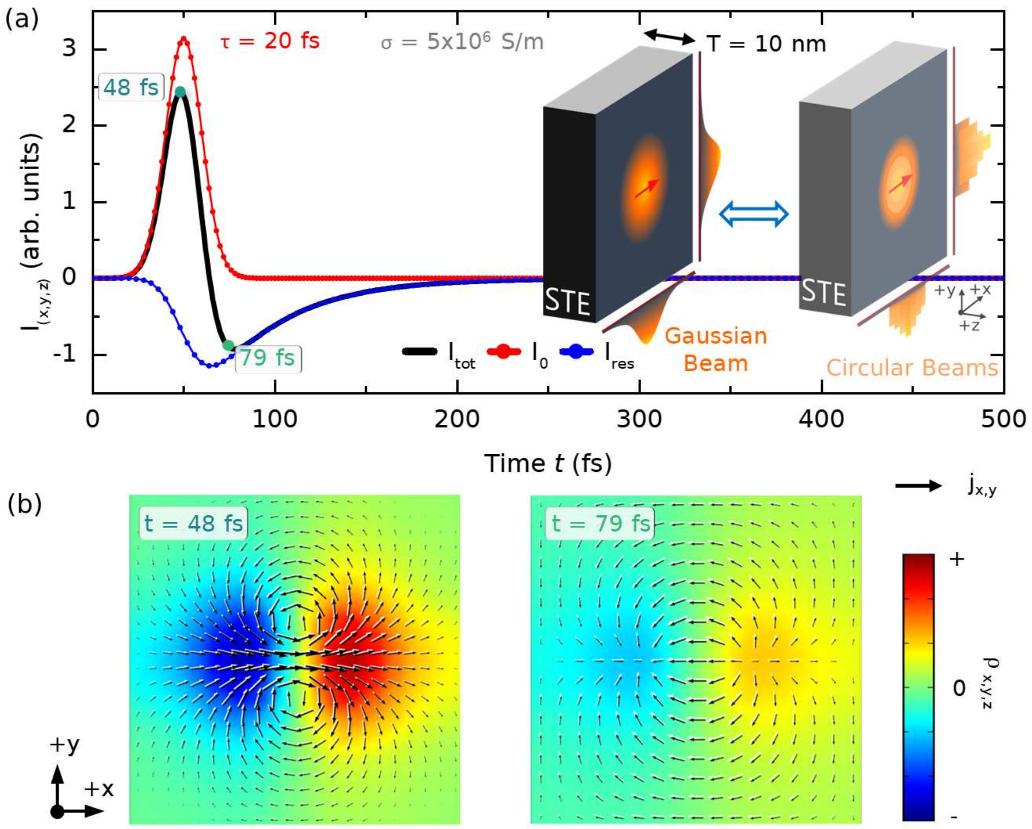

Figure 4.6: (a) Current vs. time and (b) charge distribution with a Gaussian beam profile. The charging was more blurred than for a circular beam in which the current dropped to zero in a step function at the edge of the beam. The current profile in time, however, was virtually identical for both beam shapes.

response. However, the simulations revealed no such effect. For spot sizes of D = 5 µm and D = 50 µm, all currents were scaled in amplitude by constant factors compared to those for D = 20 µm, while the timing remained unaffected (see figure 4.5). This can be understood because the effect is fully linear and allows for superposition.

As a consequence of this, even when a Gaussian beam profile was employed, as opposed to a circle with constant intensity, the calculated current profile vs. time shows the same timing, because the Gaussian beam profile can be perceived as a superposition of circular beams with varying radii and intensities (see figure 4.6). Moreover, the corresponding charge distribution is similar to that of a circular beam (see figure 4.1). Although the charge was distributed much more widely than that obtained for a circular beam, the timing remains virtually identical.

4.3.2 Effect of laser temporal width and shape

In this section the effect of temporal changes in the shape of the laser pulse on the charge dynamics was addressed. For this two different situations were tested by varying the pulse width to $\tau = 100\,\text{fs}$ (see figure 4.7 (a)) and $\tau = 0.5\,\text{ps}$ (see figure 4.7 (c)) and comparing with $\tau = 20\,\text{fs}$ corresponding to S_{ref} (see figure 4.1).

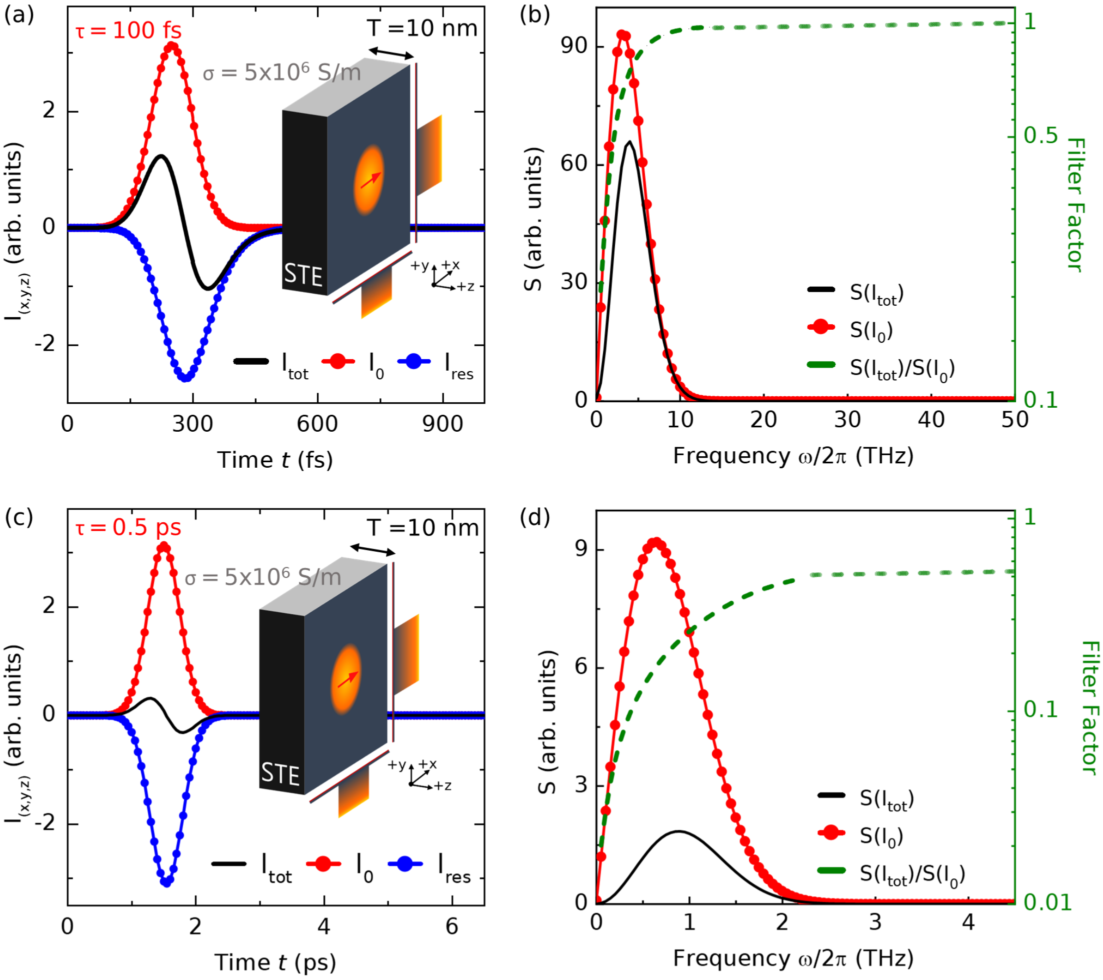

Figure 4.7: Time domain signals for (a) 100 fs and (c) 0.5 ps wide pulses, and their Spectral Amplitudes (b) and (d), respectively. $\vec{I}_0(t)$ (red) and its corresponding response current $\vec{I}_{\text{res}}(t)$ (blue) leading to $\vec{I}_{\text{tot}}(t)$ (black). The characteristic Filter Factors are shown in dashed green.

For the 100 fs pulse width, the excitation pulse was longer, while the RC constant of the emitter remained the same. On the timescale of $\vec{I}_0(t)$, the backflow started earlier and increased faster, compared to the case for the 20 fs pulse. In the spectrum (see figure 4.7 (b)), the total intensity I_{tot} was much more reduced from I_0 as compared to that of the 20 fs pulse. This is merely a result of the more abundant lower frequency components due to the longer pulse. It should be noted that counterintuitively, only the finite RC time constant of the system allows the positive current peak to exist. Without the system capacitance, $\vec{I}_0(t)$ and $\vec{I}_{\text{res}}(t)$ would be simultaneous and $\vec{I}_{\text{tot}}(t)$ would be 0, with no THz emission.

The results of the simulation for a 0.5 ps pulse width (see figure 4.7 (c)) further emphasised the effect. $\vec{I}_0(t)$ had considerable contributions up to more than 1 THz (see figure 4.7 (d)). The backflow, however, more or less got completely annihilated in this frequency regime. Hence, studying the laser pulse width duration revealed the physics behind the system's response.

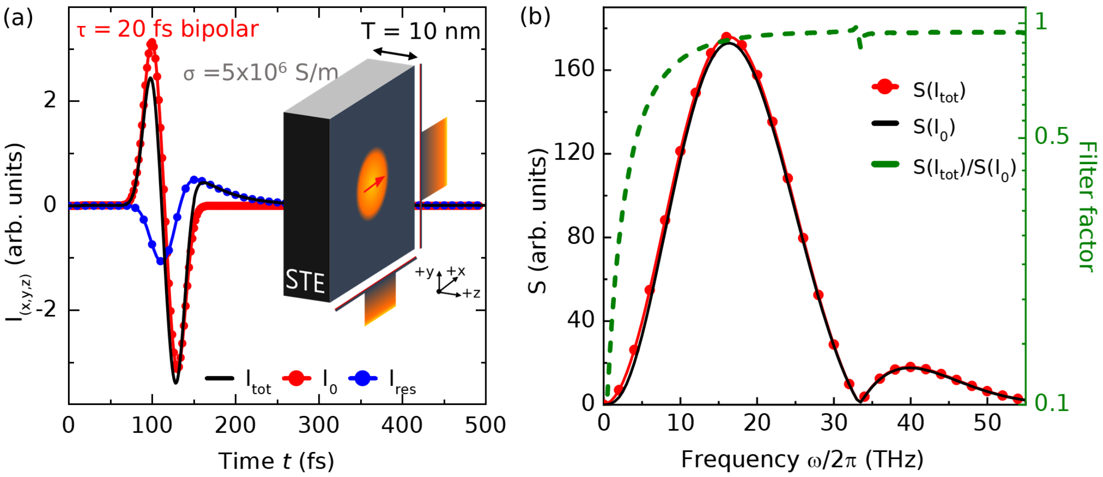

Figure 4.8: (a) Time domain signals and (b) spectra for 20 fs wide antisymmetric bipolar pulse. Since this pulse had fewer low-frequency contributions for $\vec{I}_{\text{tot}}(t)$ (black) as compared to the $\vec{I}_0(t)$ (red), the effect on the lower part of the spectrum was less visible, than that for a single pulse as shown in figure 4.7, but still a reduction was observed up to almost 20 THz.

Since a simple Gaussian profile (see figure 4.6) oversimplified the ultrafast spin current, a more complex excitation was chosen to address majority and minority charge spin current-induced bipolar charge currents. Therefore, for an STE of 10 nm thickness, a sequence of two identical Gaussian pulses with opposite signs was used to form a bipolar antisymmetric shape for $\vec{I}_0$ (see figure 4.8 (a)). The resulting $\vec{I}_{\text{tot}}(t)$ lost this symmetry and even had a small positive trailing pulse. From the spectral amplitude (see figure 4.8 (b)), it became clear that the convolution of two pulses in the time domain resulted in a dip in the frequency domain. As shown in the comparison of filter characteristics, the modification of the spectrum is similar to STE$_{\text{ref}}$ (see figure 4.11 (d)). It is important to understand that the charge current featuring only a single positive and a trailing negative component must be the result of a single positive spin current pulse. On the contrary, a bipolar excitation induces a more complex signal.

4.3.3 Effect of STE electrical conductivity

With reference to the Charge Dynamics Model introduced in equation 4.12, the high-pass characteristics were influenced by the RC time constant. While keeping all laser parameters similar to S$_{\text{ref}}$, the R for the STE system was varied.

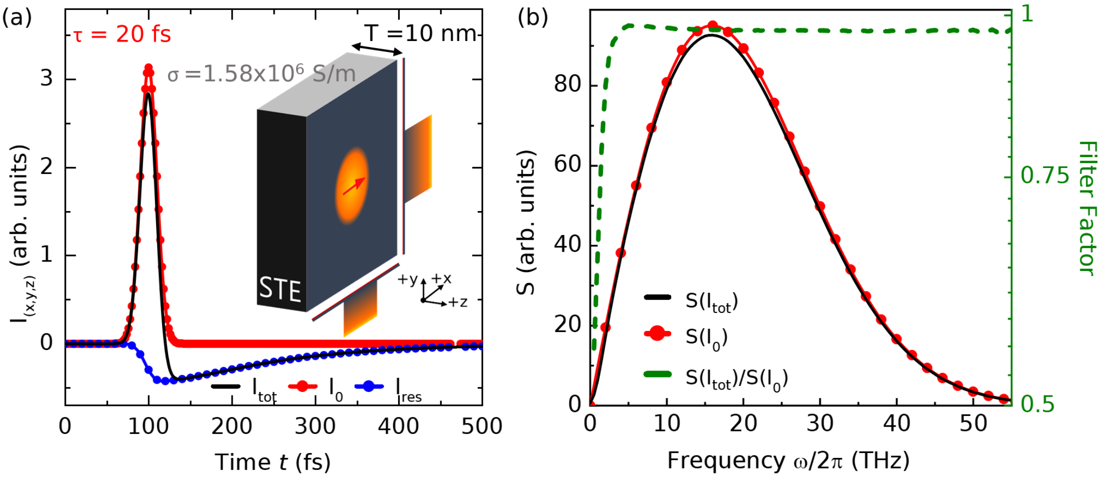

Figure 4.9: (a) Time domain signals for 20 fs wide pulse (red) with a conductivity reduced to 1.58×10^6 S/m and its corresponding (b) Spectral Amplitude. The increase in the time constant of I_{res} (blue) reduced the cutoff frequency, as observed from the filter factor (green), making the impact on the spectrum very small.

Since $R \propto 1/\sigma$, σ was reduced to 1.58×10^6 S/m (see figure 4.9 (a)). From the decay of $\vec{I}_{\text{res}}(t)$, which was determined by the RC time constant, it was seen that the discharge is slower. As is quite evident from the Spectral Amplitude (see figure 4.9 (b)), the lower frequencies were less suppressed than for the STE$_{\text{ref}}$ with the preliminary tested conductivity. Hence, the filter characteristic shown with the dashed green line has a lower cutoff frequency.

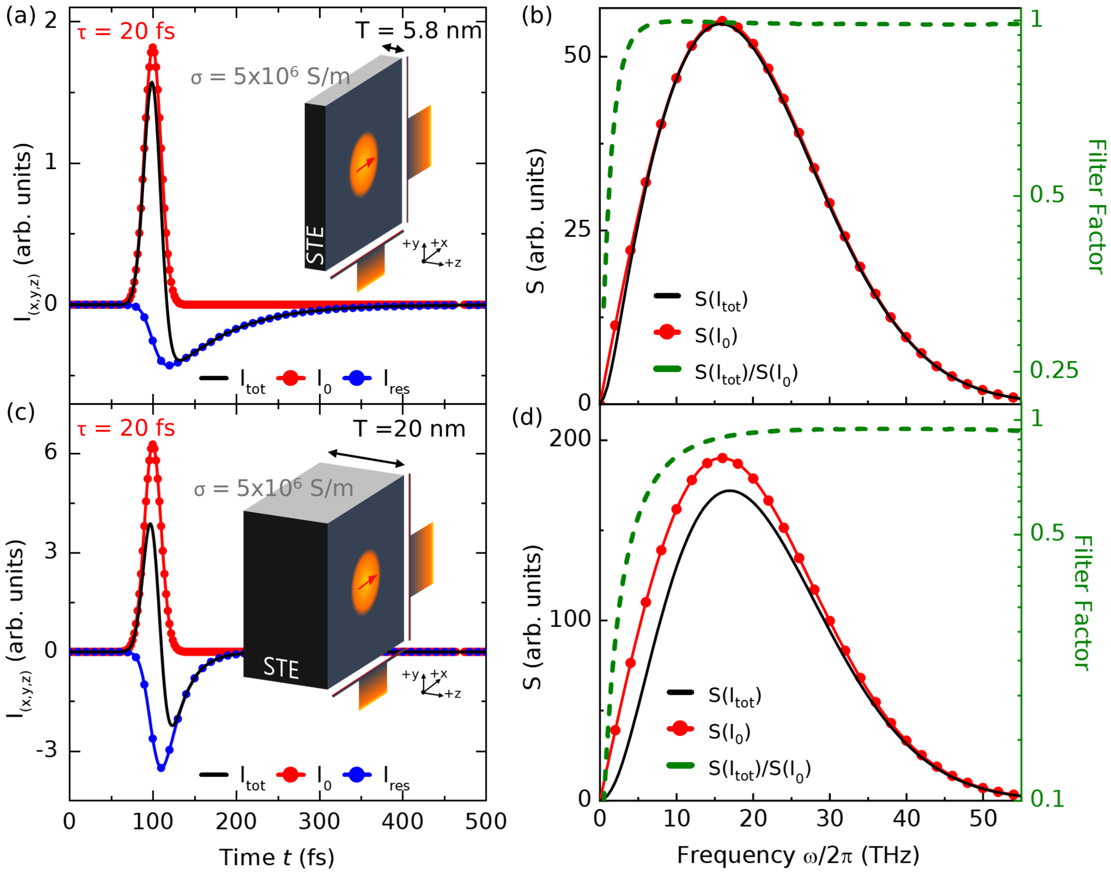

Figure 4.10: Time domain signals for STE$_{\mathrm{ref}}$ with thicknesses (a) 5.8 nm and (c) 10 nm and their spectral amplitudes (b) and (d), respectively. The increased area resistance in(a) had a similar effect as shown in figure 4.9. Decreasing the resistance by making STE$_{\mathrm{ref}}$ thicker as in (c) shifted the cutoff frequency to higher values and decreased the overall signal.

Another possibility to change the R can be achieved by changing the thickness of the layers, which changes the in-plane σ while keeping C virtually unchanged. The thicknesses were varied to 5.8 nm and 20 nm keeping all other parameters similar to the STE$_{\mathrm{ref}}$. A larger time constant (see figure 4.10 (a)) was expected for the 5.8 nm thin film compared to that of the original emitter, which was observed as a lower cutoff frequency seen in the spectral amplitude and filter characteristics (see figure 4.10 (b)). For 20 nm thick STE (see figure 4.10 (c)) the time constant decreased, thereby increasing the cutoff frequency. The spectral amplitude (see figure 4.10 (d)) at 5 THz was still suppressed by almost a factor of 2, and even at f = 20 THz, the intensity was only back to 92% of the original value obtained for the

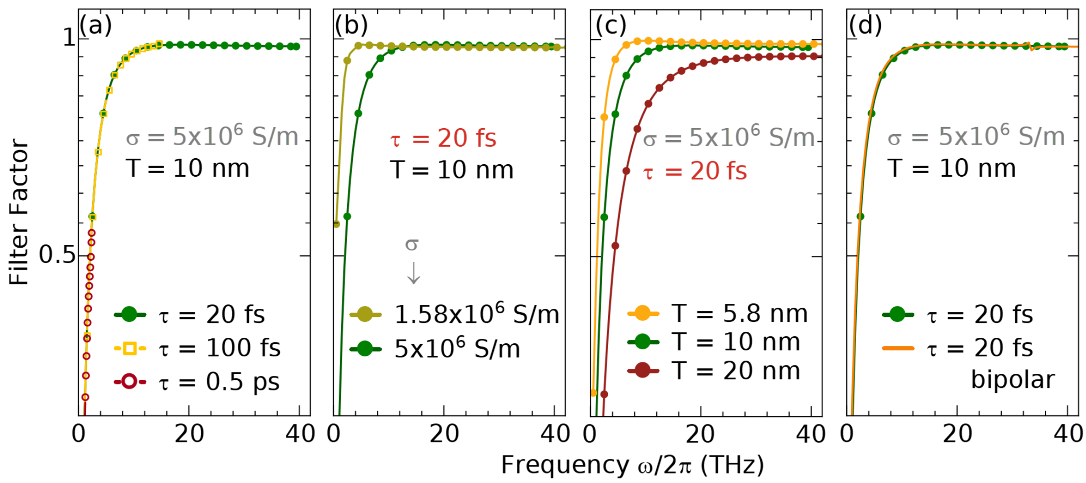

Figure 4.11: Filter characteristics for the different STE experiments. Shown are the (a) identical cutoff frequencies for different pulse widths, (b) low-frequency cutoff favored by an increase in σ, (c) low-frequency cutoff favored by a decrease in area resistance due to an increase in STE thickness and (d) the result for an antisymmetric bipolar pulse using STE_{ref} which shows similar filter characteristics as STE_{ref}.

STE_{ref}. It is important to note that, in a bandwidth-limited measurement, the decrease at lower frequencies will give the impression of a general reduction in THz emission, although this is not the case.

By comparing the filter characteristics, it can be seen that the cutoff frequencies were identical for different pulse widths (see figure 4.11 (a)). The relative suppression at the respective frequencies was the same as for the 20 fs pulse because the material parameters and thus the filter characteristics were not altered. However, with the variation in the conductivity of the STE (which also includes the change in conductivity due to a variation in the thickness of the STE) (see figure 4.11 (b, c)), a shift in the cutoff frequency was observed. For higher conductivity, the cutoff frequency was shifted up, while it was shifted down for lower conductivity. Upon comparison of the bipolar pulse with similar pulse width as the unipolar pulse (see figure 4.11 (d)) the filter characteristics showed similar behaviour with a small kink pertaining to the suppression observed at 34 THz (see figure 4.8 (b)).

Finally, the C of the system was addressed which is also important in determining the RC constant. Since $C \propto \epsilon$, frequency-dependent permittivity $\tilde{\epsilon}(\omega)$ was taken for different substrates, namely sapphire [151], glass [152] and MgO [21]. The simulation was done in the frequency domain with a Gaussian beam profile, keeping all other STE parameters the

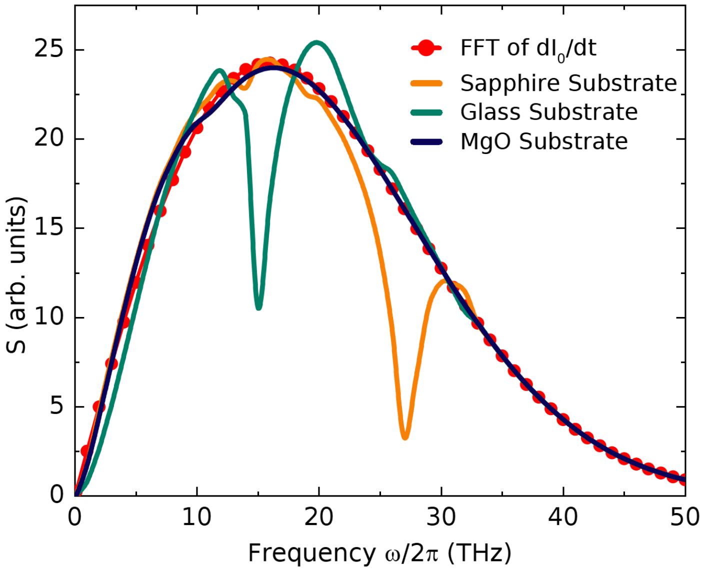

Figure 4.12: Spectral Amplitudes (S) for different substrates showed different frequency-dependent filter characteristics and features.

same. Prominent frequency-dependent features were observed, which were transcended from the respective $\tilde{\epsilon}(\omega)$ of the different substrates (see figure 4.12). The dips at 15 THz and 25 THz for sapphire or a single dip at 15 THz for glass could be used to engineer frequency selective bandwidths or multiple bandwidths by carefully choosing the substrates. However, it should be noted that the features were observed due to the effect of characteristic $\tilde{\epsilon}(\omega)$ on the charge distribution. In actual THz experiments, the characteristic wave impedance and substrate-specific attenuation also play role in determining the shape of the THz response unless the effect of charge dynamics becomes dominant.

Conclusion and Outlook

In this study a vital link was identified between the spin current and the observed terahertz pulse, which requires careful consideration for an accurate interpretation of both. Understanding the dynamics that occur after the conversion of spin to charge is crucial, as it primarily involves charge diffusion, electric fields, and the emitter and laser spot geometry. This understanding can be essential for designing STEs in order to shape the current pulse.

The model used in this study did not involve a number of aspects such as inductive effects, for reasons of simplification. However, if included this would only contribute minor modifications to the model and will not alter the underlying physics.

Due to the system's time constant, the emitted spectrum's lower frequencies are suppressed, and as the emitter's conductivity increases, the corresponding cutoff frequency rises. This might create the impression of a decrease in total THz emission, particularly in a measurement setup with an upper frequency limit between 5 and 10 THz, while, in reality, higher frequencies beyond the detection range remain unaltered. Intriguingly, a larger time constant does not impact the higher frequencies but reduces the suppression of the spectrum's lower frequency regime, thereby extending the spectral width towards higher frequencies.

5 Nanopatterned Spintronic THz emitters

It is quite evident from the insights gathered about charge dynamics in the previous chapter that charge accumulation and backflow impact the extraction of spin current, and in turn THz radiation. The results of the study presented in this chapter validate the model theoretically and experimentally by using charge dynamics to modify the emission spectrum of periodically patterned STEs in a well-controlled way. A notable decrease in spectral intensity was observed at frequencies below 4 THz, along with distinct reductions around 15 THz and 24 THz. Even when the size of the STE was decreased, while the features were amplified, the frequencies of these dips did not change. This phenomenon was caused by the charging of the edges of the structures, leading to backflow and its interaction with the initial charge current pulse. These findings are in agreement with a comprehensive analytical model that was consistent with controlled experiments. The results of this study provide a deeper understanding of charge dynamics in STEs and a strategy for controlled shaping of STE emission spectra through nanoscale patterning.

Publication information The major portion of this chapter was published as: "*Controlling charge dynamics in nanopatterned spintronic terahertz emitters*" by B. Das-Mohapatra, R. Rouzegar, E. Th. Papaioannou, T. Kampfrath, and G. Schmidt in Phys. Rev. Applied 23, 1 (2025) p. 014024,

DOI: https://doi.org/10.1103/PhysRevApplied.23.014024

Author contributions GS, TK, RR and BDM conceived the experiments. BDM fabricated the samples and analysed the data with the support of GS and ETP. RR performed the experiments. The manuscript was written by BDM and GS with the help of, and after discussions with, ETP, RR and TK.

Introduction

Based on the results presented in the previous chapter, it is understood that local charge accumulation, followed by its relaxation process, can significantly alter the emission spectrum, predominantly by reducing low-frequency elements [54]. However, demonstrating this effect in experiments proved to be challenging. Firstly, extracting the pertinent geometrical parameters involving conductance and capacitance from the layered structure, which are crucial for precise analysis, was difficult. Secondly, altering the structure of the STE's layers could impact emission traits in multiple manners [142], making it difficult to directly link spectrum alterations to the underlying charge dynamics. This challenge was addressed by formulating a series of experiments with nanopatterned STE arrays, specifically squares and rectangles, enabling the management and showcasing of these charge dynamics. With dimensions shrinking to less than 1 µm, the squares and rectangles being assessed were smaller than the 30 µm exciting laser spot, ensuring a homogeneous illumination. These make boundary conditions distinct from a constrained laser spot on a large area emitter. Furthermore, both the dimensions and spacing of the arrays were smaller than the 100 THz wavelength in a vacuum, ensuring that interference effects were avoided in the desired spectral range.

Recently, the impact of patterning, on the THz emission from STEs, has been explored. As an illustration, emissions from 5 µm wide stripe patterns for different angles between the stripes and the external magnetic field, demonstrated a decrease in intensity, accompanied by a blue shift [37, 153] for perpendicular orientation where the induced charge current was along the width. On the contrary, tests involving stripes spanning several hundred microns in width underwent no change in the frequency of the intensity maximum at 1 THz but an increase at lower frequencies, which was attributed to multi-slit interference [154]. Furthermore, Song et al. [155] investigated rectangles with a short side ranging from 20 µm to 320 µm. In their investigations they also observed a marked reduction in intensity and a distinct blue shift. It is imperative to highlight that these studies did not venture into the spectral domain beyond 5 THz.

The structures used in this study were more than an order of magnitude smaller than those investigated before [37, 153–155] which could emit a THz response with a spectral range of up to frequencies of 30 THz, which gives access to the whole range of frequencies influenced by the charge dynamics.

5.1 Experimental details

A trilayer STE with the layer stacks W(2 nm)/$Co_{20}Fe_{60}B_{20}$(1.8 nm)/Pt(2 nm), thus, with total thickness d =5.8 nm, on a sapphire(0001) substrate was taken (see figure 5.1) for optimum terahertz output [15, 156]. This metallic heterostructure was grown on a sapphire substrate using ultrahigh-vacuum DC magnetron sputtering. The sapphire substrate provides optimum transmittance and less attenuation for THz detection. The trilayer utilises both the ultrafast laser pulse-induced forward propagating spin currents to the top (Pt) and backward propagating spin currents to the bottom (W) layers. The spin currents are converted to transient charge current pulses, in phase, perpendicular to the magnetisation $\vec{M}$ by ISHE (see section 2.6) due to the opposite signs of their spin-Hall angles (θ_{SH}) with $\theta_{SH}^{Pt} = +0.12$ [157] and $\theta_{SH}^{W} = -0.04$ [158]. The total transient current leads to the emission of a THz pulse that easily covers the 1 to 30 THz range when excited with 10 fs laser pulses [15].

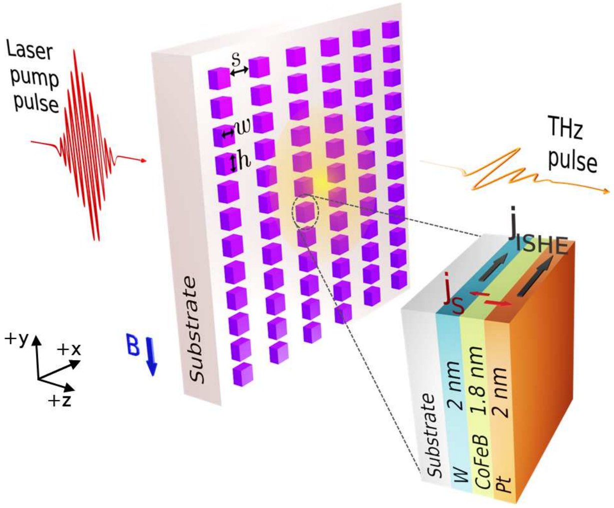

Figure 5.1: Sketch of THz emission by optically excited nanopatterned STEs. The pattern is a two-dimensional lattice of rectangles of width(w), height(h) and spacing(s). Here a trilayer STE with the layer stack W(2 nm)/CoFeB(1.8 nm)/Pt(2 nm) was used.

The free space THz radiation from STE nanostructures was measured using pump-probe electro-optic sampling (see section 3.6.1). The nanoSTEs were illuminated using fs-laser pulses from a Ti:sapphire laser with a beam of wavelength 800 nm, 10 fs pulse duration, and a pulse energy of 2 nJ with an approximate spot size of 30 µm FWHM and the THz response was detected in the far-field.

5.2 Nanopatterned STEs

Square and rectangular emitters were nanopatterned using electron-beam lithography and a subsequent Ar-ion milling using an electron-beam evaporated AlO_x etching mask (see section 3.4.2), with lateral sizes of width w, height h and spacing s, that had sub-wavelength dimensions with respect to the THz wavelength. For quantitative analysis, the array dimensions were taken to be significantly larger than the laser spot diameter with a considerable filling factor which was determined by $(w \times h)/((w+s) \times (h+s))$, which can be observed from the Scanning Electron Microscope (SEM) (see section 3.3.2) images (see figure 5.2).

5.2.1 THz emission from square nanoSTEs

The initial set of investigated nanoSTEs were square shaped with lateral sizes 'w' of 900 nm, 1.8 µm, 4.5 µm, 9.0 µm and 18.0 µm. These were in sub-wavelength dimensions compared to THz wavelength with a constant filling factor of 81%, which was maintained by having the spacing 's' in both lateral dimensions set to ~1/9 of the square's side length. The peak-to-peak amplitudes of detected signals in the time domain decreased slightly with decreasing structure size, and for the smallest structures of 900 nm, it was less than 50% of the signal for a continuous STE thin film. Furthermore, the emitted THz pulse shape varied with decreasing size compared to that of the STE thin film (see figure 5.3 (a)).

The spectral amplitudes (see figure 5.3 (b)) for the different samples were obtained from the time domain data by FFT using a von Hann window [159] (see appendix A.4). For an unpatterned STE, emission of up to ~ 30 THz was observed within the dynamic range of the measurement. The dip at 5 THz appeared due to the absorption by the ZnTe crystal [160], and the dip at 10 THz originated from the Ge wafer behind the STE [161]. Further dips [15] at 13, 17 and 19 THz were due to the refractive index [151, 162] of the sapphire substrate which can also be observed from the calculated STE wave impedance $\tilde{\eta}(\omega)$ (see section 2.1) including the substrate using the relation [15],

$$\frac{1}{\tilde{\eta}(\omega)} = \frac{\tilde{n}_1(\omega) + \tilde{n}_2(\omega)}{\eta_0} + \int_0^T dz\, \tilde{\sigma}(\omega) \tag{5.1}$$

where, $\eta_0 \approx 377\,\Omega$ [53], $\tilde{n}_1(\omega)$ and $\tilde{n}_2(\omega)$ are the refractive indices for substrate and air half-spaces respectively, and $\int_0^T dz\, \tilde{\sigma}(\omega)$ is the sheet conductance of the metal stack with thickness T.

(a) Square STEs : Filling Factor 81%

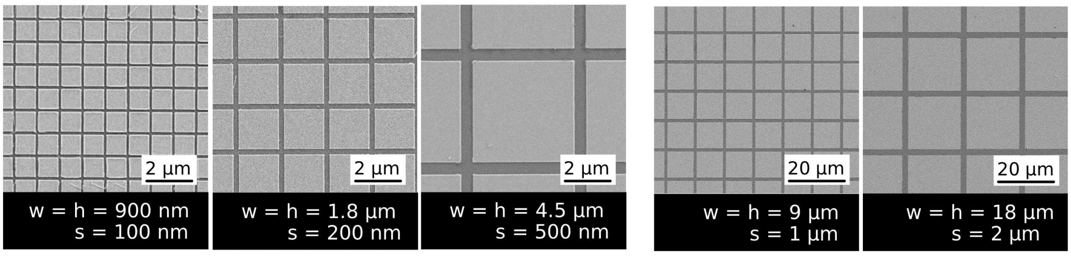
2 µm
w = h = 900 nm
s = 100 nm
2 µm
w = h = 1.8 µm
s = 200 nm
2 µm
w = h = 4.5 µm
s = 500 nm
20 µm
w = h = 9 µm
s = 1 µm
20 µm
w = h = 18 µm
s = 2 µm

(b) Rectangular STEs : h = 900 nm; s = 100nm

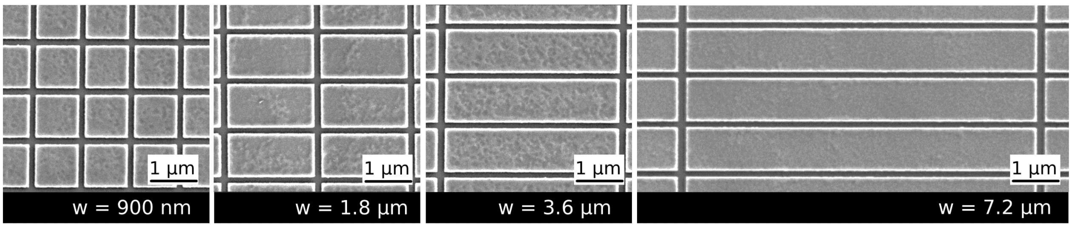
1 µm
w = 900 nm
1 µm
w = 1.8 µm
1 µm
w = 3.6 µm
1 µm
w = 7.2 µm

(c) Square STEs : w = h = 900 nm

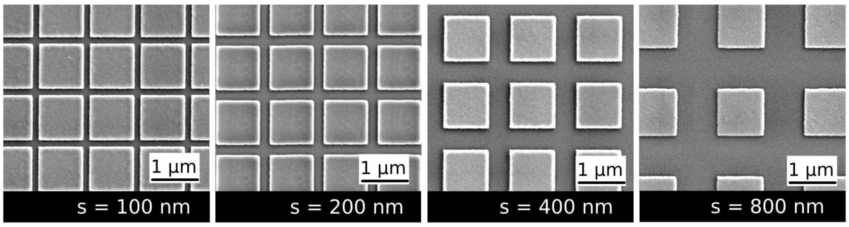
1 µm
s = 100 nm
1 µm
s = 200 nm
1 µm
s = 400 nm
1 µm
s = 800 nm

(d) Rectangular STEs : w = 1.8 µm; h = 900 nm

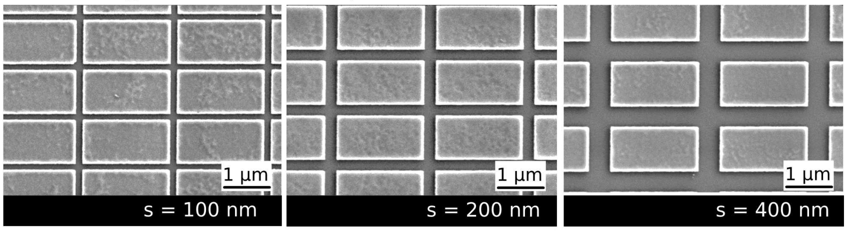
1 µm
s = 100 nm
1 µm
s = 200 nm
1 µm
s = 400 nm

Figure 5.2: SEM images of various STEs nanopatterned into square and rectangular nanostructures with different w, h and s. (a) Square NanoSTEs with varying w and h and constant filling factor of 81%. (b) Rectangular NanoSTEs with varying w. (c) Square NanoSTEs and (d) Rectangular NanoSTEs with varying s.

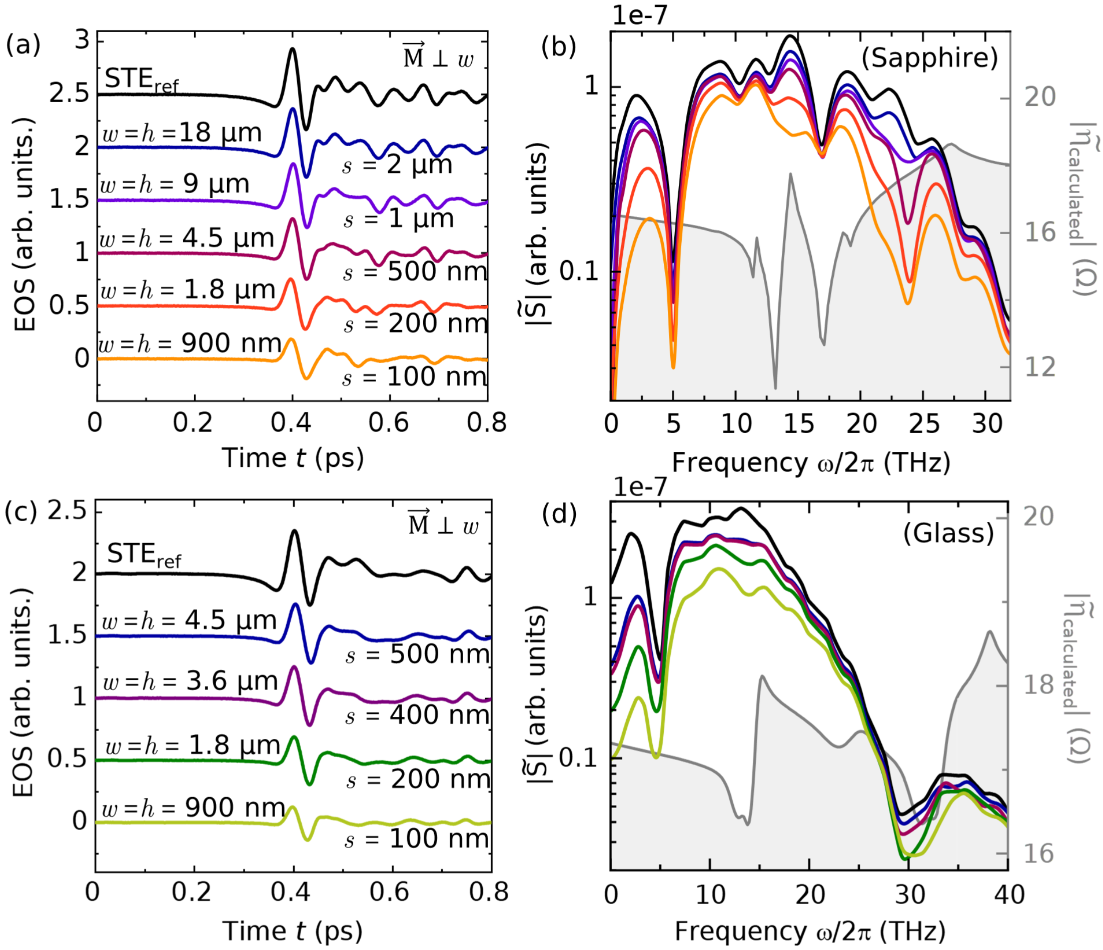

Figure 5.3: Time domain Electro-optic Sampling (EOS) from nanopatterned STEs with different square sizes, (a) $w = h = 900\,\text{nm}$; 1.8 µm; 4.5 µm; 9 µm; 18 µm all with a filling factor of 81% on sapphire substrates and (c) $w = h = 900\,\text{nm}$; 1.8 µm; 3.6 µm; 4.5 µm all with a filling factor of 81% on glass substrates. Amplitude spectra $|\tilde{S}(\omega)|$ obtained for different square sizes by FFT of the EOS for (b) the sapphire substrates and (d) the glass substrates. The grey lines show the calculated characteristic wave impedance $|\tilde{\eta}(\omega)|$ for the sapphire and glass substrates.

For nanoSTEs, a slight reduction in amplitude compared to continuous film STEs was observed. Additionally, a few specific characteristics became more evident as the structures got smaller. The amplitudes for frequencies below 4 THz underwent significant reduction, almost by a factor of five for the smallest tested dimensions, compared to the spectral amplitude for the large area emitter. A similar decline was noticeable around the frequencies of 15 THz and 24 THz, leading to two notable dips in the spectral amplitudes. However, the amplitudes were nearly the same across all the structure sizes for higher frequencies, and the frequencies at which the dips occured remained consistent regardless of the structure size. It should also be noted that the interference effects and plasmonic effects upon laser light absorption can be excluded since the structures were much larger than the wavelength of the incident laser light which was verified by electromagnetic simulations using CST Microwave Studio [163] to analyse various transmission coefficients for propagation of radiation and different electromagnetic field patterns (Transverse Electric (TE) and Transverse Magnetic (TM) modes) (see appendix A.1) of the radiation (see figure 5.4). The simulation involved square structures of Pt metal with $\sigma = 3 \times 10^6$ S/m and dimensions 900 nm, 1.8 µm, 4.5 µm and 9 µm with spacing 100 nm, 200 nm, 500 nm and 1 µm respectively.

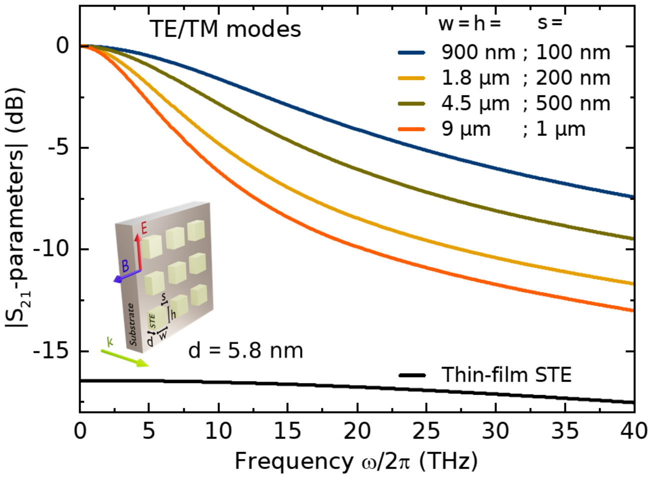

Figure 5.4: CST simulation using electromagnetic wave propagation ($\vec{k}$) through nanoSTEs of varying dimensions to identify TE/TM modes in transmission.

To better understand the characteristics related to the substrate, similar experiments were performed with square-shaped nanoSTEs on glass substrates with lateral sizes 'w' of 900 nm, 1.8 µm, 3.6 µm and 4.5 µm (see figure 5.3 (c)). The frequency dependence of the dielectric constant of glass is different from that for the sapphire substrate. The amplitude spectrum for the STE thin film on glass substrate had a peak at approx. 15 THz and a dip at 30 THz which was in accordance with the $|\tilde{\eta}(\omega)|$ for the glass substrate. Furthermore, a relative reduction at 15 THz and a further increase in the dip at 30 THz was seen for nanoSTEs, which increased with a decrease in nanoSTE size (see figure 5.3 (d)). However, the characteristic dip observed for the sapphire substrate at 24 THz was absent, as expected, due to the features of the dielectric constant.

5.2.2 Charge dynamics in nanoSTE

Time domain COMSOL [143] simulations with the electric current submodule of the AC/DC module (see chapter 4 and appendix A.2) was used to study electric current and charge dynamics. These were induced after a spin-to-charge conversion event, for nanoSTEs with lateral sizes similar to the experiments, i.e. $w = h = 900\,\text{nm}$, $1.8\,\mu\text{m}$, $4.5\,\mu\text{m}$, $9\,\mu\text{m}$ and $18\,\mu\text{m}$. The parameters used for the model were, $\sigma = 10^{-12}\,\text{S/m}$ and $\epsilon_r = 3.064$ [144] for the sapphire substrate and $\sigma = 3 \times 10^6$ S/m [15, 145, 146], $\epsilon_r = 903$ [147] and $T = 10\,\text{nm}$ for the metallic trilayer, which was taken as Pt for simplicity. In the simulation, $\vec{j}_0$ was set proportional to the light intensity with a Gaussian profile that has a FWHM of $D = 30\,\mu\text{m}$ and pulse width of $\tau = 20\,\text{fs}$, which was in accordance with the experiment.

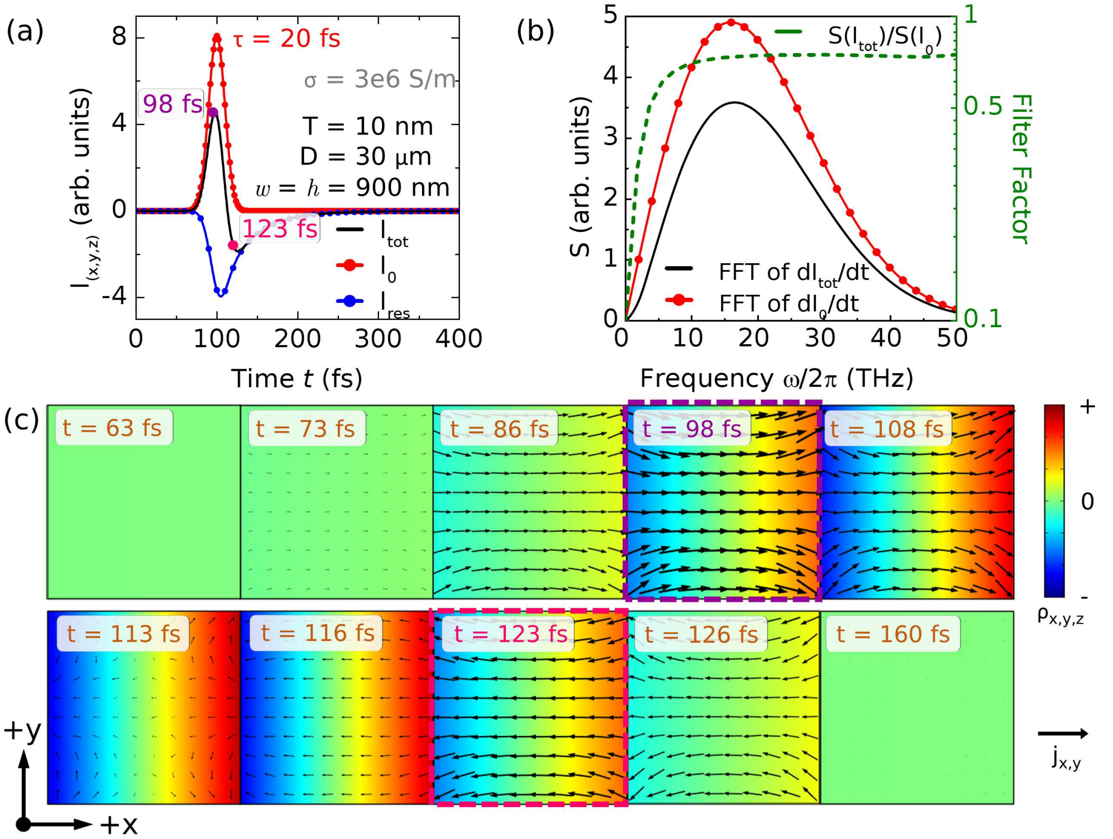

Figure 5.5: (a) Time domain current dynamics for the nanoSTEs of $w = h = 900\,\text{nm}$ with $\vec{I}_0$ showing charge accumulation on NanoSTE boundaries and backflow, with maxima of $\vec{I}_{\text{tot}}$ at $t = 98\,\text{fs}$ and minima at $t = 123\,\text{fs}$. (b) Spectral Amplitude for the time derivative of the $\vec{I}_0$ and $\vec{I}_{\text{tot}}$ and the Filter Factor. (c) Charge dynamics and spatial current density for different times in the nanoSTEs.

The lateral ISHE current $\vec{I}_0$ in the '$+x$' direction led to charge accumulation in the boundaries of the structure and discharging to create $\vec{I}_{\text{res}}$, and together they resulted in $\vec{I}_{\text{tot}}$ which was the actual source of the THz radiation (see figure 5.5 (a)). Charge accumulation and backflow were validated from charge dynamics and current density at each point in time with maxima $\vec{I}^{\text{max}}_{\text{tot}}$ at 98 fs, and minima $\vec{I}^{\text{min}}_{\text{tot}}$ at 123 fs (see figure 5.5(c)). The Spectral Amplitudes obtained from the FFT of the time derivative of $\vec{I}$ were proportional to the electric field observed in far-field, and the ratio of the Spectral Amplitudes of nanoSTEs to that of the initial current led to the obtained Filter Factor (see figure 5.5 (b)). When comparing the filter factor, simulations for varying nanoSTEs w showed similar highpass filter characteristics with cutoff frequencies shifting to higher frequencies as the size of the nanoSTEs was decreased (see figure 5.6).

It is essential to comprehend how geometry governs the behaviour of transient charge. In the case of a large-area emitter, when a fs-laser pulse induced spin current is initially generated, it triggers a lateral current density proportional to the local light intensity (see chapter 4) [54]. Consequently, this causes local accumulation of charge at the boundaries of the illuminated region, leading to a backflow both inside and outside of the spot. In the context of a nanostructured STE, an additional boundary condition of $\vec{j} = 0$ comes into play beyond the illuminated region, specifically beyond the square area, effectively constraining the backflow to remain within the illuminated region.

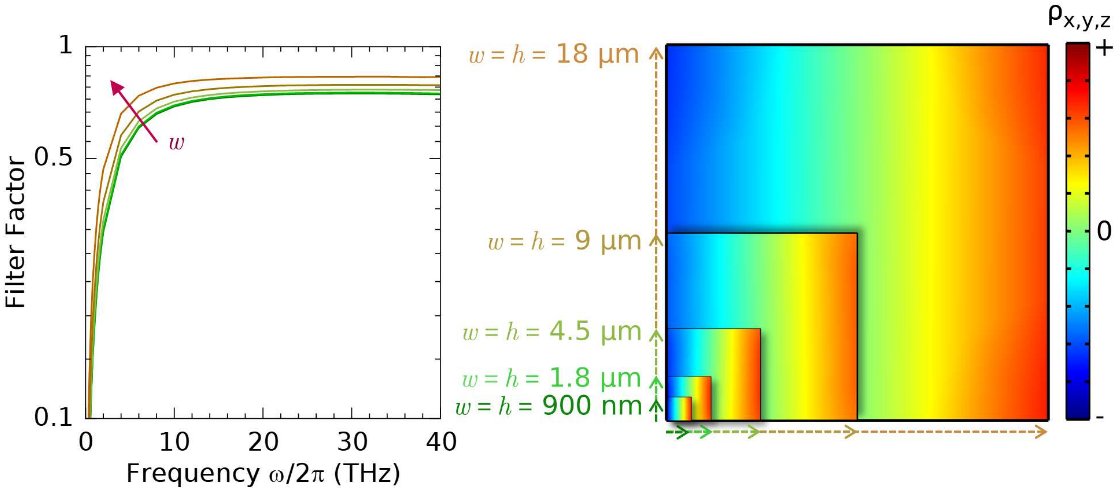

Figure 5.6: Comparison of Filter Factor $|\tilde{S}(I_{tot})/\tilde{S}(I_0)|$ for nanoSTEs of different lateral sizes, $w = h = 900$ nm, 1.8 µm, 4.5 µm, 9 µm and 18 µm. Their respective $\rho_{x,y,z}$ at $\vec{I}^{t=max}_{tot}$ obtained from COMSOL simulation.

Under uniform illumination conditions, charging occured at opposite edges of the structure, where $\vec{\nabla}\cdot\vec{j} \neq 0$ and thus $\partial\rho/\partial t \neq 0$. Since a uniform current density was present perpendicular to the edges, charging along the edges also remained uniform. This uniform charging along the edges resulted in a backflow that was perpendicular to the edges and opposed the initial direction of the current, consequently transforming this into a quasi-one-dimensional problem. It is worth noting that the charged area was extremely narrow and only extended over a distance defined by the Thomas-Fermi screening length [164], which was negligible when compared to the overall w of the structures.

5.2.3 THz emission from rectangular nanoSTEs

In order to understand the dimensional effects in the Spectral Amplitude, it was also worth investigating the dependence of the lateral dimensions. Therefore, the subsequently investigated nanoSTEs were rectangular in shape with constant h = 900 nm, s = 100 nm and varying w = 900 nm, 1.8µm, 3.6µm and 7.2µm on the sapphire substrate. The EOS signals in the time domain were obtained with the configuration of $\vec{M} \perp w$, and show similar effects as observed for square nanoSTEs. The peak-to-peak amplitude for the time domain signal decreased, and the pulse shape also changed with the decrease in w compared to the EOS of STE_{ref} (see figure 5.7 (a)). The Spectral Amplitude obtained by FFT also showed a behaviour similar to that of square nanoSTEs. The reduction in amplitude for frequencies below 4 THz and at 15 THz and 24 THz showed similar trend to the square nanoSTEs with decreasing width (see figure 5.7 (b)).

The dependence of h was investigated by effectively changing the configuration of $\vec{M} \parallel w$ so that $\vec{j}_0$ was along h. Consequently, for this case h was effectively w for the system and the effective h was now the w that was varied. From the experiments, the time domain EOS signals were obtained with similar pulse shape and almost equal amplitudes compared to each other but smaller in amplitude and different in shape compared to the EOS signals of STE_{ref} (see figure 5.7 (c)). This was also validated by the Spectral Amplitudes of the EOS signals obtained by FFT. The behaviour at low frequencies and at 15 THz and 24 THz were similar to a 900 nm square nanoSTEs (see figure 5.7 (d)).

The charge dynamics in rectangular nanoSTEs was analysed using COMSOL [143] simulations based on the setup described in the previous section. Filter Factors obtained for nanoSTEs with varying w under the condition that $\vec{M} \perp w$, showed clear high pass filter characteristics which decreased with increasing w (see figure 5.7 (e)).

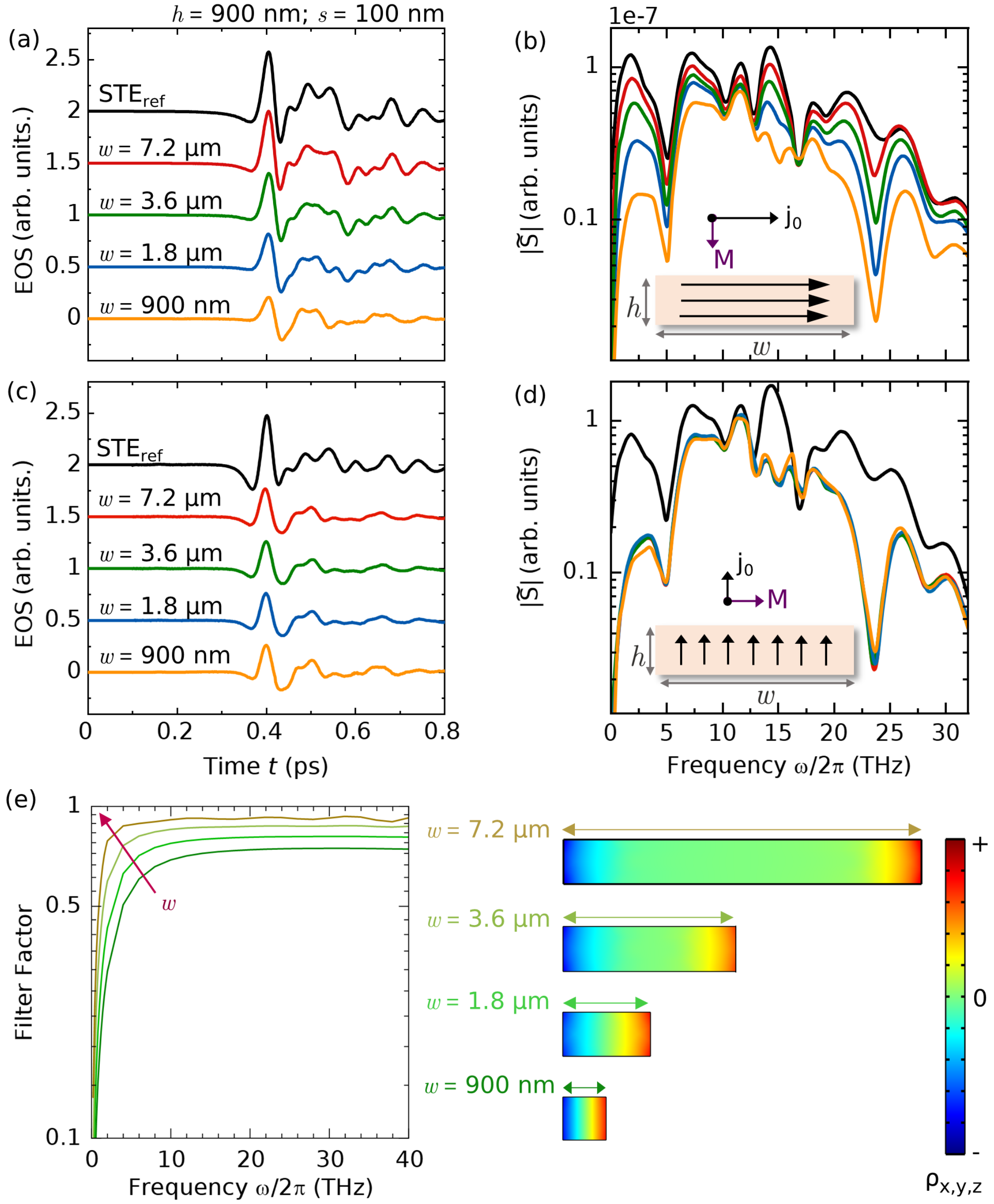

Figure 5.7: (a) Time domain EOS signals and corresponding (b) Spectral Amplitudes for rectangular nanopatterned STEs with different widths, w = 900 nm; 1.8 µm; 3.6 µm and 7.2 µm all with h = 900 nm and spacing s = 100 nm with $\vec{M} \perp w$. (c) Time domain EOS signals and corresponding (d) Spectral Amplitudes for the magnetisation direction $\vec{M} \parallel w$ so that the effective w and h were interchanged. (e) Comparison of Filter Factors $|\tilde{S}(I_{\text{tot}})/\tilde{S}(I_0)|$ for rectangular nanoSTEs for $\vec{M} \perp w$ with their corresponding $\rho_{x,y,z}$ at $\vec{I}_{\text{tot}}^{t=\text{max}}$ obtained from COMSOL simulations.

5.2.4 Effect of spacing between nanoSTEs

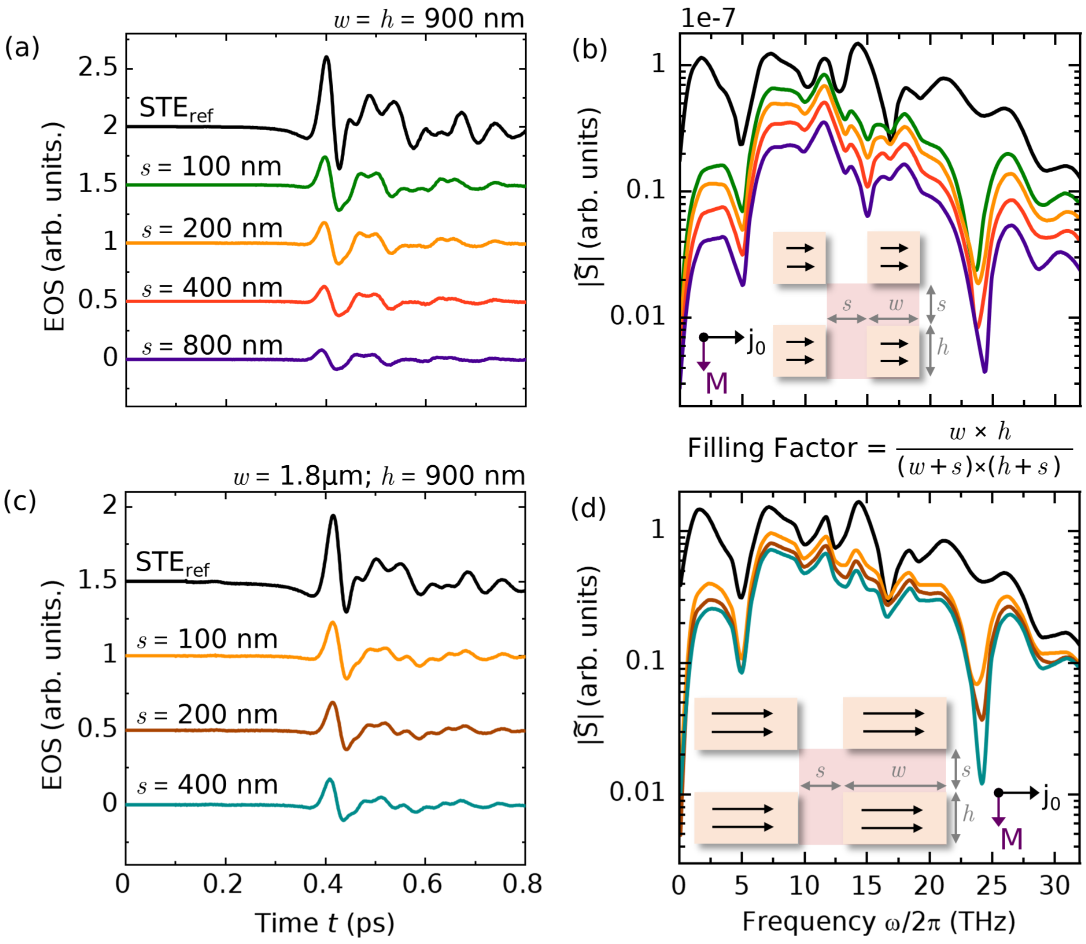

Figure 5.8: (a) Time domain EOS signals and (b) Spectral Amplitudes from arrays of square nanoSTEs with $w = h = 900$ nm and $s = 100$ nm; 200 nm; 400 nm and 800 nm. (c) Time domain EOS signals and (d) Spectral Amplitudes from arrays of rectangular nanoSTEs with $w = 1.8$ μm; $h = 900$ nm and $s = 200$ nm; 400 nm and 800 nm. The plots in black show the EOS responses and spectral amplitudes from the STE$_{ref}$. An increase in s decreases the filling factor (as shown) thus decreasing the overall spectral amplitude.

The final set of nanoSTE arrays investigated were square and rectangular in shape with variation of s between the structures. Square nanoSTEs comprised dimensions $w = h = 900$ nm and $s = 100$ nm; 200 nm; 400 nm or 800 nm. The rectangular nanoSTEs were comprised of dimensions, $w = 1.8$ μm; $h = 900$ nm and $s = 200$ nm; 400 nm or 800 nm. The obtained time domain EOS signal shape was different compared to that of $|\tilde{S}_{\text{ref}}|$ (see figure 5.8 (a, c)). The corresponding Spectral Amplitude showed a similar shape with a reduction of low-frequency components and dips at 15 THz and 24 THz (see figure 5.8 (b, d)). However, the EOS amplitude decreased with increasing spacing due to the decreasing filling factor, which was also reflected in the Spectral Amplitude.

5.2.5 Charge accumulation in nanoSTEs

The insight gained from the simulations of nanoSTEs for their geometrical dependence of charge dynamics led to the consideration of a one-dimensional current flow. Additionally, it can be assumed that the time-dependent current density $\vec{j}(t,x)$ flows in x- direction only in $x-y$ plane due to symmetric reasons and the z coordinate due to the thin metal stack of only a few nanometer thickness. For this a current $\vec{I}(t,x)$ can be written as $\vec{j}(t,x)\cdot h\cdot d$. A homogeneous current density $\vec{j}_0(t)$ was induced in the emitter by laser excitation, yielding $\vec{I}_0(t)=\vec{j}_0(t)\cdot h\cdot d$, leading to far-field emission proportional to $w\cdot\vec{I}_0(t)$.

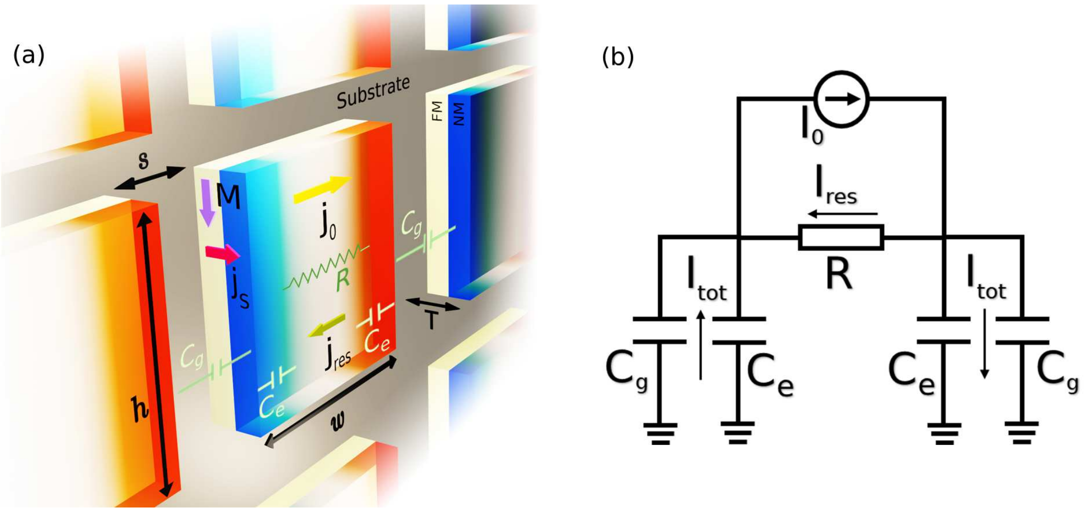

Figure 5.9: (a) Sketch of nanoSTEs showing the charge current density $\vec{j}_0$, the edge capacitance C_e, the capacitance between emitters C_g, the resistance in the nanoSTE R, and the charge accumulation along the edges. (b) Equivalent RC-circuit for the nanoSTE unit cell.

Two opposite boundaries of the structure along h can be viewed as two individual capacitors C_e that were charged with opposite polarity. Contrary to what might be expected, the opposing edges were not treated as two plates of a single capacitor; instead, they were considered to be separate capacitors. When the structure was positioned close to another structure, additional capacitance was believed to be introduced due to the interactions between the structures, resulting in the formation of two opposing plates of a plate capacitor, termed C_g. A balance of the opposing charges from the two opposite edges was achieved by a response current $\vec{I}_{\text{res}}(t,x) = \vec{j}_{\text{res}}(t,x) \cdot h \cdot d$ that flowed through the resistance R which was defined by the total resistance encountered along the x-axis that connects the two edge capacitors (see figure 5.9 (a)). This can be represented using an equivalent RC-circuit (see figure 5.9 (b)). In order to describe the combined contribution, the pertinent time constants are required to be identified.

5.2.6 Modelling the THz spectrum for nanoSTE

By taking the equivalent circuit as the reference and understanding various capacitive and resistive elements in the nanoSTE, the charge dynamics was modelled analytically. Since the circuit contained two capacitors C_e and C_g in parallel, the total net capacitance was C given by the sum of C_e and C_g. The equivalent circuit was then described by the following differential equation:

$$2 \cdot C \frac{dU_C(t)}{dt} = I_0(t) - \frac{U_C(t)}{R} \tag{5.2}$$

where U_C is the voltage across the capacitors and $-U_C/R$ corresponds to $\vec{I}_{res}$. A multiplication factor of 2 was used to accommodate the capacitors from both edges. The Fourier transform of this differential equation yields (see appendix A.3)

$$2 \cdot i\omega C \tilde{U}_C(\omega) = \tilde{I}_0(\omega) - \frac{\tilde{U}_C(\omega)}{R} \tag{5.3}$$

with

$$\tilde{I}_{\text{tot}}(\omega) = \tilde{I}_0(\omega) + \tilde{I}_{\text{res}}(\omega) \tag{5.4}$$

which yields

$$\tilde{I}_{\text{tot}}(\omega) = 2 \cdot i\omega C \tilde{U}_C(\omega) = \tilde{I}_0(\omega) \frac{1}{1 + \frac{1}{2 \cdot i\omega RC}} = \tilde{F}_{\text{T}}^{\text{nSTE}}(\omega) \tilde{I}_0(\omega). \tag{5.5}$$

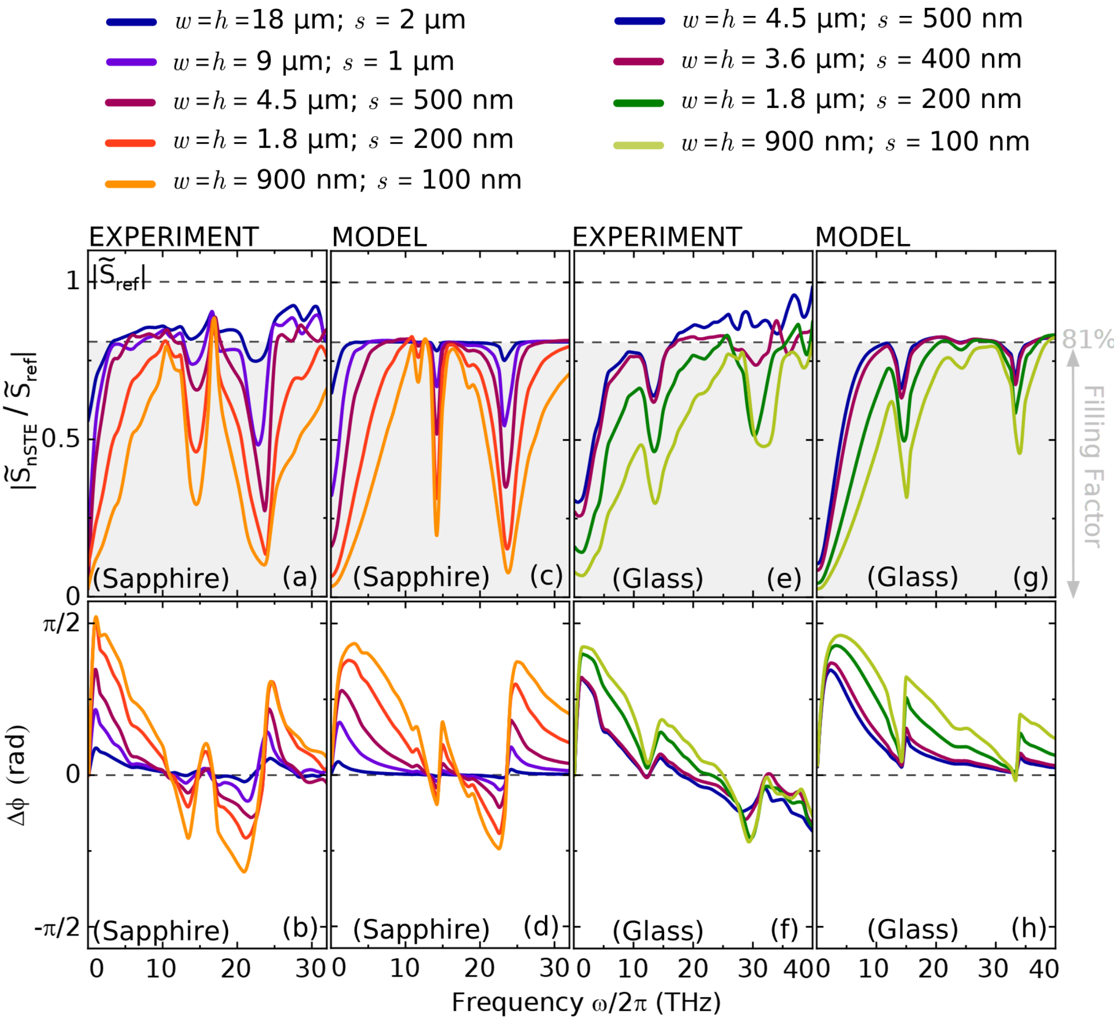

Figure 5.10: (a) Amplitude and (b) phase for the relative change of square nanoSTEs $\tilde{S}_{\text{nSTE}}(\omega)/\tilde{S}_{\text{ref}}(\omega)$ as compared to the thin film reference STE on a sapphire substrate. (c) Amplitude and (d) relative phase for nanoSTEs as obtained from the analytical model. (e) Amplitude and (f) relative phase for square nanoSTEs on a glass substrate and the corresponding (g) Amplitude and (h) relative phase from the analytical model.

In this context, the transfer function $\tilde{F}_{\text{T}}^{\text{nSTE}}(\omega)$ is the factor by which the current $\tilde{I}_0(\omega)$ must be multiplied to obtain the nanoSTE response. This demonstrated that the nanoSTE's total current $\tilde{I}_{\text{tot}}(\omega)$ is primarily composed of the initial current $\tilde{I}_0(\omega)$, but it is subject to modification by a high-pass filter function. Unlike the charge dynamics for a large area emitter, where the RC constant of the high-pass filter relied solely on material parameters, both C and R were geometry dependent, and the RC constant could be controlled by altering the w of the structure.

For the case of the large area reference emitter where RC is very large, it results in $\tilde{I}_0(\omega)$ or a transfer function $\tilde{F}_{\mathsf{T}}^{ref}(\omega) \simeq 1$, regardless of frequency, as expected. While, this barely influences the amplitude of the transfer function, the phase can change considerably. The high pass filter [54] (see chapter 4) functions for a large area emitter was used to estimate the $\tilde{I}_0(\omega)$ in terms of $\tilde{I}_{\text{tot}}(\omega)$ and $\tilde{F}_{\mathsf{T}}^{\mathsf{STE}}(\omega)$ for the thin film. In the next step, the estimated $\tilde{I}_0(\omega)$ was multiplied with the filling factor times $\tilde{F}_{\mathsf{T}}^{\mathsf{nSTE}}(\omega)$ to obtain the nanoSTE response. The time constant RC can be expressed as $k \cdot \tilde{\epsilon}(\omega)/\tilde{\sigma}(\omega)$ where the factor k is correlated to the geometry of the nanoSTE with $\tilde{\epsilon}(\omega)$ and $\tilde{\sigma}(\omega)$ being the complex frequency-dependent dielectric constant and conductivity, respectively.

For simplification, $\tilde{\epsilon}(\omega)$ for sapphire [151] and $\tilde{\sigma}(\omega)$ for Pt [165] were used in the model to approximate the conductivity of the stack (see appendix A.5). To obtain k, the transfer function $\tilde{F}_{\mathsf{T}}(\omega)$ was calculated from the ratio of the spectral amplitude of the nanoSTE to that of the reference STE i.e. $\tilde{S}_{\mathsf{nSTE}}(\omega)/\tilde{S}_{\mathsf{ref}}(\omega)$ obtained from experiments. Using this ratio as a medium of comparison, the spectral alterations caused by the setup and detection methods can be disregarded since they were identical for all the measurements. By taking only k as a free parameter for a single value of w and a large RC constant for the high pass filter function of a large area reference emitter, fitting was done for $\tilde{S}_{\mathsf{nSTE}}(\omega)$. It should be noted that k_g for the RC_g constant corresponding to C_g was already included in the fitting of k corresponding to RC. Therefore, the final equation obtained for modelling was

$$\tilde{S}_{\mathsf{nSTE}}(\omega) = \frac{w \times h}{(w+s) \times (h+s)} \frac{1 + \dfrac{1}{i\omega(RC)_{\mathsf{ref}}}}{1 + \dfrac{1}{2 \cdot i\omega RC}} \tilde{S}_{\mathsf{ref}}(\omega) \tag{5.6}$$

which gives

$$\tilde{S}_{\mathsf{nSTE}}(\omega)/\tilde{S}_{\mathsf{ref}}(\omega) = \frac{w \times h}{(w+s) \times (h+s)} \frac{1 + \dfrac{1}{i\omega(RC)_{\mathsf{ref}}}}{1 + \dfrac{1}{2 \cdot i\omega RC}} = \tilde{F}_{\mathsf{T}}(\omega). \tag{5.7}$$

For the RC time constant of a w =900 nm nanoSTE, the fitting parameter k = 120 was obtained. Similarly, k for nanoSTEs with w = 1.8 µm, 4.5 µm, 9 µm and 18 µm were 240, 600, 1200 and 2400, respectively, (see appendix A.5.1) and a k_{ref} for STE$_{\text{ref}}$ was 6000 (see appendix A.5). From this it was clear that $k \propto w$ as seen in the analytical model. From this model the transfer functions for square nanoSTEs were obtained, which agreed well with the experimental observations. The amplitude and phase of $\tilde{S}_{\text{nSTE}}(\omega)/\tilde{S}_{\text{ref}}(\omega)$ determined the relative change with respect to $\tilde{S}_{\text{ref}}$.

Comparing the relative change, the high pass characteristics were observed as predicted before [54] (see chapter 4) as the cutoff frequency increased with decreasing w because R and thus also RC became smaller. Additionally, the dips at 15 and 24 THz were clearly reproduced since both imaginary and real parts of $\tilde{\epsilon}(\omega)$ of sapphire [151] exhibited extrema around those frequencies that reduced $|\tilde{F}_{\text{T}}(\omega)|$ at the same frequencies (see figure 5.10(a, c)). The calculated phase change also showed a similar dependence as obtained in the experiment (see figure 5.10(b, d)). Moreover, the high pass filtering in the frequency domain had a strong contribution to the main peak in the time-domain peak-to-peak amplitude for nanoSTEs which decreased with decreasing structure size, by up to 50% of the STE$_{\text{ref}}$ amplitude for the smallest 900 nm structures. By using the dielectric properties of glass [152] in the model (see appendix A.5.2), the amplitude and phase of the relative change was appropriately reproduced (see figure 5.10(e, f, g, h)). Hence, an estimation of spectra was achieved as per the model by including the dielectric parameters of the substrates.

The modelling of rectangular nanoSTEs for the $\vec{M} \perp w$ configuration revealed a similar k for the RC constant to that seen for square nanoSTEs, i.e. k = 120, 240, 480 and 960 (see appendix A.5.3) for rectangles with w = 900 nm, 1.8 µm, 3.6 µm and 7.2 µm, respectively, with constant h = 900 nm and s = 100 nm. However, the fitting parameters for the $\vec{M} \parallel w$ configuration showed similar values of k = 120 (see appendix A.5.3) for all rectangles, which was the same as that of the square nanoSTE of size 900 nm. The analytical model is in good agreement with the experimental observations as seen from the amplitude and phase for $\tilde{S}_{\text{nSTE}}(\omega)/\tilde{S}_{\text{ref}}(\omega)$ (see figure 5.11).

Normalised $|\tilde{S}_{\text{nSTE}}(\omega)/\tilde{S}_{\text{ref}}(\omega)|$ for square nanoSTEs of w = h = 900 nm and various s revealed an additional effect due to capacitance C_g. The fitting parameter k was 120, which was similar to that of the square nanoSTE of w = h = 900 nm; however, the fitting of k_g gave values of 12, 6, 3, and 1.5 (see appendix A.5.4) for the square nanoSTEs with s = 100 nm, 200 nm, 400 nm and 800 nm respectively. Similar fitting parameters were observed for rectangular nanoSTEs with constant w = 1.8 µm, h = 900 nm and various s. The fitting parameter was k = 240 corresponding to the square nanoSTE with size w = h = 1.8 µm and the k_g values were 6, 3 and 1.5 (see appendix A.5.5) for s = 200 nm, 400 nm and 800 nm respectively. The relative phase was equivalent to each other for all the cases, which was reflected in both the experiment and the model (see figure 5.12).

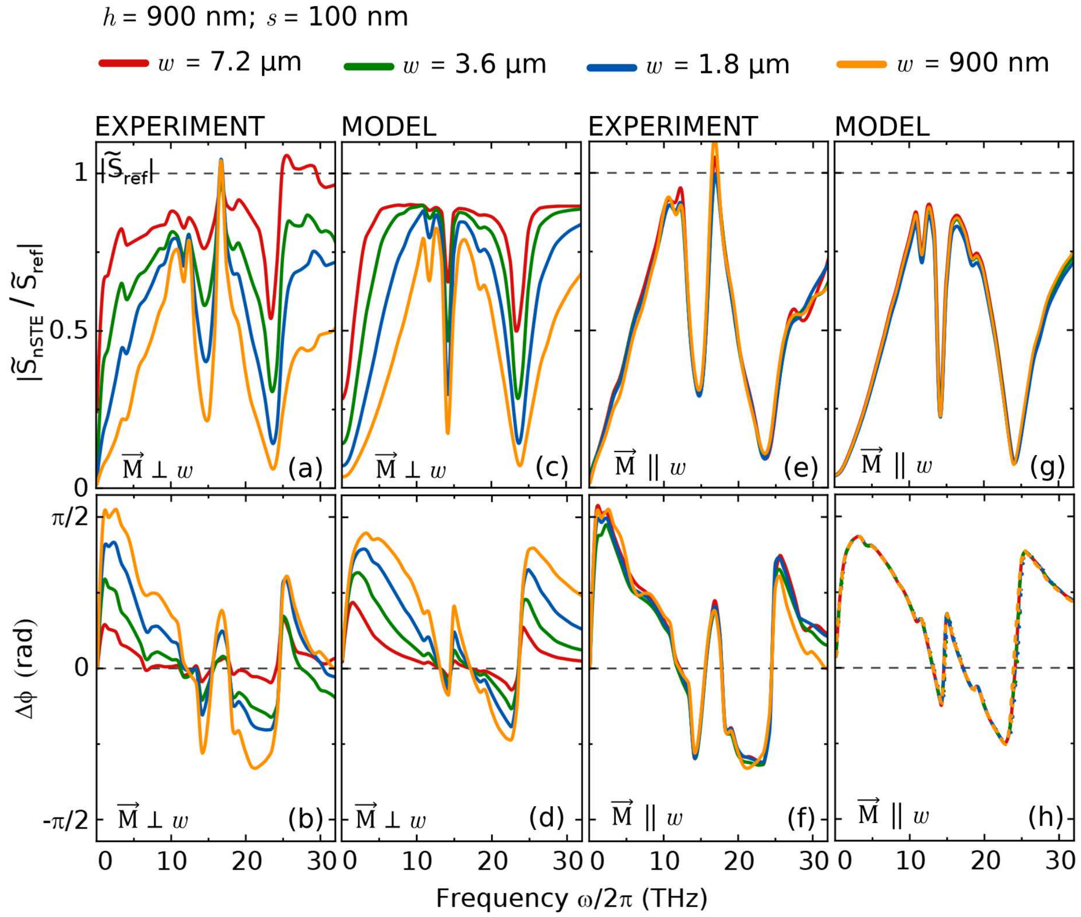

Figure 5.11: (a) Amplitude and (b) phase for the relative change of rectangular nanoSTEs as compared to the thin film reference STE for $\vec{M} \perp w$ configuration with w = 900 nm, 1.8 µm, 3.6 µm and 7.2 µm and constant h = 900 nm and s = 100 nm. Their corresponding (c) Amplitude and (d) relative phase were obtained from the analytical model. (e) Amplitude and (f) relative phase for $\vec{M} \parallel w$ configuration and their corresponding (g) Amplitude and (h) relative phase obtained from the analytical model.

From the analytical model, it was evident that C_e was influenced by the geometry and complex dielectric functions $\tilde{\epsilon}(\omega)$ of the STE and the substrate. Consequently, C_e is frequency-dependent since $C_e \propto \tilde{\epsilon}(\omega)$. C_e can be considered to be independent of w as long as w is larger than the relevant screening length, which is consistent with the experimental conditions. Moreover, a positive linear relationship was observed between C_e and h. C_g, similarly, was not affected by w and was proportionate to h, although it should also be noted that it exhibited an approximately inverse proportionality to the spacing s.

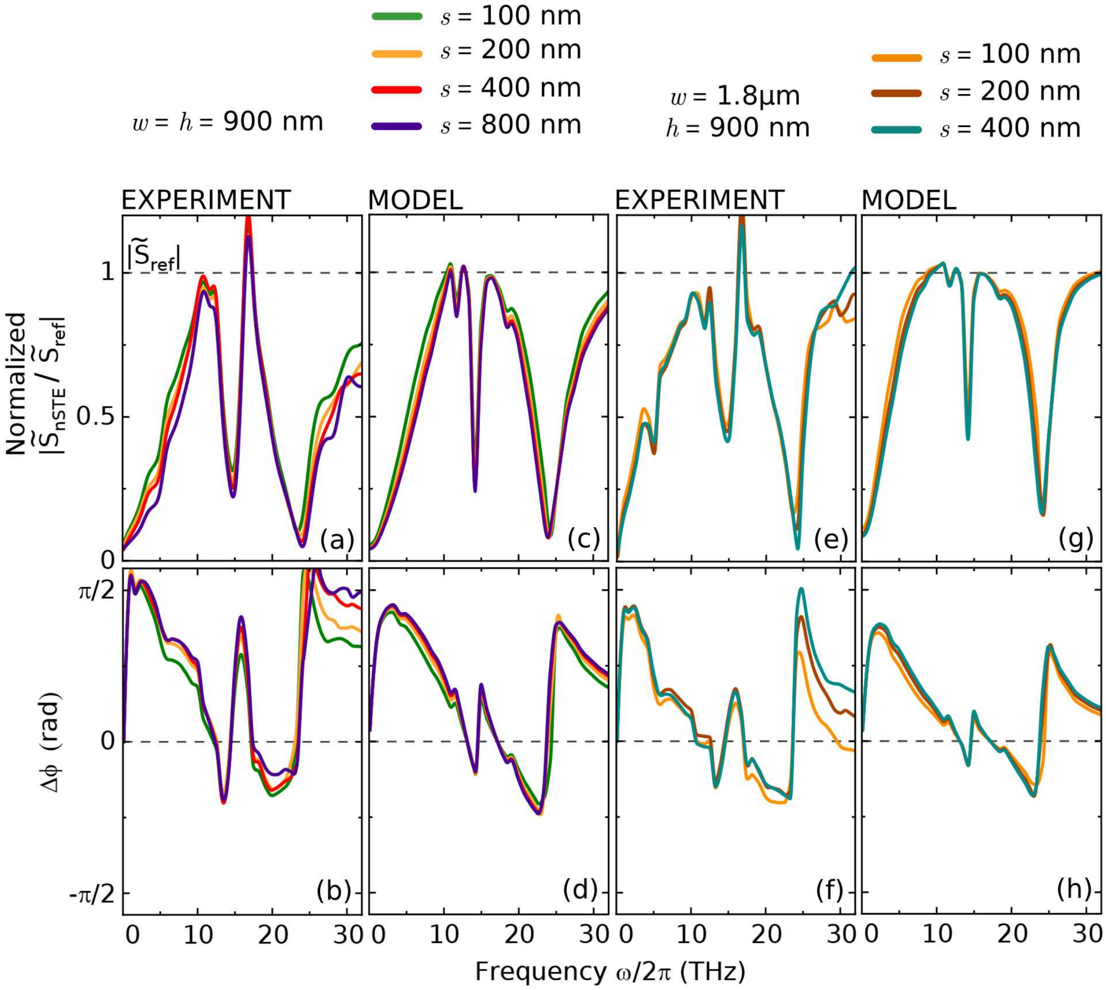

Figure 5.12: (a) $|\tilde{S}_{\mathrm{nSTE}}(\omega)/\tilde{S}_{\mathrm{ref}}(\omega)|$ (normalised based on the filling factor) and (b) relative phase obtained for an array of nanoSTE squares of size 900 nm and spacing, s = 100 nm, 200 nm, 400 nm or 800 nm from the experiment and (c, d) the model. (e) Normalised $|\tilde{S}_{\mathrm{nSTE}}(\omega)/\tilde{S}_{\mathrm{ref}}(\omega)|$ and (f) relative phase for an array of rectangles of constant h = 900 nm, w = 1.8 µm and s = 200 nm, 400 nm or 800 nm from the experiment and (g, h) the model.

The resistance R was determined by the conductivity in the x direction, exhibiting an inverse relationship with h and a positive relationship with w. Consequently, an increase in w with constant h resulted in a linear increase in RC. Contrastingly, alterations in h impacted R, C_e, and C_g while maintaining a constant value for $R(C_e + C_g)$. It should be noted that although RC remains constant, the initial current is directly proportional to h.

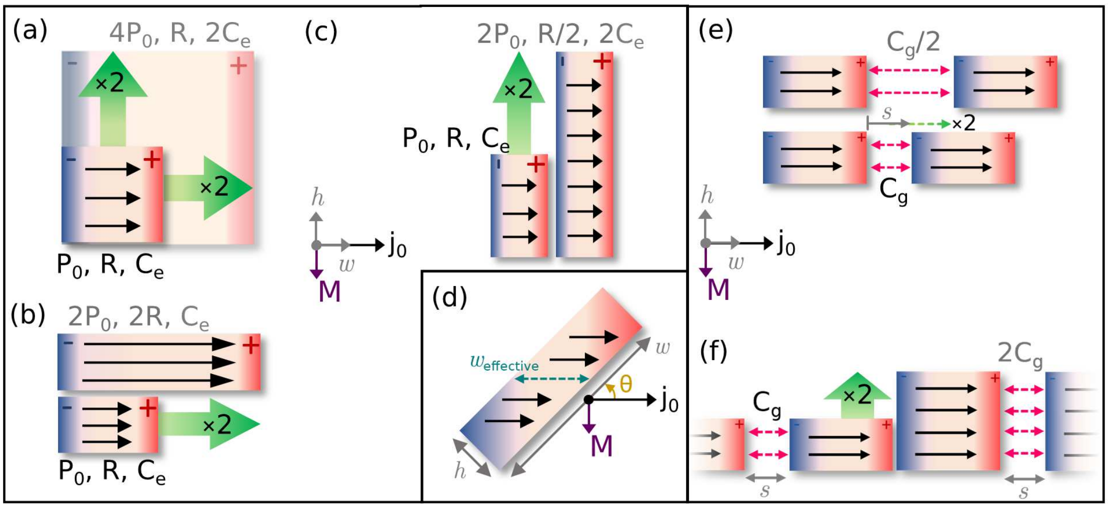

Figure 5.13: Correlation of geometry on RC circuit. $P_0\,(= V \cdot I_0) \propto w \times h$; $R \propto h$; $C_e \propto h$ as inferred from (a) square and rectangular nanoSTEs with dependence on (b) w, (c) h, and (d) θ between w and $\vec{j}_0$. Effect of spacing s with (e) $C_g \propto 1/s$ and (f) $C_g \propto h$.

In summary, the geometrical dependence of the RC time constant can be deduced from the previous arguments. The RC time constant depends on w and not h of the nanoSTEs. The total induced current $I_0 \propto h$ while the voltage $V \propto w$. Hence, the power $P_0 = V \cdot I_0$ is proportional to $w \times h$. For square shaped nanoSTEs with constant filling factor, doubling the size w and h each, the area $w \times h$ increases by 4. Hence, I_0 and V are doubled, while P_0 increases by 4 times. However, R remains the same since $R \propto w/h$ remains the same. C_e increases by 2 since $C_e \propto h$. Thus, RC_e increases by 2 (see figure 5.13 (a)). For rectangular nanoSTEs, when w is increased by 2 whilst keeping h constant for the configuration $\vec{M} \perp w$, I_0 remains constant while V is doubled, thus doubling P_0. Moreover, R increases by 2 since w/h increases by 2 and C_e is constant since h is constant. Hence, RC_e is increased by 2 (see figure 5.13 (b)). For the configuration $\vec{M} \perp h$, I_0 is doubled while V remains constant, thus doubling P_0. R decreases by 2 since w/h decreases by 2 and C_e increases by 2 following the increase of h by 2. Thus, RC_e stays constant (see figure 5.13 (c)). Consequently, for a scenario where the STE is at an angle to $\vec{M}$ where θ is the angle between w and $\vec{j}_0$, as shown in previous studies [37, 153], the THz response can be attributed to the effective length ($w_{\text{effective}}$) of the rotated STE in the direction of $\vec{j}_0$ (see figure 5.13 (d)). For an array of such nanoSTE, $C_g \propto h/s$. Thus, an incremental increase in spacing 's' leads to a decrease in C_g hence, a decrease in RC_g (see figure 5.13 (e)) while an incremental increase in h leads to an increase in C_g hence, an increase in RC_g (see figure 5.13 (f)).

5.3 STE stripes

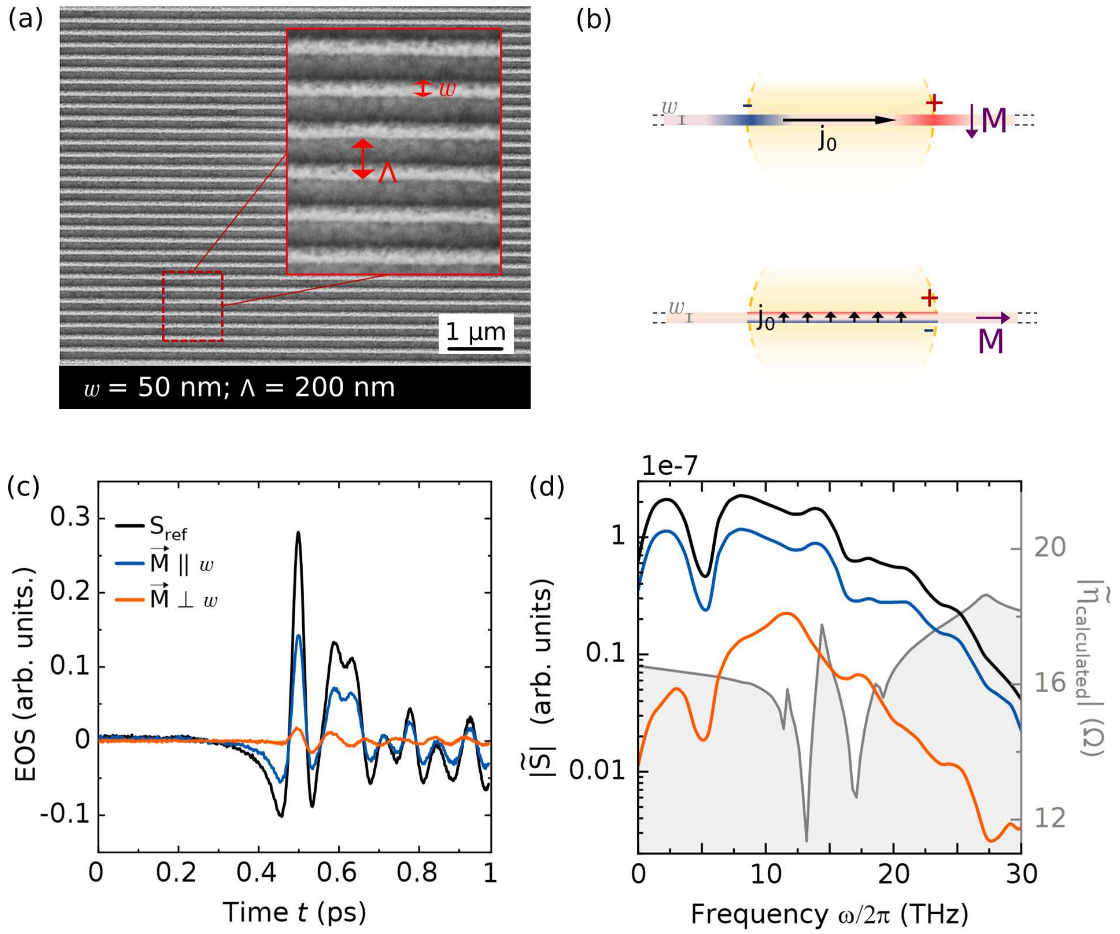

Figure 5.14: (a) SEM image for STE stripes with w = 50 nm and period Λ = 200 nm. (b) Charge current induced in STE stripes for both the configurations when $\vec{M} \parallel w$ and $\vec{M} \perp w$ as compared to STE$_{\text{ref}}$.(c) EOS signal for both the configurations and their (d) Amplitude Spectra. The grey curve in (d) shows the calculated STE wave impedance.

The modelling of nanopatterned STEs in the previous sections provided insight into the role of STE geometry in shaping the THz spectrum. The THz response is related to the relevant RC time constant of the device which is dependent on the STE geometry, specifically the length along which $\vec{j}_0$ is induced. An STE nanopatterned as a stripe could be designed to have a small C due to a very thin width, thereby keeping the R across the length similar which is effective within the FWHM of incident laser pulse. This would eventually lead to a very small RC time constant, which would eventually give the same $\vec{I}_{tot}$ as the $\vec{I}_0$. Therefore, a trilayer STE [15, 156] was patterned using Laser Interference Lithography with a subsequent Ar-ion mill using an e-beam evaporated $\mathrm{AlO_x}$ mask (see section 3.4.2), in order to obtain stripes of width w = 50 nm and a period Λ = 200 nm.

The pulse shape of the EOS signal (see section 3.6.1) for the configuration when $\vec{j}_0$ was along the length of the stripe was similar to that of $\mathrm{STE_{ref}}$ however, with a reduced overall amplitude which can be attributed to a reduced filling factor of the STE material. A similar change was also observed in the corresponding Spectral Amplitude which follows the $\tilde{\eta}(\omega)$ for the STE on the sapphire substrate. The charging was expected to occur along the boundaries of the laser spot, very similar to the case for a thin film STE discussed in the previous chapter (see chapter 4). However, when $\vec{j}_0$ was induced along the width of the stripe there was a comparatively smaller EOS amplitude. The features of the spectral amplitude were similar to those observed for the small-sized nanoSTEs as shown in previous sections. The typical reduction in amplitude for lower frequencies and at 15 THz and 24 THz, shows the effect of charging along the STE edges (see figure 5.14).

Another significant factor which becomes quite relevant in the case of STE stripes is their larger dimensional ratio compared to nanoSTEs since, the optical effects of the incident light can no longer be disregarded and differences in the THz responses can be expected for different polarisations of the incident light. Thus, a polarisation-dependent study was carried out on striped STEs. As a reference, the polarisation of incident light was considered to be $0°$ or p-polarised when it was parallel to the base and $90°$ s-polarised when it was perpendicular to the base. Considering the uniformity of the thin film in both the directions, the polarisation direction of light was not expected to affect the RMS amplitude of the thin film STE. However, it was observed that the s-polarisation of the incident pulse on the thin film STE showed a small increase in the RMS amplitude compared to p-polarisation. This was the result of the sample being illuminated at an angle of approximately within 5° to 10° along the vertical axis with respect to the incident light propagation direction to avoid reflection back to the laser (see section 3.6.1). This indicates a decreased absorption of incident light for p-polarised incidence than s-polarised incidence.

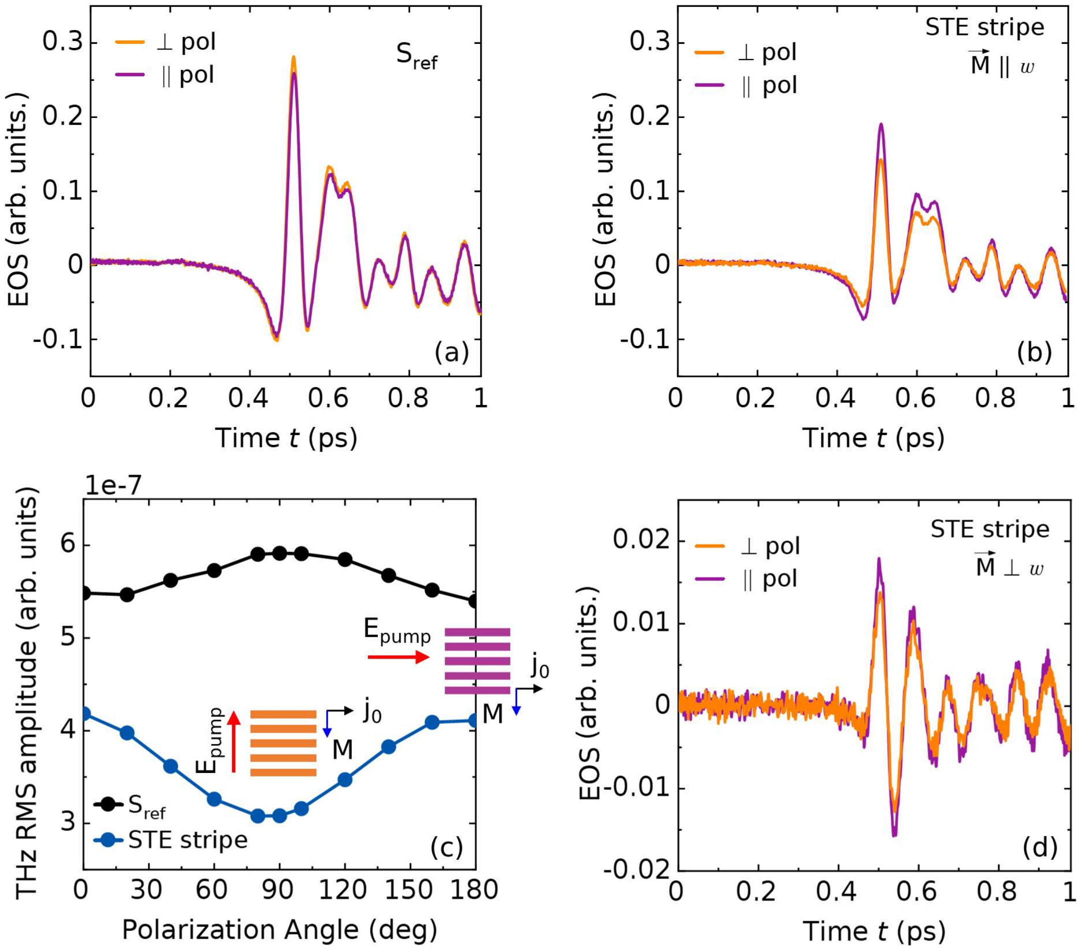

Figure 5.15: EOS with parallel and perpendicular polarisation of incident laser pulse for (a) a thin film STE and (b) striped STE with stripes aligned parallel to the base and magnetisation aligned perpendicular to the stripes. (c) RMS amplitude for thin film STE and striped STE for different incident pulse polarisation. (d) EOS for parallel and perpendicular polarisation of the incident pulse when the magnetisation was parallel to the STEs stripes.

In an ideal situation where the STE surface is perpendicular to the direction of incident light propagation, both the polarisations should result in equal amplitudes. However, for the striped STEs with stripes parallel to the base and magnetisation perpendicular to the stripes ($\vec{M} \parallel w$), the incident laser pulse with s-polarisation showed a decrease in the RMS amplitude (see figure 5.15 (a, b, c)) compared to that with p-polarised incidence. A similar trend was also observed for both the incident light polarisations when the magnetisation direction was parallel to the stripes ($\vec{M} \perp w$) (see figure 5.15 (d)).

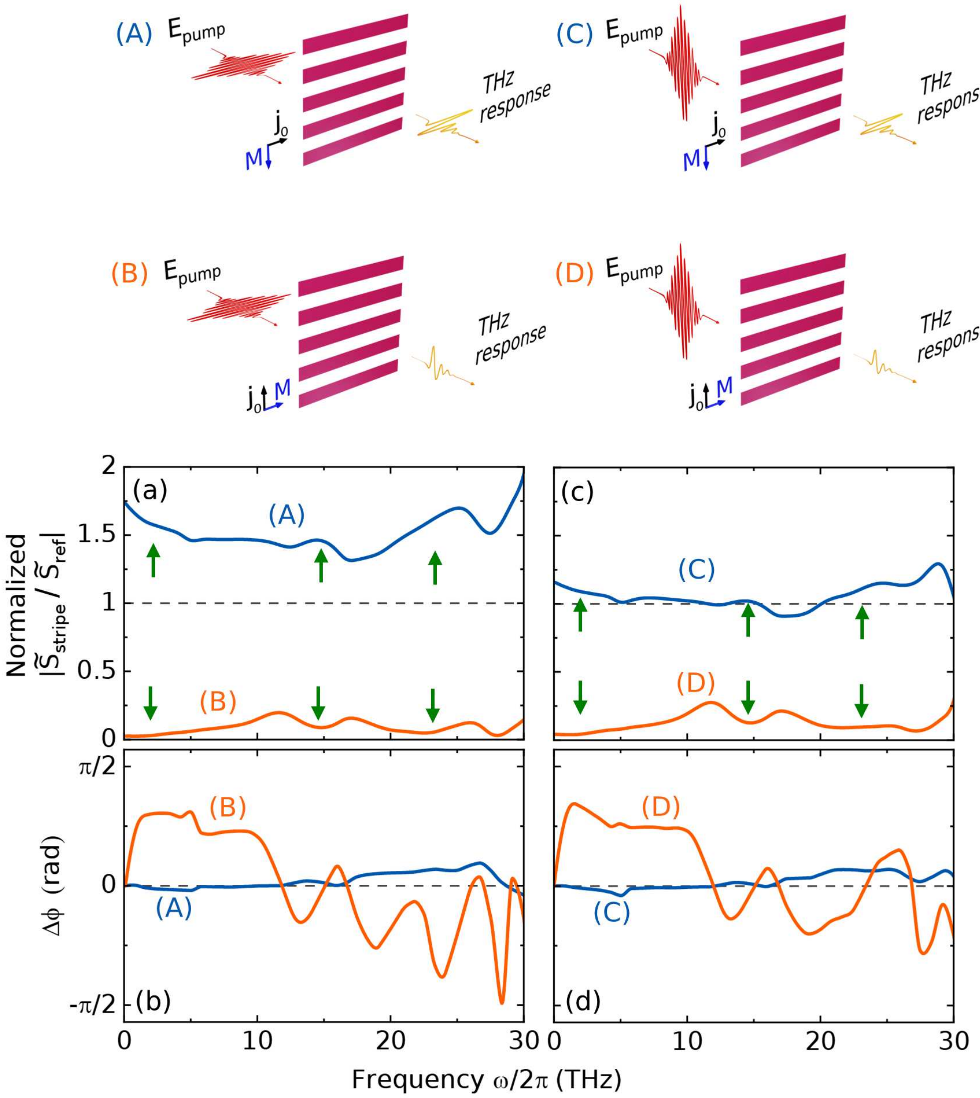

Figure 5.16: (a) Normalised transfer function for striped STEs for both magnetisation directions when the polarisation of incident pulse was parallel to the stripes and their respective (b) relative phase. (c) Normalised transfer function for striped STEs for both magnetisation directions when the polarisation of incident pulse was perpendicular to the stripes and the respective (d) relative phase. The sketch at the top shows each configuration corresponding to the respective graphs. The green arrows in (a) and (c) mark the features that are opposite to the trend.

As seen from the $|\tilde{S}_{\text{nSTE}}(\omega)/\tilde{S}_{\text{ref}}(\omega)|$ that was normalised on the basis of the filling factor, the THz response of the striped STEs with $\vec{j}_0$ perpendicular to the length behaved in a similar way as the square nanoSTEs with dips at 15 and 24 THz and reduction at lower frequencies (see figure 5.16 (a, c)). The relative phase (see figure 5.16 (b, d)) also followed the trend in terms of features observed for the relative phase of nanoSTE. In contrast, normalised $|\tilde{S}_{\text{nSTE}}(\omega)/\tilde{S}_{\text{ref}}(\omega)|$ for $\vec{j}_0$ parallel to the length of the stripes showed an inverted trend with overall normalised amplitude higher than that of $\tilde{S}_{\text{ref}}$.

The observed features include a negative slope with higher amplitudes for lower frequencies and peaks for 15 and 24 THz (see figure 5.16 (a, c)). This suggests that the stripes have less high-pass filtering due to the influence of charging and backflow compared to a thin film STE. The relative phase (see figure 5.16 (b, d)) also has inverted features compared to the relative phase of rectangular nanoSTE.

A similar trend in transfer function and relative change was observed irrespective of the polarisation of the incident laser pulse. However, the overall amplitude of the transfer function was significantly higher for the configuration when the incident light polarisation was parallel to the stripe length (see figure 5.16 (a)). This was attributed to the fact that the nanoSTE stripes act as polarisers. The parallel alignment of polarisation and the stripes leads to more absorption and electric fields drives currents along the stripes. For perpendicular configuration, the electric field oscillates across the narrow gaps between stripes and leads to less absorption. As a result, more this gives rise to an increased intensity of THz response for the parallel configuration. However, the behaviour of relative phase stayed unchanged irrespective of polarisation of incident laser pulse (see figure 5.16 (b)) indicating that the transmission or reflectance remains almost similar for both the configurations.

COMSOL [143] simulations were performed for the input parameters, as used in the previous chapter (see chapter 4), for a stripe of width 50 nm, giving an $\vec{I}_0 \equiv I_{\text{tot}}$ in the x-direction. The filter factor obtained from the FFT of the time derivatives of $\vec{I}_0$ and $\vec{I}_{\text{tot}}$ showed high pass characteristics (see figure 5.17). However, the cutoff frequency for $\vec{j}_0$ across the length had a much smaller cutoff frequency than that for $\vec{j}_0$ across the width. For these cases the effective excitation area was the length corresponding to the diameter of the laser spot.

The resistances for both the arrangements were equal, corresponding to an equal illumination area. In the first case, $\vec{j}_0$ flowed along the longer side, and the charge accumulated along the edges of the FWHM of the laser was much less due to smaller C. This eventually led to the charge neutralisation and backflow along the stripe length, which occurred very slowly due to a smaller RC time constant compared to that of a structure with length shorter than the FWHM of the laser. It should also be noted that the current backflow took place only along the STE stripe illuminated by the laser, in contrast to the thin film STE with current backflow occurring within the laser spot as well as through the surrounding STE material. In the second case, $\vec{j_0}$ flowed across the smaller side with a larger C, therefore, a larger RC time constant, which led to a higher cutoff frequency. Hence, the electric field radiated by the $\vec{j_0}$ induced in a striped structure along its length did not undergo high pass filtering, thus providing a direct relation between the laser-induced $\vec{j_s}$ and the THz radiation (see figure 5.17). It should be noted that the simulation only shows the charge dynamics in nanostriped STEs without any optical effects such as interference. Hence, the simulation does not explain the polarisation dependent behaviour as observed previously (see figure 5.16).

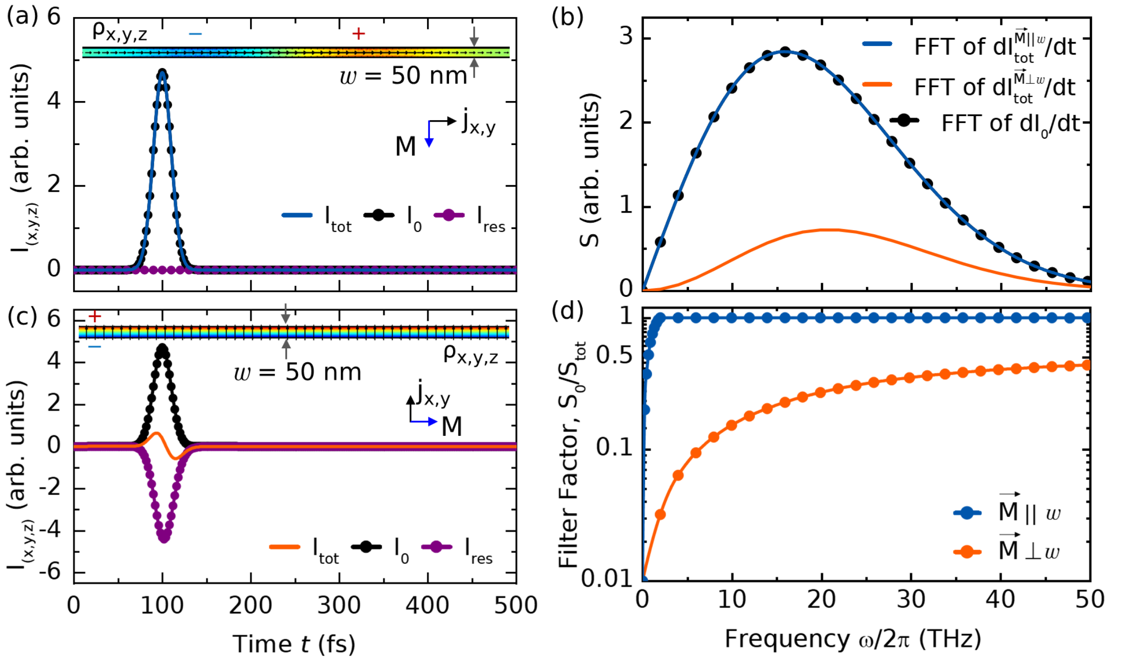

Figure 5.17: COMSOL simulations for an STE stripe with w = 50 nm, h = 150 µm and T = 10 nm on a sapphire substrate of size 150 µm×150 µm for (a) $\vec{M} \perp w$ and (c) $\vec{M} \perp w$. Their corresponding (b) Spectral Amplitude and (d) Filter Factor. The insets in (a) and (c) show the charge density ($\rho_{x,y,z}$) and the direction of current density($j_{x,y}$) at $t = 100\,fs$ from the COMSOL simulation.

5.4 STE metastructures

In recent years, metamaterials based on Split Ring Resonator (SRR) have gained wide recognition for their ability to efficiently manipulate the propagation of THz waves [166] and also as a source of broadband THz emission [167]. An SRR is a metallic structure specially engineered to interact with electromagnetic waves to enable exotic behaviours such as reversed Snell's law in negative-index metamaterials [168]. It comprises a highly conductive ring interrupted at one or more locations by a non-conductive gap filled with air or another dielectric medium. In the SRR, when subjected to a time-varying magnetic field, a circular current is induced resulting in charge accumulation across the gaps due to an effective capacitance C. The electric field established at these gaps opposes the induced current, thereby localising electric energy predominantly in the gap regions. In contrast, magnetic energy is confined within the area enclosed by the ring where the ring loop contributes to an effective inductance L. This can be simplified into an LC circuit with a resonance frequency (ω_m) expressed as $\omega_m = \frac{1}{\sqrt{LC}}$. In the resonance condition, a pronounced magnetic moment can be generated, and an array of subwavelength SRRs can lead to substantially negative permittivity μ_{eff}, which has been shown previously [169–172]. These studies usually involved a single layer of SRRs fabricated on a substrate with the excitation direction perpendicular to the plane of the SRR. This approach leverages the coupling of the electric field to the magnetic resonance of the SRRs through structural asymmetry [173]. Hence, SRR shaped STEs is a promising candidate to study the STE physics with regard to electromagnetic interaction via magnetic field coupling and shaping of the THz response.

An array of **U**-shaped structures were nanopatterned in an STE trilayer [15, 156] on sapphire substrate using e-beam lithography and subsequent Ar-ion etching involving AlOx as an etching mask (see section 3.4.2). These metaSTE structures had a width of 110 nm and a height of 106 nm with a split of 30 nm between the two legs. The STE-SRR arrays were excited with a fs-laser pulse with a wavelength of 800 nm (see section 3.6.1). The time domain EOS signal was much smaller in amplitude compared to S_{ref} due to a smaller filling factor and the size of the structures. The configurations for upright or horizontal positions of legs w.r.t $\vec{M}$ are referred to as **U** and **C**, respectively, in the rest of the text. The Spectral Amplitude for both shows similar behaviour with equivalent amplitudes across most of the spectrum apart from a low-frequency suppression and a reduction at 15 THz and 24 THz, which were similar to the features seen in the Spectral Amplitude of small-sized square nanoSTEs (see figure 5.18). $|\tilde{S}_{\text{mSTE}}(\omega)/\tilde{S}_{\text{ref}}(\omega)|$, which was normalised based on the filling factor, showed absorption dips and high pass filtering.

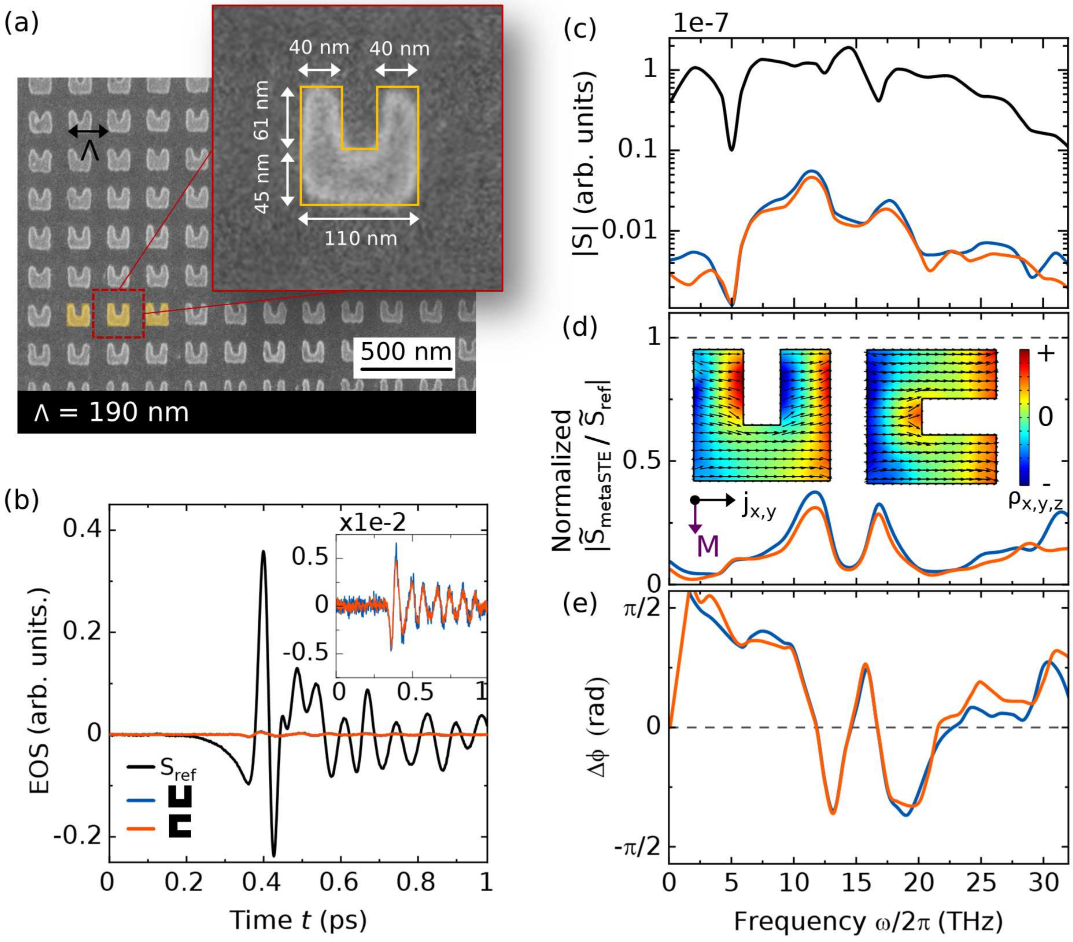

Figure 5.18: (a) SEM images of metaSTEs with a width of 110 nm, height of 106 nm, with a split of 30 nm between the two legs, and period Λ of 190 nm. (b) Time domain EOS signal for metaSTEs in **U** and **C** configuration with respect to the direction of $\vec{M}$ (The inset shows enlarged plots for metaSTE responses) and their corresponding (c) Spectral Amplitudes. (d) $|\tilde{S}_{\text{mSTE}}(\omega)/\tilde{S}_{\text{ref}}(\omega)|$ for the metaSTE, normalised based on the filling factor and its (e) relative phase as compared to S_{ref}. The inset in (d) shows charge density and current density of metaSTE for both **U** and **C** configurations as obtained from the COMSOL simulation.

A similar behaviour was also seen in the relative phase as observed in the case of nanoSTEs. The charge dynamics was understood on the basis of a COMSOL [143] simulation with similar input parameters as used for the work presented in the previous chapter (see chapter 4), which shows that the metaSTEs in the **U** and **C** configurations behaved as a combination of rectangular nanoSTEs. Additionally, the comparison of relative THz amplitudes emitted from the metaSTEs for both configurations showed a larger amplitude for the **C** configuration, indicating an additional capacitance at the legs of the SRR.

In the following step, the behaviour of THz response was observed for different polarisation of incident light. The **U** configuration of SRR was taken and the convention for polarisation of incident light was considered to be 's'-polarised ($\theta = 0°$) or 'p'-polarised ($\theta = 90°$) based on the polarisation parallel(perpendicular) or perpendicular(parallel) to the legs(gaps), respectively. It was observed that the EOS response is prominent for 's'-polarisation while there was an approximately flat response for 'p'-polarisation (see figure 5.19 (a)). A polarisation sweep from $\theta = 0°$ to 90° showed a decreasing trend of RMS-THz amplitude while further increasing the polarisation upto 150° led to an increasing trend in RMS-THz amplitude (see figure 5.19 (b)).

Since the SRR was excited by a laser with 800 nm wavelength perpendicular to the SRR plane, the transmission and reflection characteristics were subsequently analysed. This was performed using an electromagnetic simulation involving the CST Microwave Studio. The SRR dimensions were taken to be similar to the experimental structure dimensions, and a sapphire substrate was taken to exist underneath the SRR. For the simulation, gold was assigned as the SRR material with a thickness of 20 nm to imitate the STE metal stack. The CST simulation for a unit cell configuration revealed dips in the transmission (S21) and reflection (S11) curves for both the 's' and 'p'-polarisations (see figure 5.19 (c)), indicating possible resonance conditions. For 's'-polarisation the dips were observed at 650 nm, while for 'p'-polarisation the dips were observed at 800 nm. Further, at 800 nm, the surface current and electromagnetic field behaviour revealed circular current for the 'p'-polarisation state which is induced due to the asymmetry of the SRR along the direction of the electric field of the incident electromagnetic wave. The strong electric field across the gaps indicated an electric dipole and the strong magnetic field in the centre indicated a magnetic dipole. This is in contrast to the behaviour observed for the 's'-polarisation state with parallel uni-directional surface currents, and strong electric and magnetic fields only on the opposite edges along the direction of electric and magnetic fields (see figure 5.19 (d)). Hence, the magnetic resonance condition is favourable at 800 nm incident wavelength for the 'p'-polarisation state, and this phenomenon is termed electric excitation coupling to the magnetic resonance (EEMR) [173]. This mechanism is particularly advantageous in magnetic resonance detection in SRR for an incident electromagnetic wave parallel to the SRR plane at optical frequencies via transmission and reflection behaviour. Additionally, SRRs also exhibit electrical resonance [174] at the ω_0 frequency for the 's'-polarisation state, here observed from the dip in transmission and reflection behaviour at ~ 650 nm.

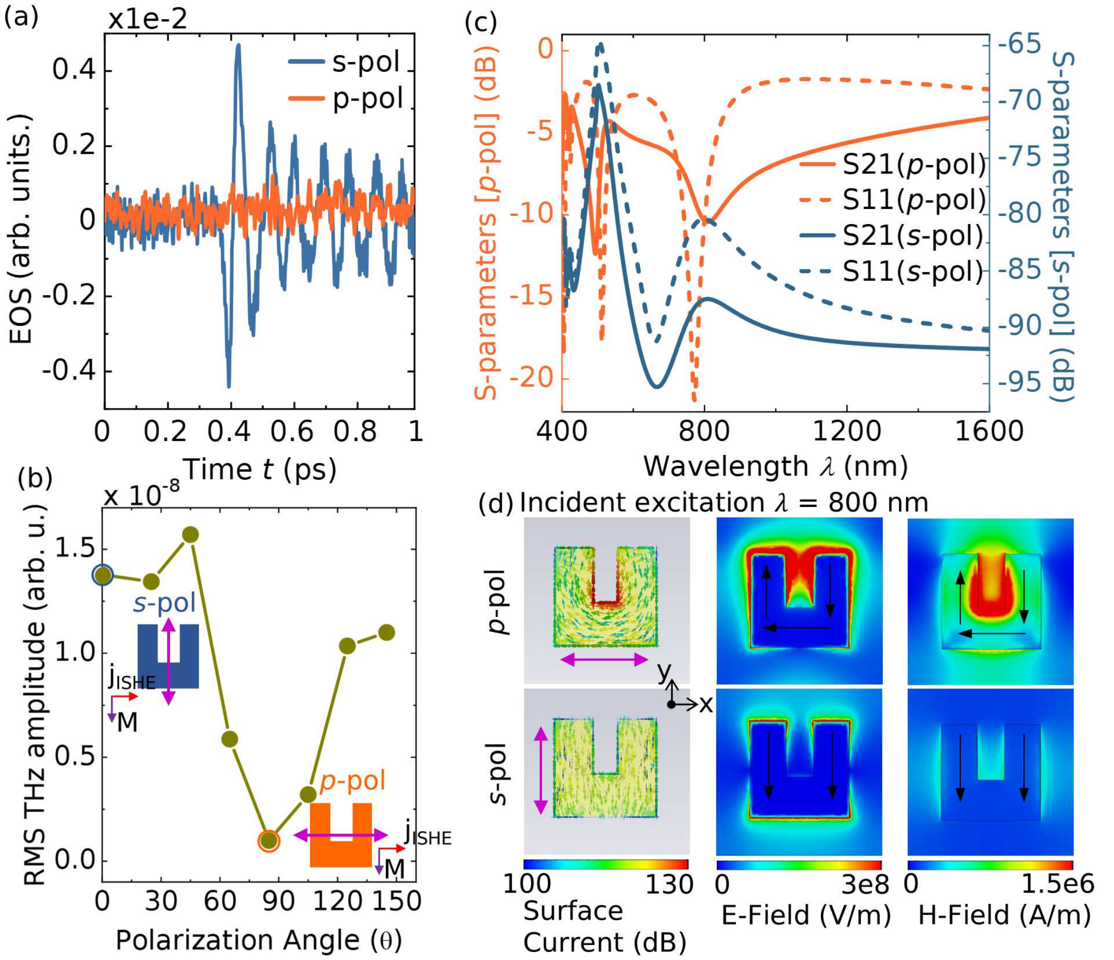

Figure 5.19: (a) EOS response from STE-SRR for 's' ($\theta = 0°$) and 'p'-polarisation ($\theta = 90°$) states of incident light where θ is the angle between the polarisation direction and the legs. (b) RMS THz amplitude from STE-SRR for different incident polarisation angles (θ). Electromagnetic simulation using CST Microwave Studio for both 's' and 'p'-polarisation states showing (c) transmission (S21) and reflection (S11) curves and behaviour of (d) surface currents, and electric and magnetic field at $\lambda = 800\,\text{nm}$. The black arrows represent the surface currents.

The trend observed for EOS amplitude of STE-SRR due to incident light polarisation, indicates there is less interaction with STE response for 's'-polarised state, which gives a prominent EOS signal while there is a counter response of magnetic resonance of SRR to the STE response for 'p'-polarised state, which gives a flat EOS signal. However, this needs further investigation to understand the nature of the interaction of the magnetic dipole with the STE response.

Conclusion and Outlook

Nanopatterned STEs exhibited significant alterations in the emission spectrum compared to the reference STE thin films owing to the fact that these structures were smaller than the laser spot size and underwent homogeneous illumination. A controlled tuning of the THz signal was obtained by changing the dimension and, thus, the resistance in the direction of the ISHE current flow, which led to a change in the RC time constant of the system. The high pass filtering seen in the nanoSTEs validates the theoretical model proposed in the previous chapter, which was also used to explore the spectral features in the form of peaks and dips pertaining to the frequency-dependent substrate dielectric constant. Within limits, this dimensional control allows for intentional modification and shaping of the THz spectrum of the STE by selecting a cutoff frequency or selecting a suitable substrate material to mute certain frequencies in the emission band, with the level of damping determined in part by the nanoemitter's dimensions.

Since, the emitted spectrum's lower frequencies were suppressed for smaller sized STEs, the corresponding cutoff frequency rose. For measurements in a setup with bandwidth limited to smaller frequencies in the range of 5 to 10 THz, this might be interpreted as a blue shift [37, 153] or a reduction in peak amplitude [155]. Hence, it is quite useful to understand the behaviour of nanostructured STEs in upper frequency regime with a broadband spectrum.

The nanopatterned STE stripes provide a suitable solution to the problem of charging, which occurs for both thin film and quadratic nanopatterned STEs. This can be an appropriate approach to obtain the relation between the spin current and the ISHE charge current and to obtain the spin current information from the broadband THz emission of STE without the influence of charging and backflow.

The metastructures of STE provided useful insights into the electromagnetic interaction of incident light with the STE THz response thus, paving the way for designing suitable STE metastructures for wide range of applications such as shaping or filtering of broadband STE THz response.

6 Terahertz Spintronic Devices

Charge Dynamics and nanostructuring significantly shape the emitted THz radiation, as seen in the previous chapters. In this chapter, various produced spintronic devices with their working regime in ultrafast timescales are realised. In order to achieve this, the concept of shaping the Power Spectral Density (PSD) of ultrafast electrical responses are considered, drawing parallels with the optical pulse shaping in the context of THz radiation. The tuning parameters relevant for pulse shaping are dependent on the length of the transmission line between STEs, which determine the central driving frequencies, and a THz burst leads to a narrowband PSD. Moreover, the choice of the FMs and STE shape to vary the switching fields of the magnetisation via shape-influenced changes in domain wall nucleation energy, is used to fabricate a THz spintronic device for Digital-to-Analog conversion applications. Finally, an alternative method of THz generation from an STE is shown by locally modulating the magnetisation via the Oersted Field generated by a dc-bias current without the need for any external magnetic field.

Publication information A portion of this chapter discussed in section "Digital to Analog Converter for ultrafast signals" was published as: *"On chip digital to analog converters using spintronic terahertz emitters"* by B. Das-Mohapatra, N. Kanistras, A. Busse, E. Th. Papaioannou, and G. Schmidt in Appl. Phys. Letters 127, 204103 (2025), DOI: https://doi.org/10.1063/5.0291032

Author contributions BDM and GS conceived the experiments. BDM, AB and NK fabricated the samples. BDM and AB performed the experiments and analysed the data with the support of GS and ETP. The manuscript was written by BDM and GS with the help of, and after discussions with, ETP, RR and TK.

Introduction

Spintronic logic devices are promising for low-power computing [175–178]. However, their adoption is limited by their slow operational speed. Although mechanisms like Spin Transfer Torque (STT) and Spin Orbit Torque (SOT) can induce fast magnetisation dynamics [16, 34], as shown theoretically, their measured record switching time is still too slow [179, 180] compared to traditional silicon field effect transistors [181]. Additionally, the state of the art devices have a limited working range in terms of frequencies of the signals, which are typically in MHz or low GHz regime. To achieve a competitive edge over charge-based devices in information technologies, it would be beneficial to increase the operational speed of spintronic technologies as well as accommodate functionality for signals with much higher frequencies.

Recent research has revealed that exciting electrons on picosecond or subpicosecond time scales, faster than electron-phonon relaxation times [182], can overcome precessional speed limits for manipulating magnetic order. Moreover, exciting new developments in THz sources are being explored and involve innovative methods that reduce the need for bulky optics setups [183, 184]. By combining THz emitters (see chapter 2) with metallic waveguide structures, on-chip experimental setups are possible. In a recent study [35] it was shown that sub-THz current and voltage pulses can be generated from STEs on waveguides via ISHE. The straightforward implementation of a multilayer and metallic waveguide makes it possible to integrate it into any sample layout, including on-chip designs. This development opens up new possibilities for spintronic applications with ultrafast timescales.

6.1 Frequency-specific Narrowband THz emission

In addition to the broadband applications of the THz spectrum, narrowband applications are also important, especially for high-resolution and low-power spectral transmissions relevant for frequency-selective applications. Optical pulse shaping of THz radiation by generating a tunable pulse train [185] and the generation of narrowband pulses via chirped pulse difference at THz frequencies have been shown in previous studies [186, 187]. Alternatively, long-range spin waves were generated from magnetoelastic materials [188] leading to narrowband THz pulses. Apart from optical pulse shaping and material selection, narrowband THz emission could also be realised via multiple emission sources for pulse shaping based on time delay between the emissions. For on-chip applications, an ultrafast electrical pulse burst could be generated to shape the overall time domain response where the time delay is engineered based on current transmission time from the emitters and obtain a narrowband power spectrum of the signal with driving frequencies in the THz regime.

6.1.1 Experimental details

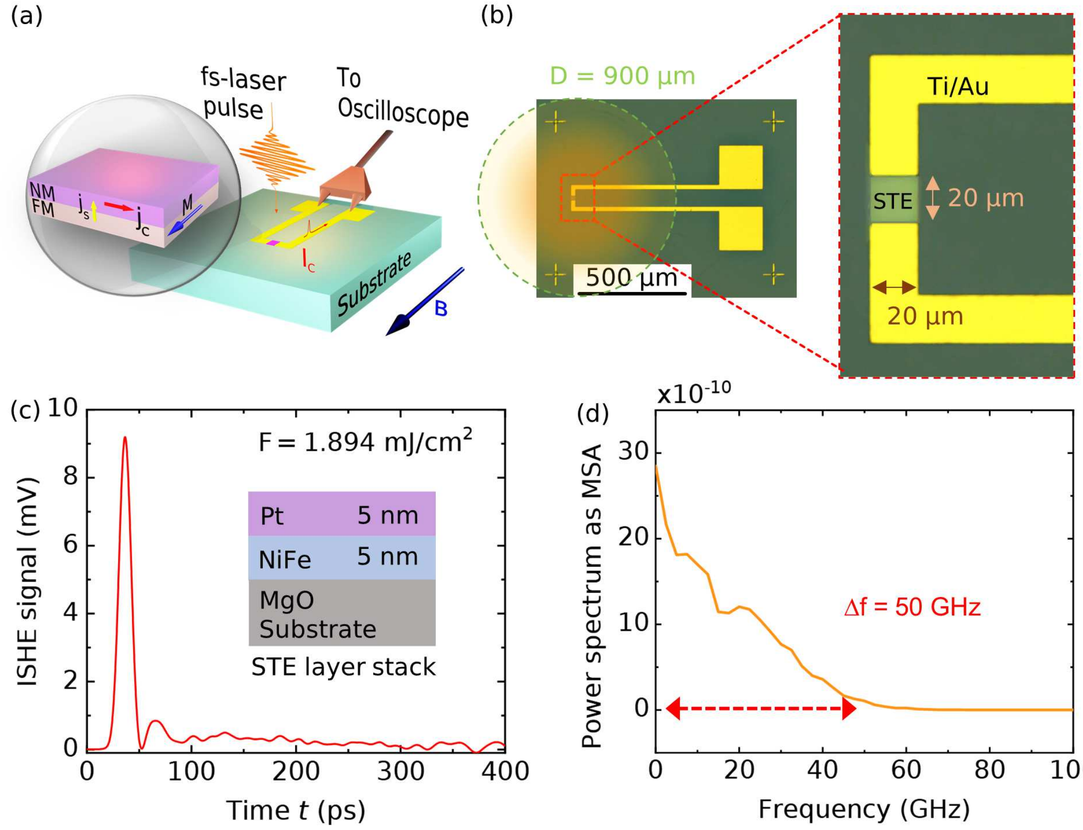

Figure 6.1: (a) The measurement schematics for the detection of an ultrafast electrical response. (b) Optical microscope image for a 20 µm by 20 µm STE on a transmission line. The circular area marked on the transmission line represents the approximate FWHM of the laser spot size D = 900 µm. (c) Time domain electrical signal from a single bilayer STE consisting of Ni$_{80}$Fe$_{20}$(5 nm)/Pt(5 nm) on MgO substrate. (d) The Power Spectral Density (PSD) for the time domain signal showing the resolution was limited by the oscilloscope at 50 GHz.

The STE, typically consisting of a bilayer of FM|NM, was comprised of Ni$_{80}$Fe$_{20}$(5 nm)/Pt(5 nm), which was fabricated by DC Magnetron Sputtering in an argon atmosphere at a base pressure of 6×10^{-8} mbar on a MgO(001) substrate. The STE was nanopatterned using e-beam lithography followed by Ar-ion etching into 20 µm by 20 µm sized structures (see section 3.4.2). This was followed by nanopatterning by e-beam lithography of a thick Ti(10 nm)/Au(150 nm) transmission line connecting the STEs and terminating in large contact pads (see section 3.4.1). The Ti/Au layer was deposited using e-beam evaporation at a base pressure of 5×10^{-7} mbar. The STE was excited using linearly polarised laser pulses at normal incidence from an amplified Yb:KGW femtosecond laser with 99.6 kHz repetition rate, a wavelength of 1030 nm and a pulse duration of 300 fs. The excitation of STEs led to a spin current from the FM layer to the NM layer, inducing a charge current pulse I_C in the lateral direction determined by the direction of magnetisation under the maximum applied magnetic field of 80 mT (see section 2.1). The electrical pulse was detected via the transmission line by a sampling oscilloscope of 50 GHz bandwidth (see section 3.6.2) (see figure 6.1 (a,b)).

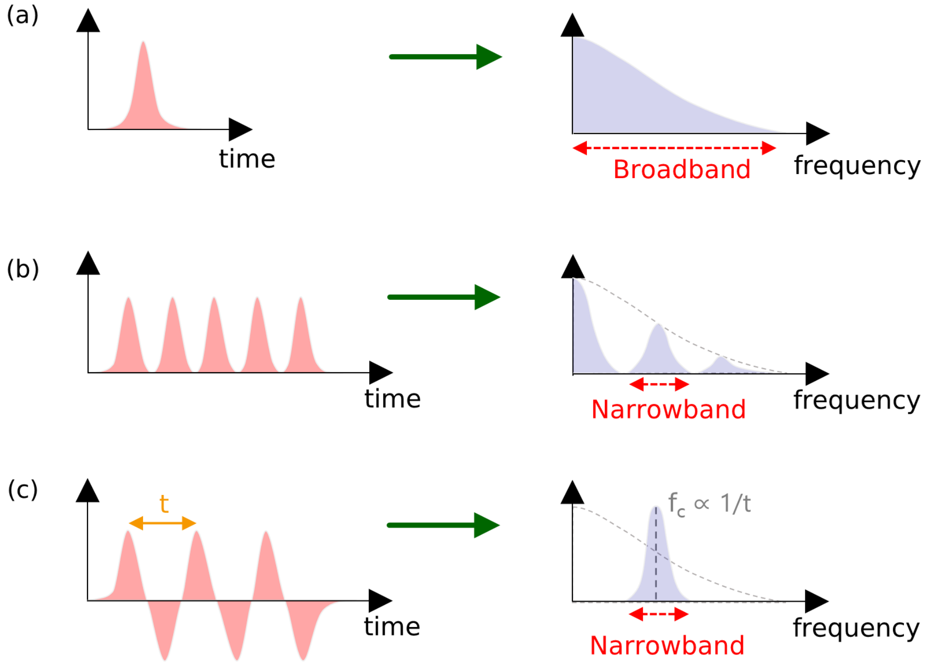

Figure 6.2: Illustration showing spectral shapes as a result of various temporal shapes:- (a) Single pulse, (b) series of pulses (burst signal) and (c) periodic pulse burst leading to frequency selective ($f_c \propto 1/t$) narrowband PSD.

The initial measurement was carried out with only one STE on a transmission line. The incident Gaussian beam had a spot diameter D of 900 µm FWHM intensity with a pulse energy of 6 µJ and an average laser power $\bar{P} = 600$ mW, resulting in an incident light intensity of $\bar{I} = 6.3$ GW/cm^2. This gave a fluence F = 1.894 mJ/cm^2 on the sample surface. It also resulted in a prominent electric pulse with a peak voltage of 9 mV. The rise time was about 10 ps which was in agreement with the 50 GHz resolution of the sampling oscilloscope (see figure 6.1 (c,d)). It should be noted that the bandwidth of THz response was limited by the incident pulse width and the carrier lifetime which was typically reported in the order of femtoseconds [189]. This would typically mean that a bandwidth of 3 THz for 300 fs pulse width (see figure 6.2 (a)) was still achievable.

In order to obtain a narrowband emission, a series of such pulses can be designed, thus giving a burst of pulses. However, the pulses defining the pulse burst will have the same polarity, thus leading to a dc-component of the signal in addition to a narrowband signal where the central frequency ($\mathrm{f_c}$) is the inverse of half of the time between the two subsequent peaks (see figure 6.2 (b)). An efficient solution to eliminate the dc-component and to obtain a large PSD signal with a narrowband was to use periodic electrical pulses with an alternative and opposite polarity. The $\mathrm{f_c}$ here was determined by the period t of the pulse burst (see figure 6.2 (c)).

6.1.2 Sequentially emitting STEs

A straightforward approach to obtain a pulse burst is through the use of simultaneous emission of STEs with different time delay paths. With regard to the propagation of the electrical pulse through the transmission line, the propagation velocity v along the transmission line is determined by the material around the transmission line. This velocity is proportional to $\frac{c}{\sqrt{\epsilon_{\mathrm{eff}}}}$ where c is the speed of light in vacuum and ϵ_{eff} is the dielectric constant for the surrounding media. Thus, the pulse duration can be estimated from the path length l, which is substantial for nanometer and micrometre scale structures at sub-THz frequencies [190, 191], and relative to v. Hence, multiple STEs on the transmission line can be arranged with equivalent intervals to simultaneously emit an electrical pulse from the STEs in order to generate a pulse burst.

One possible approach to obtain the inverse polarity of each alternate STEs, is to use an opposite magnetisation on adjacent STEs, which is in agreement with the proportionality of induced $\vec{j}_c$ direction to $\vec{j}_s \times \vec{M}$. Another possibility is to flip the FM|NM layer to NM|FM for each alternative STE. In either case, it is quite complicated to achieve these configurations. A simpler solution would be to modify the transmission line containing the STEs into a meander shape. Although the STEs generate pulses in the same in-plane direction with the same polarity, the convention also satisfies the interpretation of the same plane being in the opposite direction with inverse polarity. Since the meander-shaped transmission line is connected in opposite directions for the STEs in alternate positions, the electrical pulses from alternate STEs have opposite polarity to the adjacent STEs while having $\vec{M}$ for all the STEs along the same direction (see figure 6.3). The adjacent STEs can be referred to as STE – 1 and STE – $\bar{1}$.

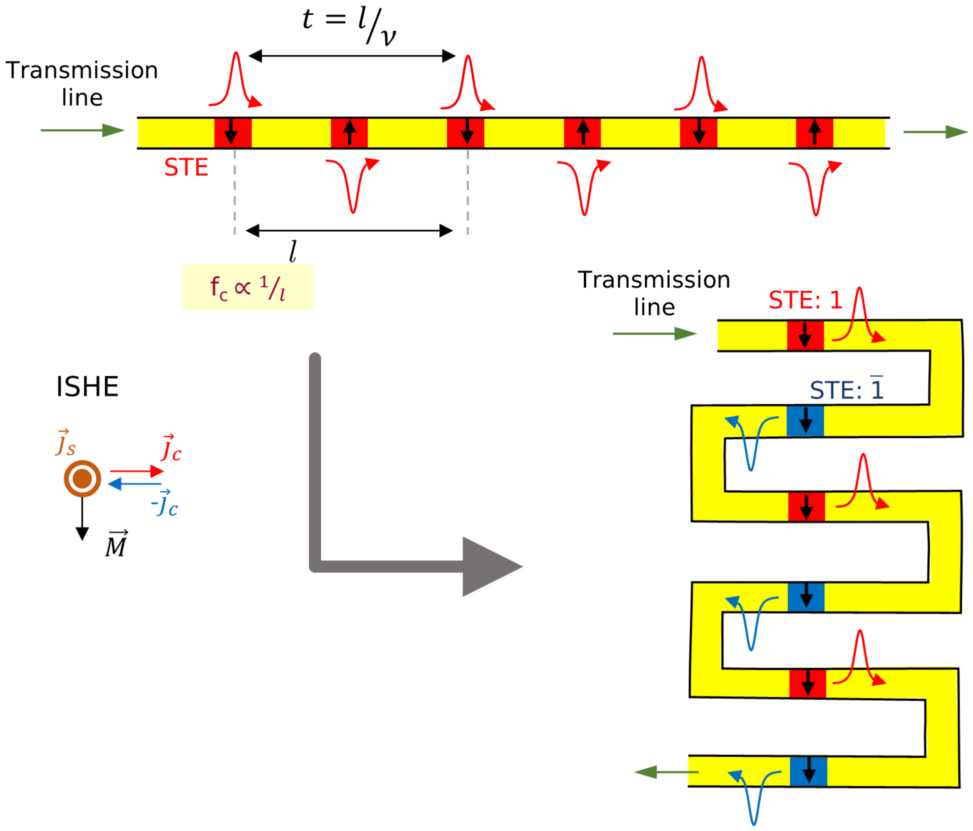

Figure 6.3: Design schematics of STEs on the transmission line to generate periodic burst signal with the period $t \propto l/v$ where v is the transmission velocity and $f_c \propto 1/l$. The black arrows represent magnetisation direction $\vec{M}$ and corresponding polarity of $\vec{j}_c$ depends on $\hat{M}$. The equivalent representation of the transmission line as a meander with $\vec{M}$ along the same direction and corresponding STE nomenclature as 1 or $\bar{1}$ for $+\vec{j}_c$ or $-\vec{j}_c$, respectively.

The 50 GHz resolution of the Sampling Oscilloscope allowed for a minimum time difference (time period, t) of 10 ps between two signals if they were to be distinguishable and an approximate length of at least 2 mm between the STEs corresponding to the half-period. However, it was quite challenging to illuminate all the STEs simultaneously due to the limitation of the laser spot size.

The use of the meander shape makes the arrangement of STEs in a smaller area possible, which is required for uniform illumination by a fs-laser pulse. Additionally, it allows for the modification of the inter-STE path length along the transmission line, which is beneficial for designing the f_c of the PSD.

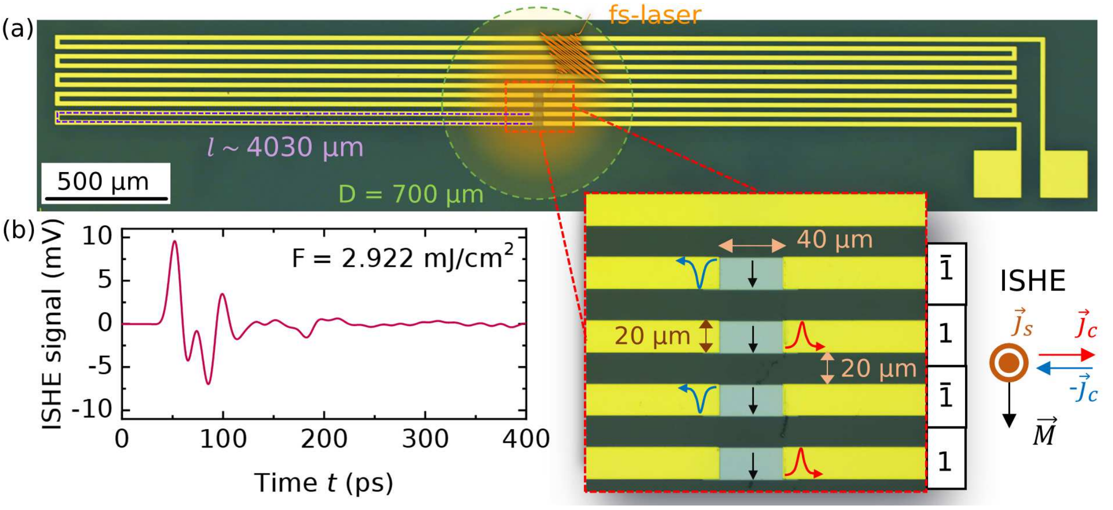

Figure 6.4: (a) Optical microscope image of a meander-shaped transmission line with multiple STEs of size 40 µm by 20 µm and its (b) electrical response. The magnetisation $\vec{M}$ was along the same direction for all the STEs, as represented by the black arrows. The path length between STEs was l= 4030 µm.

By taking the above reasons into consideration, a meander-shaped transmission line was patterned to accommodate multiple STEs of size 40 µm × 20 µm, with STEs placed in the middle of the meander (see figure 6.4 (a)). Upon uniform illumination with a fs-laser pulse with a FWHM of spot size diameter of 700 µm and a fluence of ~ 3 mJ/cm^2, a combination of electrical pulses was observed with multiple peaks and dips (see figure 6.4 (b)). Therefore, the proof of principle was established (see figure 6.4). In this design the magnetisation of the STEs were all aligned in the same direction and the length between STEs was 4030 µm. The STE combination used here followed the convention $1\bar{1}1\bar{1}$.

In a similar manner, different combinations of the STEs on the transmission lines were fabricated with conventions 1000, $1\bar{1}00$, $1\bar{1}10$, 1010 and $0\bar{1}0\bar{1}$. The first set of structures comprised equal-sized STEs (see figure 6.5 (a)). The total current generated by the STE was proportional to the STE size since it was proportional to the illuminated area. Hence, variation of STE size was expected to result in a proportional total charge current, which allowed a certain modification of the individual pulse. This was observed for a similar meander-shaped transmission line with varying STE sizes (see figure 6.5 (b)).

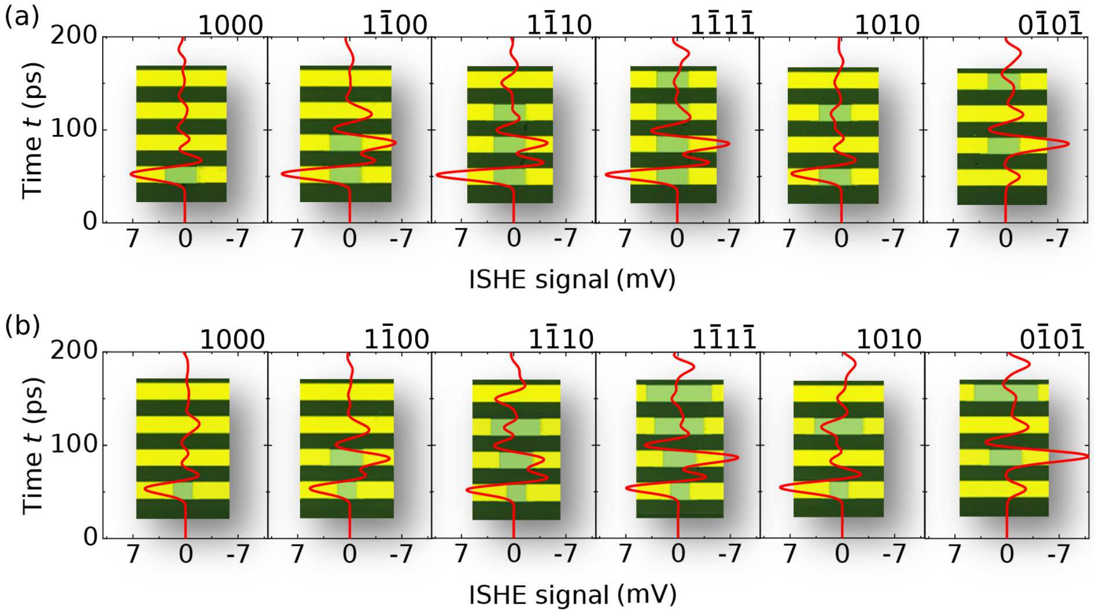

Figure 6.5: Electrical responses from different combinations of STEs as shown in the underlying optical microscope images when the STE sizes were (a) equal (w = 40 µm) and (b) of varying sizes (w = 20 µm, 40 µm, 60 µm and 90 µm) proportional to the arrangement order. This presentation arrangement was helpful in identifying the individual responses from each STE and the timeshift of t= 33 ps between STEs.

The 1000 configuration gave a single pulse. The pulse from the second STE was determined from the response of the $1\bar{1}00$ and $0\bar{1}0\bar{1}$ configurations with a large negative pulse dip appearing after t = 33 ps of the first peak. Thus, the actual signal velocity through the transmission line was given by $v = {}^{l}/_{t} = 0.4 \times 3 \times 10^{8}$ m/s (velocity of light in vacuum), considering the relative path length of l = 4030 µm between the STEs. However, it should be noted that the dips from the first and the second STEs also had a time delay of about 20 ps. The pulse from the third STE was observed for the $1\bar{1}10$ and 1010 configurations with a peak appearing about 66 ps after the first peak. Similarly, the final STE pulse was observed in $0\bar{1}0\bar{1}$ configuration about 99 ps after observation of the first peak. Although the pulses from the third and the fourth STEs were very low, they could be clearly distinguished using these configurations. As a result, the complete shape was given by the $1\bar{1}1\bar{1}$ configuration with sequential pulses. In addition, the 1010 and $0\bar{1}0\bar{1}$ configurations showed an increase in amplitudes of the third and fourth STE pulses and a decrease in amplitude of the first STE pulse owing to their relative sizes.

The variation in the total current response due to changes in the amplitude of individual pulses was quite clear. However, this effect was very small since the design led to significant crosstalk between the parallel levels of the transmission line. The effects of the crosstalk were also visible from the PSD of the signal (see figure 6.6 (a)). Due to the limitation of the sampling resolution, the frequency characteristics had to be observed within 50 GHz. The device corresponding to the 1000 configuration showed a plateau, as a single pulse spanned the sampling frequency. Similar features were observed for the 1010 configuration and, to some extent, for the $0\bar{1}0\bar{1}$ configuration. The PSD for the $1\bar{1}00$ and $1\bar{1}1\bar{1}$ configurations reflected the bandwidth central frequency f_c of 15 GHz, which corresponded to the relative path length between the STEs. It should be noted that the sidebands in this case corresponded to the timeshift between the individual pulses.

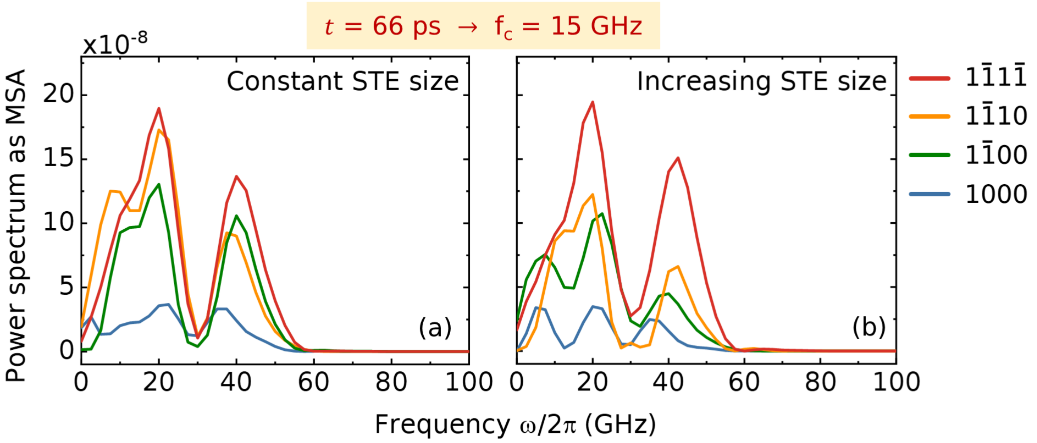

Figure 6.6: PSD for the electrical responses (see figure 6.5) from different STE configurations with STE size (a) equal and (b) varying across the arrangement. The central frequency was f_c = 15 GHz. Here t= 66 ps corresponded to the time period between two alternate STEs.

Typically, the Gain (Q-factor) is determined using $= f_c/\Delta f$ [192, 193] of the signal where f_c is the central frequency and Δf is the bandwidth. Hence, a broader bandwidth can be achieved for a lower Gain and a narrower bandwidth for a higher Gain. Considering the $1\bar{1}1\bar{1}$ configuration, larger amplitudes were obtained for the PSDs. Hence, a device with a series of $1\bar{1}$ STE configurations could be used to obtain more power and a better Gain, thus obtaining a narrowband emission. A similar trend could also be observed in the devices with increasing STE size. (see figure 6.6 (b))

6.1.3 Pulse burst from coplanar waveguide

In the next step, the Pulse Burst Emitter was optimised in order to reduce the crosstalk and the path length in order to align the positive pulse with the inverted pulse from the subsequent STEs about 20 ps apart, thus forming a periodic temporal shape. Hence, a meander-shaped Coplanar Waveguide (CPW) was fabricated (see section 3.4.1) with STEs placed centrally on the signal line (see section 3.4.2), with a square shape of 25 µm side length and ground lines twice as wide (see figure 6.7 (a)). The STEs were equally spaced with a path length l = 2160 µm corresponding to 18 ps, calculated by considering the velocity of the signal $v = {}^{l}\!/_{t} = 0.4 \times 3 \times 10^8\,\mathrm{m/s}$ through the transmission line. A larger incident laser spot of diameter D of 900 µm FWHM of the intensity was used with a pulse energy of 6 µJ and $\bar{\mathrm{P}}$ = 600 mW, resulting in fluence F = 1.89 mJ/cm^2 (see section 3.6.2).

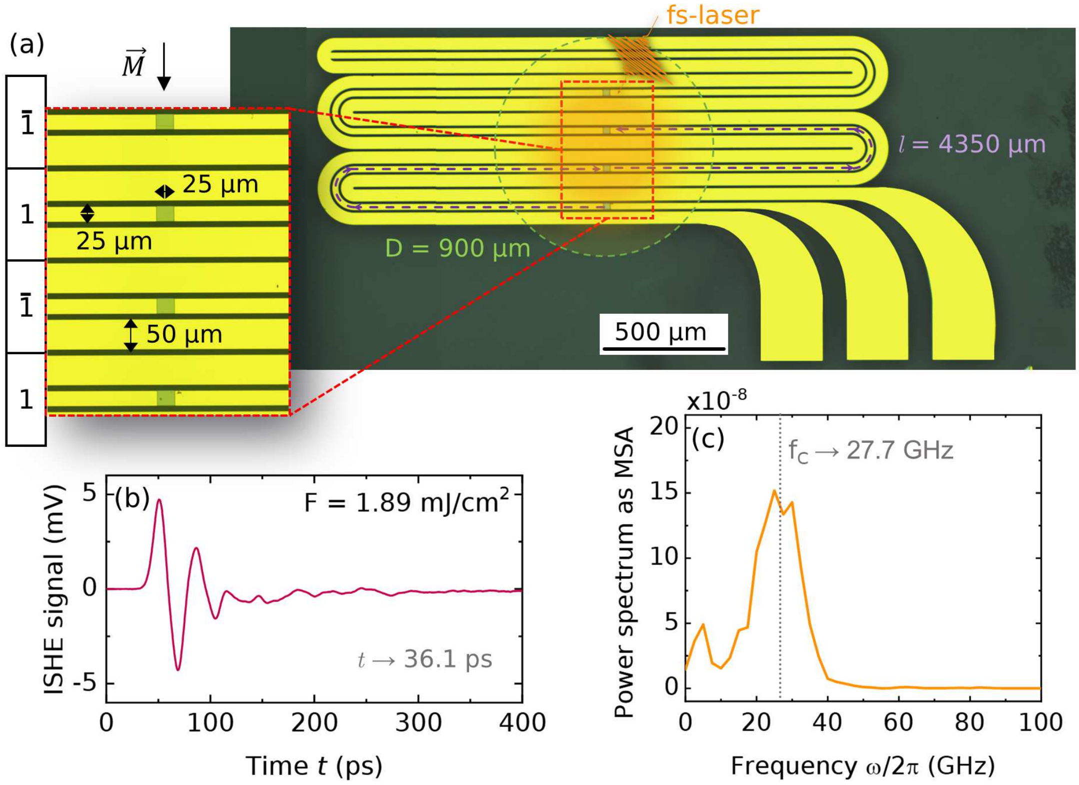

Figure 6.7: (a) Optical microscope image of STEs on a meander-shaped CPW with l= 4350 µm and the (b) electrical response upon simultaneous illumination of STEs by femtosecond laser with t= 36.1 ps and its (c) PSD with f$_c$ = 27.7 GHz. The circular area on the CPW-Pulse Burst Emitter represents approximate FWHM of the laser spot-size D = 900 µm.

The electrical response was obtained upon simultaneous illumination of STEs, forming a $1\bar{1}1\bar{1}$ STE configuration, with a fs-laser pulse. This resulted in a lower amplitude of output signal than obtained in the previous section. The peaks and dips corresponding to the emission of each STE were clearly observed at the desired relative time duration (see figure 6.7 (b)). There was an overall reduction in the peak amplitude owing to the reduced incident light intensity but with more uniform illumination of the STEs compared to the earlier measurements. Moreover, the large oscillations due to crosstalk were significantly reduced owing to the waveguide structure. However, the peak amplitudes decreased with increasing delay path from the STEs due to the dissipation of power along the transmission line. The PSD showed a narrowband feature with the driving central frequency at $f_c = 26$ GHz (see figure 6.7 (c)). The peak spectral amplitude increased owing to a periodic temporal profile of the pulse burst. The f_c being at 26 GHz corresponded well to the pulse duration determined by the path difference between the alternate STEs.

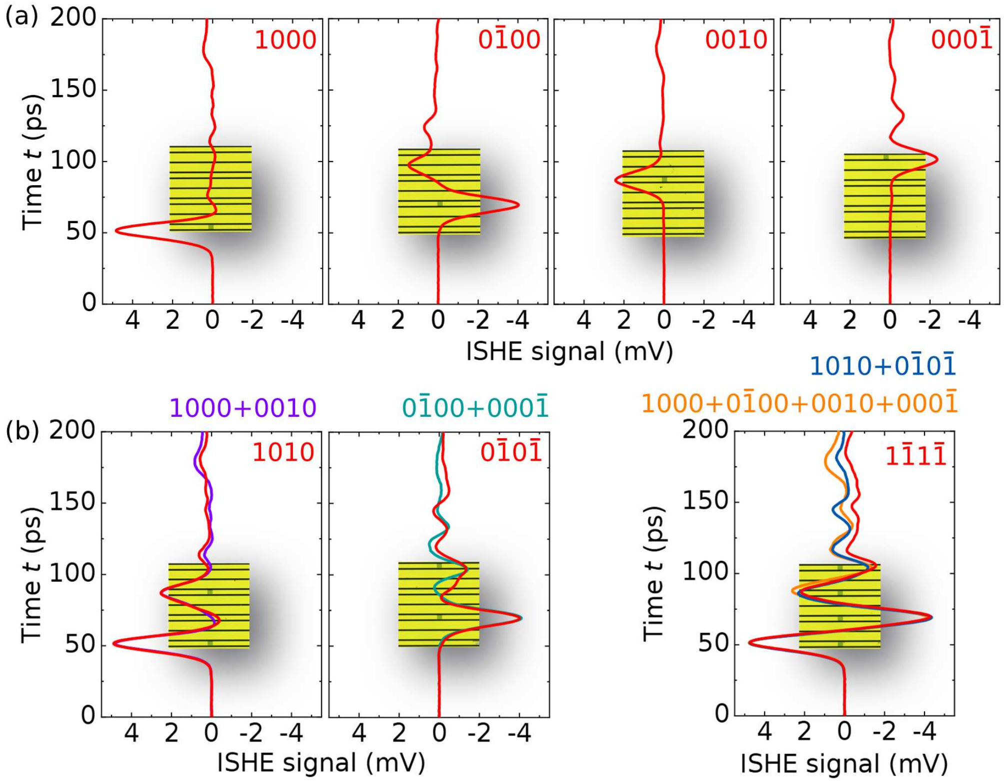

Figure 6.8: (a) Electrical responses from CPW-Pulse Burst Emitter for STEs at different positions and (b) for different combinations of STEs and comparison with signal addition of corresponding individual STE responses. The STE positions and the combinations are shown in the underlying optical microscope images.

In this work the timeshift in the amplitude peak due to the waveguide path was verified by STEs positioned at different equally spaced waveguide locations (see figure 6.8 (a)) as observed from their electrical responses. These were defined as having the elementary configurations 1000, $0\bar{1}00$, 0010 and $000\bar{1}$. It was observed that the electrical pulse appeared at exactly equal delay time corresponding to their positions, and the peak amplitude gradually decreased with position. Multiple STEs in the coplanar waveguide also represented the pulse peaks corresponding to each STE as seen from 1010, $0\bar{1}0\bar{1}$ and $1\bar{1}1\bar{1}$ configurations (see figure 6.8 (b)). In addition, the electrical responses followed superposition where the electrical response from the combination of STEs at different delay paths were equivalent to the superposition of electrical responses from the isolated STEs. For instance, adding the electrical responses of the 1000 and 0010 configurations was the same as the electrical response of the 1010 configuration. Similarly, the combination of the $0\bar{1}00$ and $000\bar{1}$ configurations gave the same output as that of $0\bar{1}0\bar{1}$ configuration. The $1\bar{1}1\bar{1}$ configuration signal was equivalent to the combination of 1010 and $0\bar{1}0\bar{1}$ configurations and also the combination of the four elementary configurations, 1000, $0\bar{1}00$, 0010 and $000\bar{1}$.

6.1.4 Frequency selectivity for narrowband emission

The central driving frequency $\mathrm{f_c}$ is determined by the time period t of the signal. It was also shown earlier that the temporal pulse position corresponding to individual STE was proportional to the path length l. As a result, $\mathrm{f_c}$ is proportional to $1/l$. Hence, the meander-shaped CPW-Pulse Burst Emitter was modified to modulate the driving frequency by reducing the inter-STE path length l to 2654 µm (see figure 6.9 (a)). The number of STEs were increased to 8 in order to increase the gain, and at the same time, the STE size was increased to 100 µm × 25 µm. The STEs were illuminated by fs-laser pulses with FWHM of the spot size 500 µm and a fluence of 3 mJ/cm^2. The time domain electrical signal was obtained which showed multiple peaks and dips corresponding to the STEs with a time period $t = 22$ ps, obtained for peaks corresponding to alternate STEs (see figure 6.9 (b)). It should be noted that the response corresponding to the STEs further along the transmission line showed decreased signals due to the dissipation of power in the transmission line. The PSD showed a $\mathrm{f_c}$ of 45 GHz corresponding to l= 2654 µm (see figure 6.9 (c)). Although the bandwidth was limited the gain was not significant.

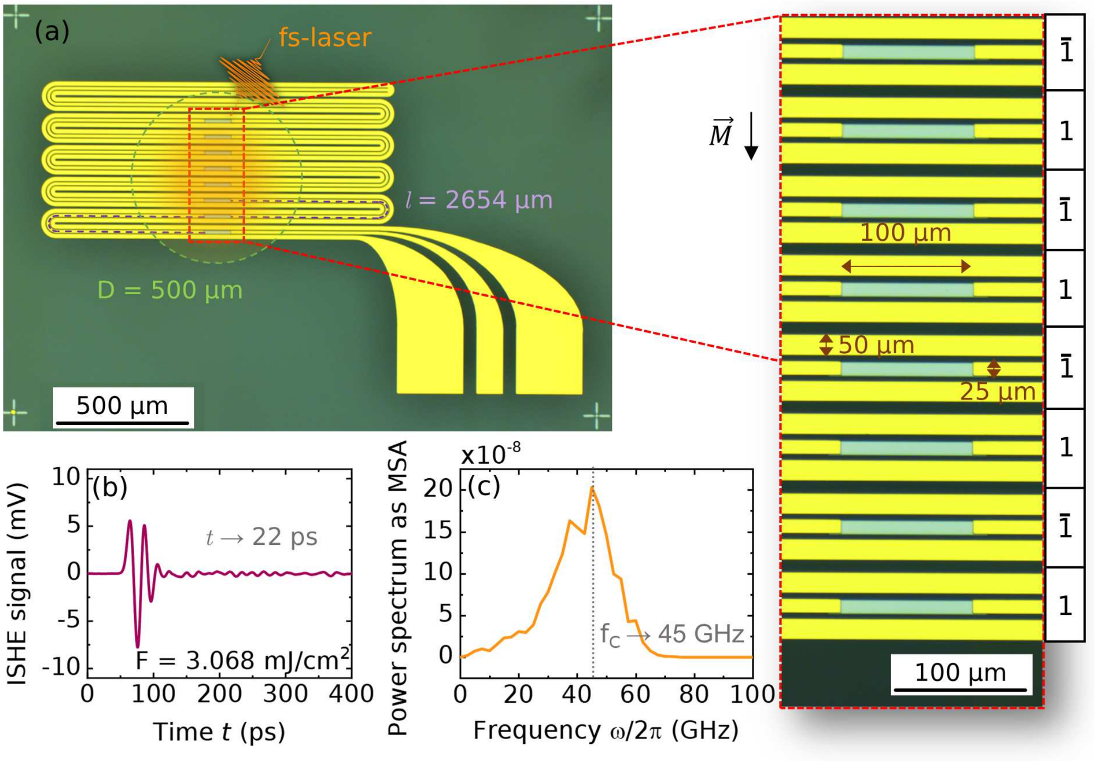

Figure 6.9: (a) Optical microscope image of STEs on a CPW-Pulse Burst Emitter with l= 2654 µm and the (b) electrical response upon simultaneous illumination of STEs by femtosecond laser with t= 22 ps and its (c) PSD with f_c = 45 GHz. The circular area on the CPW-Pulse Burst Emitter represents approximate FWHM of the laser spot-size D = 500 µm.

6.1.5 Optimisation for high Q-factor of narrowband spectrum

To improve the gain for the narrowband emission, the number of temporal pulses was increased in addition to being periodic in shape. For this the number of the STEs was increased. Additionally, it was observed that the emissions of the STEs lying further along the transmission line undergo greater loss through transmission. Hence, these STEs can be increased in size to have increased amplitude for their respective pulses in order to compensate for the transmission loss.

With the modified parameters, the CPW-Pulse Burst Emitter was fabricated (see section 3.4.1 & 3.4.2) with 20 STEs. Additionally, the size of the STEs increased from 40 µm to 420 µm in length, but with a constant width of 25 µm. The l between the alternate STEs was 4000 µm (see figure 6.10 (a)). Upon illumination with a fs-laser pulse of spot size with

FWHM diameter of 1616 µm and a fluence of ~ 1 mJ/cm^2, a pulse burst comprising of 20 electrical pulses from the STEs was observed (see section 3.6.2). The t was 33 ps which corresponded to the l between the alternate STEs. Finally, the PSD showed a sharp peak at f_c = 30 GHz, which was in accordance with the t and l (see figure 6.9 (b)). Moreover, from the PSD a gain of 6.38 was achieved with a narrowband emission of bandwidth Δf = 4.7 GHz.

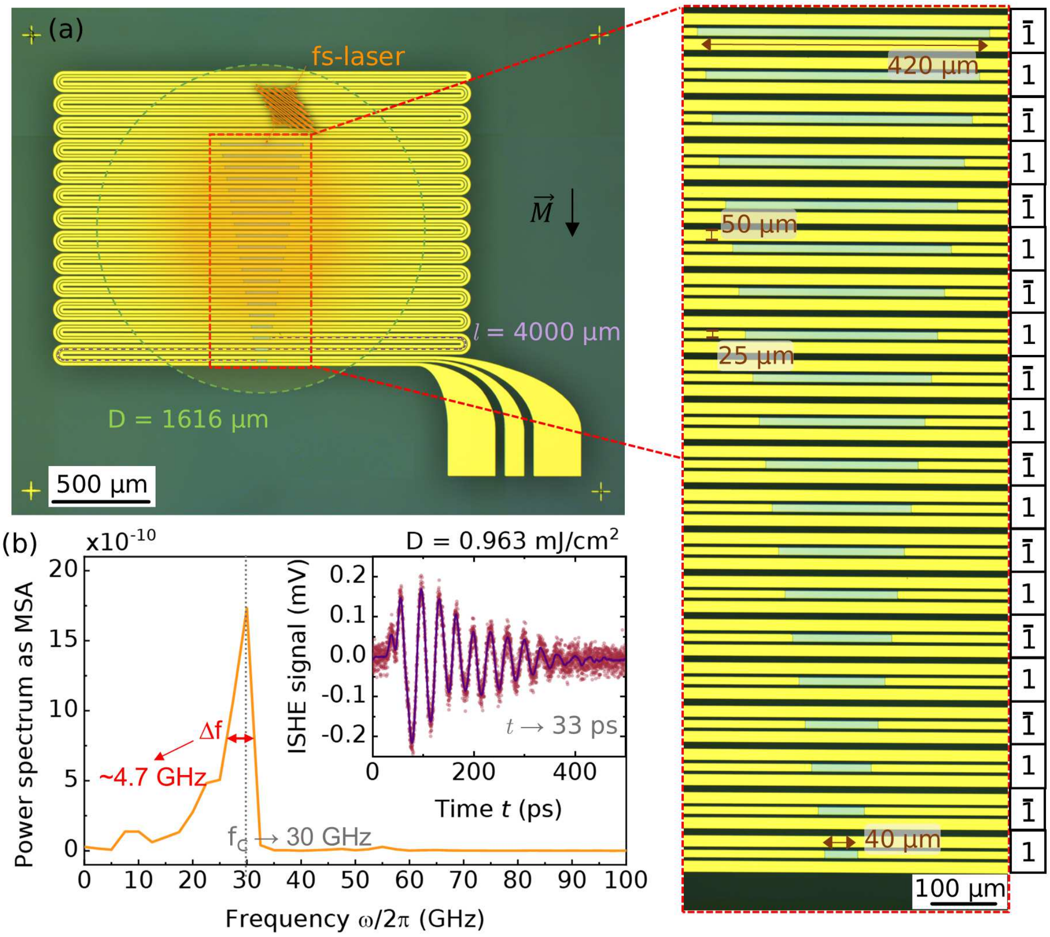

Figure 6.10: (a) Optical microscope image of STEs on a CPW-Pulse Burst Emitter with l= 4000 µm and (b) the electrical response upon simultaneous illumination of STEs by femtosecond laser pulse. The enlarged image shows the STEs with increasing size from the bottom to top. The PSD with f_c = 30 GHz and $\Delta f \simeq$ 4.7 GHz obtained from the temporal electrical response with t= 33 ps which is shown in the inset. The circular area on the CPW-Pulse Burst Emitter represents approximately the FWHM of the laser spot-size D = 1616 µm.

6.2 Digital to Analog Converter for ultrafast signals

For a device involving multiple STEs, the influence of the inter-STE path length along the transmission line and size in terms of electrical response and pulse shaping is discussed above. Another factor which can be used to modulate the electrical response is the individual control of the magnetisation $\vec{M}$ direction of the STEs. This method of control can lead to many applications, for instance a DAC can be designed which has THz bandwidth owing to the STEs being the building blocks.

As discussed in previous chapters, the THz response, or the ultrafast electrical response, are dependent on the $\vec{M}$ which is controlled via an external magnetic field $\vec{H}$. Owing to the magnetic behaviour of the FM involved in the STEs, the polarity of the response changes when the direction of $\vec{M}$ flips as the coercive field H_C is overcome by the applied $\vec{H}$. Hence, the typical scheme to achieve separate switching of the STEs was by having FMs of different H_C. Alternatively, this can also be achieved by varying domain wall nucleation energy (see chapter 2) via manipulation of geometry such as in the case of nanostripes (see figure 6.11).

6.2.1 Experimental details

A trilayer stack of Ta(20 nm)/$Co_{20}Fe_{60}B_{20}$(5 nm)/Pt(5 nm) was deposited using DC magnetron sputtering in an argon atmosphere at a base pressure of 5×10^{-8} mbar on Glass substrate. The Ta layer was deposited on the substrate as a seeding layer in addition to its function as a conducting layer for current transmission across the STE stripes. Moreover, its negative spin hall angle θ_{SH} (see section 2.1) ensured a net charge current induced in the same direction as the one induced due to ISHE in Pt with a positive θ_{SH}. The trilayer was nanopatterned into STE stripes (see figures 6.11 and 6.12 (a)) of various widths of w = 200 nm, 300 nm, 400 nm, 500 nm, 600 nm, 1 µm, 5 µm, 10 µm, 20 µm and 50 µm.. There was also a 2 µm gap between the stripes created by e-beam lithography to obtain a very nice resolution of the structures [194] and subsequent Ar-ion milling down to the Ta layer with AlO_x as the etching mask (see section 3.4.2). The total surface area of the STE stripes was kept constant with respect to the 20 µm stripe by taking multiple stripes of similar width. This was done to achieve the generation of electrical responses of equivalent amplitude. The contact pads were nanopatterned by e-beam lithography and via liftoff (see section 3.4.1), a subsequent e-beam evaporation of Ti(10 nm)/Au(150 nm) at a base pressure of 5×10^{-7} mbar.

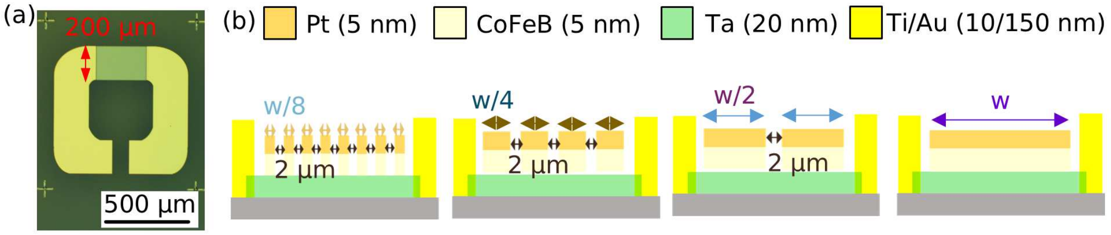

Figure 6.11: (a) Optical microscope image of the device containing STE stripes of width 'w' and length 200 µm. (b) The STE layer stack was Ta(20 nm)/$Co_{20}Fe_{60}B_{20}$(5 nm)/Pt(5 nm) on glass substrate. The spacing between the STE stripes was 2 µm and the extended contact pads were Ti(10 nm)/Au(150 nm).

The device was excited using linearly polarised laser pulses with normal incidence on the surface from an amplified Yb:KGW femtosecond laser with 99.6 kHz repetition rate, a wavelength of 1030 nm and a pulse duration of 300 fs. The response was detected using a 50 GHz bandwidth sampling oscilloscope (see section 3.6.2). The laser spot size with FWHM of 500 µm led to a fluence F = 4.1 mJ/cm^2 on the STE stripes which resulted in prominent ultrafast electrical responses (see figure 6.12 (b)). The shape of the response pulse was same for all the STE stripes as obtained for a 20 µm STE stripe due to the physical normalisation based on 20 µm surface area which is achieved by taking suitable number of stripes for each set of similar stripe widths. The only exception is 50 µm stripe whose amplitude is compared to a single 20 µm stripe by multiplying a factor of 0.4.

6.2.2 Coercive fields of STE stripes

The H_C for a thinfilm STE was 1.45 mT which was determined using MOKE as shown in the hysteresis curve (see figure 6.12 (c)). For the devices with different STE stripes H_C values were determined from the electrical responses by monitoring the external field which led to switching in the device (see section 2.4.2) and it was found that H_C was higher for the STE stripes below 1 µm and exponentially increased for narrower widths (see figure 6.12 (d)). This behaviour can be attributed to the nucleation volume and domain wall propagation for the stripes of different widths [71, 195–199]. The minimisation of the magnetostatic energy (see section 2.4.3) dictates the magnetisation reversal process initiation only through the domain formation at the edges due to the additional stray fields or around the defects without affecting the surface magnetic charges. As a result effective nucleation area is of the order of the width of the stripe and the domain wall nucleation energy is more for narrower stripes leading to higher H_C. Hence, STEs with different H_C values were obtained which emit electrical responses in ultrafast timescales.

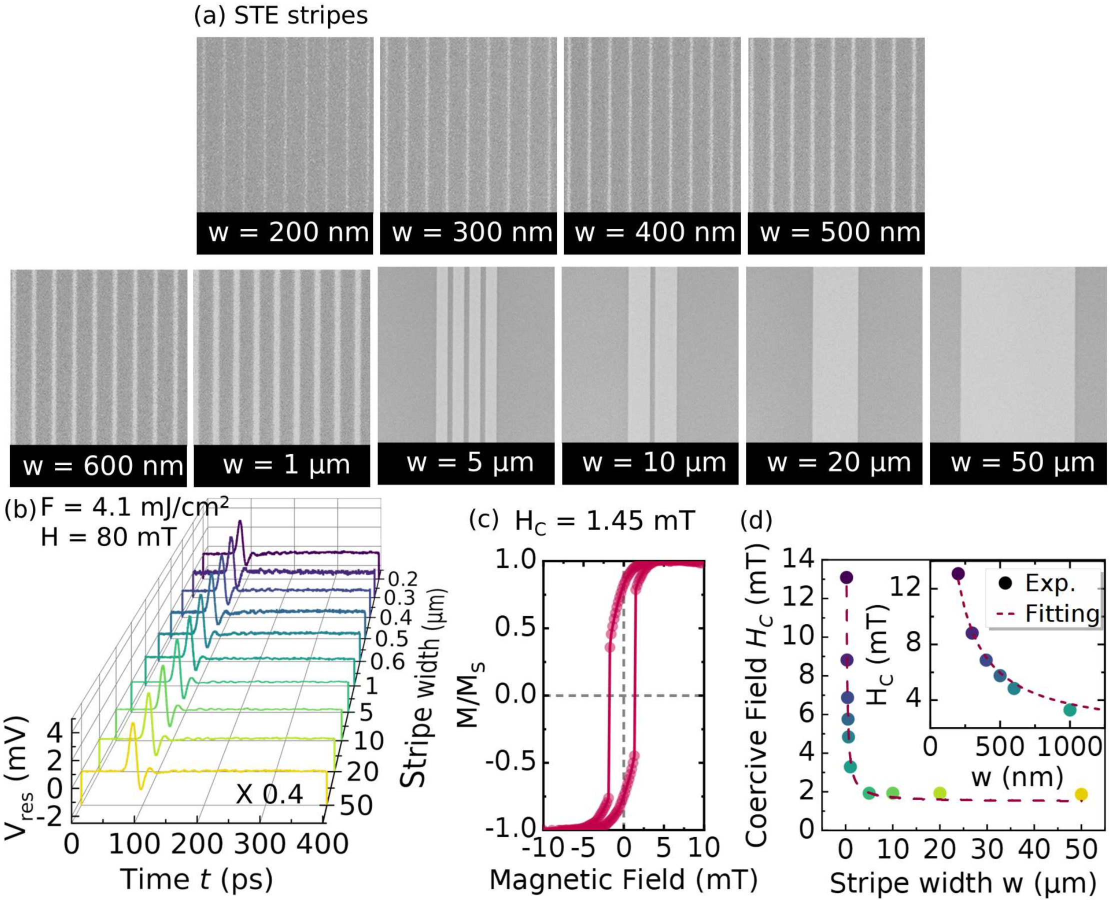

Figure 6.12: (a) Optical microscope images for the nanopatterned STE stripes with the widths w = 200 nm, 300 nm, 400 nm, 500 nm, 600 nm, 1 µm, 5 µm, 10 µm, 20 µm and 50 µm. The number of stripes of each widths were determined w.r.t 20 µm stripe surface area. (b) Ultrafast electrical responses, from the STE stripes upon excitation by fs-laser pulse with fluence F = 4.1 mJ/cm^2 at external B field of 80 mT, showing similar output due to the equivalent STE surface area. Coercive fields for STE (c) thin film and (d) stripes for respective widths. The dotted red line is the fitting with inverse proportionality to w. The inset is the zoomed plot for the STE stripes with smaller widths.

In magnetostatic terms, the H_C can be fitted with respect to a first order approximation [196] to 1/w as,

$$H_C(\mathrm{w}) = H_\infty + \frac{\beta}{\mathrm{w}} \tag{6.1}$$

where H_∞ and β are free fitting parameters. Here, H_∞ signifies the coercive field for infinitely wide stripe, which is a thin film. The equation nicely fit the coercive field values for stripes with different widths (see figure 6.12 (c)) and the fitting produced H_∞= 1.51 mT which was in accordance with the H_c= 1.45 mT determined earlier using MOKE for the thin film layer stack of Ta(20 nm)/$Co_{20}Fe_{60}B_{20}$(5 nm)/Pt(5 nm).

6.2.3 4-bit DAC with STE stripes

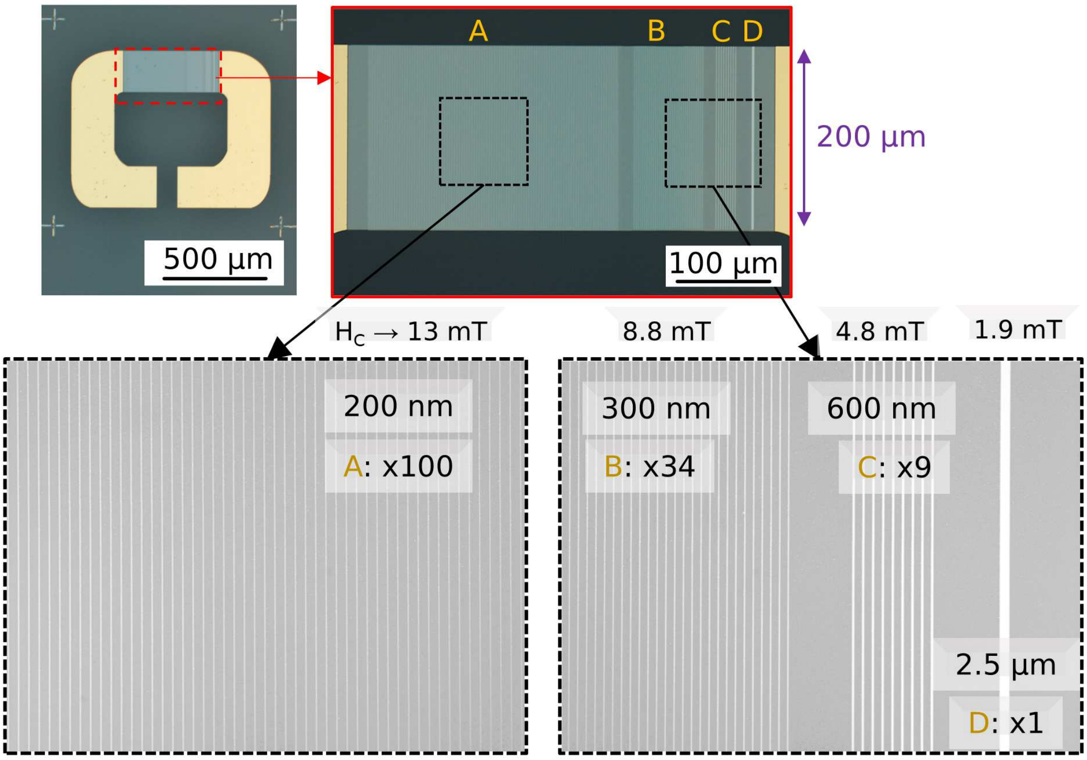

Figure 6.13: Optical microscope image showing combination of STE stripes with 4 different stripe widths w = 200 nm, 300 nm, 600 nm and 2.5 µm making it a 4-bit device. The number of stripes with the same widths was chosen to obtain the response from 4-bits (A B C D) in the ratio $2^3 : 2^2 : 2^1 : 2^0$ which is 8 : 4 : 2 : 1.

In accordance with the electrical responses and the coercive fields of different STE stripes, a 4-bit DAC device was designed by selecting STE stripes of widths 200 nm, 300 nm, 600 nmand 2.5 μm with H_C values of 13 mT, 8.8 mT, 4.8 mT and 1.9 mT, respectively. The responses from the bits were controlled by varying the number of STE stripe forming each type of bit in order to obtain the ratio of $2^3 : 2^2 : 2^1 : 2^0$ which is $8 : 4 : 2 : 1$. The ratio was determined to be this as each bit can have 2 states, which are + and −, owing to the magnetisation states. In addition, the 4 bits were distinguished by the states of the bits as 2^3, 2^2, 2^1 and 2^0. Hence, 100 stripes of 200 nm, 34 stripes of 300 nm, 9 stripes of 600 nm and one stripe of 2.5 µm were used which lead to a ratio of $8 : 4 : 2 : 1$ in terms of surface areas (see figure 6.13).

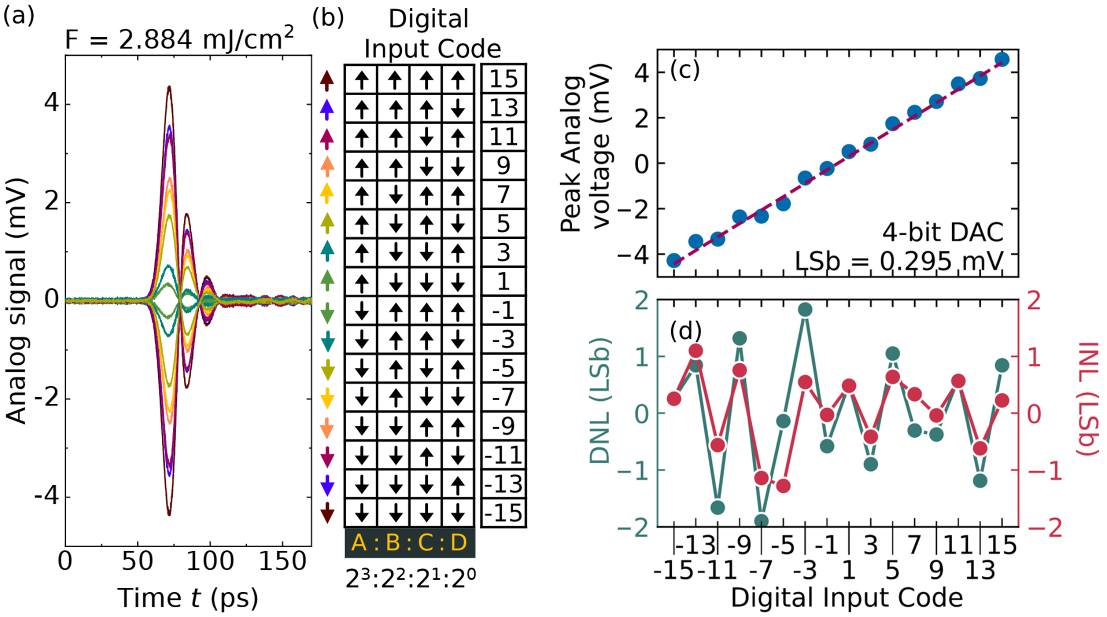

Figure 6.14: (a) Ultrafast electrical responses from 4-bit THz DAC device upon excitation by fs-laser pulse with a fluence F = 2.884 mJ/cm^2. (b) Different configurations of the bits in the device and their corresponding digital codes which take into account the electrical response ratio from each individual bit. (c) The peak electrical responses from different configurations corresponding to the positive digital codes with Least Significant bit (LSb)= 0.295 mV. The red dotted line shows the ideal response as corresponding to the LSb. (d) The Differential Non-Linearity (DNL) and the Integral Non-Linearity (INL) for the device corresponding to different Digital Code Inputs.

The excitation of the 4-bit THz DAC device by fs-laser pulses with a fluence F = 2.884 mJ/cm^2 led to an ISHE (see section 2.6) electrical response with a peak voltage of 4.5 mV (see figure 6.14 (a)). The magnetisation states of all the bits were in the same direction. Hence, the output was assigned as the analog output corresponding to the digital code of 15, which was the result of the sum of all values of each bit, i.e. $8 + 4 + 2 + 1$ or $2^3 + 2^2 + 2^1 + 2^0$. After this the $\vec{H}$ was driven to the H_C in the opposite quadrant corresponding to the lowest bit. This switched the bit and the final digital output was $2^3 + 2^2 + 2^1 - 2^0 = 8 + 4 + 2 - 1 = 13$. The ISHE electrical response was similar to the previous state with a decreased peak amplitude of 4 mV. Subsequently, other configurations were achieved by driving to the respective H_C by following major loops or minor loops (see section 2.4.2) when required (see figure 6.14 (b)). The respective digital codes were obtained, and subsequently, this led to different ISHE electrical responses (see figure 6.14 (a)). A digital input in terms of the magnetisation states of the bits led to a specific analog ultrafast response where the analog outputs of the configuration of the bits were their corresponding peak voltages. It should be noted that the magnetisation switching driven by external magnetic field was slow. However, the DAC has a large driving bandwidth. Based on the analog outputs the LSb of the device was calculated as 0.295 mV (see figure 6.14 (c)).

It is quite evident that the analog outputs that were measured were not ideal as they can be seen deviating from the ideal outputs derived from the LSb, which is also shown as the red dotted line in the plot (see figure 6.14 (c)). These deviations or non-linearities are the important metrics relevant to the device since these cannot be eliminated by calibration and are the characteristics of the device. The deviation can be either expressed as the deviation from the ideal output step size, which is referred to as DNL, or by accounting for the maximum deviation from the ideal slope, referred to as INL (see appendix A.6). INL can be understood as the cumulative effect of DNL. Both the DNL and INL have been obtained for the device (see figure 6.14 (d)). The deviations were expressed in terms of counts and, as can be seen, they both lied in the range of −2 to +2.

6.2.4 3-bit DAC with STEs of different FMs

As an alternative approach a THz DAC was also designed by taking FMs with different H_C values (see section 2.4.2) as the STE bits required for the DAC. A 3-bit DAC was designed with 3 different STEs with a layer stack of FM(10 nm)/Pt(3 nm). For this the FMs were $Co_{20}Fe_{60}B_{20}$, $Ni_{80}Fe_{20}$ or $Co_{50}Fe_{50}$ with H_C values of 1.65 mT, 0.75 mT and 10 mT, respectively. Each layer stack was nanopatterned using e-beam lithography over a MgO(100) substrate, followed by the DC-Magnetron sputtering of layer stacks and liftoff (see section 3.4.1). The choice of substrate was made due to the favourable growth of *bcc*-structured Co-Fe alloys on the MgO which also has cubic crystal structure in the 100 crystal direction. Finally, the contact pads were nanopatterned using e-beam lithography followed by e-beam evaporation of Ti(10 nm)/Au(150 nm) and liftoff (see section 3.4.1). The structures of the FMs were taken to be of equal length of 200 µm and the widths w were optimised for different

FMs based on the electrical response with w = 65 µm, 70 µm and 50 µm for $Co_{20}Fe_{60}B_{20}$, $Ni_{80}Fe_{20}$ and $Co_{50}Fe_{50}$, respectively. This led to a ratio of $4:2:1 = 2^2:2^1:2^1$ for the bits (see figure 6.15 (a)).

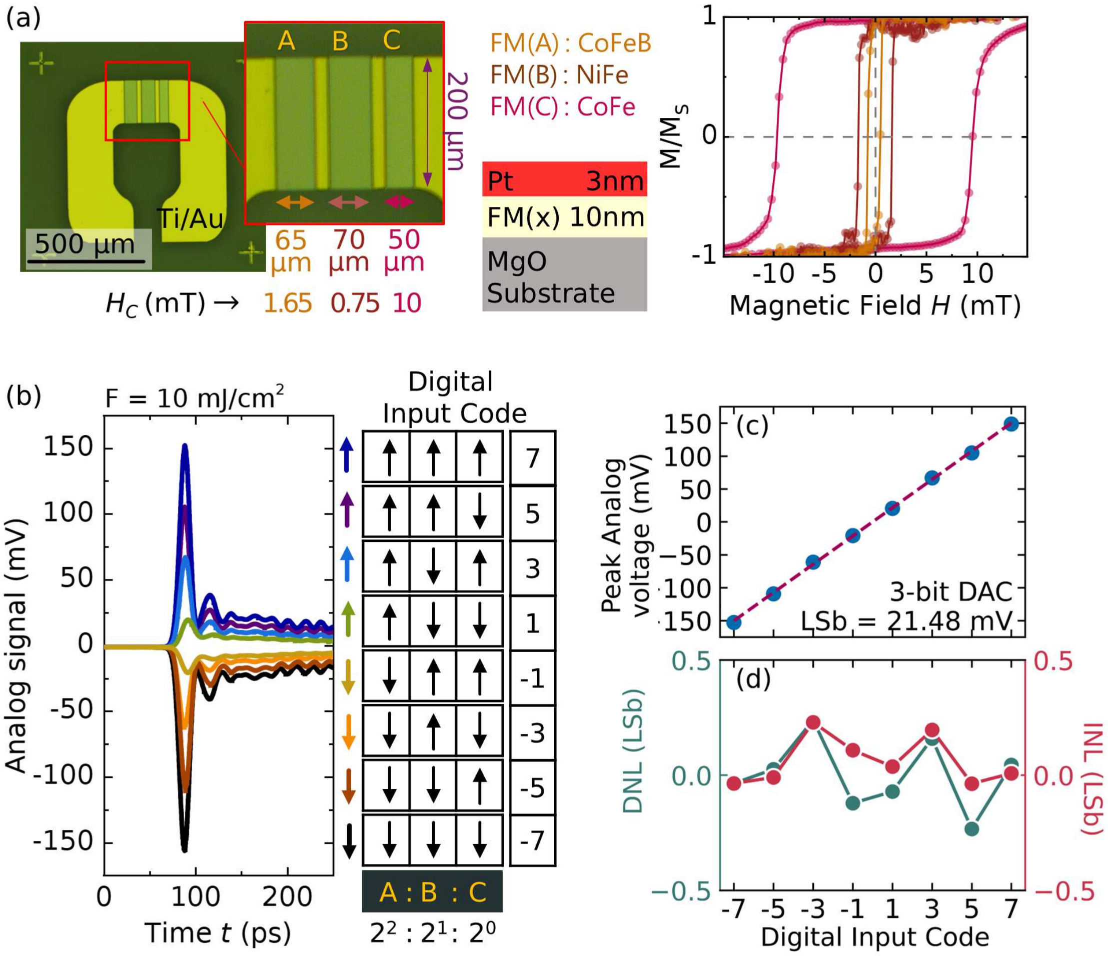

Figure 6.15: (a) Optical microscope image for a 3-bit DAC device with different FMs for different bits used in the layer stack FM(10 nm)/Pt(3 nm) on a MgO substrate. The FMs have different H_C values determined from MOKE measurements of respective thinfilms. The lengths of the bits were 200 µm and the widths of each individual bits were decided after optimisation to obtain an electrical response in the ratio $2^2 : 2^1 : 2^0$ which is $4 : 2 : 1$. (b) Ultrafast electrical response for different 3-bit configurations upon excitation by fs-laser pulses with fluence $F = 10\,\mathrm{mJ/cm^2}$. (c) The peak voltage (Analog Voltage) for different configurations (Digital Code Input). The dotted line represents the ideal output voltage for different input codes. The LSb for the device was 21.48 mV. (d) The non-linearities (DNL and INL) for different configurations (Digital Code Input).

Upon excitation by fs-laser pulses with a fluence of F = 10 mJ/cm^2 and with the magnetisation of all the bits along the same direction (see section 3.6.2), an ultrafast electrical response was obtained with a peak voltage of 150 mV. This corresponded to the digital code of 7. In the same way, all the configurations were obtained by driving the external field to different H_C values of the FMs following major and minor loops (see figure 6.15 (b)). The ISHE peak voltage (analog output), followed the same ratio as the different digital codes. The LSb=21.8 mV was obtained (see figure 6.15 (c)) and the DNL and INL were calculated from the deviation compared to ideal output voltage (see figure 6.15 (d)). It should be noted that the deviation was less compared to the 4-bit DAC discussed earlier due to very high output voltage and lesser number of bits.

6.3 Ultrafast current control by Oersted fields

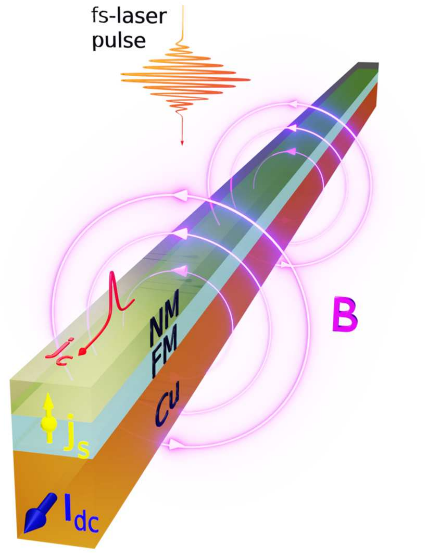

Figure 6.16: Illustration showing Oersted Field across an STE stripe induced by in-situ Cu wire underneath when a dc-current (I_{dc}) was applied through the stripe.

It is quite evident from above that ultrafast spintronic devices can be designed with multiple STEs as the core element based on their H_C values and the time delay between the signals from the STEs. The working principle of an STE is dependent on the direction of the external magnetic flux density, $\vec{B}_{\mathrm{external}}$. It is also possible to modulate the cluster of STEs in a single device separately by deriving a locally switchable $\vec{B}$ source through the generation of an Oersted Field by I_{dc} (see section 2.6.3). Subsequently, the STEs, each in the vicinity of such a source, can be modulated separately. In order to achieve this in-situ Cu/STE stripes were deposited (see figure 6.16).

In order to estimate the induced $\vec{B}_0$ due to the Oersted Fields, COMSOL [143] simulations were performed using the 'AC/DC' module for a metal stripe with thickness 50 nm and width of 500 nm. For this the conductivity was taken to be 2.85×10^7 S/m [200] for a Cu stripe. Upon application of dc-current, B surrounding the stripes was calculated to vary with distance from the stripe. For I_{dc}= 5 mA, 10 mA and 20 mA through the Cu stripe, $\vec{B}_0$= 6 mT, 12 mT and 24 mT, respectively, was obtained at a distance of 2.5 nm from the top surface of the Cu stripe where the FM experienced the effective magnetic flux density which was the source of net magnetisation in the FM layer (see figure 6.17).

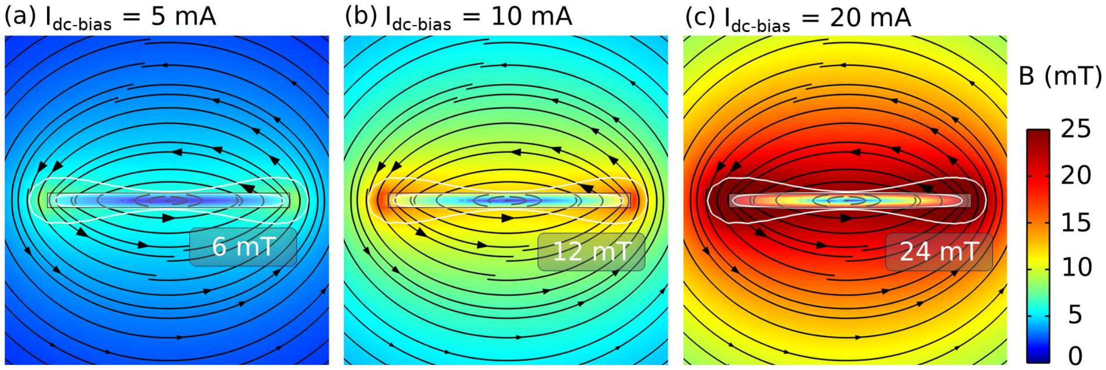

Figure 6.17: COMSOL simulation showing magnetic flux density, B_0 of (a) 6 mT, (b) 12 mT and (c) 24 mT around a stripe of Cu ($\sigma_{\text{Cu}} = 2.85 \times 10^7$ S/m) with dimension 500 nm × 50 nm due to I_{dc}= 5 mA, 10 mA and 20 mA, respectively, at a distance of 2.5 nm from the Cu stripe surface.

6.3.1 Experimental details

The Cu(50 nm)/$Co_{20}Fe_{60}B_{20}$(5 nm)/Pt(5 nm) trilayer was prepared by DC magnetron sputtering in an argon atmosphere at a base pressure of 6×10^{-8} mbar on a Sapphire(0001) substrate. The nanopatterning of 100 µm × 500 nm stripes was done using e-beam lithography and Ar-ion etching against an AlO_x etching mask deposited via e-beam evaporation (see section 3.4.2). Multiple stripes were prepared (see figure 6.18) to increase the total amplitude of the electrical response. In the intermediate step the remaining AlO_x was removed and contact pads were prepared by nanopatterning via e-beam lithography and Ti(10 nm)/Au(150 nm) deposition by e-beam evaporation at a base pressure of 5×10^{-7} mbar, followed by liftoff (see section 3.4.1).

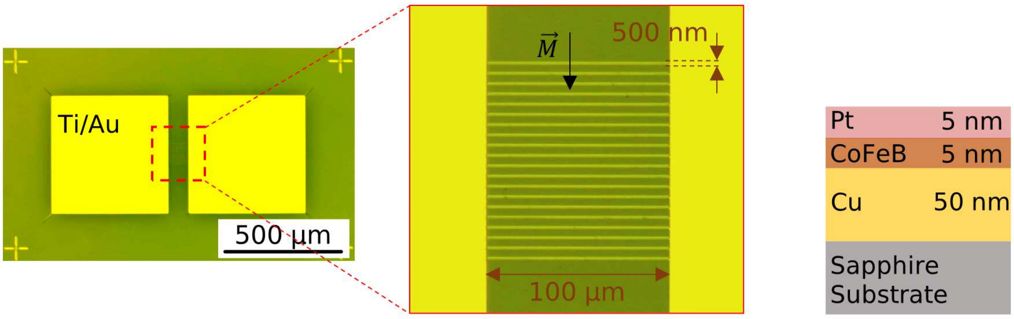

Figure 6.18: Optical microscope image for Cu(50 nm)/$Co_{20}Fe_{60}B_{20}$(5 nm)/Pt(5 nm) stripes of width 500 nm and length 100 µm.

6.3.2 Fluence and magnetisation dependence of Cu/STE stripes

The stripes were excited using normal incident linearly polarised laser pulses from an amplified Yb:KGW femtosecond laser with 99.6 kHz repetition rate, a wavelength of 1030 nm and a pulse duration of 300 fs. In the first step, the magnetisation, $\vec{M}$ was controlled by B_{external}= 70 mT for different laser powers, hence for different fluences. The response was detected using a 50 GHz bandwidth sampling oscilloscope (see section 3.6.2). The $\vec{M}$ was perpendicular to the stripes along the hard axis (see figure 6.19 (a)). The primary source of the output signal was due to ISHE. In second step, the B_{external} was removed and a dc-current, I_{dc}= 5 mA was applied across the stripes for different fluences. The shape of the electrical response was different from the response due to ISHE (see section 2.6). Moreover, the polarity of the electrical response was found to be dependent on the direction of the I_{dc}. It was expected that I_{dc} along the Cu wire would produce B_0 perpendicular to the stripes (see figure 6.19 (b)).

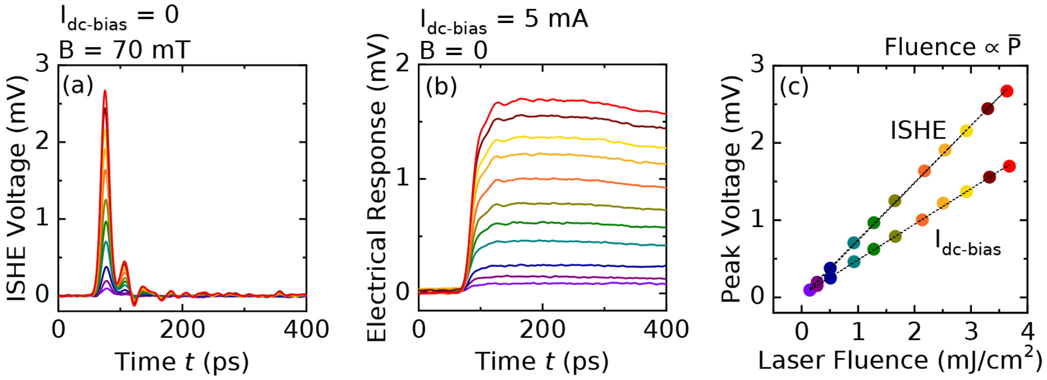

Figure 6.19: Electrical response from the stripes upon fs-laser excitation with contributions primarily due to (a) ISHE for B_{external}= 70 mT, (b) I_{dc}= 5 mA and (c) their laser fluence dependence.

The shape of the obtained electrical response involved a sharp rise followed by a plateau and a slow decay. Moreover, the dependence on fluence of the electrical response originating from the I_{dc} was linear, similar to the electrical response originating via ISHE however, with a different slope (see figure 6.19 (c)). This suggested that the electrical response corresponding to the I_{dc} was due to Joule heating (see section 2.7) which was parasitic with the laser excitation. Hence, a suitable methodology was required to extract the electrical response component generated by Oersted fields.

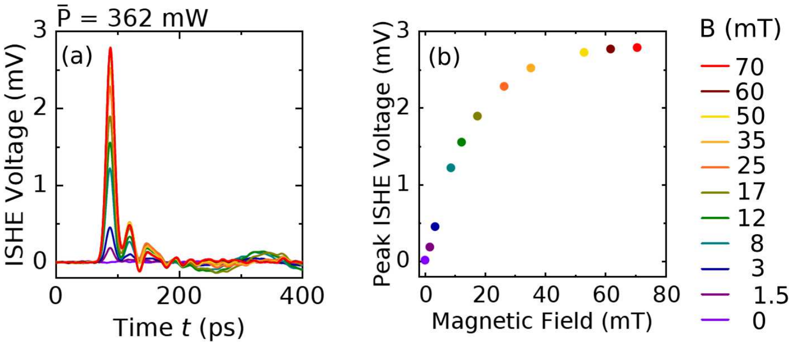

Figure 6.20: (a) Electrical response from the stripes upon fs-laser excitation of Cu/STE for different B_{external} varying from 0 to 70 mT and (b) their corresponding peak voltages.

In addition to the fluence dependence measurement of the device, a magnetisation dependence study was also performed at a constant laser power of P̄= 362 mW, which gave a fluence of F = 3.7 mJ/cm^2. Hence, the electrical response was obtained for different $\vec{B}$ from 0 to 70 mT and the peak ISHE amplitude was observed to increase with increasing $\vec{M}$ as expected (see figure 6.20 (a)). For small magnetic fields, the increase was sharp, but eventually, there was a saturation at fields higher than 40 mT (see figure 6.20 (b)).

6.3.3 Extraction of electrical response contributions

In the next step, the electrical responses were obtained for $\vec{M}$ due to both $\vec{B}_{\text{external}}$ and $\vec{B}_0$. The $\vec{B}_{\text{external}}$ was modulated for both the polarities (see figure 6.21 (a)). Hence, the electrical response due to ISHE corresponding to $\vec{B}_{\text{external}}$ was extracted by taking the subtraction of the signals for $+\vec{B}_{\text{external}}$ and $-\vec{B}_{\text{external}}$ (see figure 6.21 (b)). The rest of the contributions were extracted by the addition of both the signals, which was the result of I_{dc} (see figure 6.21 (c)). Hence this was assumed to be the combination of Joule heating and the contribution due to ISHE for $\vec{B}_0$.

The above dependencies can be clearly observed for the cases when $\vec{B}_{\text{external}}$ = 3.5 mT and I_{dc}= 5 mA, 10 mA or 20 mA (see figure 6.21 (d)). The ISHE contribution due to $\vec{B}_{\text{external}}$ was clearly observed with an equal response for all the three cases and a peak value of 0.25 mV (see figure 6.21 (e)). It should be noted that the electrical response for small magnetic fields showed a prominent secondary peak after 200 ps of the initial ISHE peak. This behaviour was also observed earlier for ISHE signal corresponding to smaller external magnetic fields (see figure 6.20 (a)) however, with smaller amplitude compared to the primary ISHE peak.

Since, an apprecible fraction of magnetic moments can still be expected to be not aligned in the net magnetisation direction determined by the smaller external magnetic fields, this secondary excitation can be an indication of alignment of these magnetic moments driven by spin-polarised current [201]. However, it needs further analysis to confirm the explanation.

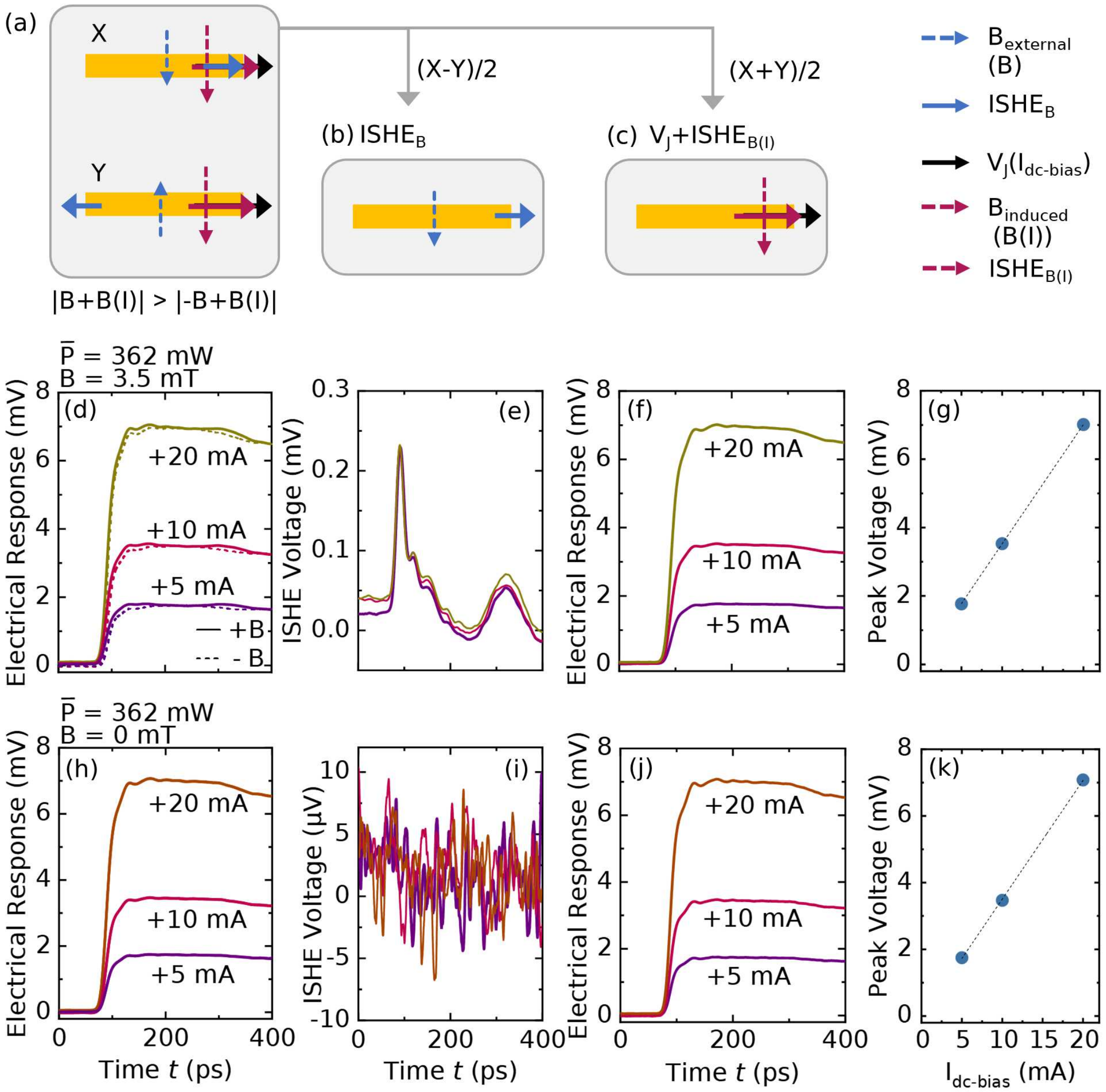

Figure 6.21: (a) Schematics and measurements showing total electrical response from the Cu/STE stripes upon fs-laser excitation with (d) B_{external}= 3.5 mT and (h) 0 mT when I_{dc}= +5 mA, +10 mA and +20 mA. The solid line represents $+B_{\text{external}}$ and dotted line represents $-B_{\text{external}}$. The extracted contribution due to (b, e, i) ISHE and (c, f, j) I_{dc} and the corresponding dependence of peak voltage of the electrical response (g) with and (k) without B_{external} are shown.

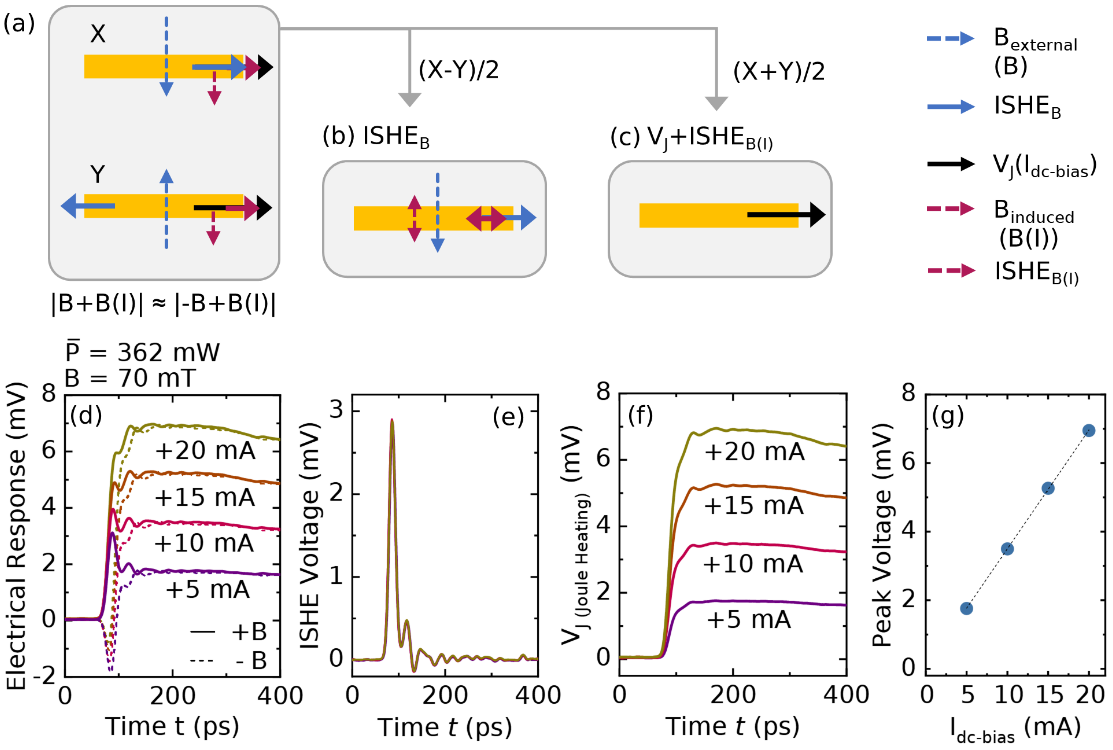

Figure 6.22: (a) Schematics showing electrical reponse upon fs-laser excitation of Cu/STE stripes with B_{external}= 70 mT and I_{dc}= 5 mA, 10 mA and 20 mA and the extraction of the contribution due to (b) ISHE and (c) I_{dc}. The corresponding plots are shown in (d), (e) and (f) respectively. (g) The dependence of peak voltage on I_{dc} is shown.

Further, the contribution due to I_{dc} shows dependencies similar to what would be expected for Joule heating (see figure 6.21 (f)). Additionally, the electrical response when $\vec{B}_{\text{external}} = 0$, did not show an ISHE contribution while the same plots indicated a Joule heating contribution (see figure 6.21 (h, i, j)). It can also be observed that the peak voltages varied proportionally with I_{dc} (see figure 6.21 (g, k)).

It should be noted that for the lowest $\vec{B}_{\text{external}}$ used it was difficult to extract the ISHE contribution of $\vec{B}_0$. This was attributed to the unequal ISHE responses for $(+\vec{B}_{\text{external}} + \vec{B})$ and $(-\vec{B}_{\text{external}} + \vec{B})$ which can be used only to extract the $\vec{B}_{\text{external}}$ contribution. However, driving $\vec{M}$ to saturation was helpful in extracting the total ISHE contribution (see figure 6.22 (a, b, c)). Hence, in the next step, a large $\vec{B}_{\text{external}} = 70\,\text{mT}$ was applied. This ensured that any variation of $\vec{B}_{\text{external}}$ did not affect $\vec{M}$ significantly (see figure 6.22 (d)). The subtraction of the signals for $+\vec{B}_{\text{external}}$ and $-\vec{B}_{\text{external}}$ gave the total ISHE contribution and the addition gave the contribution purely due to Joule heating (see figure 6.22 (e, f)). The response was also linear for different I_{dc} (see figure 6.22 (g)).

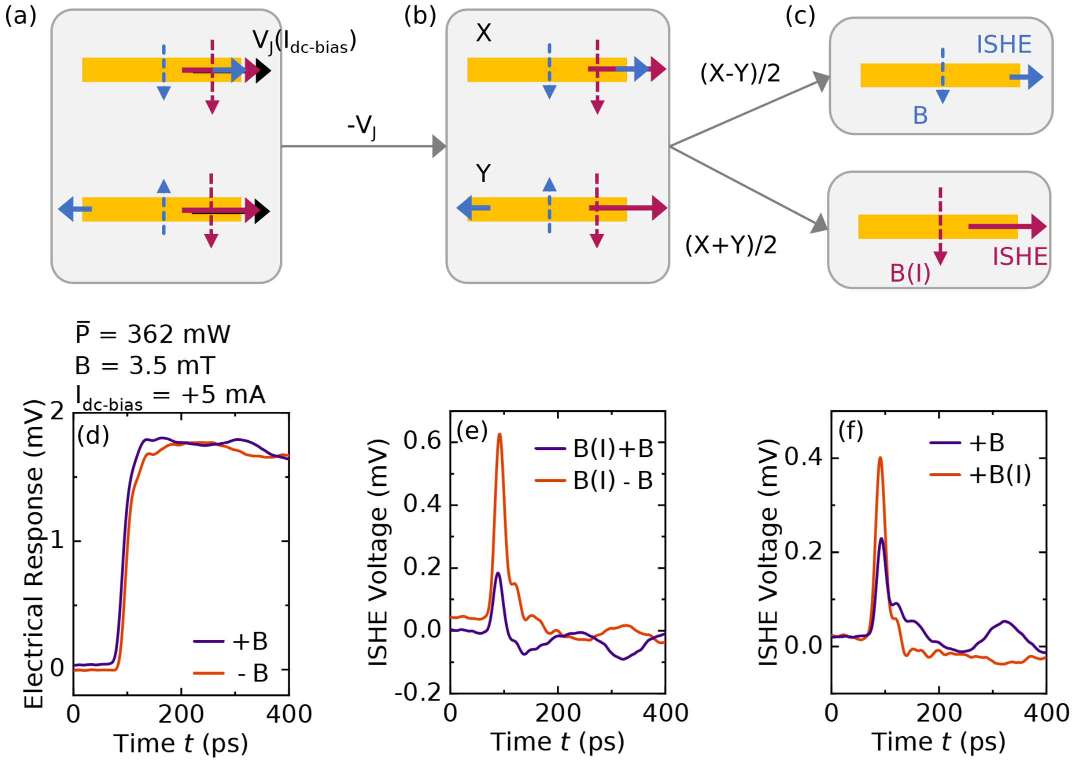

Figure 6.23: Schematics showing (a) electrical response upon fs-laser excitation of Cu/STE stripes with B_{external}= 70 mT and I_{dc}= 5 mA, and (b) the removal of Joule heating contribution and (c) the extraction of individual contribution from ISHE for B_{external} and B_{oersted}. The respective plots are shown in (d), (e) and (f) respectively.

Finally, the electrical response comprised of the contribution for $\vec{B}_0$ for I_{dc}= 5 mA and $\vec{B}_{\text{external}}$ = 3.5 mT was obtained as shown earlier (see figure 6.21 (d)) and the contribution due to Joule heating (see figure 6.22 (f)) was subtracted from it to obtain total ISHE contributions. Eventually, the separate contributions due to $\vec{B}_{\text{external}}$ and $\vec{B}_0$ were obtained (see figure 6.23).

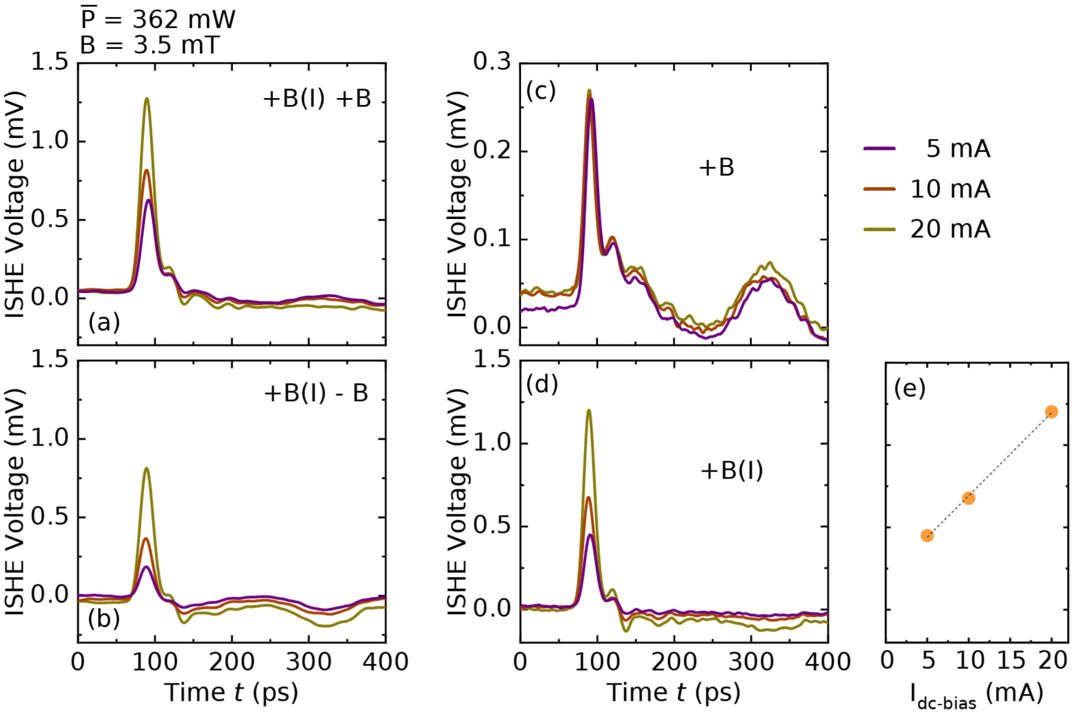

Figure 6.24: The contribution due to ISHE (ISHE(B_{external})+ISHE(I_{dc})) from fs-laser excitation of the Cu/STE stripes for (a) $+B_{\text{external}}$ and (b) $-B_{\text{external}}$, and the extraction of (c) ISHE(B_{external}) and (d) ISHE(I_{dc}) which was due to Oersted field. The dependence of ISHE due to Oersted field with I_{dc}.

Similarly, the ISHE contributions arising from $\vec{B}_0$ for other dc-currents, I_{dc}= 5 mA, 10 mA and 20 mA was obtained using the procedure followed above. The ISHE contributions corresponding to $\vec{B}_{\text{external}}$ = 3.5 mT gave equal responses for all the cases. The peak voltage was 0.26 mV, which was in agreement with the ISHE response obtained earlier (see figure 6.21 (e)). The ISHE contributions due to $\vec{B}_0$ were proportional to I_{dc} with peak voltages of 0.4 mV, 0.7 mV and 1.25 mV corresponding to I_{dc}= 5 mA, 10 mA and 20 mA, respectively. This provided evidence of control of terahertz response both in terms of polarisation and magnitude by an Oersted field generated by applied dc-current.

Conclusion and Outlook

In this work, spintronic devices were designed and realised for applications in ultrafast timescales.

In the first spintronic device an ultrafast electrical pulse burst signal was obtained from simultaneous excitation of a series of STEs along the waveguide. The final response pulse originating from the combination of these pulse bursts was shaped by finding suitable tunable parameters, thus, directly influencing the signal bandwidth. These pulse burst emitters could be manipulated based on the size and path length of the STEs in order to obtain power gain and different driving central frequencies, respectively.

In the second spintronic device, a DAC was realised with ultrafast working frequencies by designing multiple STEs with different Coercive fields and controlling each STE separately.

In the third spintronic device, an alternate method of controlling terahertz response in an STE was realised by locally controlling the magnetisation by Oersted field generated via an in-situ dc-current carrying wire beneath the STEs.

7 THz excitation of magnetic multilayers

While the focus in the previous chapters were on heterostructures containing a single ferromagnetic layer, the magnetisation dynamics in multilayers containing multiple ferromagnetic layers in ultrafast timescales is of relevance especially due to the configurations of currently used Spintronic Devices such as pseudo spin-valves showing Giant Magnetoresistance (GMR). This chapter contains an exploration of the fs-laser interaction with pseudo spin-valve devices via ultrafast electrical measurements. In addition, the effect of laser heating and application of decoupled ferromagnets in multiple ferromagnetic layers were explored and the later was optimised to realise Switchable Terahertz emitters.

Introduction

The fundamental mechanism involved in spintronic devices is based on Spin Transfer Torque (STT) which is used to excite or reverse the magnetisation of a ferromagnet [202], especially in Giant Magnetoresistance (GMR) [3, 4] and Tunneling Magnetoresistance (TMR) [5, 203, 204] devices. For these the currents in magnetic multilayers are spin-polarised and can carry enough angular momentum that can cause magnetic reversal and induce stable precession of the magnetisation in thin magnetic layers. Due to the interest of driving the processes in ultrafast timescales, the evidence of hot-electron transport and its influence on ultrafast demagnetisation has been studied in magnetic multilayers [205, 206]. It was shown that, in a multilayer made of two FM layers separated by a metallic layer of Ru, the initial demagnetisation was larger and faster in the case of an anti-parallel alignment compared to a parallel alignment. This was attributed to the laser-excited spin-polarised hot electrons that were created in both magnetic layers and travelled ballistically from one to the other, thereby transferring angular momentum [205]. In addition to an efficient ultrafast demagnetisation for an antiparallel alignment of both FM magnetisations in CoFeB/MgO/CoFeB magnetic tunnel junctions, the laser fluence-dependent superdiffusive spin transport induced other effects [206]. Thus the study of multilayers, particularly GMR devices, is needed to obtain the effects of their functionality in ultrafast timescales.

7.1 Pseudo spin-valve multilayer optimisation for GMR

The pseudo spin-valve multilayer thin films were fabricated on Sapphire(0001) substrates using DC-Magnetron Sputtering in an argon atmosphere at a base pressure of 5×10^{-8} mbar (see section 2.6.2) . The pseudo spin-valve layer stacks configuration usually consists of FM1|NM(spacer)|FM2 with FM1 and FM2 being the hard and soft magnetic layers (see section 2.4.2), respectively. The magnetically hard layer of $Co_{50}Fe_{50}$(5 nm) was grown on a seeding layer of Ta(5 nm) which plays a critical role in promoting the formation of a stable and energetically favoured texture; thus facilitating magnetic stability [207]. Moreover, a capping layer of Ru(3 nm) was used. Initially, the free layer FM2 was a thinner layer of $Co_{50}Fe_{50}$ as compared to the hard layer FM1 in order to achieve lower Coercivity [208] of the FM2 layer compared to the FM1 layer and the spacer layer of Cu taken was 1.5 nm, 2 nm, 2.5 nm and 3 nm.

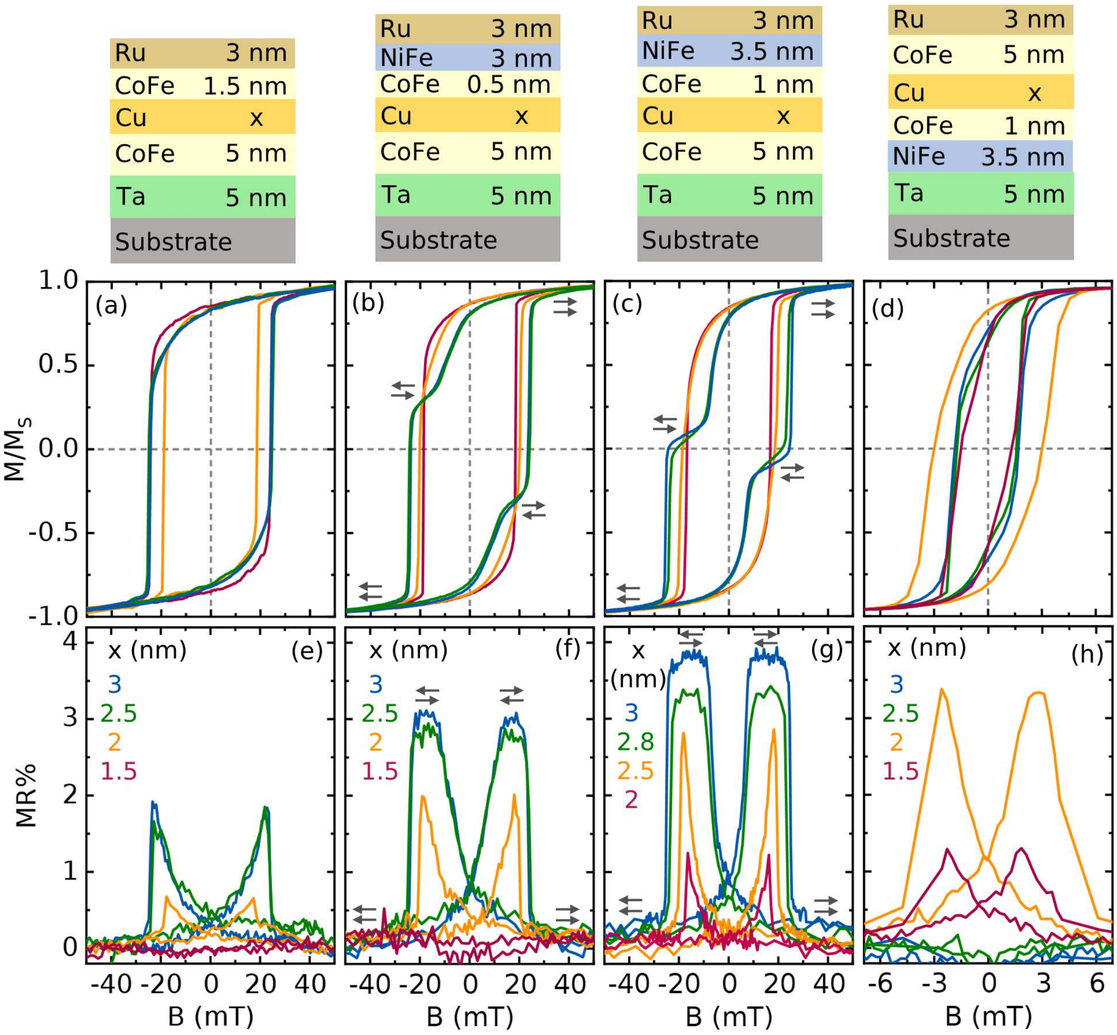

Figure 7.1: Hysteresis curves measured using MOKE for different layer stacks with varying Cu thicknesses. (a) $Co_{50}Fe_{50}$ as both the FM layers. $Co_{50}Fe_{50}$ as FM1 layer and $Co_{50}Fe_{50}/Ni_{80}Fe_{20}$ as FM2 layer with thicknesses (b) 3.5 nm and (c) 4.5 nm. (d) $Co_{50}Fe_{50}/Ni_{80}Fe_{20}$ as FM1 layer and $Co_{50}Fe_{50}$ as FM2 layer. Here Ta(5 nm) and Ru(3 nm) were used as seeding layer and capping layers, respectively. The respective MR (e), (f), (g) and (h) were measured using a Room Temperature (RT) probe station and a MR of upto 3.9% was obtained for the layer stack $Co_{50}Fe_{50}$(5 nm)/Cu(3 nm)/$Co_{50}Fe_{50}$(1 nm)/$Ni_{80}Fe_{20}$(3.5 nm).

For the Ta(5 nm)/$Co_{50}Fe_{50}$(5 nm)/Cu(3 nm)/$Co_{50}Fe_{50}$(1.5 nm)/Ru(3 nm) layer, although the MOKE measurements (see section 3.5.1) did not show any anti-parallel magnetisation states from the hysteresis at the H_C of 20 mT (see figure 7.1 (a)), the transport measurements (see section 3.5.2) showed a small MR with a maximum value of 2% (see figure 7.1 (e)). The MR was defined using R for parallel (↑↑) and antiparallel (↑↓) states using the relation,

$$\text{MR\%} = \frac{R_{\uparrow\downarrow} - R_{\uparrow\uparrow}}{R_{\uparrow\uparrow}} \times 100. \tag{7.1}$$

In the next step, the free layer for the pseudo spin-valve was changed to a $Co_{50}Fe_{50}$/$Ni_{80}Fe_{20}$ bilayer which was necessitated by the fact that an effective free layer should be magnetically soft with a low coercivity. This is an attribute of the $Ni_{80}Fe_{20}$ layer [208], yet in this bilayer there was an effective spin polariser of conduction electrons, which is an attribute of the $Co_{50}Fe_{50}$ layer [209]. Hence, the FM2 layer was $Co_{50}Fe_{50}$(0.5 nm)/$Ni_{80}Fe_{20}$(3 nm) and the Cu spacer was varied as 1.5 nm, 2 nm, 2.5 nm or 3 nm. From this an anti-parallel magnetisation state was achieved for the Cu thickness 2.5 nm and 3 nm (see figure 7.1 (b)). For the layer stack Ta(5 nm)/$Co_{50}Fe_{50}$(5 nm)/Cu(3 nm)/$Co_{50}Fe_{50}$(0.5 nm)/$Ni_{80}Fe_{20}$(3 nm)/Ru(3 nm), a maximum MR of 3% was observed (see figure 7.1 (f)) from the transport measurements (see section 3.5.2).

The increase in the thicknesses of the layers in FM2 with $Co_{50}Fe_{50}$(1 nm)/$Ni_{80}Fe_{20}$(3.5 nm) showed very prominent anti-parallel states of magnetisation for Cu spacer thicknesses 2.8 nm and 3 nm (see figure 7.1 (c)). The transport measurement showed a prominent MR of 3.9% for Ta(5 nm)/$Co_{50}Fe_{50}$(5 nm)/Cu(3 nm)/$Co_{50}Fe_{50}$(1 nm)/$Ni_{80}Fe_{20}$(3.5 nm)/Ru(3 nm) (see figure 7.1 (g)). The layer stacks with the FMs swapped showed a lower coercive field and a soft magnetic behaviour (see figure 7.1 (d)) while the MR was observed to be maximum for 2 nm Cu spacer and for a thicker Cu no MR was observed (see figure 7.1 (h)).

A further increase in the FM2 thickness with $Co_{50}Fe_{50}$(1 nm)/$Ni_{80}Fe_{20}$(4 nm) and a variation of Cu thickness from 1.5 nm to 4.5 nm with an approximate increment of 0.3 nm showed prominent antiparallel magnetisation states for all the cases except for Cu thickness of 1.5 nm and 1.8 nm (see figure 7.2 (a)). The transport measurement showed varying MR% for all the configurations while 1.5 nm showed no MR. The maximum MR achieved was 4.7% for the Ta(5 nm)/$Co_{50}Fe_{50}$(5 nm)/Cu(2.1 nm)/$Co_{50}Fe_{50}$(1 nm)/$Ni_{80}Fe_{20}$(4 nm)/Ru(3 nm) layer (see figure 7.2 (b)) and the Cu spacer thickness dependent MR showed a sharp increase in MR for 2.1 nm Cu compared to lower thicknesses. However, it gradually decreased as the Cu thickness decreased which showed an influence of interlayer exchange coupling (see figure

7.2 (c)). The pseudo spin-valve layer stack with a Cu thickness of 3 nm was used, which showed a GMR of 3.9% for the THz experiments shown below in this chapter.

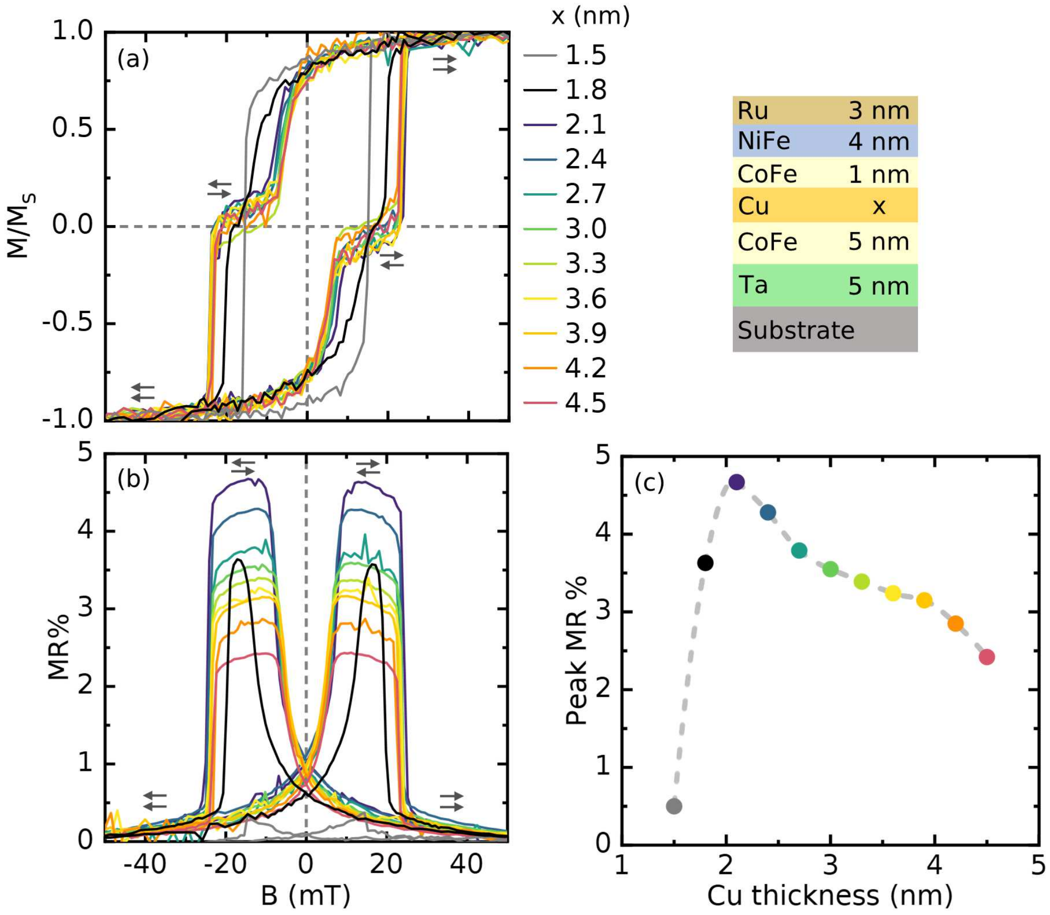

Figure 7.2: (a) Hysteresis loops from MOKE measurements and (b) MR measured from a RT probe station for the pseudo spin-valve layer stack. The antiparallel $\vec{M}$ states achieved for B ≈ 15 mT for layer stacks with different Cu spacer thicknesses varying from 1.5 nm to 4.5 nm. (c) The maximum MR of 4.7% was achieved for Cu spacer thickness of 2.1 nm.

7.2 Ultrafast excitation of CIP-GMR device

7.2.1 Experimental details

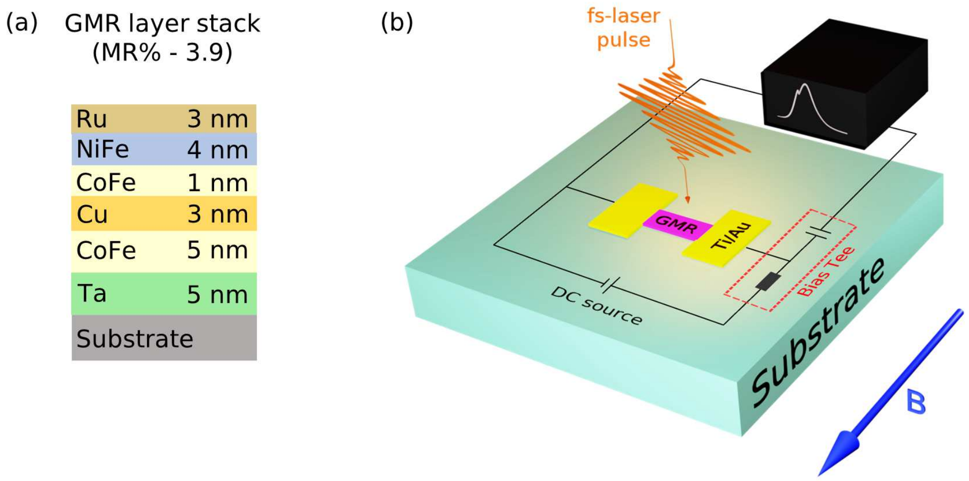

Figure 7.3: (a) Pseudo spin-valve layer stack for THz experiment and measurement scheme used to obtain the electrical response upon excitation by fs-laser pulse while $I_{\mathrm{dc-bias}}$ was applied across the multilayer in CIP geometry by using a bias-tee.

The optimised pseudo spin-valve thin film stack with a GMR of 3.9% (see figure 7.3 (a)) was nanopatterned by optical lithography with an image reversal technique into a 200 μm by 10 μm stripe followed by Ar-ion etching with resist as an etching mask (see section 3.4.2) The pseudo spin-valve structures were connected to thick Ti(10 nm)/Au(150 nm) large contact pads using optical lithography. The contact pads were patterned into two configurations to facilitate horizontal and vertical alignment of the pseudo spin-valve stripe with respect to the fixed position of probe tips and magnetic field direction of the THz electrical setup. The Ti/Au layer was deposited using e-beam evaporation at a base pressure of 5×10^{-7} mbar followed by liftoff (see section 3.4.1). The pseudo spin-valve was excited using normally incident linearly polarised laser pulses from an amplified Yb:KGW femtosecond laser with 99.6 kHz repetition rate, a wavelength of 1030 nm and a pulse duration of 300 fs (see section 3.6.2). The magnetisation was either along or perpendicular to the direction of the pseudo spin-valve stripe length for vertical and horizontal configurations. In addition, a dc-bias current $I_{\mathrm{dc-bias}}$ was applied through the probe tips via a bias-tee upto 5 mA. The generated electrical pulses were detected via the transmission line by a sampling oscilloscope of 50 GHz bandwidth (see figure 7.3 (b)).

7.2.2 Ultrafast electrical response from pseudo spin-valve stripe

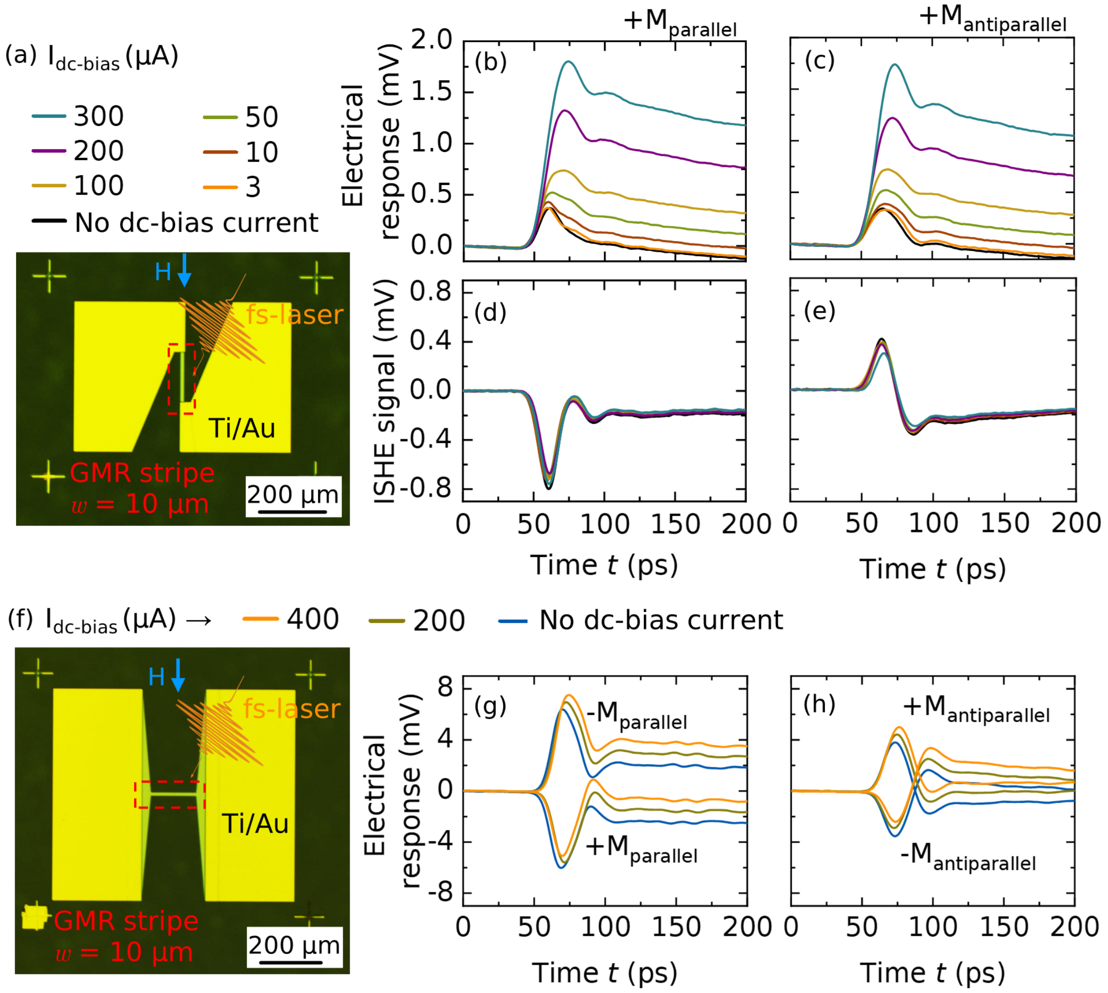

Figure 7.4: Electrical response from pseudo spin-valve stripes upon excitation by fs-laser pulses with power P = 96.8 mW creating a fluence F = 1 mJ/cm^2 across a spot size of 500 µm diameter with various $I_{\mathrm{dc-bias}}$. (a) Optical microscope image for the stripe along the $\vec{H}$ direction and the electrical responses for the (b) parallel and (c) antiparallel alignments of FM layers. The corresponding ISHE contributions (for small $\vec{M}$ components perpendicular to the stripes) extracted for both the (d) parallel and (e) antiparallel configurations. (f) Optical microscope image for the stripes perpendicular to $\vec{H}$ and corresponding electrical responses for (g) parallel and (h) antiparallel alignments of $\vec{M}$ for FM layers.

The fs-laser pulse was incident on the pseudo spin-valve stripe with a power P = 98.6 mW and a fluence of 1 mJ/cm^2 over an area of 500 µm diameter. For the vertical configuration,

$\vec{H}$ was applied along the length of the pseudo spin-valve stripe (see figure 7.4 (a)). The ultrafast electrical response when $\vec{\mathrm{I}}_{\mathrm{dc-bias}}$ = 3 μA, 10 μA, 50 μA, 100 μA, 200 μA and 300 μA were applied, showed fast signals with a rise time of ~ 10 ps followed by a slow decay signal for the parallel and antiparallel $\vec{M}$ configuration achieved for H= 80 mT and 15 mT respectively (see figure 7.4 (b, c)). However, a slight reduction of the signal amplitude was observed for antiparallel $\vec{M}$. The electrical response was also proportional to the applied $I_{\mathrm{dc-bias}}$.

In addition to the slow decay signal, the response corresponding to the $\vec{M}$ component perpendicular to the stripe was extracted by subtraction of the electrical responses for positive and negative polarity of $\vec{M}$. The parallel configuration gave a negative signal, while a positive signal, smaller in amplitude, was obtained for the antiparallel configuration (see figure 7.4 (d, e)). These responses were due to the transfer of spin angular momentum between the FM and the NM [205] and ISHE (see section 2.6) in the FM|NM.

To verify the dependence of the electrical response on the applied $I_{\mathrm{dc-bias}}$, the horizontal configuration (see figure 7.4 (f)) was used where $\vec{H}$ was applied across the width of the pseudo spin-valve stripe. Upon fs-laser excitation (see section 3.6.2) oppositely polarised ultrafast electrical responses were obtained for positive and negative $\vec{H}$ directions, implying electrical response of magnetic origin. However, the response in the antiparallel configuration at H= 15 mT had opposite polarity when compared to that of parallel configuration at H= 80 mT for same direction of $\vec{H}$. Moreover, the overall response increased proportionally with the $I_{\mathrm{dc-bias}}$ which was not influenced by the $\vec{H}$ direction (see figure 7.4 (g, h)).

7.2.3 Joule heating due to dc-bias current

In the next step, the $I_{\mathrm{dc-bias}}$ dependent signal was analysed. Hence, a waveguide was fabricated (see section 3.4.1) comprising of a pseudo spin-valve multilayer patterned into rectangular patch of dimension 50 μm × 1000 μm (see section 3.4.2) with $\vec{M}$ along the multilayer length and a dc-resistance R_{dc}= 193.3 Ω for the parallel configuration (see figure 7.5 (a)). As observed in the previous section, the ultrafast electrical response (see section 3.6.2) had a fast rise time leading to a peak followed by a slow decay for both parallel and antiparallel configurations. Next, a waveguide with a rectangular patch of Pt was taken with R_{dc}= 22.5 Ω and the normalised electrical response with $I^{\mathrm{GMR}}_{\mathrm{dc-bias}}$ showed the proportionality of the signal as compared to the $I^{\mathrm{Pt}}_{\mathrm{dc-bias}}$. The response was similar to the patterned pseudo spin-valve multilayer, thus indicating the contribution due to Joule heating (see section 2.7 and figure 7.5 (b)). However, the antiparallel configuration compared to the parallel configuration showed a reduced signal for the same $I_{\mathrm{dc-bias}}$ which was analysed in terms of the electrical response over a span of 1 ns (see figure 7.5 (c)). In the next step, the fluence dependence of the peak amplitude was analysed with and without $I_{\text{dc-bias}}$ and it was observed that the response was proportional to the laser fluence for both cases, suggesting no additional thermal contribution apart from Joule heating (see figure 7.5 (d, e)).

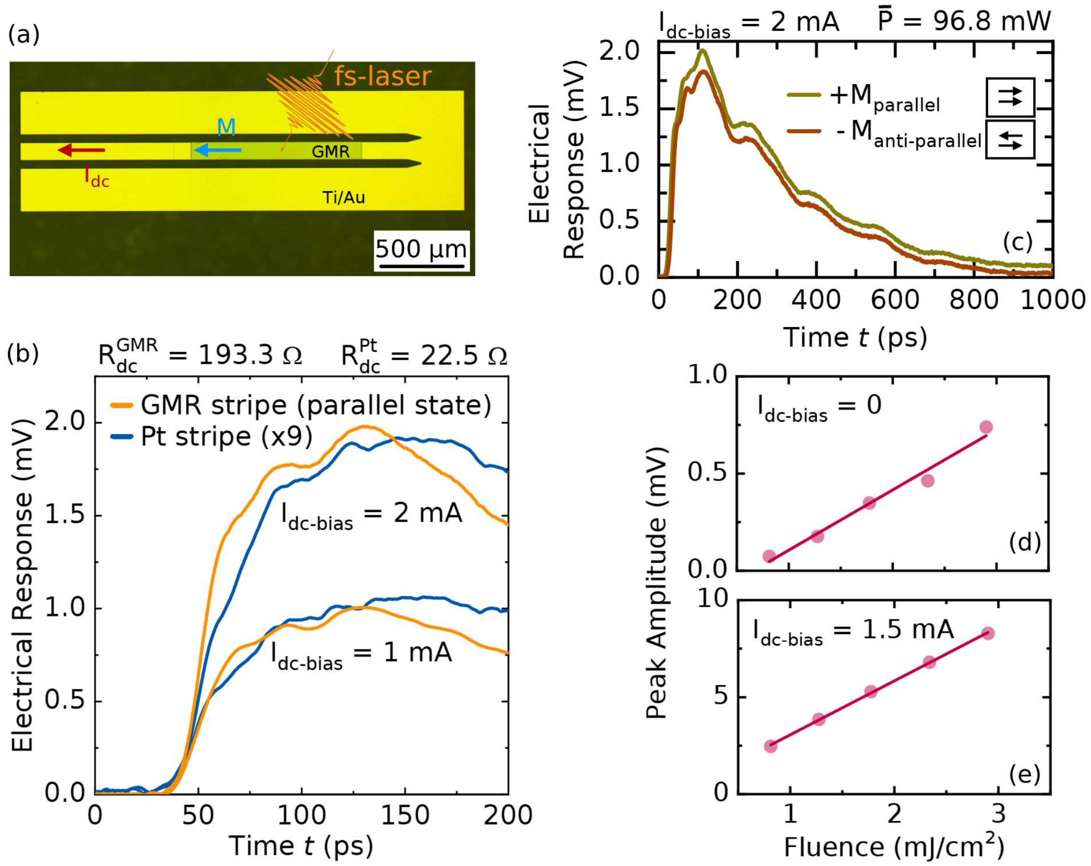

Figure 7.5: (a) Optical microscope image for waveguide with pseudo spin-valve multilayer rectangular patch and the measurement schematics with $I_{\text{dc-bias}}$ and $\vec{M}$ along the direction of pseudo spin-valve multilayer patch length. (b) Ultrafast electrical responses for parallel and antiparallel states with $I_{\text{dc-bias}}$= 2 mA, showing Joule heating contribution with a large decay time. (c) Comparison of Joule heating from ultrafast electrical response of multilayer structure having $R_{\text{dc-parallel}}$= 193.3 Ω with a Pt rectangle having R_{dc}= 22.5 Ω after normalisation based on R for the $I_{\text{dc-bias}}$= 1 mA and 2 mA. Linear dependence of fluence on the pseudo spin-valve device on waveguide (d) with and (e) without $I_{\text{dc-bias}}$.

7.2.4 Heating of metal interface thermocouple by fs-laser pulse

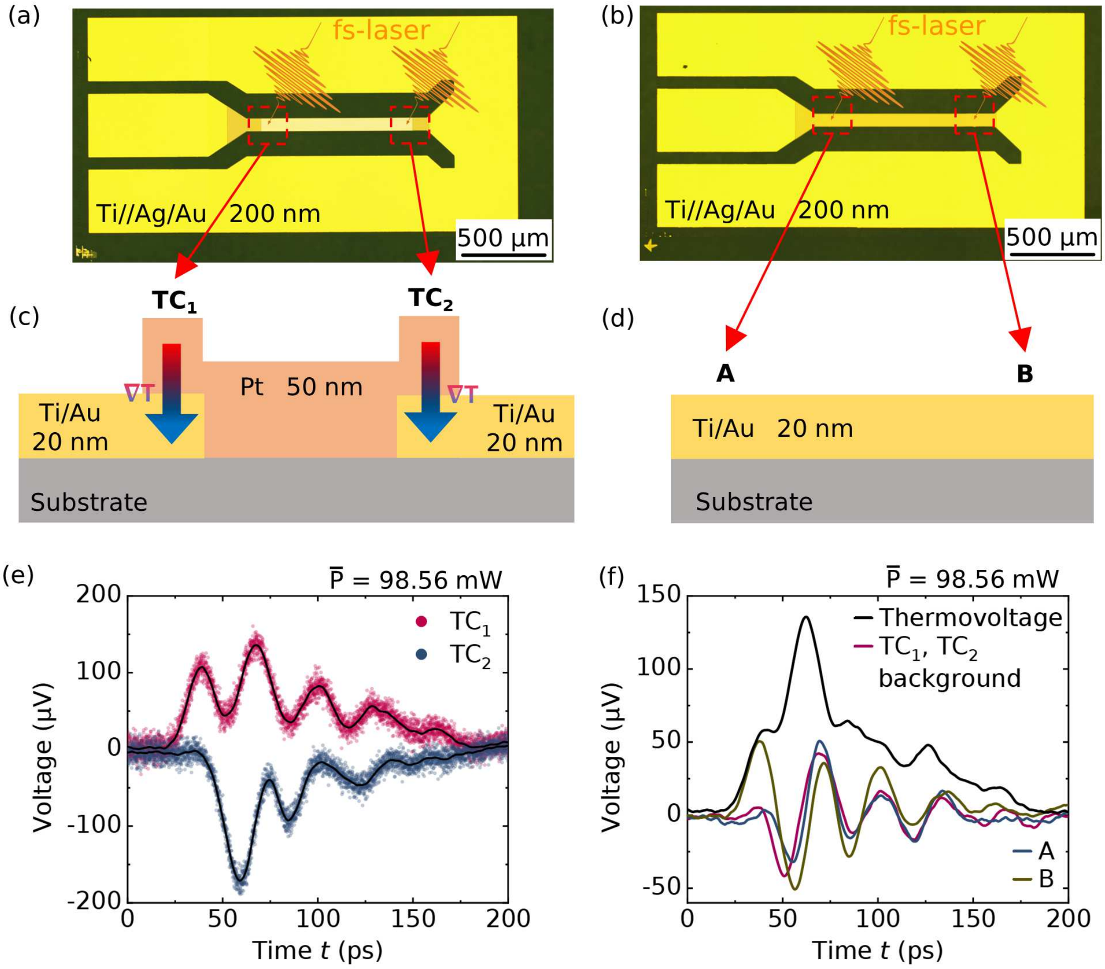

Figure 7.6: Optical microscope image showing waveguides (a) with Pt/Au and Au/Pt thermocouples and (b) without the thermocouples and the lateral schematics of layer stacks as shown in (c) and (d), respectively. (e) Excitation of thermocouples by fs-laser laser pulse with power P = 98.56 mW creating a fluence of 1 mJ/cm^2 over a spot size of 500 µm and their respective electrical responses. (f) The contribution due to the thermovoltage was obtained by subtracting the electrical responses from Pt/Au and Au/Pt thermocouples.

Since the pseudo spin-valve layer stacks were part of a waveguide which was subjected to fs-laser heating, it was also necessary to consider the signal response due to the heat gradient from the overlapping regions of metal layer stacks and Au layers of the waveguide. In order to verify the effect of thermovoltage generation (see section 2.7), the electrical response from the waveguide with a Pt rectangular patch was compared with the waveguide with a Au rectangular patch (see figure 7.6 (a, b)). The fs-laser pulse was directed towards the overlapping junctions on both sides of the Pt patch.

The Pt patch was expected to create a thermocouple (see section 2.7) with the Au layer in both ends (see figure 7.6 (c)). In contrast, the waveguide with just a Au patch did not form any thermocouple (see figure 7.6 (d)). Upon excitation with a fs-laser pulse with power P = 98.56 mW, a fluence of F = 1 mJ/cm^2 was achieved over a spot of 500 µm diameter (see section 3.6.2). This led to an ultrafast electrical response with multiple peaks and a voltage in the range of µV, whereas the excitation of the second thermocouple on the opposite end led to multiple peaks of opposite polarity. The subtraction of one response from the other gave the signal due to the thermovoltage, which were opposite in polarity due to the inverted thermocouple configurations (see figure 7.6 (e)). The thermovoltage ($\varepsilon_{\mathrm{th}}$) obtained was 145 µV which was accounted for by,

$$\varepsilon_{\mathrm{th}} = -S\,\nabla T \tag{7.2}$$

where S is the Seebeck Coefficient of the materials, and ∇T is the temperature gradient arising due to the difference in temperature between the two ends. Upon addition of the responses from both the thermocouples, the background can be obtained which can be seen as small oscillations due to the waveguide reflections. These responses were also similar to the responses from the Au patch waveguide without the thermocouple (see figure 7.6 (f)). However, it should be noted that the change in magnetisation direction did not have any effect on the polarity of the electrical response, and the response was smaller compared to the electrical response due to fs-laser-induced electronic effects.

7.2.5 Ultrafast excitation of pseudo spin-valve on waveguide

In light of the effects due to heating as described in the previous section, the waveguide with pseudo spin-valve was excited with a fs-laser pulse (see section 3.6.2). For an external magnetic field along the structure length, the $\vec{M}$ was expected to be along the length since it was the easy axis. However, a small component could have still affected the electrical response in either directions. In order to properly disentangle the ISHE signal (see section 2.6), the $\vec{M}$ direction was kept at an angle 30° (see figure 7.7) with respect to the pseudo spin-valve stripe along the length so that both the $\vec{M}$ components can have prominent effects. This was helpful in disentangling the ISHE contribution from the electrical response. The laser power of 170 mW was used, which led to a fluence of 1 mJ/cm^2 over a spot of size

650 µm and $I_{\text{dc-bias}}$ = 5 mA was applied. The response w.r.t. $I_{\text{dc-bias}}$ in both directions was measured in order to remove the background. As a result symmetric signals were achieved for +ve and −ve $I_{\text{dc-bias}}$ for both the parallel and antiparallel configurations in both the $\vec{M}$ directions. The difference in responses of parallel and antiparallel configurations were clearly observed (see figure 7.7).

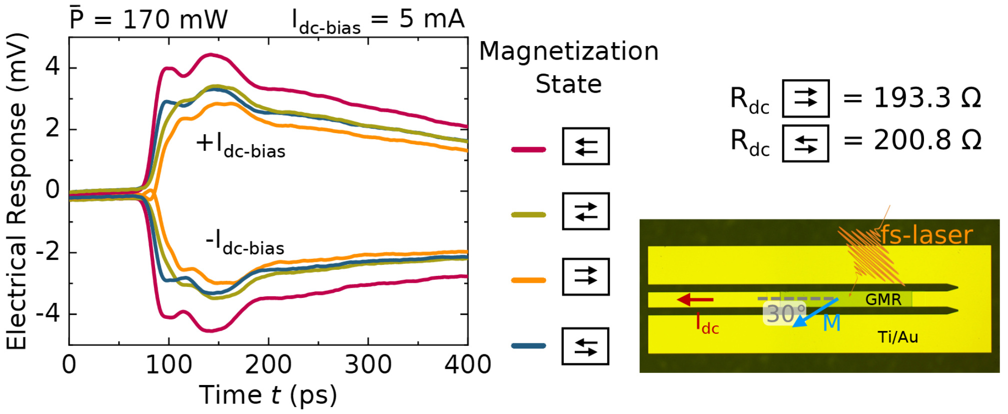

Figure 7.7: Electrical response from pseudo spin-valve device on waveguide upon excitation by fs-laser pulses with power P = 170 mW creating a fluence F = 1 mJ/cm^2 across a spot size of 650 µm diameter with $I_{\text{dc-bias}}$ = 5 mA for both parallel and antiparallel alignments of the $\vec{M}$. The polarity of the response switched with the direction of the $I_{\text{dc-bias}}$ and the $\vec{M}$ was directed 30° w.r.t. the pseudo spin-valve patch length.

In the next step, the signals for opposite polarities of each state were subtracted to cancel out the signals which were not dependent on the $\vec{M}$ direction, thus giving the ISHE responses. This was also verified from the response without applying any $I_{\text{dc-bias}}$ (see figure 7.8 (a, b)). It followed a similar trend as observed earlier when the parallel state with +ve polarity gave a negative signal, and the corresponding antiparallel state, which was the −ve polarity, gave a positive signal but with reduced amplitude. Subsequently, the addition of the signals, to rule out the ISHE signal, gave a fast-rising signal followed by a slow decay. The antiparallel state gave a reduced signal for the same $I_{\text{dc-bias}}$ although the dc-resistance for the antiparallel state was R_{dc} greater than the $R_{\text{dc}}^{\uparrow\uparrow}$= 200.8 Ω, which was greater than the dc-resistance for the parallel state $R_{\text{dc}}^{\uparrow\uparrow}$= 193.3 Ω (see figure 7.8 (c)).

Furthermore, the dc-voltage was calculated based on $I_{\text{dc-bias}}$ and R_{dc}, and the difference between relative change of resistances for both the parallel and antiparallel configurations, $\frac{\Delta R(\uparrow\downarrow)}{R} - \frac{\Delta R(\uparrow\uparrow)}{R}$ was obtained where ΔR represents change in resistance from dc to the resistance in excited state. As a result, the relative resistance change showed a fast initial decrease followed by a relaxation to return to the initial resistance state (see figure 7.8 (d)). This can be attributed to the fact that excitation by a laser led to demagnetisation (see section 2.6.2). This led to a decrease in resistance for antiparallel state than parallel state due to the increase in mobility of electrons which was more in the antiparallel state than in the parallel state. However, further experiments and analyses are required to understand the spin accumulation and the fs-laser excitation affecting electron mobility in pseudo-spin valve devices.

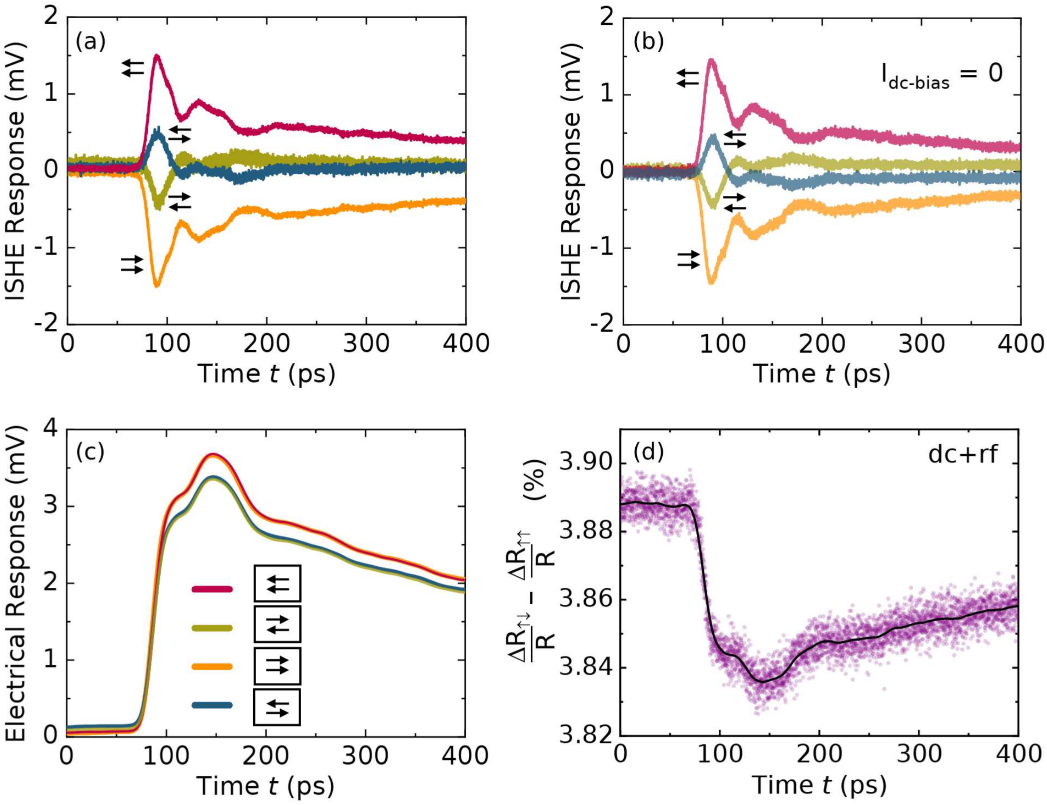

Figure 7.8: (a) ISHE component extracted from the ultrafast electrical response from pseudo spin-valve device on the waveguide with $I_{\text{dc−bias}}$= 5 mA for $\vec{M}$ directed 30° w.r.t. the pseudo spin-valve patch length and (b) ISHE response when $I_{\text{dc−bias}}$= 0. (c) The extracted contribution for the response w.r.t. the spin-polarised currents due to the $I_{\text{dc−bias}}$ along with the Joule heating contribution for parallel and anti-parallel states of $\vec{M}$. (d) The difference between corresponding relative change in resistances from dc state to the laser excited state, $\frac{\Delta R(\uparrow\downarrow)}{R} - \frac{\Delta R(\uparrow\uparrow)}{R}$ obtained for parallel and antiparallel states. The scatter points were averaged to be represented as the purple curve.

7.3 THz excitation of FM|NM|FM trilayer

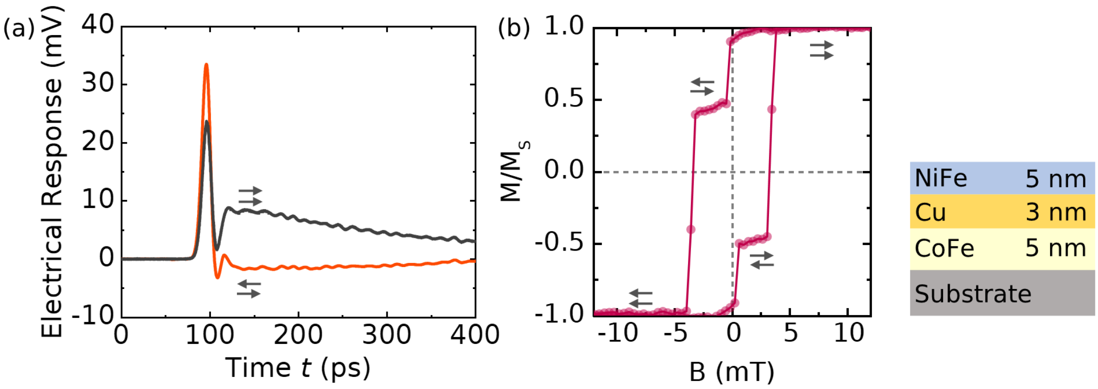

(c) FM/NM/FM trilayer $\vec{j}_c$ response

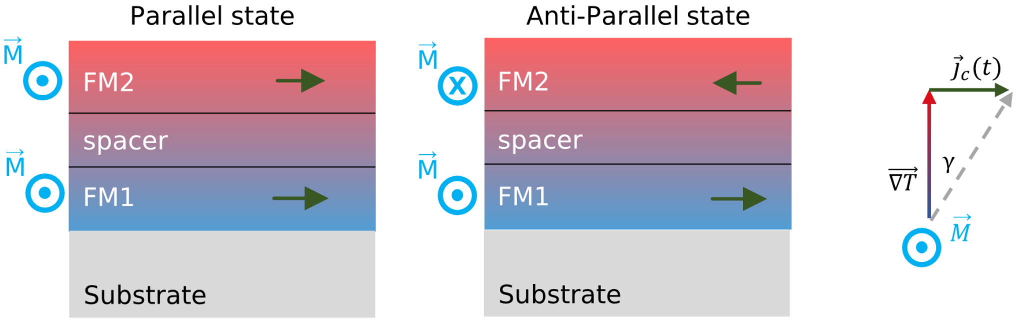

Figure 7.9: (a) Ultrafast electrical signal from $Co_{50}Fe_{50}$(5 nm)/Cu(3 nm)/$Ni_{80}Fe_{20}$(5 nm) trilayer on MgO substrate in parallel and antiparallel $\vec{M}$ states as seen from (b) the hysteresis loop of MOKE measurements. The initial fast response peak corresponded to the ISHE and AHE, whereas the second peak with a slow decay originating from the (c) heat gradient ($\vec{\nabla}T$) and $\vec{M}$ directions for the FM layers. Here, γ is the conversion factor.

In the previous section, the observed $\vec{M}$ dependent electrical responses were presented (see figure 7.8 (b)). The obtained signals were primarily composed of charge currents produced via ISHE and AHE (see section 2.6), which are usually short responses in time. In order to investigate the contribution of FMs in the layer stacks without the influence of the bottom Ta and the top Ru capping layers, a FM|NM|FM trilayer was studied next. The thin film of the layer stack $Co_{50}Fe_{50}$(5 nm)/Cu(3 nm)/$Ni_{80}Fe_{20}$(5 nm) was prepared by DC magnetron sputtering (see section 3.1) on MgO(100) substrates where the substrate favoured the growth of $Co_{50}Fe_{50}$ due to its bcc crystal arrangement [210]. The thin film was excited by fs-laser pulses with power P = 450 mW giving a fluence of 4.5 mJ/cm^2 over a 500 µm diameter spot and $\vec{M}$ was perpendicular to the contact direction between the two tips of the probe (see section 3.6.2).

Prominent short responses (see figure 7.9 (a)) were observed for both parallel (B= 80 mT) and antiparallel (B= 2.5 mT) states where these states were determined from the hysteresis loops obtained through MOKE (see section 3.5.1) (see figure 7.9 (b)). In addition to the short responses, a prominent slow decay response was observed after 10 ps of the appearance of the short response peak of the signal. Interestingly, these responses were dependent on $\vec{M}$ and have contributions from both the FMs as can be deduced from the signal polarities and amplitudes where the slow response almost vanished for the antiparallel state (see figure 7.9 (c)).

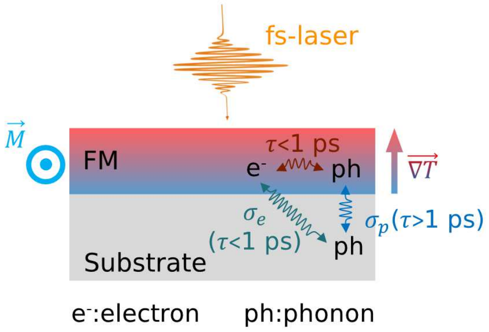

Figure 7.10: Illustration showing heat gradient $\vec{\nabla}T$ due to fs-laser heating in FM layer. The direction of electrical response was determined by the direction of $\vec{M}$ and $\vec{\nabla}T$. The signal had a fast component corresponding to the initial interaction between FM electron and substrate phonon, whereas the origin of secondary slow decay signal attributed to the interaction between FM phonon and substrate phonon accompanied by heat dissipation.

To account for the slower component of the signal, an understanding of energy exchange between the electronic levels of the metals and the lattice of both metals and the substrates was required (see figure 7.10). It was shown earlier [211] that the fs-laser heating leads to $e^- - e^-$ interaction within the metal, which occurs within the first picosecond of excitation, and e^- – ph interaction between metal electron and substrate phonon which also occurs in a similar timescale. However, a secondary channel has also been discussed, where ph – ph interaction occurs between the metal phonon and substrate phonon which has a time constant of 100 ps. Since a slow decay could be an indication of a slow dissipation of heat from the heat gradient ($\vec{\nabla}T$) in the metals to the substrate, the charge current can be assumed to be originating from thermal effects such as SSE and ANE (see section 2.7).

7.3.1 SSE mediated ultrafast electrical response

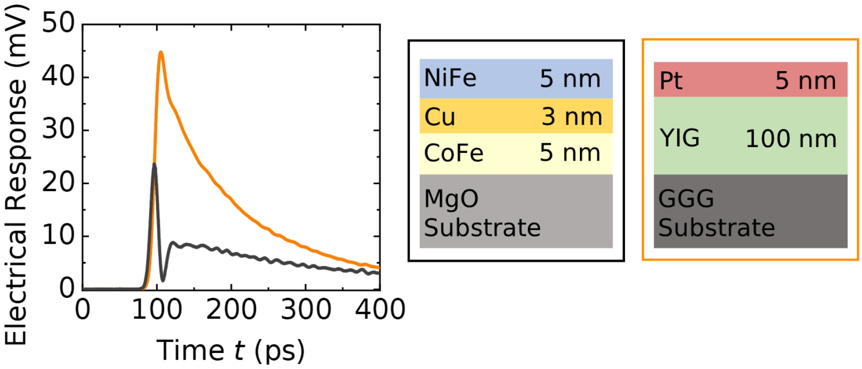

Figure 7.11: Ultrafast electrical signal via SSE from YIG(100 nm)/Pt(5 nm) grown on a GGG substrate as compared to the reference FM|NM|FM trilayer, comprising of a short response signal peak due to ISHE/AHE and secondary peak with slow decay due to ANE and SSE. Here, YIG : $Y_3Fe_5O_{12}$ and GGG : $Gd_3Ga_5O_{12}$.

To understand the thermal origin of the slow decay response, the electrical signal from a pure SSE contribution was also studied. To achieve this YIG ($Y_3Fe_5O_{12}$) was a suitable candidate [212] since it only contributes to the pure spin current transport via magnons (see section 2.5.3) which is suitable to observe a pure SSE effect. For this a 5 nm Pt was deposited by dc-magnetron sputtering on an Liquid Phase Epitaxy (LPE) grown YIG (100 nm) on a GGG ($Gd_3Ga_5O_{12}$) substrate. Upon fs-laser excitation, this gave a single response peak followed by a slow decay response of the signal with a time constant similar to the slow decay component in the trilayer stacks (see figure 7.11). The sharp increase of the response can be explained as the contribution from ISHE in the Pt layer where the spin current was driven via SSE in the YIG layer due to the temperature gradient from the laser heating. However, the slow decay of the signal can be attributed to the timescale of the heat dissipation, as seen in previous sections. In both the cases the decay times were estimated to be ~ 120 ps which aligned well with the metal phonon and substrate phonon interaction time constant as discussed earlier.

7.3.2 Understanding the contribution of FM layers

To further understand the contributions of each FM to this effect, single layer thin films of $Co_{50}Fe_{50}$(5 nm) and $Ni_{80}Fe_{20}$(5 nm) were grown on MgO substrates (see figure 7.12 (a)). It was observed that a $Co_{50}Fe_{50}$ layer gives a signal with a short response time of negative polarity as compared to the trilayer, suggesting a negative contribution from AHE, whereas the $Ni_{80}Fe_{20}$ layer gave a positive short response signal. In both cases, the slow decay responses had the same polarities which can be attributed to the same direction of $\vec{\nabla}T$ (see figure 7.12 (a)) indicating that their origin was ANE [213].

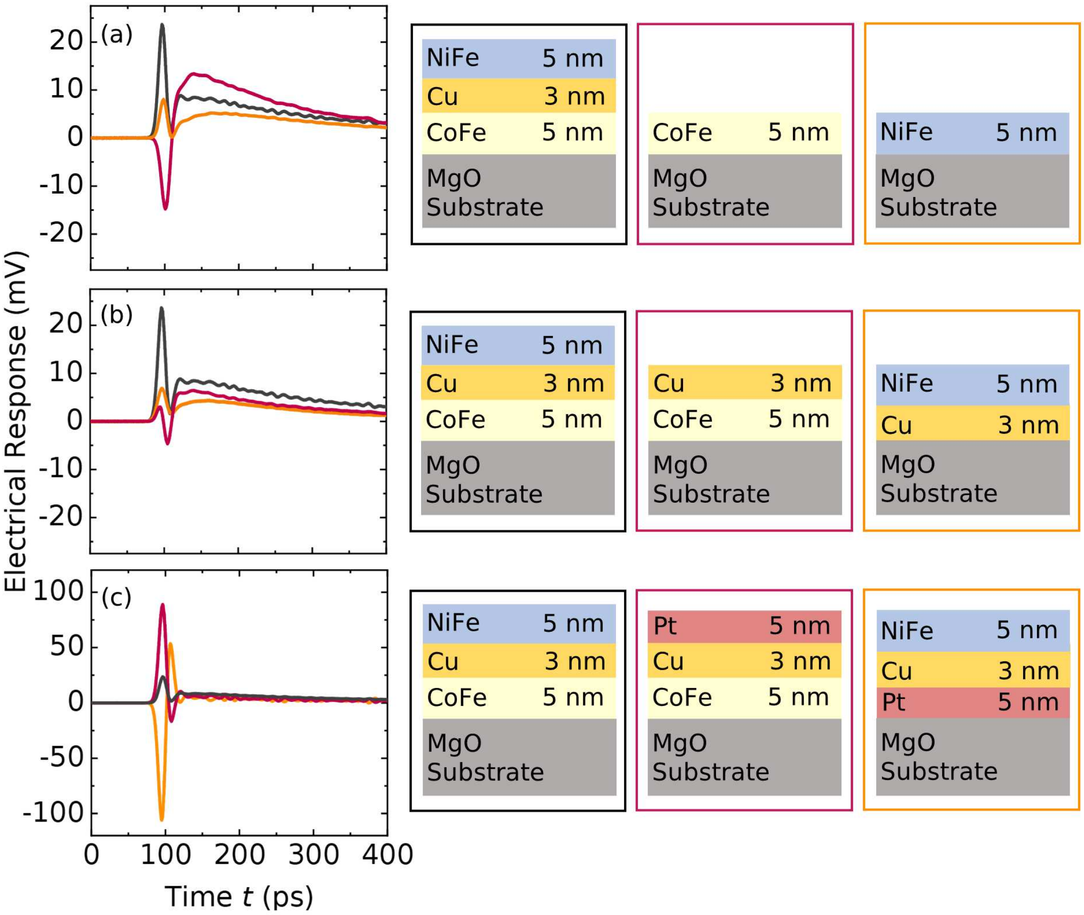

Figure 7.12: Ultrafast electrical signal, when excited with a laser power of P = 400 mW with fluence of 4.1 mJ/cm^2 over a spot size of 500 µm diameter, from a trilayer of $Co_{50}Fe_{50}$(5 nm)/Cu(3 nm)/$Ni_{80}Fe_{20}$(5 nm) on an MgO substrate as compared to (a) single FM layers of $Co_{50}Fe_{50}$(5 nm) and $Ni_{80}Fe_{20}$(5 nm), (b) Cu(3 nm) on $Co_{50}Fe_{50}$(5 nm) and $Ni_{80}Fe_{20}$(5 nm) on Cu(3 nm), and (c) Pt(5 nm) on the Cu side.

However, bilayer thin films of the FMs with a Cu(3 nm) having the arrangement of layer stacks as per the trilayer shown earlier, showed a decrease in amplitude of the short response peak as compared to single FM thin films (see figure 7.12 (b)). Further, the addition of a

Pt(5 nm) layer on the Cu layer drove a strong spin current from the FM layer, which created a large short response signal overshadowing the slow decay response (see figure 7.12 (c)).

7.3.3 Influence of FM|substrate interface

To understand the combined contributions of the FMs in the unsymmetric FM|NM|FM trilayer, electrical responses from the symmetric layer stacks with the same FMs material were compared. For the $Ni_{80}Fe_{20}$(5 nm)/Cu(3 nm)/$Ni_{80}Fe_{20}$(5 nm) thin film, a reduction in amplitude for the short response peak of the signal was observed which can be explained as an effective reduction of spin angular momentum transfer and subsequent conversion via ISHE or AHE while the slow decay response was similar to that observed for the unsymmetric trilayer. For the $Co_{50}Fe_{50}$(5 nm)/Cu(3 nm)/$Co_{50}Fe_{50}$(5 nm) layer stack, the signal did not contain the short response peak which can be attributed to net zero spin angular momentum transfer; however, the slow decay response was only observed (see figure 7.13 (a)).

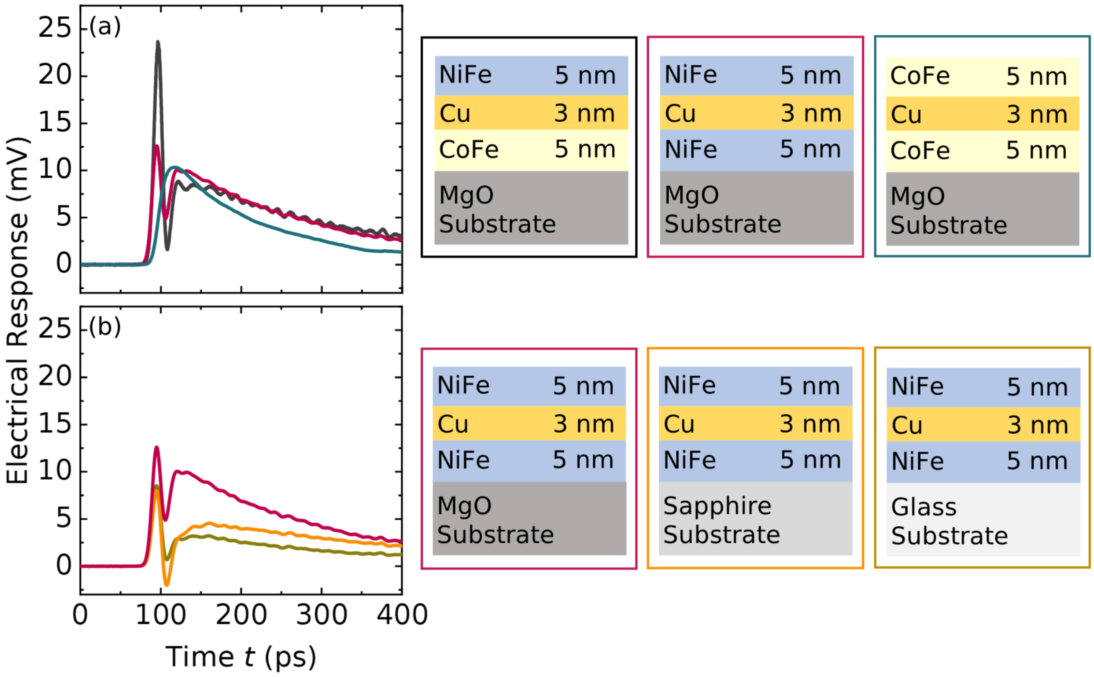

Figure 7.13: Effect on $\vec{M}$ dependent ultrafast electrical signals due to (a) symmetric FM|NM|FM trilayers separated by a Cu spacer layer, and (b) the effect of different substrates on the secondary slow decay response.

To verify the thermal energy exchange between the metal and the substrate symmetric $Ni_{80}Fe_{20}$(5 nm)/Cu(3 nm)/$Ni_{80}Fe_{20}$(5 nm) trilayers were prepared on different substrates namely sapphire and glass and compared to the same system grown on MgO. As a consequence, a significant impact on the slow decay responses of the signals were observed for the layer stacks on sapphire and the glass substrates (see figure 7.13 (b)). The observed reduction in amplitude can be attributed to the reduction in the exchange of energy between the metal phonons and substrate phonons (see figure 7.10) since the substrates have different thermal properties and lattice parameters.

7.3.4 Influence of spacer layer

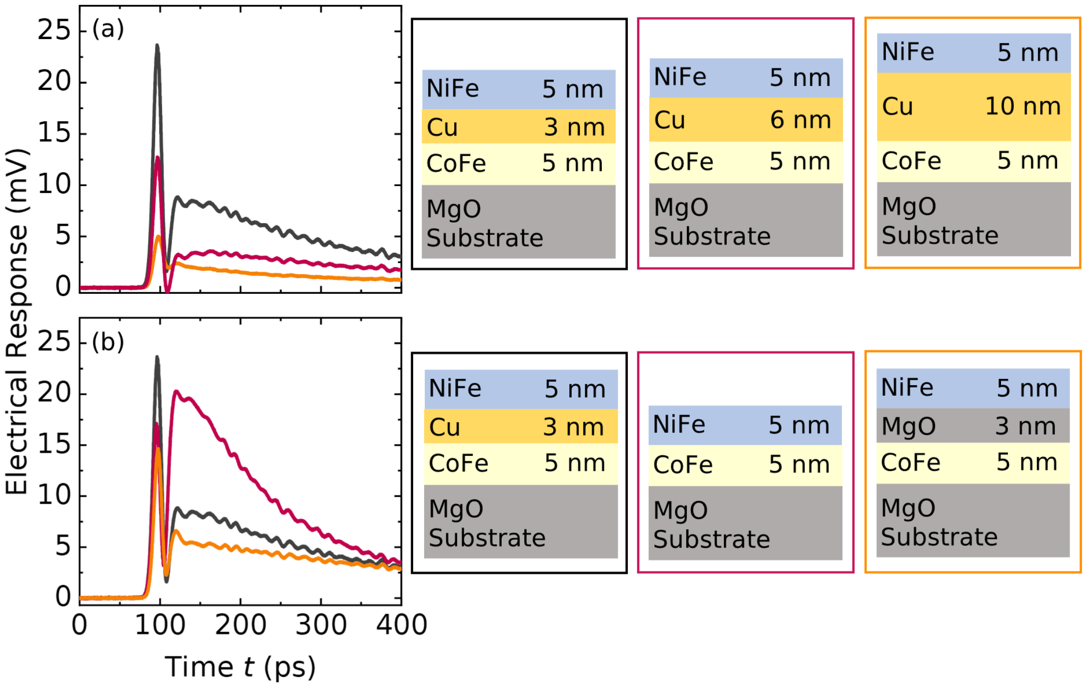

Figure 7.14: (a)The role of Cu spacer layer thickness as seen from trilayers with varying Cu thickness of 6 nm and 10 nm, as compared to 3 nm Cu spacer in trilayer. (b) Influence on electrical signal response when a $Co_{50}Fe_{50}$(5 nm)/$Ni_{80}Fe_{20}$(5 nm) bilayer and a trilayer with insulating spacer layer of 3 nm MgO were taken.

Next, the influence of the spacer layer on the electrical response was studied. For variable Cu thicknesses, decrease in amplitudes of short response peaks and slow decay responses of the signals were observed following the increasing Cu thickness. This can be explained as an increase in scattering events of the spins from the $Co_{50}Fe_{50}$ layer to the Cu layer (see figure 7.14 (a)) where the scattering increases Cu layer thickness. With the intention of excluding the scattering in the FM and Cu spacer layer interface, a bilayer of $Co_{50}Fe_{50}$(5 nm)/$Ni_{80}Fe_{20}$(5 nm) was grown on MgO substrate. A strong electrical signal was observed with both short response and slow decay response components. However, a larger amplitude of the slow decay response of the signal was observed as compared to that of the trilayer (see figure 7.14 (b)). This can be an indication of increase in number of available electrons for interactions between the metal phonons and substrate phonons due to the absence of Cu spacer layer and hence, less interface scattering.

For the MgO spacer layer, a similar electrical signal was observed as for the case of the Cu spacer layer, however, with a decreased overall amplitude of the signal, since the contribution from the $Co_{50}Fe_{50}$ layer was not mediated through the insulating MgO layer (see figure 7.14 (b)).

However, further investigation is necessary on the layer systems with multiple FMs to understand the thermal effects and carefully segregate and quantify the SSE and ANE contributions.

7.4 Switchable THz emitters

As observed in the previous sections, the $\vec{M}$ in the FMs in a multi ferromagnetic layer can be controlled individually to obtain parallel and antiparallel alignments. The parallel states were usually for large magnetic fields at saturation and antiparallel states were represented by a plateau in the hysteresis (see section 2.4.2) between the two switching fields. The electrical response from antiparallel states showed reduced amplitudes compared to that of parallel states upon excitation by fs-laser pulse (see section 3.6.2). These responses can be used to design a STE with switchable functionality. The multilayer used in the previous section as a pseudo spin-valve (see section 2.6.2) device gave an ultrafast response with negative amplitude for the parallel state and a small amplitude for the antiparallel state (see figure 7.15 (a)). In addition, the replacement of Ru with Ta as a capping layer gave a positive amplitude for the parallel state (see figure 7.15 (b)).

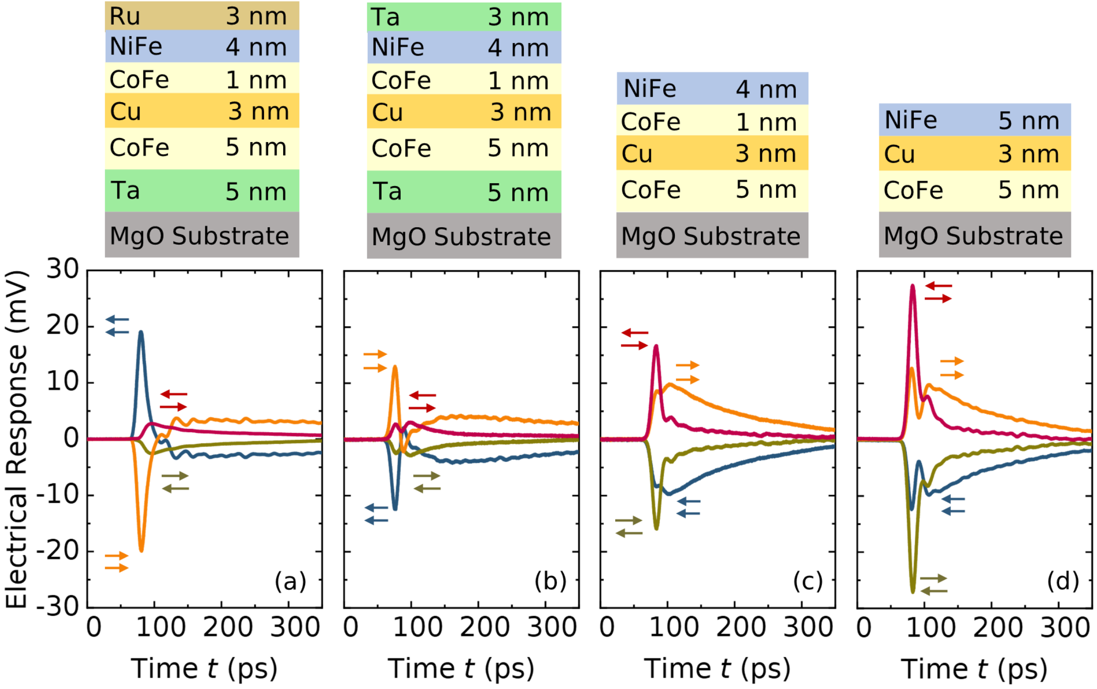

Figure 7.15: Ultrafast electrical response based on ISHE corresponding to parallel and antiparallel $\vec{M}$ states, showing different amplitudes for the spin valve based STE layer stacks comprising of: (a) pseudo spin-valve multilayer stack with (b) Ta(3 nm) capping layer (c) without the Ta seeding layer and capping layer, and (d) $Co_{50}Fe_{50}$(5 nm)/Cu(3 nm)/$Ni_{80}Fe_{20}$(5 nm) trilayer. This mechanism provides a switching ability to the STE.

Furthermore, the layer stack $Co_{50}Fe_{50}$(5 nm)/Cu(3 nm)/$Co_{50}Fe_{50}$(1 nm)/$Ni_{80}Fe_{20}$(4 nm) after the exclusion of seeding layer and capping layer showed higher amplitude with positive polarity for antiparallel state while the parallel state gave a positive but smaller amplitude compared to the layer stacks with Ta and Ru (see figure 7.15 (c)). A similar behaviour was observed when the second FM layer was replaced with $Co_{50}Fe_{50}$(5 nm); however, this had an increased amplitude for the antiparallel state (see figure 7.15 (d)).

Similar to the spin valve structures, a sandwiched structure comprising of two FMs and a heavy metal NM spacer layer such as Pt with an appropriate thickness to decouple the FMs was selected. Based on the electrical response via ISHE, the FMs could achieve parallel and antiparallel state. As per the configuration, the FMs would lead to $\vec{j}_s$ in either direction, with a parallel $\vec{M}$ state converting $\vec{j}_s$ to $\vec{j}_c$ in opposite directions. However, for the antiparallel state, the $\vec{j}_s$ would be converted to $\vec{j}_c$ in the same direction with positive polarity. Depending on the selection of the FM, the parallel state might lead to a positive or negative response, depending on the effective $\vec{j}_s$ into the HM layer (see figure 7.16 (a)). For initial proof of concept, a trilayer of $Co_{50}Fe_{50}$(5 nm)/Pt(6 nm)/$Co_{20}Fe_{60}B_{20}$(5 nm) was deposited on MgO substrate, along with an MgO capping layer to prevent the oxidation of $Co_{20}Fe_{60}B_{20}$. The electrical response showed different amplitudes for the parallel state (H= 80 mT) and the antiparallel state (H= 1.5 mT) (see figure 7.16 (b)). However, the difference between the amplitudes was not significant enough to differentiate and use for switchable functionalities.

It should be noted that the parallel and antiparallel states corresponding to fixed magnetisation direction of the bottom $Co_{50}Fe_{50}$ layer resulted in electrical response with amplitudes of opposite polarity. Since the amplitude of parallel state was more than the antiparallel state, it was safe to assume that the contribution corresponding to the $Co_{20}Fe_{60}B_{20}$ layer was more than that of $Co_{50}Fe_{50}$ layer. This difference can be optimised by varying the thickness of $Co_{20}Fe_{60}B_{20}$ layer in the subsequent step and taking the layer stack $Co_{50}Fe_{50}$(5 nm)/Pt(6 nm)/$Co_{20}Fe_{60}B_{20}$(2.5 nm). It was observed that the ratio of amplitudes was large enough (see figure 7.16 (c)) for the layer stack to be used as a switchable emitter. However, the overall amplitude drastically reduced since a major portion of the signal was contributed from the $Co_{20}Fe_{60}B_{20}$ layer and the signal amplitude was also comparable to the secondary slow decaying signal originating from thermal exchange between the bottom $Co_{50}Fe_{50}$ layer and the substrate similar to the signal observed in previous sections (see section 7.3). The layer stacks which are shown so far consist of HM layer sandwiched between the two FM layers. As a result, primary source for the electrical response can be safely attributed to the spin-to-charge conversion in HM layer which is Pt in this case.

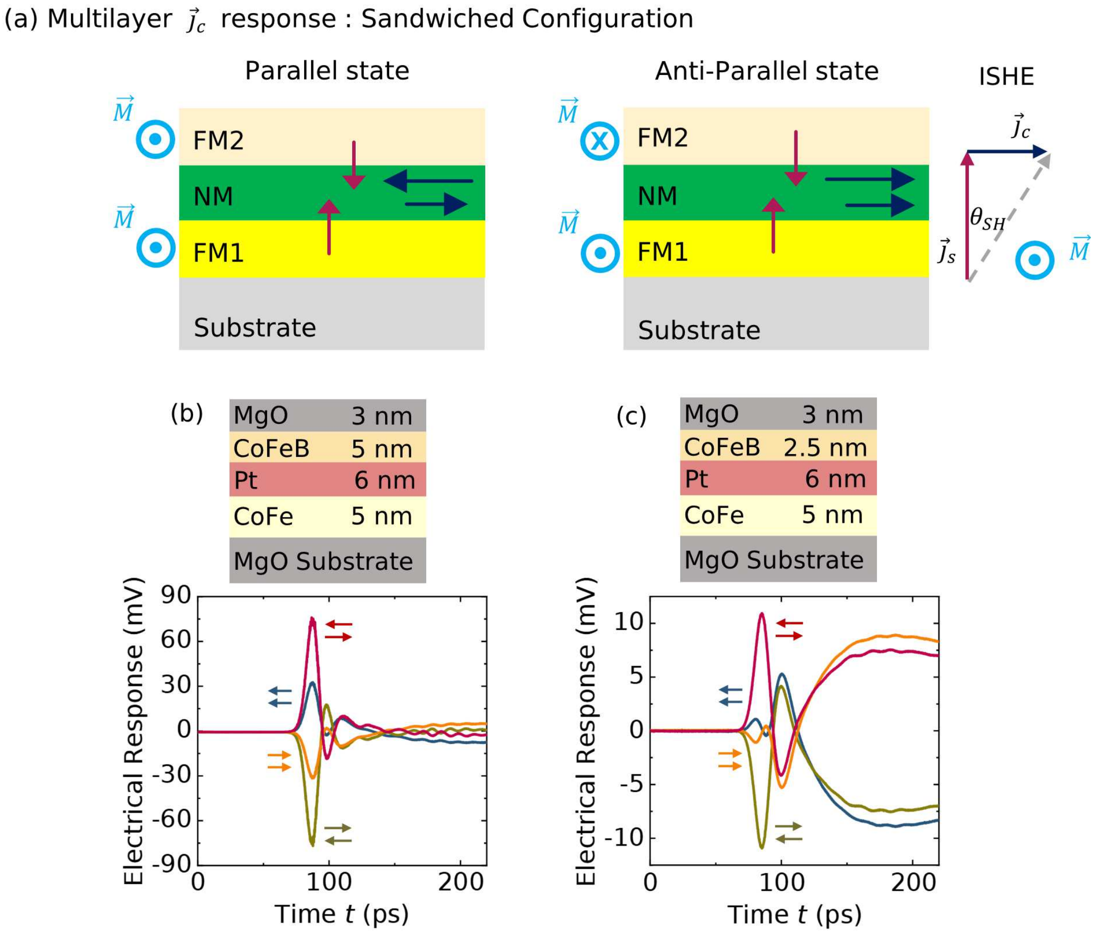

Figure 7.16: (a) A FM|NM|FM sandwiched configuration of multilayers with a heavy metal NM spacer. The parallel and antiparallel alignments of $\vec{M}$ corresponding to the FMs resulted in an ultrafast electrical response with different amplitudes. Layer stack of (b) $Co_{50}Fe_{50}$(5 nm)/Pt(6 nm)/$Co_{20}Fe_{60}B_{20}$(5 nm) and (c) $Co_{50}Fe_{50}$(5 nm)/Pt(6 nm)/$Co_{20}Fe_{60}B_{20}$(2.5 nm) gave different amplitudes for parallel and antiparallel $\vec{M}$ configurations. The ratio between these amplitudes were increased by reducing $Co_{20}Fe_{60}B_{20}$ thickness to 2.5 nm.

Alternatively, the contribution from individual FM can be controlled by introducing a NM spacer such as Cu, between the FM and the Pt, which could reduce the spin transport by scattering. The electrons at the FM|Cu interface carry a spin polarization due to the exchange splitting in the FM [214] and undergo minimal spin-flip scattering due to weak spin-orbit coupling. In the Cu spacer, there is primarily elastic scattering [215] with spin conservation primarily dominated by the Elliot-Yafet type [128, 129] spin relaxation mechanism. At the

Cu|Pt interface, spin-to-charge conversion occurs via ISHE.

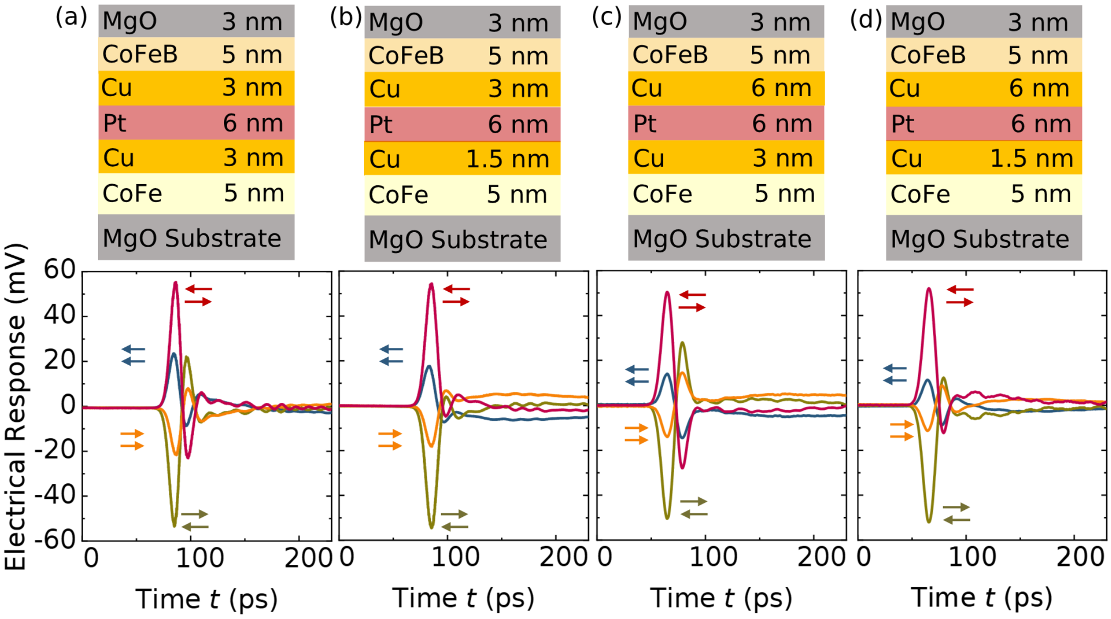

Figure 7.17: Ultrafast electrical response based on ISHE corresponding to parallel and antiparallel $\vec{M}$ states showing different amplitudes for the FM|Cu|HM|Cu|FM layer stacks. The amplitude was controlled by changing the Cu layer thicknesses. The respective multilayers comprised of (a) equal Cu thicknesses showing difference in peak amplitudes and (b, c, d) unequal Cu thicknesses with maximum difference achieved in (d).

Hence, Cu layers were introduced in between the FMs and the Pt layer. It was observed that an equal thickness of Cu (3 nm) led to the same ratio between the amplitudes of parallel and antiparallel states, although with a reduced overall amplitude for both the states due to scattering, as compared to that for the sandwiched trilayer without Cu. Subsequently, the Cu thickness was varied on either side, and it was observed that a reduction of Cu thickness to 1.5 nm on the $Co_{50}Fe_{50}$ side led to a further increase in the ratio. On the $Co_{20}Fe_{60}B_{20}$ side an increase in Cu thickness to 6 nm also increased the ratio. The increase in the ratio was due to the compensation of the larger spin current from $Co_{20}Fe_{60}B_{20}$ as compared to $Co_{50}Fe_{50}$. Finally, both the schemes were applied together by taking 1.5 nm and 6 nm Cu for the $Co_{50}Fe_{50}$ and $Co_{20}Fe_{60}B_{20}$ sides respectively. For this the ratio increased from 2.3 to 5 and it could be further increased by optimising the Cu thicknesses. Therefore, a terahertz emitter with switchable functionality was achieved, which was controlled via an external magnetic field.

Conclusion and Outlook

The effect of fs-laser induced excitations in multilayers with multiple ferromagnets was investigated with a focus on GMR pseudo spin-valve devices when a dc-bias current was applied. It was observed from the ultrafast electrical response that the antiparallel state of the pseudo spin-valve device gave a reduced signal compared to the parallel state which was also reflected in the observed $\frac{\Delta R(\uparrow\downarrow)}{R} - \frac{\Delta R(\uparrow\uparrow)}{R}$, taking both dc and rf contribution, which showed an abrupt reduction upon fs-laser excitation. This indicates an increase in spin population leading to a current driving with a decreased resistance, especially for the antiparallel state. This led to the investigation involving the multilayers without dc-bias current in order to understand the thermal effects, which were reflected by slowly decaying peaks in the ultrafast electrical response. The observations in different multilayer configurations indicated a response via SSE or ANE due to the temperature gradient caused by laser heating. Moreover, the thermal gradient-induced electrical response in a FM was believed to be an observation of ANE. However, this needs further analysis and detailed investigation.

Subsequently, the parallel and antiparallel magnetisations of decoupled ferromagnets in a multilayer were studied. This involved the designing of a sandwiched multi-ferromagnetic layer stack to achieve decoupling of the FMs and the amplitude difference was controlled via Cu interlayer scattering to realise switchable terahertz emitters. Thus, the switchable emitters provide the 'ON' and 'OFF' mechanism via an external magnetic field.

8 Summary

This thesis highlighted various spintronic effects due to fs laser excitation of different magnetic multilayers, which included the conventional STEs and GMR heterostructures and analysis of the geometrical influence on emitted response due to various electrical, magnetic and thermal dynamics. Moreover, various techniques were discussed to engineer new spintronic devices for terahertz applications. This is elaborately discussed below:

Significance of charge dynamics in spintronic terahertz emitters: The core research of ultrafast spin dynamics for STEs involves the study of ultrafast spin currents. In the past the usual way of ultrafast spin current estimation involved direct conversion of the emitted terahertz radiation by using a plane wave approximation. However, it lacked a significant role of charge dynamics, which is necessary to be taken into account during terahertz radiation to ultrafast spin current conversion [15, 18, 21, 34] due to a finite excitation spot in thin film STE and charge accumulation. This was discussed using finite element method simulation in chapter 4. The effect of charge accumulation is followed by current backflow, and the finite process involving a time constant derived from the resistive and capacitive effects of the metal. Moreover, a high pass filtering effect on the emitted charge current spectrum was observed due to a finite time constant. Influences of various factors, such as spatial and temporal shapes of the laser and material properties on the charge current spectrum were compared as shown in chapter 4.

Observation and control of charge dynamics in nanostructured STEs: The effect of charge dynamics was verified experimentally via miniaturisation of the STEs by nanostructuring to dimensions less than the laser spot and the charge dynamics was controlled with STE geometry which was discussed in chapter 5. The influence of the time constant relevant to the current backflow with the STE geometry was estimated analytically. It was established that the geometry plays a significant role in determining the RC constant of the analytical circuit for charge accumulation and backflow. This was reflected in the emitted spectra in the form of increased high pass filtering for smaller sized nanostructured STEs which can be mistakenly interpreted as a blue shift with reduction in peak amplitude for a narrow bandwidth setup [37, 153, 155]. Moreover, STEs in the form of nanoscale SRR did not provide any significant optical effects due to the dominance of terahertz emission originating from internal spin dynamics. Finally, it was observed that the STEs in the shape of stripes provided an optimal solution to avoid the high pass filtering in the emitted spectrum, with the induced charge current along the length of the stripes. This was also discussed in chapter 5. The terahertz emission obtained from STE stripes can provide appropriate information regarding the ultrafast spin dynamics as the ultrafast spin current can be correctly derived from the THz emission due to negligible effects from charge dynamics. Overall, the influence of various tuning parameters was understood, which can be appropriately selected to shape the emitted terahertz spectrum.

THz pulse burst emitter for narrowband emitted spectrum: The broadband spectrum of STEs have been extensively investigated. With the intention of obtaining narrowband emission at higher central frequencies, a device was designed using a series of STEs emitting pulse burst. This was shown in chapter 6. The STEs were arranged with a calculated time path for excitation signal based on the intended central frequency, and the pulse burst was emitted from the STEs upon simultaneous excitations. The overall power of the emitted spectrum was also seen to be dependent on laser power and larger STE size. Finally, a working device with a high Q-factor was achieved by exciting a higher number of STEs within the laser spot to create a pulse burst. These devices can provide suitable narrowband for frequency-selective applications.

STE based DAC device for ultrafast signals: With the intention of designing a DAC for ultrafast signals, spintronic devices were designed with multiple STEs stripes as shown in chapter 6. The STEs comprised different-sized stripes with different coercive fields due to different domain nucleation energy. Alternatively, STEs stripes of different FMs with different coercive fields were also designed. The difference in coercive fields provided control of emitted current amplitude, and the operating number of bits for the DAC was achieved based on the number of incidents of magnetisation switching of STEs altogether. Finally, devices with 4-bit and 3-bit DACs were obtained to show the working principle. However, a further increase in the operating number of bits and their optimisation to have minimal non-linearities can be achieved.

Electrical switching of STE response: The conventional STE excitations only involve a bias magnetic field. With the intention to achieve switching of magnetisation of FM electrically, a device was designed with stripes of STEs on thick Cu where applied dc-bias current created Oersted fields to control magnetisation. The amplitude of the emitted signal was also extracted by separation of Joule heating contribution and a control of emitted signal amplitude was achieved through the magnitude of applied dc-bias current. This study can be extended by modulating the bias current using an ac-current pulse to modulate the THz signal.

Effect of fs-laser excitation on magnetoresistance: In the chapter 7, the investigation of fs-laser excitation on pseudo spin-valve devices was shown. The multilayer system comprising of two decoupled FMs with a spacer layer in between, was optimised to achieve 4 % GMR in the antiparallel state of magnetisations with a dc-bias current. The devices of pseudo spin-valve layer stacks were studied upon fs-laser excitation, and a momentary decrease in magnetoresistance was observed due to the demagnetisation. However, further investigations are required to understand the effect pertaining to the transport properties in fs-laser excited pseudo spin-valve multilayer system. This could have implications in future GMR based devices with operating speeds at ultrafast timescales.

Signatures of spin-caloritronic effects in magnetic heterostructures via fs-laser excitation: The study of GMR multilayer system in chapter 7 was primarily done using dc-bias current with the magnetisation direction along the direction of flow of current. However, the GMR layer stack was simplified into a trilayer with a thin spacer layer sandwiched between two decoupled FMs and the fs-laser excitation without any application of dc-bias current resulted in an additional slowly decaying peak. The effect was studied using a series of layer stacks with variable layer thickness and materials to deduce the origin of the effect. The results indicated various spin-caloritronic effects with the slow decay response linked to a thermal exchange between the metal phonons and substrate phonons. However, further investigations are necessary to quantify the effect properly and to establish this technique for direct measurement of spincaloritronic effects such as SSE or ANE which are difficult to measure with the present experimental techniques.

Switchable terahertz emitters: A switchable terahertz emitting device was designed using a heterostructure with a NM layer sandwiched between two FM layers. This is discussed in chapter 7. The working principle involved the parallel and antiparallel magnetisation states of the FMs, with different amplitudes. A series of sandwich structures such as GMR multilayers were identified to get the working principle of the device. In the subsequent steps, a layer stack was designed with optimisation based on FM layer thicknesses and the introduction of scattering through a spacer layer to reduce contribution from individual FM layers. Finally, a switchable terahertz emitter was achieved with a high ratio of amplitudes between the parallel and antiparallel states. This functionality can be used for applications involving switching between signals based on different amplitudes.

A Appendix

A.1 Wave Propagation

A.1.1 TE/TM modes

The propagation of electromagnetic waves along the waveguide is determined by the existence of fields within the waveguide. With the waves propagating with different modes, a mode is defined as the transverse field pattern characterised by consistent amplitude and polarisation profiles along the longitudinal or z coordinate of the waveguide. They can be primarily categorised into:

TE mode:

This waveguide mode relies on transverse electric waves. These waves are characterised by the electric vector $\vec{E}$ always being perpendicular to the direction of propagation in $z-$direction.

TM mode:

Transverse magnetic waves are distinguished by the magnetic vector $\vec{H}$, which is consistently perpendicular to the direction of propagation in $z-$direction.

A.1.2 CST electromagnetic simulation

The CST electromagnetic simulation is performed in order to determine the plasmonic effects in the arrays of nanoSTEs with dimensions of sub-micrometer subjected to illumination with fs-laser pulse of wavelength 800 nm.

For the simulations electromagnetic module with the submodule for periodic structures is taken. The simulated nanoSTE dimensions were 900 nm and 4.5 μm with a thickness of

10 nm with the nanoSTE material being Pt with $\sigma = 3 \times 10^6$ S/m. The substrate material was used as sapphire with $\sigma = 10^{-12}$ S/m and $\epsilon_r = 3.064$ [144]. The substrate dimension is nanoSTE dimension along with the spacing which is 100 nm and 500 nm for 900 nm and 4.5 μm nanoSTEs, respectively.

A unit cell is excited with a 100 THz signal using the two Floquet ports to have the two modes, TE and TM, in order to model the radiation of a linearly polarised wave. The Floquet boundaries are taken at least quarter wavelength apart from the radiating surface. Out of the various default S-parameters obtained from the simulation, the S-parameters corresponding to the TE and the TM modes in transmission are SZmax1.Zmin1 and SZmax2.Zmin2, respectively, where Zmax and Zmin are the excitation and probing ports respectively.

A.2 COMSOL AC/DC Simulation

For the simulations the COMSOL [143] electric current submodule, which is part of the AC/DC module is used to study electric current and the material parameters required were Electrical Conductivity (σ) and relative permittivity (ϵ_r). For a sapphire substrate layer $\sigma = 10^{-12}$ S/m and $\epsilon_r = 3.064$ [144] was used. For the STE thin film, an average $\sigma = 5 \times 10^6$ S/m was used, which is in good agreement with the conductivity values for multilayer thin films with W, CoFeB, and Pt [15, 145, 146] and an ϵ_r of 903 for Pt [147]. The parameters taken for the reference STE (STE$_{\text{ref}}$) were D = 20 μm, τ = 20 fs, and a thickness $t = 10$ nm.

A.3 Fourier Transform of differential equation

For U$_C$(t) the inverse fourier transform is,

$$U_C(t) = \frac{1}{4\pi} \int_{-\infty}^{\infty} U_C(\omega) e^{i\omega t}\, d\omega. \tag{A.1}$$

The differential of this equation gives,

$$\begin{aligned} \frac{dU_C(t)}{dt} &= \frac{1}{4\pi} \int_{-\infty}^{\infty} U_C(\omega)(i\omega e^{i\omega t})\, d\omega \\ &= \frac{1}{4\pi} \int_{-\infty}^{\infty} (i\omega U_C(\omega)) e^{i\omega t}\, d\omega \end{aligned} \tag{A.2}$$

which is the inverse Fourier transform of $i\omega U_C(\omega)$ Hence,

$$\mathrm{FFT}\left[\frac{dU_C(t)}{dt}\right] = i\omega U_C(\omega). \tag{A.3}$$

A.4 Signal Processing

A.4.1 Von Hann Window

The Hann window is one of many window functions for smoothing values. It uses a Hann function [216] on the dataset (see figure A.1). It is particularly useful for dealing with discontinuities or sharp transitions in the FFT due to truncated waveforms that arise when the measured signal does not form complete periods, which is also referred to as Spectral Leakage. It is also used for smoothing discontinuities in the measured signals or the generation of smooth FFTs for the case of a small number of time domain datapoints.

The Hanning function is defined as,

$$w(n) = \frac{1}{2} - \frac{1}{2}\cos\frac{2\pi n}{M-1} \tag{A.4}$$

where $0 \le n \le M-1$ with M denoting the total number of data points.

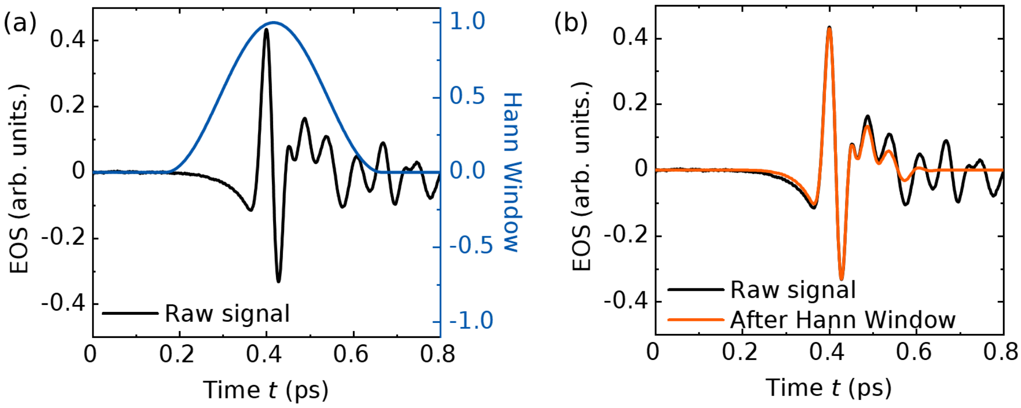

Figure A.1: Illustration showing Hann function. (a) Raw electro-optic signal for thin film STE and Hann window. (b) Electro-optic signal after application of Hann window over a time of 0.4 ps centered at 0.4 ps in contrast to the raw signal.

A.5 Fitting of Spectral Amplitude using analytical model

The analytical model for nanoSTEs consists of an RC constant which can be expressed as $k \cdot \tilde{\epsilon}(\omega)/\tilde{\sigma}(\omega)$ where $\tilde{\epsilon}(\omega)$ and $\tilde{\sigma}(\omega)$ are material-specific frequency dependent complex parameters which were obtained from the literature [151, 152, 165]. The contribution due to gap capacitance C_g is given by $k_g \cdot \tilde{\epsilon}(\omega)/\tilde{\sigma}(\omega)$. Overall the model accounts for the features of $\tilde{\epsilon}(\omega)$ and $\tilde{\sigma}(\omega)$ (see figure A.2 (a)) with frequency specific effects primarily arising due to different k and k_g.

In a first step the k value was varied over a range in order to find the k value for which the R^2 value was at least 0.6 using the analytical model and compared to the experimental spectral amplitude of thin film STE, along with an error band. In addition, the approximation of model calculated and experimental spectral amplitude of thin film STEs were established for a k value of 6000 along with its corresponding error band and R^2 value. This has been calculated for both sapphire and glass substrates (see figure A.2 (b)).

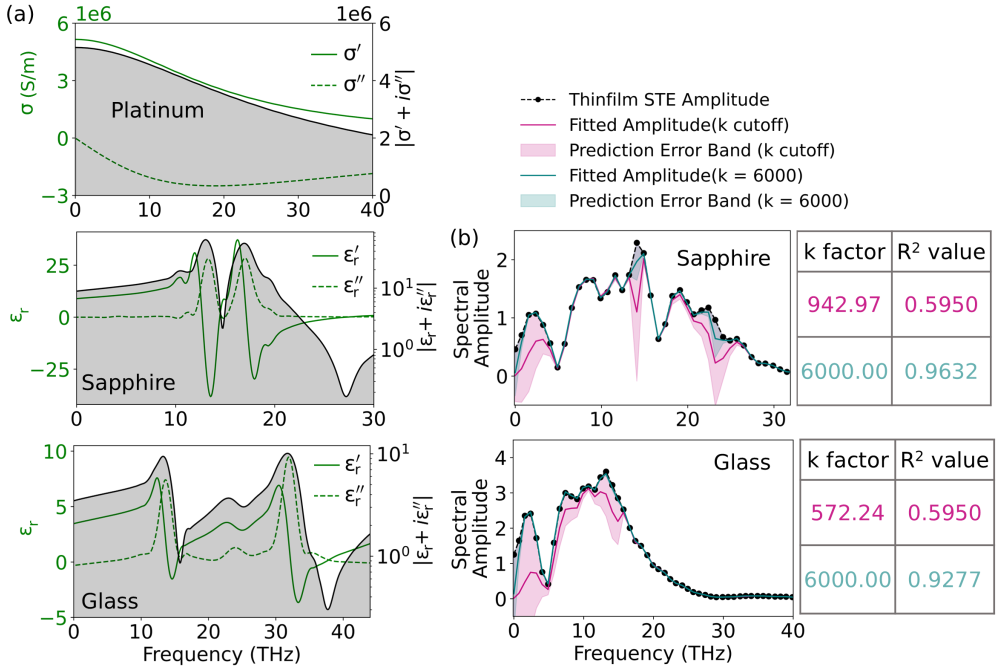

Figure A.2: (a) Conductivity ($\tilde{\sigma}(\omega)$) of metal (Platinum) and electrical permittivity ($\tilde{\epsilon}(\omega)$) of different substrates (sapphire and glass) used in the (b) modelling and curve fitting to find k values for thin film STEs from the analytical model.

A.5.1 Square nanoSTEs on sapphire substrate

For the square shaped nanostructured STEs the k values were fitted for each frequency to find the k value that minimises the difference between the measured and calculated amplitudes of thinfilm STEs. It should be noted that the k_{ref} value in the model was taken as 6000, corresponding to thin film STE (see figure A.2). The number of successful amplitudes at corresponding frequencies (counts) for specified k values are represented by a histogram (see figure A.3 (a)). A subsequent statistical analysis was made to extract the mean and median of the k values. The total amplitude for the entire frequency range was calculated using the model with the obtained mean and median k values and the corresponding fit quality was evaluated by computing R^2.

Additionally, spectral amplitudes over the entire frequency range were calculated and R^2 values computed. These were compared for a range of k values. The k value was determined for the best R^2 value in agreement with the experimental amplitude and the rounded k values with corresponding R^2 values were compared (see figure A.3 (b)). It should be noted that, beyond a certain threshold the k value for the best R^2 value cannot be computed since the spectral amplitude values become closer to the experimental values of the thin film STE. Hence, in those cases the best k values are computed from k values close to the median achieved in the histogram.

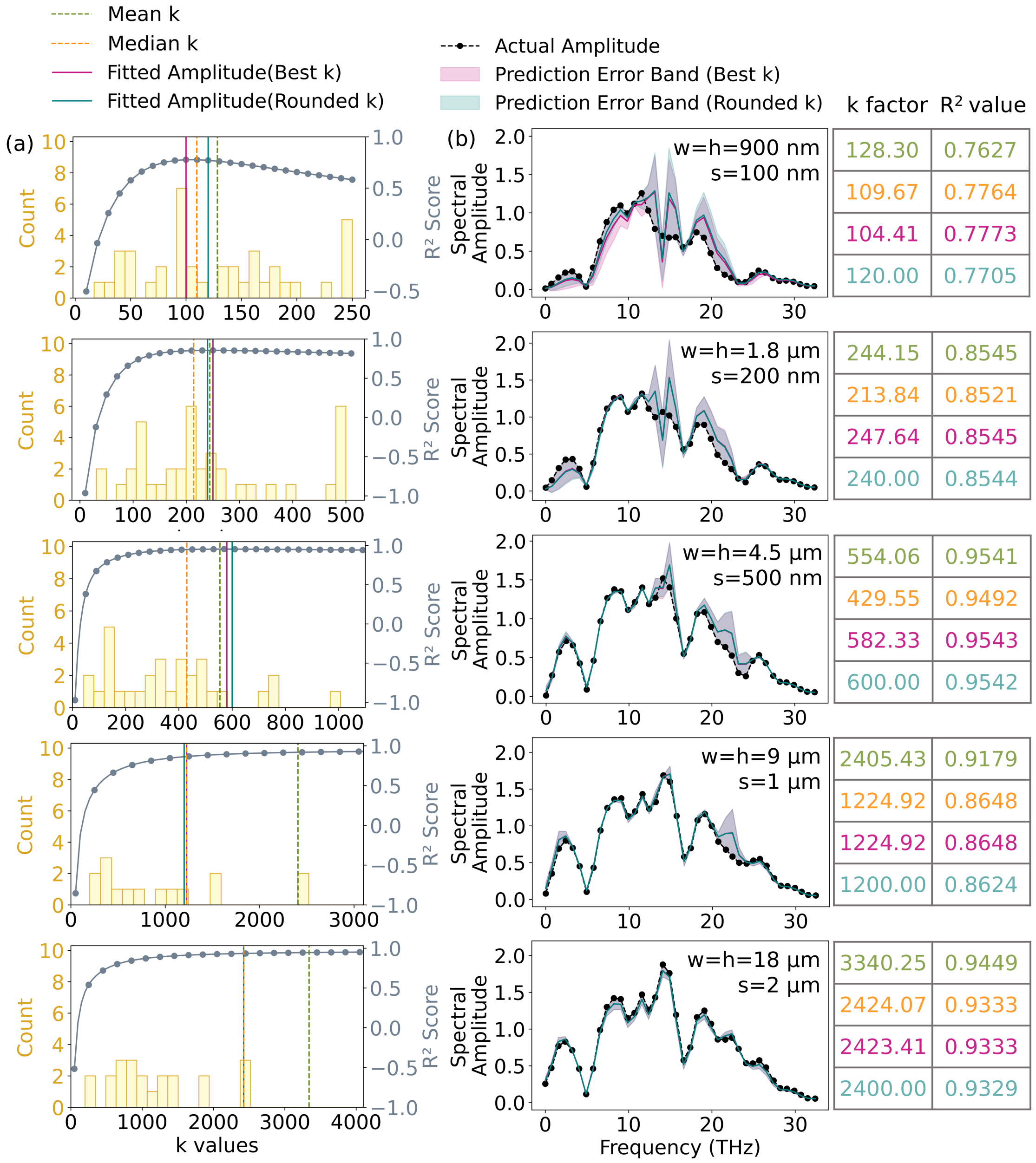

k factor	R² value
128.30	0.7627
109.67	0.7764
104.41	0.7773
120.00	0.7705
244.15	0.8545
213.84	0.8521
247.64	0.8545
240.00	0.8544
554.06	0.9541
429.55	0.9492
582.33	0.9543
600.00	0.9542
2405.43	0.9179
1224.92	0.8648
1224.92	0.8648
1200.00	0.8624
3340.25	0.9449
2424.07	0.9333
2423.41	0.9333
2400.00	0.9329

Figure A.3: (a) Statistical analysis to obtain the mean k, median k values compared to best k values based on R^2 value and rounded k value used for fitting. (b) Curve fitting of spectral amplitudes of square nanoSTEs on sapphire substrate using the analytical model for best k value and rounded k value.

A.5.2 Square nanoSTEs on glass substrate

The histograms (see figure A.4 (a)) and the fitting of spectral amplitudes (see figure A.4 (b)) for glass substrate were also achieved in a similar way. It should be noted that the k_{ref} value in the model is taken as 6000, corresponding to thin film STE (see figure A.2).

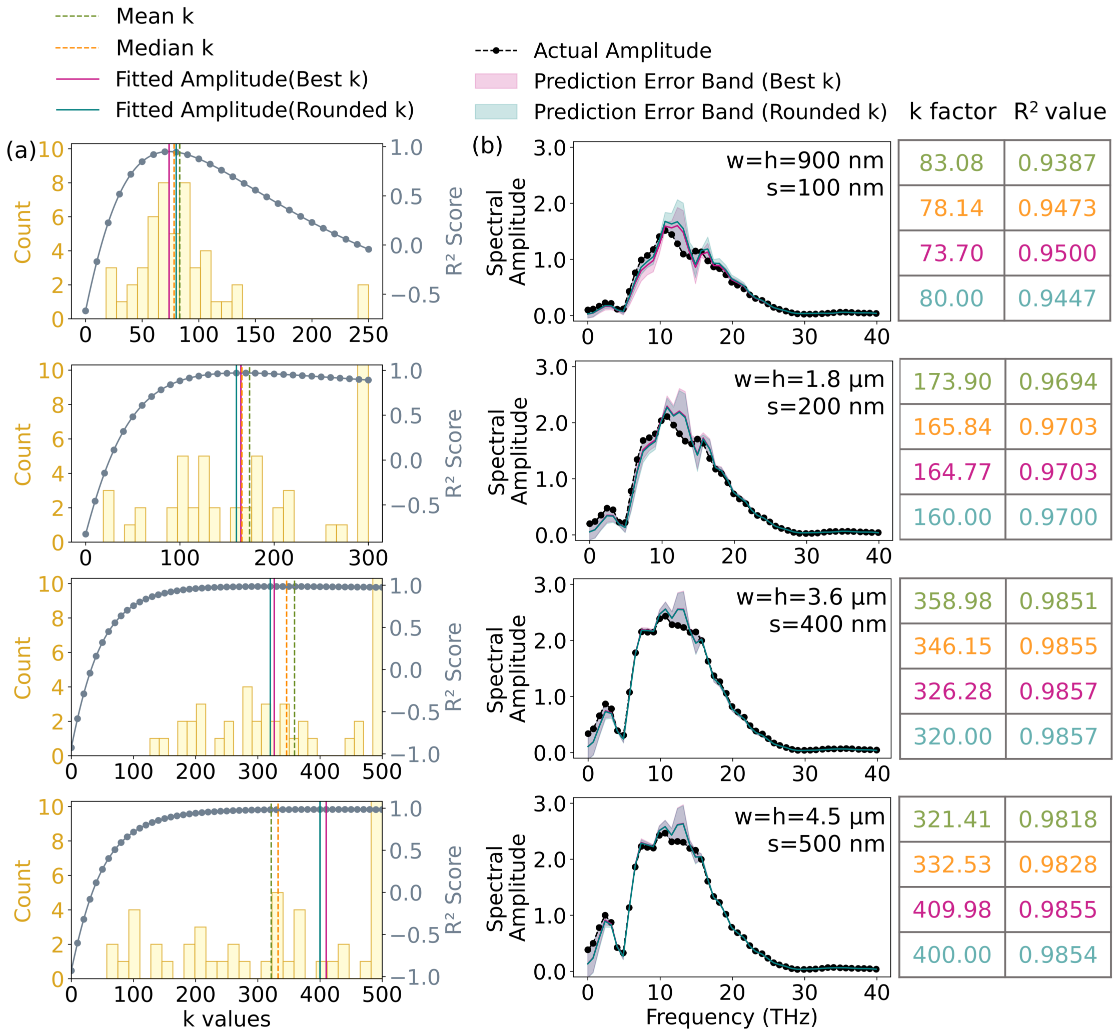

k factor	R² value
83.08	0.9387
78.14	0.9473
73.70	0.9500
80.00	0.9447

k factor	R² value
173.90	0.9694
165.84	0.9703
164.77	0.9703
160.00	0.9700

k factor	R² value
358.98	0.9851
346.15	0.9855
326.28	0.9857
320.00	0.9857

k factor	R² value
321.41	0.9818
332.53	0.9828
409.98	0.9855
400.00	0.9854

Figure A.4: (a) Statistical analysis to obtain the mean k, median k values compared to best k values based on R^2 value and rounded k value used for fitting. (b) Curve fitting of spectral amplitudes of square nanoSTEs on glass substrate using the analytical model for best k value and rounded k value.

A.5.3 Rectangular nanoSTEs

In a similar manner to the previous cases the histograms (see figure A.5 (a)) and curve fitting (see figure A.5 (b)) for rectangular STEs were done for the configurations where the $\vec{M}$ is parallel to constant h and perpendicular to constant h (see figure A.6 (a, b)).

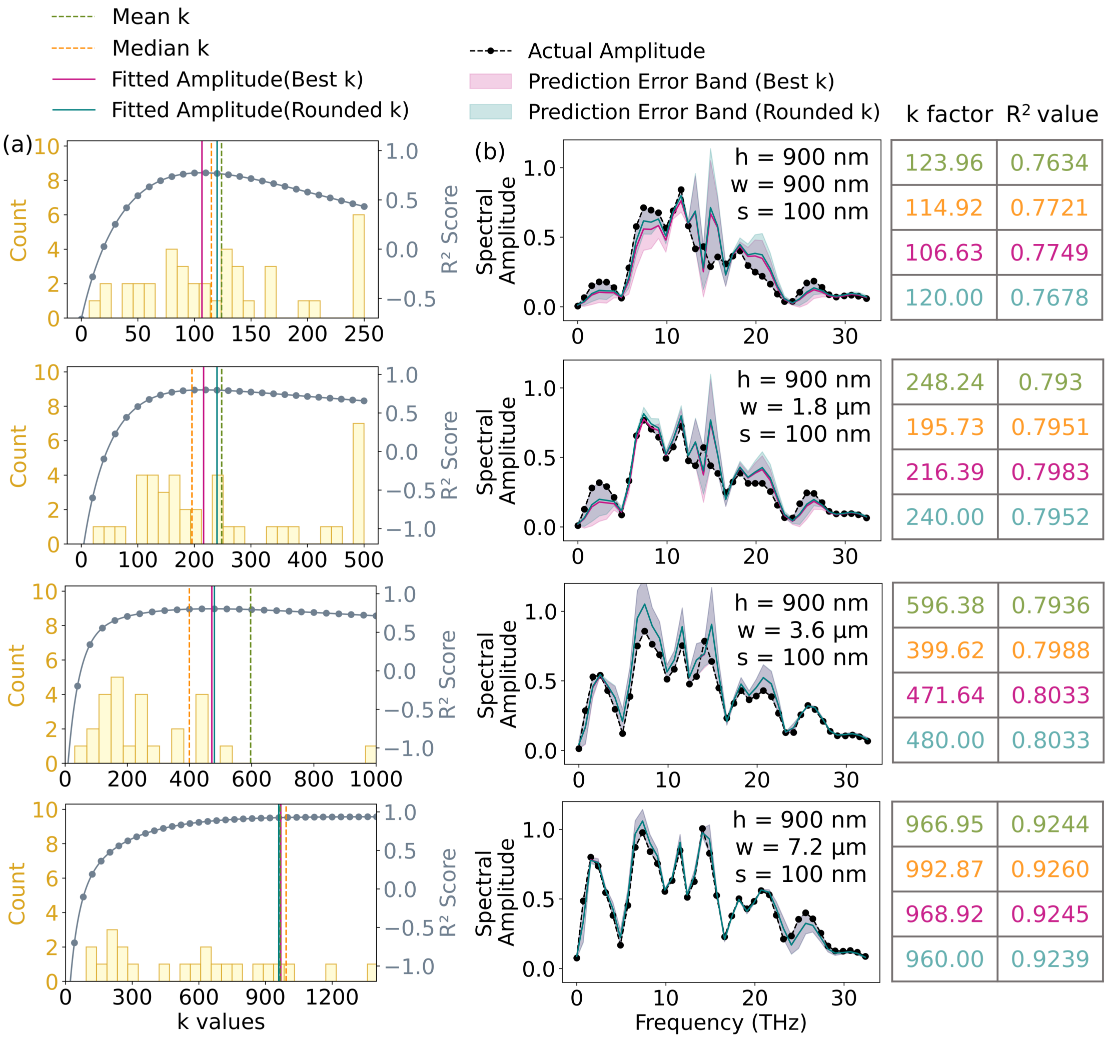

k factor	R² value
123.96	0.7634
114.92	0.7721
106.63	0.7749
120.00	0.7678
248.24	0.793
195.73	0.7951
216.39	0.7983
240.00	0.7952
596.38	0.7936
399.62	0.7988
471.64	0.8033
480.00	0.8033
966.95	0.9244
992.87	0.9260
968.92	0.9245
960.00	0.9239

Figure A.5: (a) Statistical analysis to obtain the mean k, median k values compared to best k values based on R^2 value and rounded k value used for fitting. (b) Curve fitting of spectral amplitudes of rectangular nanoSTEs for the parallel configuration ($\vec{M} \parallel h$) by using the analytical model for best k value and rounded k value.

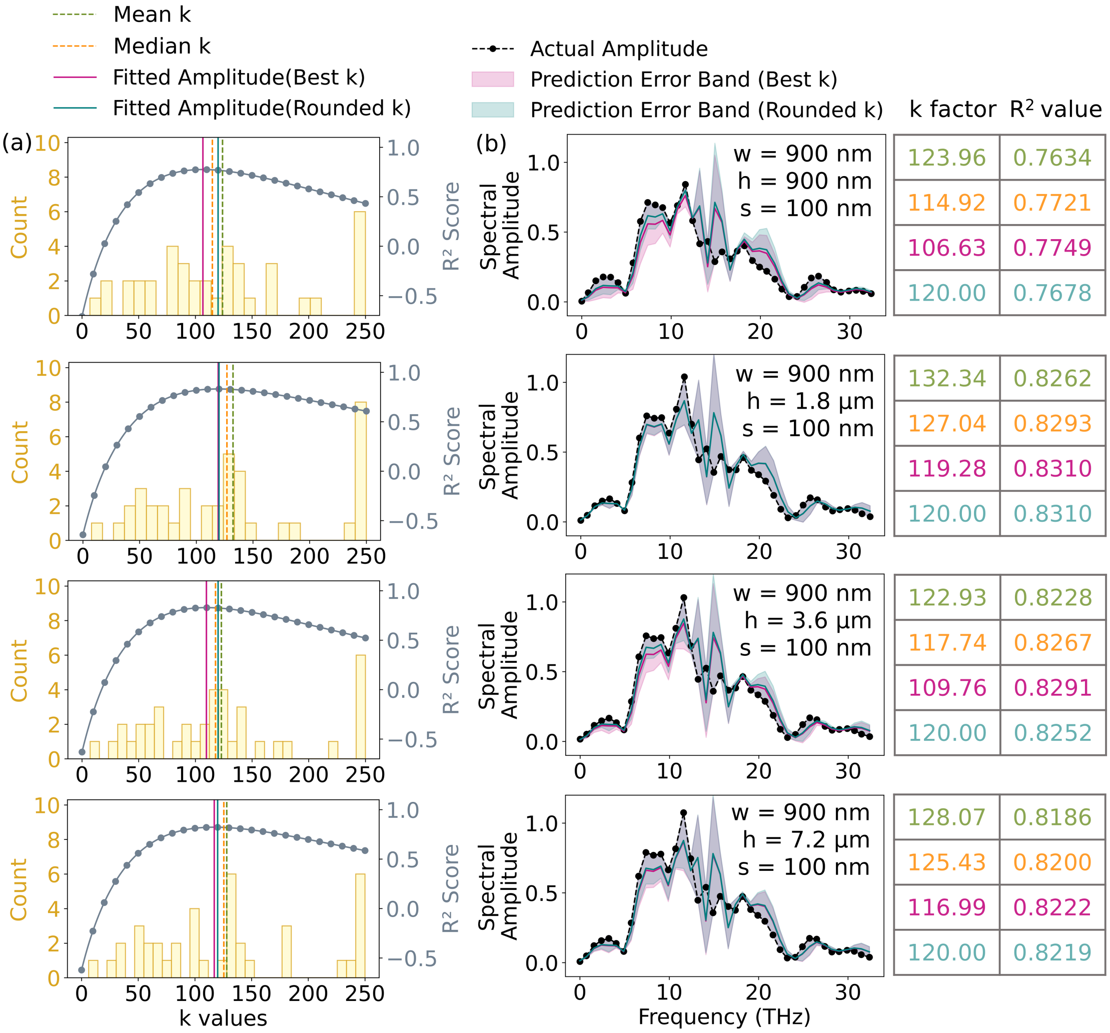

k factor	R^2 value
123.96	0.7634
114.92	0.7721
106.63	0.7749
120.00	0.7678

132.34	0.8262
127.04	0.8293
119.28	0.8310
120.00	0.8310

122.93	0.8228
117.74	0.8267
109.76	0.8291
120.00	0.8252

128.07	0.8186
125.43	0.8200
116.99	0.8222
120.00	0.8219

Figure A.6: (a) Statistical analysis to obtain the mean k, median k values compared to best k values based on R^2 value and rounded k value used for fitting. (b) Curve fitting of spectral amplitudes of rectangular nanoSTEs for the perpendicular configuration ($\vec{M} \perp h$) by using the analytical model for best k value and rounded k value.

A.5.4 Square nanoSTEs with varying spacing

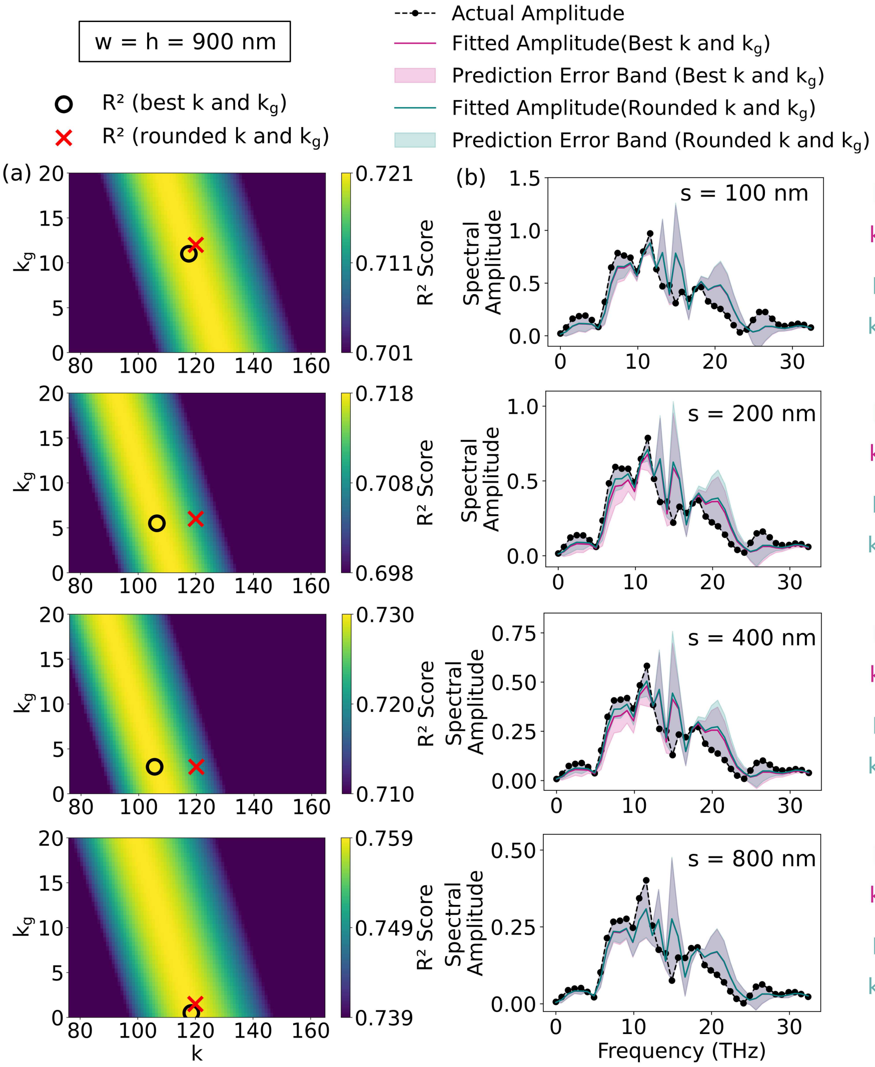

	k factor	R² value
k	117.59	0.7206
k_g	11.0	
k	120	0.7203
k_g	12	
k	106.53	0.7180
k_g	5.5	
k	120	0.7103
k_g	6	
k	105.53	0.7305
k_g	3	
k	120	0.7219
k_g	3	
k	118.59	0.7591
k_g	0.5	
k	120	0.7589
k_g	1.5	

Figure A.7: (a) Statistical analysis to obtain the mean k and k_g, median k and k_g values compared to best k and k_g values based on R^2 value and rounded k and k_g values used for fitting. (b) Curve fitting of spectral amplitudes of square nanoSTEs with varying spacing using the analytical model for best and rounded k and k_g values.

For curve fitting of square nanoSTEs with different spacing the best combination of two model parameters (k and k_g) that fit the experimental frequency-dependent spectral amplitude data was analysed by maximising the R^2 value over a 2D parameter grid of k and k_g values, which is visualised as a heatmap (see figure A.7 (a)). Finally, the best k and k_g

values as per the heatmap and the rounded whole number k and k_g values were fitted corresponding to the experimental spectral amplitudes along with error band (see figure A.7 (b)).

A.5.5 Rectangular nanoSTEs with varying spacing

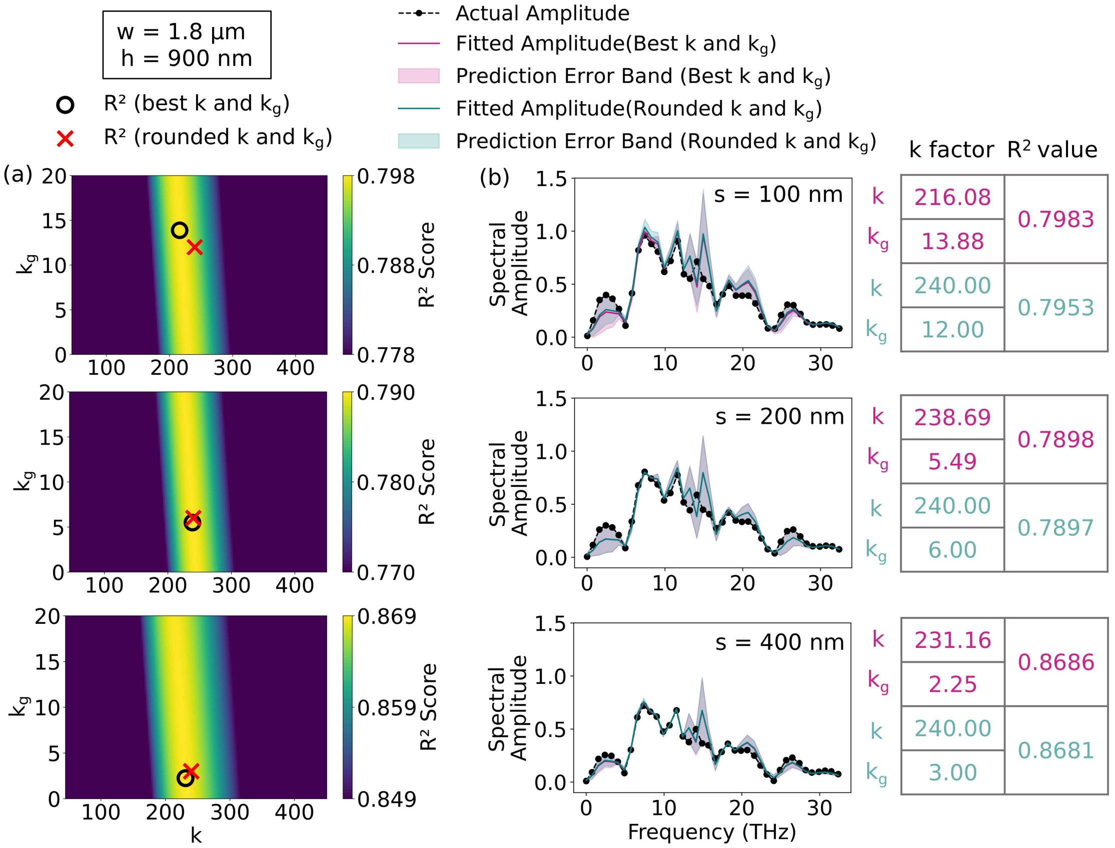

Figure A.8: (a) Statistical analysis to obtain the mean k and k_g, median k and k_g values compared to best k and k_g values based on R^2 value and rounded k and k_g values used for fitting. (b) Curve fitting of spectral amplitudes of rectangular nanoSTEs with varying spacing using the analytical model for best and rounded k and k_g values.

Similarly, the k and k_g values are determined for rectangular nanoSTEs with varying spacing (see figure A.8 (a, b)).

A.6 Electronics

The performance of a Digital to Analog Converter (DAC) or Analog-to-Digital Converter (ADC) is characterised by various parameters, which describe the linearity of a DAC's output i.e its ability to produce a proportional and consistent analog output as a response to a digital input.

A.6.1 Differential Non Linearity

The Differential Non-Linearity (DNL) is a critical linearity parameter for ADCs or DACs and is determined by measuring the difference between the deviations of the ideal and actual output voltages from the corresponding digital inputs [217]. It is then expressed as LSb which is expressed as an ideal deviation of voltage when the difference between the voltages of corresponding digital inputs are calculated. A larger DNL signifies a continuous waveform generation with less deformity. The DNL for the digital code D can be calculated as,

$$\mathrm{DNL_D} = \frac{(\mathrm{V_{D+1}} - \mathrm{V_D}) - (\mathrm{V^{ideal}_{D+1}} - \mathrm{V^{ideal}_{D}})}{\mathrm{V^{ideal}_{D+1}} - \mathrm{V^{ideal}_{D}}} \tag{A.5}$$

where $0 < \mathrm{D} < 2^{\mathrm{N}}$, $\mathrm{V_D}$ is the analog output value corresponding to the digital input code D, N is the total number of bits. The DNL can also be expressed as

$$\mathrm{DNL_D(LSb)} = (\mathrm{V_{D+1}} - \mathrm{V_D})_{\mathrm{LSb}} - \mathrm{V^{ideal}_{LSb}} \tag{A.6}$$

in terms of LSb where $\mathrm{V^{ideal}_{D+1}} - \mathrm{V^{ideal}_{D}}$ is the difference between the analog outputs of two adjacent digital input codes, also referred to as LSb.

A.6.2 Integral Non Linearity

Integral Non-Linearity (INL) is another critical linearity parameter for ADCs or DACs, and it is obtained by adding up all the discrepancies between the desired output and the actual output for each digital input and then expressing the outcome as a fraction of the LSb of the device [217]. Greater accuracy and precision in analog conversion is indicated by smaller INL errors since these errors can lead to significant distortions in the output signal, causing subsequent cumulative system errors which are crucial for precision control. The INL for the digital code D can be calculated as,

$$\mathrm{INL_D} = \sum_{i=0}^{2^N} \mathrm{DNL_i} = \frac{(V_{D+1} - V_{min}) - (V_{D+1}^{ideal} - V_{min}^{ideal})}{V_{D+1}^{ideal} - V_{D}^{ideal}} \tag{A.7}$$

where $0 < D < 2^N$, V_D is the analog output value corresponding to the digital output code D, N is the total number of bits, V_{min}^{ideal} is the voltages corresponding to the minimum digital input. In terms of LSb,

$$\mathrm{INL_D(LSb)} = (V_{D+1} - V_{D+1}^{ideal})_{LSb} \tag{A.8}$$

where $V_{min} = V_{min}^{ideal}$ and $LSb = V_{D+1}^{ideal} - V_{D}^{ideal}$.

B References

[1] S. A. Wolf et al. “Spintronics: a spin-based electronics vision for the future”. en. In: *Science (New York, N.Y.)* 294.5546 (2001), 1488–1495. DOI: `10.1126/science.1065389`.

[2] V. Sverdlov and S. Selberherr. “Silicon spintronics: Progress and challenges”. en. In: *Physics reports* 585 (2015), 1–40. DOI: `10.1016/j.physrep.2015.05.002`.

[3] M. N. Baibich et al. “Giant magnetoresistance of (001)Fe/(001)Cr magnetic superlattices”. en. In: *Physical review letters* 61.21 (1988), 2472–2475. DOI: `10.1103/PhysRevLett.61.2472`.

[4] G. Binasch et al. “Enhanced magnetoresistance in layered magnetic structures with antiferromagnetic interlayer exchange”. en. In: *Physical review. B, Condensed matter* 39.7 (1989), 4828–4830. DOI: `10.1103/physrevb.39.4828`.

[5] J. S. Moodera et al. “Large Magnetoresistance at Room Temperature in Ferromagnetic Thin Film Tunnel Junctions”. In: *Phys. Rev. Lett.* 74 (16 1995), pp. 3273–3276. DOI: `10.1103/PhysRevLett.74.3273`.

[6] C. H. Back et al. “Magnetization reversal in ultrashort magnetic field pulses”. en. In: *Physical review letters* 81.15 (1998), 3251–3254. DOI: `10.1103/physrevlett.81.3251`.

[7] Y. Shiota et al. “Induction of coherent magnetization switching in a few atomic layers of FeCo using voltage pulses”. en. In: *Nature materials* 11.1 (2012), 39–43. DOI: `10.1038/nmat3172`.

[8] T. Nozaki et al. “Recent Progress in the Voltage-Controlled Magnetic Anisotropy Effect and the Challenges Faced in Developing Voltage-Torque MRAM”. In: *Micromachines* 10.5 (2019). DOI: `10.3390/mi10050327`.

[9] J. Grollier et al. “Switching the magnetic configuration of a spin valve by current-induced domain wall motion”. In: *Journal of Applied Physics* 92.8 (10 2002), 4825–4827.

[10] G. E. W. Bauer, E. Saitoh, and B. J. van Wees. “Spin caloritronics”. In: *Nature Materials* 11.5 (May 2012), 391–399.

[11] K. Uchida et al. “Observation of the spin Seebeck effect”. In: *Nature* 455.7214 (Oct. 2008), 778–781.

[12] A. Roe, D. Bhattacharya, and J. Atulasimha. “Resonant acoustic wave assisted spin-transfer-torque switching of nanomagnets”. en. In: *Applied physics letters* 115.11 (2019). DOI: `10.1063/1.5121729`.

[13] T. Kleine-Ostmann and T. Nagatsuma. “A review on terahertz communications research”. en. In: *Journal of infrared, millimeter and terahertz waves* 32.2 (2011), 143–171. DOI: `10.1007/s10762-010-9758-1`.

[14] E. Beaurepaire et al. “Ultrafast Spin Dynamics in Ferromagnetic Nickel”. In: *Phys. Rev. Lett.* 76 (22 1996), pp. 4250–4253. DOI: `10.1103/PhysRevLett.76.4250`.

[15] T. S. Seifert et al. “Efficient metallic spintronic emitters of ultrabroadband terahertz radiation”. In: *Nature Photonics* 10.7 (2016), pp. 483–488. DOI: `10.1038/nphoton.2016.91`.

[16] T. J. Huisman et al. “Femtosecond control of electric currents in metallic ferromagnetic heterostructures”. In: *Nature Nanotechnology* 11.5 (2016), pp. 455–458. DOI: `10.1038/nnano.2015.331`.

[17] J. Walowski and M. Münzenberg. “Perspective: Ultrafast magnetism and THz spintronics”. In: *Journal of Applied Physics* 120.14 (2016), p. 140901. DOI: `10.1063/1.4958846`.

[18] Y. Wu et al. “High-Performance THz Emitters Based on Ferromagnetic/Nonmagnetic Heterostructures”. In: *Advanced Materials* 29.4 (2017), p. 1603031.

[19] G. Torosyan et al. “Optimized Spintronic Terahertz Emitters Based on Epitaxial Grown Fe/Pt Layer Structures”. In: *Scientific Reports* 8.1 (2018), p. 1311. DOI: `10.1038/s41598-018-19432-9`.

[20] E. T. Papaioannou et al. “Efficient Terahertz Generation Using Fe/Pt Spintronic Emitters Pumped at Different Wavelengths”. In: *IEEE Transactions on Magnetics* 54.11 (2018), pp. 1–5.

[21] D. M. Nenno et al. “Modification of spintronic terahertz emitter performance through defect engineering”. In: *Scientific Reports* 9.1 (2019), p. 13348. DOI: `10.1038/s41598-019-49963-8`.

[22] T. H. Dang et al. “Ultrafast spin-currents and charge conversion at 3d-5d interfaces probed by time-domain terahertz spectroscopy”. In: *Applied Physics Reviews* 7.4 (2020), p. 041409. DOI: `10.1063/5.0022369`.

[23] E. T. Papaioannou and R. Beigang. “THz spintronic emitters: a review on achievements and future challenges”. In: *Nanophotonics* 10.4 (2021), pp. 1243–1257. DOI: `doi:10.1515/nanoph-2020-0563`.

[24] C. Bull et al. “Spintronic terahertz emitters: Status and prospects from a materials perspective”. In: *APL Materials* 9.9 (2021), p. 090701. DOI: `10.1063/5.0057511`.

[25] O. Gueckstock et al. “Terahertz Spin-to-Charge Conversion by Interfacial Skew Scattering in Metallic Bilayers”. In: *Advanced Materials* 33.9 (2021), p. 2006281. DOI: `10.1002/adma.202006281`.

[26] Z. Feng et al. “Spintronic terahertz emitter”. In: *Journal of Applied Physics* 129.1 (2021), p. 010901. DOI: `10.1063/5.0037937`.

[27] D. Khusyainov et al. “Polarization control of THz emission using spin-reorientation transition in spintronic heterostructure”. In: *Scientific Reports* 11.1 (2021), p. 697. DOI: `10.1038/s41598-020-80781-5`.

[28] R. Gupta et al. “Co2FeAl full Heusler compound based spintronic terahertz emitter”. In: *Adv. Opt. Mater.* 9 (2021), p. 2001987. DOI: `10.1002/adom.202001987`.

[29] T. S. Seifert et al. “Spintronic sources of ultrashort terahertz electromagnetic pulses”. In: *Applied Physics Letters* 120.18 (2022), p. 180401. DOI: `10.1063/5.0080357`.

[30] T. S. Seifert et al. “Femtosecond formation dynamics of the spin Seebeck effect revealed by terahertz spectroscopy”. In: *Nature Communications* 9.1 (2018), p. 2899. DOI: `10.1038/s41467-018-05135-2`.

[31] R. Schneider et al. “Spintronic GdFe/Pt THz emitters”. In: *Applied Physics Letters* 115.15 (2019), p. 152401. DOI: `10.1063/1.5120249`.

[32] M. Fix et al. “Thermomagnetic control of spintronic THz emission enabled by ferrimagnets”. In: *Applied Physics Letters* 116.1 (2020), p. 012402. DOI: `10.1063/1.5132624`.

[33] K. Cong et al. “Coherent control of asymmetric spintronic terahertz emission from two-dimensional hybrid metal halides”. In: *Nature Communications* 12.1 (2021), p. 5744. DOI: `10.1038/s41467-021-26011-6`.

[34] T. Kampfrath et al. “Terahertz spin current pulses controlled by magnetic heterostructures”. In: *Nature Nanotechnology* 8 (Mar. 2013), p. 256.

[35] W. Hoppe et al. “On-Chip Generation of Ultrafast Current Pulses by Nanolayered Spintronic Terahertz Emitters”. In: *ACS Applied Nano Materials* 4.7 (2021), pp. 7454–7460. DOI: `10.1021/acsanm.1c01449`.

[36] H. S. Qiu et al. “Layer thickness dependence of the terahertz emission based on spin current in ferromagnetic heterostructures”. In: *Opt. Express* 26.12 (2018), pp. 15247–15254. DOI: `10.1364/OE.26.015247`.

[37] D. Yang et al. “Powerful and Tunable THz Emitters Based on the Fe/Pt Magnetic Heterostructure”. In: *Advanced Optical Materials* 4.12 (2016), pp. 1944–1949.

[38] Z. Feng et al. “Highly Efficient Spintronic Terahertz Emitter Enabled by Metal Dielectric Photonic Crystal”. In: *Advanced Optical Materials* 0.0 (2018), p. 1800965. DOI: `10.1002/adom.201800965`.

[39] Y. Ogasawara et al. “Laser-induced terahertz emission from layered synthetic magnets”. In: *Applied Physics Express* 13.6 (2020), p. 063001. DOI: `10.35848/1882-0786/ab88c2`.

[40] J. Li et al. “Magnetic-field-free terahertz emission from a magnetic tunneling junction”. In: *Japanese Journal of Applied Physics* 58.9 (2019), p. 090913. DOI: `10.7567/1347-4065/ab3b75`.

[41] X. Chen et al. “Generation and manipulation of chiral broadband terahertz waves from cascade spintronic terahertz emitters”. In: *Applied Physics Letters* 115.22 (2019), p. 221104. DOI: `10.1063/1.5128979`.

[42] Y. Sasaki, K. Z. Suzuki, and S. Mizukami. "Annealing effect on laser pulse-induced THz wave emission in Ta/CoFeB/MgO films". In: *Applied Physics Letters* 111.10 (2017), p. 102401. DOI: `10.1063/1.5001696`.

[43] L. Scheuer et al. "THz emission from Fe/Pt spintronic emitters with L1_0-FePt alloyed interface". In: *iScience* 25.5 (2022), p. 104319. DOI: `10.1016/j.isci.2022.104319`.

[44] G. Li et al. "Laser induced THz emission from femtosecond photocurrents in Co/ZnO/Pt and Co/Cu/Pt multilayers". In: *Journal of Physics D: Applied Physics* 51.13 (2018), p. 134001. DOI: `10.1088/1361-6463/aaab8f`.

[45] J. Hawecker et al. "Spin Injection Efficiency at Metallic Interfaces Probed by THz Emission Spectroscopy". In: *Advanced Materials* 9.17 (2021), p. 2100412. DOI: `10.1002/adom.202100412`.

[46] R. Rouzegar et al. "Broadband Spintronic Terahertz Source with Peak Electric Fields Exceeding 1.5 MV/cm". In: *Phys. Rev. Appl.* 19 (3 2023), p. 034018. DOI: `10.1103/PhysRevApplied.19.034018`.

[47] R. I. Herapath et al. "Impact of pump wavelength on terahertz emission of a cavity-enhanced spintronic trilayer". In: *Applied Physics Letters* 114.4 (2019), p. 041107. DOI: `10.1063/1.5048297`.

[48] B. Y. Shahriar et al. "Enhanced directive terahertz radiation emission from a horn antenna-coupled W/Fe/Pt spintronic film stack". In: *Applied Physics Letters* 119.9 (2021), p. 092402. DOI: `10.1063/5.0061055`.

[49] M. Talara et al. "Efficient terahertz wave generation of diabolo-shaped Fe/Pt spintronic antennas driven by a 780 nm pump beam". In: *Applied Physics Express* 14.4 (2021), p. 042008. DOI: `10.35848/1882-0786/abeea0`.

[50] U. Nandi et al. "Antenna-coupled spintronic terahertz emitters driven by a 1550 nm femtosecond laser oscillator". In: *Applied Physics Letters* 115.2 (2019), p. 022405. DOI: `10.1063/1.5089421`.

[51] D. L. Mills. *Nonlinear Optics: Basic Concepts*. en. 2nd ed. Berlin, Germany: Springer, 2012.

[52] R. Rouzegar et al. "Laser-induced terahertz spin transport in magnetic nanostructures arises from the same force as ultrafast demagnetization". In: *Phys. Rev. B* 106 (14 2022), p. 144427. DOI: `10.1103/PhysRevB.106.144427`.

[53] C. Haslett. *Essentials of Radio Wave Propagation*. The Cambridge Wireless Essentials Series. Cambridge University Press, 2008.

[54] G. Schmidt, B. Das-Mohapatra, and E. T. Papaioannou. "Charge Dynamics in Spintronic Terahertz Emitters". In: *Phys. Rev. Appl.* 19 (4 2023), p. L041001. DOI: `10.1103/PhysRevApplied.19.L041001`.

[55] C. Kittel. *Introduction to solid state physics*. en. 8th ed. Nashville, TN: John Wiley Sons, 2004.

[56] W. Nolting and A. Ramakanth. *Quantum theory of magnetism*. en. Berlin, Germany: Springer, 2009.

[57] J. Sthr and H. C. Siegmann. *Magnetism: From fundamentals to nanoscale dynamics. Springer series in solid-state sciences, volume 152*. New York, NY: Springer, 2006.

[58] T. Helgaker et al. “Recent advances in wave function-based methods of molecular-property calculations”. en. In: *Chemical reviews* 112.1 (2012), 543–631. DOI: `10.1021/cr2002239`.

[59] M. T. Johnson et al. “Magnetic anisotropy in metallic multilayers”. In: *Reports on progress in physics. Physical Society (Great Britain)* 59.11 (1996), 1409–1458. DOI: `10.1088/0034-4885/59/11/002`.

[60] S. Blundell. *Magnetism in Condensed Matter*. en. London, England: Oxford University Press, 2001.

[61] R. M. White. *Quantum theory of magnetism*. New York, NY: Springer, 2014.

[62] P. Mohn. *Magnetism in the solid state: An introduction*. en. 1st ed. Berlin, Germany: Springer, 2006.

[63] L. Landau and E. Lifshitz. “On the theory of the dispersion of magnetic permeability in ferromagnetic bodies”. In: *Perspectives in Theoretical Physics*. Elsevier, 1992, 51–65.

[64] *Spin dynamics in confined magnetic structures II*. en. 2003rd ed. Berlin, Germany: Springer, 2003.

[65] T. Gilbert. “A phenomenological theory of damping in ferromagnetic materials”. In: *IEEE Transactions on Magnetics* 40.6 (2004), pp. 3443–3449. DOI: `10.1109/TMAG.2004.836740`.

[66] N. Bloembergen. “On the Ferromagnetic Resonance in Nickel and Supermalloy”. In: *The Physical review* 78.5 (1950), 572–580. DOI: `10.1103/physrev.78.572`.

[67] G. Woltersdorf. “Spin-pumping and two-magnon scattering in magnetic multilayers”. In: (2004). DOI: `10.25673/1448`.

[68] J. Stohr and H. C. Siegmann. *Magnetism: From fundamentals to nanoscale dynamics*. en. Berlin, Germany: Springer, 2016.

[69] A. H. Jun et al. “Magnetic properties of amorphous Ta/CoFeB/MgO/Ta thin films on deformable substrates with magnetic field angle and tensile strain”. en. In: *Sensors (Basel, Switzerland)* 23.17 (2023). DOI: `10.3390/s23177479`.

[70] L. Sagnotti. “Magnetic Anisotropy”. In: *Encyclopedia of Solid Earth Geophysics*. Ed. by H. K. Gupta. Dordrecht: Springer Netherlands, 2011, 717–729.

[71] R. P. Cowburn. “Property variation with shape in magnetic nanoelements”. In: *Journal of physics D: Applied physics* 33.1 (2000), R1–R16. DOI: `10.1088/0022-3727/33/1/201`.

[72] A. Aronov. “Spin injection and polarization of excitations and nuclei in superconductors”. In: *Zh. Eksp. Teor. Fiz* 71 (1976), pp. 370–376.

[73] G. Schmidt et al. “Fundamental obstacle for electrical spin injection from a ferromagnetic metal into a diffusive semiconductor”. In: *Phys. Rev. B* 62 (8 2000), R4790–R4793. DOI: `10.1103/PhysRevB.62.R4790`.

[74] M. Büttiker et al. “Generalized many-channel conductance formula with application to small rings”. en. In: *Physical review. B, Condensed matter* 31.10 (1985), 6207–6215. DOI: `10.1103/physrevb.31.6207`.

[75] M. Büttiker. “Four-terminal phase-coherent conductance”. en. In: *Physical review letters* 57.14 (1986), 1761–1764. DOI: `10.1103/PhysRevLett.57.1761`.

[76] P. C. van Son, H. van Kempen, and P. Wyder. “Boundary Resistance of the Ferromagnetic-Nonferromagnetic Metal Interface”. In: *Phys. Rev. Lett.* 58 (21 1987), pp. 2271–2273. DOI: `10.1103/PhysRevLett.58.2271`.

[77] E. I. Rashba. “Theory of electrical spin injection: Tunnel contacts as a solution of the conductivity mismatch problem”. In: *Physical review. B, Condensed matter* 62.24 (2000), R16267–R16270. DOI: `10.1103/physrevb.62.r16267`.

[78] E. I. Rashba. “Diffusion theory of spin injection through resistive contacts”. In: *The European physical journal. B* 29.4 (2002), 513–527. DOI: `10.1140/epjb/e2002-00316-5`.

[79] M. Battiato, K. Carva, and P. M. Oppeneer. “Superdiffusive spin transport as a mechanism of ultrafast demagnetization”. en. In: *Physical review letters* 105.2 (2010), p. 027203. DOI: `10.1103/PhysRevLett.105.027203`.

[80] V. P. Zhukov, E. V. Chulkov, and P. M. Echenique. “Lifetimes of Excited Electrons In Fe And Ni: First-Principles GW and the T-Matrix Theory”. In: *Phys. Rev. Lett.* 93 (9 2004), p. 096401. DOI: `10.1103/PhysRevLett.93.096401`.

[81] V. P. Zhukov, E. V. Chulkov, and P. M. Echenique. “$GW + T$ theory of excited electron lifetimes in metals”. In: *Phys. Rev. B* 72 (15 2005), p. 155109. DOI: `10.1103/PhysRevB.72.155109`.

[82] V. P. Zhukov, E. V. Chulkov, and P. M. Echenique. “Lifetimes and inelastic mean free path of low-energy excited electrons in Fe, Ni, Pt, and Au: Ab initio $\mathrm{GW} + \mathrm{T}$ calculations”. In: *Phys. Rev. B* 73 (12 2006), p. 125105. DOI: `10.1103/PhysRevB.73.125105`.

[83] F. Bloch. “Zur Theorie des Ferromagnetismus”. In: *Zeitschrift für Physik* 61.3 (1930), 206–219.

[84] A. V. Chumak et al. “Magnon spintronics”. en. In: *Nature physics* 11.6 (2015), 453–461. DOI: `10.1038/nphys3347`.

[85] S. Takahashi and S. Maekawa. “Spin current, spin accumulation and spin Hall effect*”. In: *Science and Technology of Advanced Materials* 9.1 (2008), p. 014105.

[86] M. I. D’Yakonov and V. I. Perel’. “Possibility of Orienting Electron Spins with Current”. In: *ZhETF Pisma Redaktsiiu* 13 (1971), p. 657.

[87] E. Saitoh et al. “Conversion of spin current into charge current at room temperature: Inverse spin-Hall effect”. In: *Applied Physics Letters* 88.18 (52006), p. 182509.

[88] L. Berger. “Side-Jump Mechanism for the Hall Effect of Ferromagnets”. In: *Phys. Rev. B* 2 (11 1970), pp. 4559–4566. DOI: `10.1103/PhysRevB.2.4559`.

[89] V. A. d. von der Fakultat fur Physik der Technischen. *Franz Dominik Czeschka*. 2011.

[90] E. H. Hall. “On a New Action of the Magnet on Electric Currents”. In: *American Journal of Mathematics* 2.3 (1879), 287–292.

[91] E. H. Hall. “On the " Rotational Coefficient”. In: *Abt* 12.5 (1881). Ed. by C. P. Mag., 1027–1028.

[92] R. Karplus and J. M. Luttinger. “Hall Effect in Ferromagnetics”. In: *The Physical review* 95.5 (1954), 1154–1160. DOI: `10.1103/physrev.95.1154`.

[93] N. Nagaosa et al. “Anomalous Hall effect”. In: *Rev. Mod. Phys.* 82 (2 2010), pp. 1539–1592. DOI: `10.1103/RevModPhys.82.1539`.

[94] M. V. Berry. “Quantal phase factors accompanying adiabatic changes”. en. In: *Proceedings of the Royal Society of London* 392.1802 (1984), 45–57. DOI: `10.1098/rspa.1984.0023`.

[95] T. Graf, C. Felser, and S. S. P. Parkin. “Simple rules for the understanding of Heusler compounds”. en. In: *Progress in solid state chemistry* 39.1 (2011), 1–50. DOI: `10.1016/j.progsolidstchem.2011.02.001`.

[96] V. Mottamchetty et al. “Direct evidence of terahertz emission arising from anomalous Hall effect”. en. In: *Scientific reports* 13.1 (2023), p. 5988. DOI: `10.1038/s41598-023-33143-w`.

[97] Q. Zhang et al. “Terahertz emission from anomalous hall effect in a single-layer ferromagnet”. en. In: *Physical review applied* 12.5 (2019). DOI: `10.1103/physrevapplied.12.054027`.

[98] J. E. Hirsch. “Spin Hall Effect”. In: *Phys. Rev. Lett.* 83 (9 1999), pp. 1834–1837. DOI: `10.1103/PhysRevLett.83.1834`.

[99] S. Zhang. “Spin Hall Effect in the Presence of Spin Diffusion”. In: *Phys. Rev. Lett.* 85 (2 2000), pp. 393–396. DOI: `10.1103/PhysRevLett.85.393`.

[100] L. Onsager. “Reciprocal Relations in Irreversible Processes. I.” In: *Phys. Rev.* 37 (4 1931), pp. 405–426. DOI: `10.1103/PhysRev.37.405`.

[101] W. M. Saslow and C. Sun. *Onsager Relations between Spin Currents and Charge Currents*. 2024.

[102] T. Kimura et al. “Room-Temperature Reversible Spin Hall Effect”. In: *Phys. Rev. Lett.* 98 (15 2007), p. 156601. DOI: `10.1103/PhysRevLett.98.156601`.

[103] K. Fuchs. “The conductivity of thin metallic films according to the electron theory of metals”. en. In: *Mathematical proceedings of the Cambridge Philosophical Society* 34.1 (1938), 100–108. DOI: `10.1017/s0305004100019952`.

[104] E. H. Sondheimer. "The mean free path of electrons in metals". In: *Advances in physics* 50.6 (2001), 499–537. DOI: 10.1080/00018730110102187.

[105] E. Y. Tsymbal and D. G. Pettifor. "Perspectives of giant magnetoresistance". In: ed. by H. Ehrenreich and F. Spaepen. Vol. 56. Academic Press, 2001, 113–237.

[106] A. Vedyayev et al. "A unified theory of CIP and CPP giant magnetoresistance in magnetic sandwiches". In: *Journal of Magnetism and Magnetic Materials* 172.1 (1997), 53–60.

[107] J. Bass. "CPP-GMR: Materials and properties". en. In: *Handbook of Spintronics*. Dordrecht: Springer Netherlands, 2016, 127–175.

[108] H. Oersted. *Experiments on the effect of a current of electricity on the magnetic needles*. Baldwin, Cradock, and Joy, 1820.

[109] H. Crew. *General Physics*. Macmillan, 1910.

[110] P. A. Adet et al. *Annales de chimie; ou recueil de memoires Concernant la chimie et les Arts qui en dependent. Par (Louis Bernard Guyton) de Morveau, (Antoine Laurent) Lavoisier, (Gaspard) Monge (comte de Peluse), (Claude Louis comte de) Berthollet, (Antoine Francois comte) de Fourcroy, (Philippe Frederic) Baron de Dietrich, (Jean Henri) Hassenfratz et (Pierre Auguste) Adet (gall.)* 1823.

[111] T. C. Chuang et al. "Enhancement of the anomalous Nernst effect in ferromagnetic thin films". In: *Phys. Rev. B* 96 (17 2017), p. 174406. DOI: 10.1103/PhysRevB.96.174406.

[112] S. Pancharatnam. "Generalized theory of interference, and its applications: Part I. Coherent pencils". en. In: *Proceedings of the Indian Academy of Sciences. Mathematical sciences* 44.5 (1956), 247–262. DOI: 10.1007/bf03046050.

[113] K.-I. Uchida et al. "Observation of longitudinal spin-Seebeck effect in magnetic insulators". In: *Applied Physics Letters* 97.17 (10 2010), p. 172505.

[114] A. Ghanbari, M. Esmaeilzadeh, and N. Pournaghavi. "Thermally induced pure and spin polarized currents in a zigzag silicene nanoribbon based FM/normal/AFM junction". In: *Physica E: Low-dimensional Systems and Nanostructures* 95 (2018), 78–85.

[115] Y. Zhou and X. Zheng. "Generating pure spin current with spin-dependent Seebeck effect in ferromagnetic zigzag graphene nanoribbons". In: *Journal of Physics: Condensed Matter* 31.31 (May 2019), p. 315301.

[116] J. Xiao et al. "Theory of magnon-driven spin Seebeck effect". In: *Phys. Rev. B* 81 (21 2010), p. 214418. DOI: 10.1103/PhysRevB.81.214418.

[117] D. Hinzke and U. Nowak. "Domain Wall Motion by the Magnonic Spin Seebeck Effect". In: *Phys. Rev. Lett.* 107 (2 2011), p. 027205. DOI: 10.1103/PhysRevLett.107.027205.

[118] M. Schreier et al. "Magnon, phonon, and electron temperature profiles and the spin Seebeck effect in magnetic insulator/normal metal hybrid structures". In: *Phys. Rev. B* 88 (9 2013), p. 094410. DOI: 10.1103/PhysRevB.88.094410.

[119] H. Adachi et al. "Theory of the spin Seebeck effect". In: *Reports on Progress in Physics* 76.3 (Feb. 2013), p. 036501.

[120] A. Scholl et al. "Ultrafast Spin Dynamics of Ferromagnetic Thin Films Observed by fs Spin-Resolved Two-Photon Photoemission". In: *Phys. Rev. Lett.* 79 (25 1997), pp. 5146–5149. DOI: `10.1103/PhysRevLett.79.5146`.

[121] U. Conrad et al. "Ultrafast electron and magnetization dynamics of thin Ni and Co films on Cu(001) observed by time-resolved SHG". In: *Applied Physics B* 68.3 (Mar. 1999), 511–517.

[122] J. Hohlfeld et al. "Nonequilibrium Magnetization Dynamics of Nickel". In: *Phys. Rev. Lett.* 78 (25 1997), pp. 4861–4864. DOI: `10.1103/PhysRevLett.78.4861`.

[123] B. Koopmans et al. "Ultrafast Magneto-Optics in Nickel: Magnetism or Optics?" In: *Phys. Rev. Lett.* 85 (4 2000), pp. 844–847. DOI: `10.1103/PhysRevLett.85.844`.

[124] L. Guidoni, E. Beaurepaire, and J.-Y. Bigot. "Magneto-optics in the Ultrafast Regime: Thermalization of Spin Populations in Ferromagnetic Films". In: *Phys. Rev. Lett.* 89 (1 2002), p. 017401. DOI: `10.1103/PhysRevLett.89.017401`.

[125] E. Beaurepaire et al. "Coherent terahertz emission from ferromagnetic films excited by femtosecond laser pulses". en. In: *Applied physics letters* 84.18 (2004), 3465–3467. DOI: `10.1063/1.1737467`.

[126] B. Koopmans et al. "Unifying Ultrafast Magnetization Dynamics". In: *Phys. Rev. Lett.* 95 (26 2005), p. 267207. DOI: `10.1103/PhysRevLett.95.267207`.

[127] B. Koopmans et al. "Explaining the paradoxical diversity of ultrafast laser-induced demagnetization". In: *Nature Materials* 9.3 (Mar. 2010), 259–265.

[128] R. J. Elliott. "Theory of the Effect of Spin-Orbit Coupling on Magnetic Resonance in Some Semiconductors". In: *Phys. Rev.* 96 (2 1954), pp. 266–279. DOI: `10.1103/PhysRev.96.266`.

[129] Y. Yafet. "g Factors and Spin-Lattice Relaxation of Conduction Electrons**Part of the work connected with the preparation of this article, in particular the work on spin-lattice relaxation, was done while the author was at the Westinghouse Research Laboratories, Pittsburgh, Pennsylvania". In: ed. by F. Seitz and D. Turnbull. Vol. 14. Academic Press, 1963, 1–98.

[130] M. Krauß et al. "Ultrafast demagnetization of ferromagnetic transition metals: The role of the Coulomb interaction". In: *Phys. Rev. B* 80 (18 2009), p. 180407. DOI: `10.1103/PhysRevB.80.180407`.

[131] E. Carpene et al. "Dynamics of electron-magnon interaction and ultrafast demagnetization in thin iron films". In: *Phys. Rev. B* 78 (17 2008), p. 174422. DOI: `10.1103/PhysRevB.78.174422`.

[132] A. Manchon et al. "Theory of laser-induced demagnetization at high temperatures". In: *Phys. Rev. B* 85 (6 2012), p. 064408. DOI: `10.1103/PhysRevB.85.064408`.

[133] J. K. Dewhurst et al. “Laser-Induced Intersite Spin Transfer”. In: *Nano Letters* 18.3 (2018), 1842–1848.

[134] F. Siegrist et al. “Light-wave dynamic control of magnetism”. In: *Nature* 571.7764 (July 2019), 240–244.

[135] M. Hofherr et al. “Ultrafast optically induced spin transfer in ferromagnetic alloys”. In: *Science Advances* 6.3 (2020), eaay8717.

[136] M. P. Suchea et al. “Functional nanostructured interfaces for environmental and biomedical applications”. en. In: Elsevier, 2019. DOI: `10.1016/c2017-0-01307-1`.

[137] A. S. Gangnaik, Y. M. Georgiev, and J. D. Holmes. “New generation electron beam resists: A review”. en. In: *Chemistry of materials: a publication of the American Chemical Society* 29.5 (2017), 1898–1917. DOI: `10.1021/acs.chemmater.6b03483`.

[138] C. Vieu et al. “Electron beam lithography: resolution limits and applications”. In: *Applied Surface Science* 164.1 (2000), 111–117.

[139] P. Tiwari et al. “Structural modification of poly (methyl methacrylate) due to electron irradiation”. In: *Measurement* 51 (2014), 1–8.

[140] Y.-S. Lee. “Introduction”. In: *Principles of Terahertz Science and Technology*. Boston, MA: Springer US, 2009, 1–9.

[141] T. Löffler et al. “Large-area electro-optic ZnTe terahertz emitters”. en. In: *Optics express* 13.14 (2005), 5353–5362. DOI: `10.1364/opex.13.005353`.

[142] J. Gorchon et al. “Is terahertz emission a good probe of the spin current attenuation length?” In: *Applied Physics Letters* 121.1 (2022). DOI: `10.1063/5.0097448`.

[143] COMSOL Multiphysics® v. 5.4. www.comsol.com. COMSOL AB, Stockholm, Sweden.

[144] A. K. Harman, S. Ninomiya, and S. Adachi. “Optical constants of sapphire ($\alpha{-}Al_2O_3$) single crystals”. In: *Journal of Applied Physics* 76.12 (1994), pp. 8032–8036. DOI: `10.1063/1.357922`.

[145] T. S. Seifert et al. “Terahertz spectroscopy for all-optical spintronic characterization of the spin-Hall-effect metals Pt, W and $Cu_{80}Ir_{20}$”. In: *Journal of Physics D: Applied Physics* 51.36 (2018), p. 364003. DOI: `10.1088/1361-6463/aad536`.

[146] S. Keller et al. “Determination of the spin Hall angle in single-crystalline Pt films from spin pumping experiments”. In: *New Journal of Physics* 20.5 (2018), p. 053002. DOI: `10.1088/1367-2630/aabc46`.

[147] M. A. Ordal et al. “Optical properties of fourteen metals in the infrared and far infrared: Al, Co, Cu, Au, Fe, Pb, Mo, Ni, Pd, Pt, Ag, Ti, V, and W.” In: *Appl. Opt.* 24.24 (1985), pp. 4493–4499. DOI: `10.1364/AO.24.004493`.

[148] H. D. Young, R. A. Freedman, and L. Ford. *University physics with modern physics*. 12th ed. Upper Saddle River, NJ: Pearson, 2007.

[149] H. Hertz. “Ueber sehr schnelle electrische Schwingungen”. en. In: *Annalen der Physik* 267.7 (1887), 421–448. DOI: `10.1002/andp.18872670707`.

[150] O. J. Lodge. “The forces of electric oscillations treated according to maxwell’s theory. By Dr, H. hertz 1”. en. In: *Nature* 39.1008 (1889), 402–404. DOI: `10.1038/039402a0`.

[151] M. R. Querry. *Optical constants*. Contractor Report, Sep. 1982 - May 1984 Missouri Univ., Kansas City. June 1985.

[152] R. Kitamura, L. Pilon, and M. Jonasz. “Optical constants of silica glass from extreme ultraviolet to far infrared at near room temperature”. In: *Appl. Opt.* 46.33 (2007), pp. 8118–8133. DOI: `10.1364/AO.46.008118`.

[153] Z. Jin et al. “Terahertz Radiation Modulated by Confinement of Picosecond Current Based on Patterned Ferromagnetic Heterostructures”. In: *physica status solidi (RRL) Rapid Research Letters* 13.9 (2019), p. 1900057. DOI: `10.1002/pssr.201900057`.

[154] W. Wu et al. “Modification of terahertz emission spectrum using microfabricated spintronic emitters”. In: *Journal of Applied Physics* 128.10 (2020), p. 103902. DOI: `10.1063/5.0013676`.

[155] B. Song et al. “Controlling terahertz radiation with subwavelength blocky patterned CoFeB/Pt heterostructures”. In: *Applied Physics Express* 12.12 (2019), p. 122003. DOI: `10.7567/1882-0786/ab4d2b`.

[156] T. Seifert et al. “Ultrabroadband single-cycle terahertz pulses with peak fields of 300 kV/cm from a metallic spintronic emitter”. In: *Applied Physics Letters* 110.25 (2017), p. 252402. DOI: `10.1063/1.4986755`.

[157] M. Obstbaum et al. “Inverse spin Hall effect in $Ni_{81}Fe_{19}$/normal-metal bilayers”. In: *Phys. Rev. B* 89 (6 2014), p. 060407. DOI: `10.1103/PhysRevB.89.060407`.

[158] S. Mondal et al. “All-optical detection of the spin Hall angle in $\mathrm{W/CoFeB/SiO_2}$ heterostructures with varying thickness of the tungsten layer”. In: *Phys. Rev. B* 96 (5 2017), p. 054414. DOI: `10.1103/PhysRevB.96.054414`.

[159] O. M. Essenwanger. “Elements of statistical analysis”. In: *World survey of climatology., General climatology ;, v. 1B* (1986).

[160] A. Leitenstorfer et al. “Detectors and sources for ultrabroadband electro-optic sampling: Experiment and theory”. In: *Applied Physics Letters* 74.11 (1999), pp. 1516–1518. DOI: `10.1063/1.123601`.

[161] A. Singh et al. “Gapless Broadband Terahertz Emission from a Germanium Photoconductive Emitter”. In: *ACS Photonics* 5.7 (2018), pp. 2718–2723. DOI: `10.1021/acsphotonics.8b00460`.

[162] O. Gueckstock et al. “Modulating the polarization of broadband terahertz pulses from a spintronic emitter at rates up to 10 kHz”. In: *Optica* 8.7 (2021), pp. 1013–1019. DOI: `10.1364/OPTICA.430504`.

[163] D. Systems. *CST Microwave Studio Suite 2022*. 2022.

[164] L. Scalfi and B. Rotenberg. “Microscopic origin of the effect of substrate metallicity on interfacial free energies”. In: *Proceedings of the National Academy of Sciences* 118.50 (2021), e2108769118. DOI: `10.1073/pnas.2108769118`.

[165] A. D. Rakić et al. "Optical properties of metallic films for vertical-cavity optoelectronic devices". In: *Appl. Opt.* 37.22 (1998), pp. 5271–5283. DOI: `10.1364/AO.37.005271`.

[166] H.-T. Chen et al. "Active terahertz metamaterial devices". In: *Nature* 444.7119 (2006), pp. 597–600.

[167] L. Luo et al. "Broadband terahertz generation from metamaterials". In: *Nature Communications* 5.1 (2014), p. 3055.

[168] J. B. Pendry et al. "Magnetism from conductors and enhanced nonlinear phenomena". In: *IEEE transactions on microwave theory and techniques* 47.11 (1999), 2075–2084. DOI: `10.1109/22.798002`.

[169] T. J. Yen et al. "Terahertz magnetic response from artificial materials". en. In: *Science (New York, N.Y.)* 303.5663 (2004), 1494–1496. DOI: `10.1126/science.1094025`.

[170] S. Linden et al. "Magnetic response of metamaterials at 100 terahertz". en. In: *Science (New York, N.Y.)* 306.5700 (2004), 1351–1353. DOI: `10.1126/science.1105371`.

[171] N. Katsarakis et al. "Magnetic response of split-ring resonators in the far-infrared frequency regime". en. In: *Optics letters* 30.11 (2005), 1348–1350. DOI: `10.1364/ol.30.001348`.

[172] C. Enkrich et al. "Magnetic metamaterials at telecommunication and visible frequencies". en. In: *Physical review letters* 95.20 (2005), p. 203901. DOI: `10.1103/PhysRevLett.95.203901`.

[173] N. Katsarakis et al. "Electric coupling to the magnetic resonance of split ring resonators". In: *Applied Physics Letters* 84.15 (42004), 2943–2945.

[174] T. Koschny et al. "Effective medium theory of left-handed materials". en. In: *Physical review letters* 93.10 (2004), p. 107402. DOI: `10.1103/PhysRevLett.93.107402`.

[175] S. A. Wolf et al. "The promise of nanomagnetics and spintronics for future logic and universal memory". In: *Proceedings of the IEEE. Institute of Electrical and Electronics Engineers* 98.12 (2010), 2155–2168. DOI: `10.1109/jproc.2010.2064150`.

[176] J. A. Currivan et al. "Low energy magnetic domain wall logic in short, narrow, ferromagnetic wires". In: *IEEE magnetics letters* 3 (2012), 3000104–3000104. DOI: `10.1109/lmag.2012.2188621`.

[177] B. Behin-Aein et al. "Proposal for an all-spin logic device with built-in memory". en. In: *Nature nanotechnology* 5.4 (2010), 266–270. DOI: `10.1038/nnano.2010.31`.

[178] D. M. Bromberg et al. "Novel STT-MTJ device enabling all-metallic logic circuits". In: *IEEE transactions on magnetics* 48.11 (2012), 3215–3218. DOI: `10.1109/tmag.2012.2197186`.

[179] T. Gerrits et al. "Ultrafast precessional magnetization reversal by picosecond magnetic field pulse shaping". en. In: *Nature* 418.6897 (2002), 509–512. DOI: `10.1038/nature00905`.

[180] K. Garello et al. "Ultrafast magnetization switching by spin-orbit torques". en. In: *Applied physics letters* 105.21 (2014), p. 212402. DOI: `10.1063/1.4902443`.

[181] K. Mistry et al. "A 45nm Logic Technology with High-k+Metal Gate Transistors, Strained Silicon, 9 Cu Interconnect Layers, 193nm Dry Patterning, and 100Pb-free Packaging". In: *2007 IEEE International Electron Devices Meeting*. 2007, pp. 247–250. DOI: `10.1109/IEDM.2007.4418914`.

[182] A. Kirilyuk, A. V. Kimel, and T. Rasing. "Erratum: Ultrafast optical manipulation of magnetic order [Rev. Mod. Phys.82, 2731 (2010)]". In: *Reviews of modern physics* 88.3 (2016). DOI: `10.1103/revmodphys.88.039904`.

[183] K. Yoshioka et al. "On-chip coherent frequency-domain THz spectroscopy for electrical transport". In: *Applied Physics Letters* 117.16 (Oct. 2020), p. 161103. DOI: `10.1063/5.0024089`.

[184] G. K. P. Ramanandan et al. "Emission of terahertz pulses from nanostructured metal surfaces". In: *Journal of Physics D: Applied Physics* 47.37 (2014), p. 374003. DOI: `10.1088/0022-3727/47/37/374003`.

[185] J. E. Nkeck et al. "Parallel generation and coding of a terahertz pulse train". In: *APL Photonics* 7.12 (Dec. 2022), p. 126105. DOI: `10.1063/5.0123697`.

[186] B. Liu et al. "Generation of narrowband, high-intensity, carrier-envelope phase-stable pulses tunable between 4 and 18&#x2009;&#x2009;THz". In: *Opt. Lett.* 42.1 (2017), pp. 129–131. DOI: `10.1364/OL.42.000129`.

[187] A. Cartella et al. "Narrowband carrier-envelope phase stable mid-infrared pulses at wavelengths beyond 10&#x2009;&#x2009;&#x03BC;m by chirped-pulse difference frequency generation". In: *Opt. Lett.* 42.4 (2017), pp. 663–666. DOI: `10.1364/OL.42.000663`.

[188] S. Zhuang et al. "A Narrowband Spintronic Terahertz Emitter Based on Magnetoelastic Heterostructures". In: *ACS Applied Materials & Interfaces* 13.41 (2021). PMID: 34617721, pp. 48997–49006. DOI: `10.1021/acsami.1c13461`.

[189] B. Globisch et al. "Iron doped InGaAs: Competitive THz emitters and detectors fabricated from the same photoconductor". In: *Journal of Applied Physics* 121.5 (22017), p. 053102.

[190] L. Smith et al. "Tapered transmission lines for terahertz systems". In: *Opt. Express* 29.11 (2021), pp. 17295–17303. DOI: `10.1364/OE.421008`.

[191] S. Yanagi et al. "Propagation of Terahertz Pulses on Coplanar Strip-lines on Low Permittivity Substrates and a Spectroscopy Application". In: *Applied Physics Express* 1.1 (2008), p. 012009. DOI: `10.1143/APEX.1.012009`.

[192] I. Hickman. "Chapter 3 - Active components". In: *Analog Electronics*. Ed. by I. Hickman. Newnes, 1990, pp. 44–75. DOI: `https://doi.org/10.1016/B978-0-434-90723-6.50008-0`.

[193] E. I. GREEN. "THE STORY OF Q". In: *American Scientist* 43.4 (1955), pp. 584–594.

[194] F Lehmann et al. "Fabrication of sub-10-nm Au–Pd structures using 30 keV electron beam lithography and lift-off". In: *Microelectronic Engineering* 65.3 (2003), pp. 327–333. DOI: `https://doi.org/10.1016/S0167-9317(02)00963-2`.

[195] M. Brands et al. "Reversal processes and domain wall pinning in polycrystalline Co-nanowires". en. In: *Physical review. B, Condensed matter and materials physics* 74.17 (2006). DOI: `10.1103/physrevb.74.174411`.

[196] A. Fernández-Pacheco et al. "Magnetization reversal in individual cobalt micro- and nanowires grown by focused-electron-beam-induced-deposition". In: *Nanotechnology* 20.47 (2009), p. 475704. DOI: `10.1088/0957-4484/20/47/475704`.

[197] B. Leven and G. Dumpich. "Resistance behavior and magnetization reversal analysis of individual Co nanowires". en. In: *Physical review. B, Condensed matter and materials physics* 71.6 (2005). DOI: `10.1103/physrevb.71.064411`.

[198] W. C. Uhlig and J. Shi. "Systematic study of the magnetization reversal in patterned Co and NiFe Nanolines". en. In: *Applied physics letters* 84.5 (2004), 759–761. DOI: `10.1063/1.1645332`.

[199] Z. Zhu et al. "Static and dynamic magnetic properties of stripe-patterned Fe20Ni80 soft magnetic films". In: *Journal of Physics D: Applied Physics* 51.4 (2018), p. 045004.

[200] W.-H. Xu et al. "Copper Nanowires as Nanoscale Interconnects: Their Stability, Electrical Transport, and Mechanical Properties". In: *ACS Nano* 9.1 (2015). PMID: 25521157, pp. 241–250. DOI: `10.1021/nn506583e`.

[201] J. A. Katine et al. "Current-Driven Magnetization Reversal and Spin-Wave Excitations in Co /Cu /Co Pillars". In: *Phys. Rev. Lett.* 84 (14 2000), pp. 3149–3152. DOI: `10.1103/PhysRevLett.84.3149`.

[202] M. Stiles and J. Miltat. "Spin-transfer torque and dynamics". In: *Spin dynamics in confined magnetic structures III*. Springer, 2006, 225–308.

[203] M. Julliere. "Tunneling between ferromagnetic films". In: *Physics Letters A* 54.3 (1975), 225–226.

[204] T. Miyazaki and N. Tezuka. "Giant magnetic tunneling effect in Fe/Al2O3/Fe junction". In: *Journal of Magnetism and Magnetic Materials* 139.3 (1995), L231–L234.

[205] G. Malinowski et al. "Control of speed and efficiency of ultrafast demagnetization by direct transfer of spin angular momentum". In: *Nature Physics* 4.11 (Nov. 2008), 855–858.

[206] W. He et al. "Ultrafast demagnetization enhancement in CoFeB/MgO/CoFeB magnetic tunneling junction driven by spin tunneling current". In: *Scientific Reports* 3.1 (Oct. 2013), p. 2883.

[207] R. Law et al. "Effects of Ta seed layer and annealing on magnetoresistance in CoFePd-based pseudo-spin-valves with perpendicular anisotropy". In: *Applied Physics Letters* 91.24 (12 2007), p. 242504.

[208] Y. K. Kim. “Soft magnetic properties of sub 10 nm NiFe and Co films encapsulated with Ta or Cu”. In: *physica status solidi (a)* 201.8 (2004), 1859–1861.

[209] L. Gao et al. “Enhanced tunneling spin polarization from ultrathin layers of amorphous CoFe”. In: *Applied Physics Letters* 95.12 (92009), p. 122503.

[210] J. J. Picconatto, M. J. Pechan, and E. E. Fullerton. “Magnetic anisotropy, coupling, and transport in epitaxial Co/Cr superlattices on MgO(100) and (110) substrates”. In: *Journal of Applied Physics* 81.8 (41997), 5058–5060.

[211] J. Lombard, F. Detcheverry, and S. Merabia. “Influence of the electron–phonon interfacial conductance on the thermal transport at metal/dielectric interfaces”. In: *Journal of Physics: Condensed Matter* 27.1 (Nov. 2014), p. 015007.

[212] V. Cherepanov, I. Kolokolov, and V. L’vov. “The saga of YIG: Spectra, thermodynamics, interaction and relaxation of magnons in a complex magnet”. In: *Physics Reports* 229.3 (1993), 81–144.

[213] Z. Duan et al. “The Longitudinal Spin Seebeck Coefficient of Fe”. In: *IEEE Magnetics Letters* 10 (2019), pp. 1–5.

[214] E. Villamor et al. “Temperature dependence of spin polarization in ferromagnetic metals using lateral spin valves”. In: *Phys. Rev. B* 88 (18 2013), p. 184411. DOI: `10.1103/PhysRevB.88.184411`.

[215] R. C. Munoz and C. Arenas. “Size effects and charge transport in metals: Quantum theory of the resistivity of nanometric metallic structures arising from electron scattering by grain boundaries and by rough surfaces”. In: *Applied Physics Reviews* 4.1 (22017), p. 011102.

[216] R. B. Blackman, J. W. Tukey, and T. Teichmann. “the measurement of power spectra”. en. In: *Physics today* 13.2 (1960), 52–54. DOI: `10.1063/1.3056826`.

[217] M. J. Demler. “Preface”. In: *High-Speed Analog-to-Digital Conversion*. Ed. by M. J. Demler. San Diego: Academic Press, 1991, i–xiv.

List of Publications(s)

- G. Schmidt, B. Das-Mohapatra, and E. T. Papaioannou. “Charge Dynamics in Spintronic Terahertz Emitters”.
  In: Phys. Rev. Appl. 19 (2023), p. L041001
  doi: *https://doi.org/10.1103/PhysRevApplied.19.L041001*

- B. Das-Mohapatra, R. Rouzegar, E. T. Papaioannou, T. Kampfrath and G. Schmidt. "Controlling charge dynamics in nanopatterned spintronic terahertz emitters".
  In: Phys. Rev. Appl. 23 (2025), p. 014024
  doi: *https://doi.org/10.1103/PhysRevApplied.23.014024*

- B. Das-Mohapatra, N. Kanistras, A. Busse, E. T. Papaioannou and G. Schmidt. "On chip digital to analog converters for ultrafast signals using spintronic terahertz emitters".
  In: Appl. Phys. Lett. 127 (20), 204103 (2025)
  doi: *https://doi.org/10.1063/5.0291032*

- B. Das-Mohapatra, E. T. Papaioannou and G. Schmidt. "Narrowband terahertz emitters". *In preparation*

- B. Das-Mohapatra, E. T. Papaioannou and G. Schmidt. "Switchable terahertz emitters". *In preparation*

Curriculum vitae

Name: Bikash Das Mohapatra

Education

2018-2023	**Doctoral studies in Physics** Martin-Luther-University Halle-Wittenberg, Halle (Saale), Germany Thesis : "Tailoring spintronic terahertz emitters for special applications"
2012-2017	**Integrated Bachelors and Masters in Physics** National Institute of Science Education and Research (NISER), Bhubaneswar, India Thesis : "Study of spin torque using ferromagnetic resonance spectroscopy"

Work Experience

2017-2018	**Graduate Research Assistant** Department of Physics and Astronomy, University of Nebraska Lincoln, Lincoln, USA
2015	**Guest Scientist** Institut für Physik, Universität Greifswald, Greifswald, Germany
2014	**Visiting Researcher** S.N.Bose National Centre for Basic Sciences (SNBNCBS), Kolkata, India

Halle (Saale), 12.09.2024 Bikash Das Mohapatra

Eidesstattliche Erklärung (Statutory declaration)

Hiermit erkläre ich, Bikash Das Mohapatra, die vorliegende Arbeit, "Tailoring spintronic terahertz emitters for special applications", selbständig und ohne fremde Hilfe verfasst zu haben. Es wurden keine anderen als die von mir angegebenen Quellen und Hilfsmittel benutzt. Die den benutzten Werken wörtlich oder inhaltlich entnommenen Stellen sind als solche kenntlich gemacht worden. Ich erkläre, die Angaben wahrheitsgemäβ gemacht, keine vergeblichen Promotionsversuche unternommen und keine Dissertation an einer anderen wissenschaftlichen Einrichtung zur Erlangung eines akademischen Grades eingereicht zu haben. Ich bin weder vorbestraft noch sind gegen mich Ermittlungsverfahren anhängig.

I, Bikash Das Mohapatra, hereby declare that I have written the present work, "Tailoring spintronic terahertz emitters for special applications". No sources other than those cited by me were used. Elements quoting directly from, or making reference to, such sources have been identified as such. I declare that I have provided this information truthfully, that I have not made any previous unsuccessful attempts at doctoral studies, and that I have not submitted either the current version or another version of this thesis to another academic institution for the purpose of obtaining an academic degree. I do not have any prior criminal convictions, nor am I subject to any preliminary investigations.

Halle (Saale), 12.09.2024 Bikash Das Mohapatra

Acknowledgement

First of all, I would like to express my sincere gratitude to Prof. Dr. Georg Schmidt for providing me with the opportunity to learn and experience various state-of-the-art fabrication and measurement techniques in the Nanostructured Materials group. I would also like to thank him for his continuous support in every situation during the doctoral period with informative discussions and guidance.

Prof. Dr. Evangelos T. Papaioannou deserves my special thanks for his continuous support with expert advice, suggestions, and mentoring throughout the doctoral period. I express my sincere thanks to Dr. Mohammad Qaid and Nikos Kanistras for various coffee break discussions and brainstorming sessions.

I would like to thank Dr. Reza Rouzegar and Prof. Dr. Tobias Kampfrath for various free space THz measurements and discussions on various projects within the project B02 of the TRR227. In addition, I would like to thank Wolfgang Hoppe and Prof. Dr. Georg Woltersdorf, for providing assistance and suggestions on various experiments performed in the THz electrical detection setup.

I would like to thank Dr. Frank Heyroth and Frank Syrowatka for providing SEM images of various samples and the productive discussions about electron beam lithography and Ms. Katrin Lehmann for helping during the fabrication process. I also thank Dr. Bodo Fuhrmann and Sven Schlenker for their active help and support in the clean room. I would like to thank Ms. Kathrin Bennewitz for taking care of all the bureaucratic work.

Furthermore, I would like to thank the DFG project, SFB-TRR227, for providing financial assistance for this work and organising various collaborations and regular meetings with other members of the consortium for the exchange of knowledge about their research. I would especially like to thank Britta for the regular organisation of PhD seminars, training modules, and soft skill courses within the iRTG, which proved quite helpful in my overall personal growth.

I would like to thank my friends Arka and Ayush, who have been constant pillars in my life since my Bachelor and Master. I would also like to thank Banabir, Rima di, Abhay, Samiran, and Anirban, who have supported me in all circumstances during my time in Halle. I also thank all my friends and colleagues , especially Dr. Richard Boucher, for proofreading my doctoral thesis and helping me make it better.

Finally, I would like to thank my family, especially my parents and grandparents, whose blessings and support have always been with me throughout my life, my wife Sheetal, who has supported me through thick and thin with constant motivation and encouragement and my little brother Bibek.